Wearable Medical Sensors Enabled by Printed Bioelectronics and Biophotonics

Yasser Khan

Electrical Engineering and Computer Sciences
University of California at Berkeley

Technical Report No. UCB/EECS-2020-189
http://www2.eecs.berkeley.edu/Pubs/TechRpts/2020/EECS-2020-189.html

December 1, 2020

Wearable Medical Sensors Enabled by Printed Bioelectronics and Biophotonics

by

Yasser Muhammad Tasif Khan

A dissertation submitted in partial satisfaction of the

requirements for the degree of

Doctor of Philosophy

in

Engineering - Electrical Engineering and Computer Sciences

in the

Graduate Division

of the

University of California, Berkeley

Committee in charge:

Professor Ana Claudia Arias, Chair
Professor Jan Rabaey
Professor Liwei Lin

Fall 2018

Wearable Medical Sensors Enabled by Printed Bioelectronics and Biophotonics

Yasser Muhammad Tasif Khan

Abstract

Wearable Medical Sensors Enabled by Printed Bioelectronics and Biophotonics

by

Yasser Muhammad Tasif Khan
Doctor of Philosophy in Engineering - Electrical Engineering and Computer Sciences

University of California, Berkeley
Professor Ana Claudia Arias, Chair

Wearable medical sensors that can monitor biosignals have the potential to transform healthcare - they encourage healthy living by providing individuals feedback on personal vital signs and enable facile implementation of both in-hospital and in-home health monitoring. To date, fabrication of wearable medical sensors heavily relies on conventional semiconductor vacuum-processing, which is expensive and has limited large-area scalability. Taking advantage of the unique manufacturing capabilities of printed electronics, we can now design wearables that are soft, lightweight, and skin-like. These soft and conformable sensors significantly improve the signal-to-noise ratio (SNR) by establishing high-fidelity sensor-skin interfaces.

This thesis presents a review of existing literature on flexible and wearable health monitoring devices, discusses different printing techniques for fabricating wearable medical sensors, and highlights two sensing modalities: bioelectronic and biophotonic. For bioelectronic sensing, the design and fabrication of flexible and inkjet-printed gold electrode arrays are demonstrated, which are implemented in a smart bandage for early-detection of pressure ulcers. Also, the efficacy of the electrodes is demonstrated on conformal surfaces and on the skin to record electrocardiography (ECG) and electromyography (EMG) signals. For biophotonic sensing, an all-organic optoelectronic sensor is demonstrated for transmission-mode pulse oximetry, which accurately measures pulse rate and oxygenation. Since transmission-mode pulse oximetry can only be performed at the extremities of the body and requires a pulsatile arterial blood signal - printed, organic, reflection-mode oximeters are reported. The design, sensing methodology, and fabrication of a flexible and printed sensor array composed of organic light-emitting diodes (OLEDs) and organic photodiodes (OPDs) are shown, which senses reflected light from tissue to determine the oxygen saturation. The sensor is implemented to measure oxygen saturation on different parts of the body and to create 2D oxygenation maps of adult forearms under pressure-cuff-induced ischemia. Finally, a key enabling technology for wearables - flexible hybrid electronics (FHE) is presented. The implementation of FHE in an integrated multi-sensor platform is discussed, where soft sensors are interfaced with hard silicon-based integrated circuits for wearable health monitoring.

This dissertation is dedicated to the joyful memories of my late father,
Dr. Md. Faiz Ahmad Khan

Contents

Contents ii

List of Figures iv

List of Tables viii

1 Introduction 1
- 1.1 Flexible health monitoring devices . . . 3
- 1.2 Fabrication process for flexible medical devices . . . 19
- 1.3 Medical sensor data processing and transmission . . . 21
- 1.4 Power requirements for flexible medical devices . . . 23
- 1.5 Scope of this thesis . . . 26

2 Printed biopotential and bioimpedance electrodes 30
- 2.1 Introduction . . . 30
- 2.2 Printed electrodes for bioelectronic interfaces . . . 32
- 2.3 Flexible inkjet-printed gold electrode array . . . 34
- 2.4 Plastic-compatible low-temperature sintering . . . 37
- 2.5 Sintering mechanism . . . 40
- 2.6 Electrical reproducibility and mechanical robustness of the printed array . . . 42
- 2.7 Electrical impedance mapping of two-dimensional surfaces using the printed array . . . 43
- 2.8 A smart bandage for early detection of pressure ulcers . . . 46
- 2.9 Printed electrocardiography (ECG) electrodes . . . 50
- 2.10 Printed electromyography (EMG) electrodes . . . 57
- 2.11 Chapter conclusions . . . 59

3 Printed transmission-mode oximeter 61
- 3.1 Introduction . . . 61
- 3.2 Pulse and oxygenation with red and green organic light-emitting diode (OLED)s 62
- 3.3 Organic optoelectronic oximeter components . . . 65
- 3.4 System design for an organic optoelectronic pulse oximeter . . . 71
- 3.5 Chapter conclusions . . . 71

4 Printed reflection-mode oximeter **74**
4.1 Introduction . . . 74
4.2 Reflectance oximeter sensor geometries and operation . . . 75
4.3 Sensor assembly and calibration . . . 78
4.4 Performance comparison among different sensor geometries . . . 79
4.5 Multi-channel photoplethysmography (PPG) sensor operation and data processing 82
4.6 Implementation of template matching (TM) and inverse-variance weighting (IVW) algorithms on the printed multi-channel PPG sensor data . . . 85
4.7 Chapter conclusions . . . 86

5 Printed reflection-mode oximeter array **88**
5.1 Introduction . . . 88
5.2 Analytical models for reflectance oximetry . . . 93
5.3 Reflectance oximeter design and placement on the body . . . 96
5.4 OLED and organic photodiode (OPD) array fabrication and characterization . . . 97
5.5 System setup and single pixel reflection-mode pulse oximetry . . . 103
5.6 *in-vivo* 2D oxygen saturation monitoring . . . 107
5.7 Chapter conclusions . . . 112

6 Flexible hybrid electronics **115**
6.1 Introduction . . . 115
6.2 Wearable sensor patch . . . 116
6.3 Single-substrate integration by direct printing of sensors on Kapton polyimide (PI) substrate . . . 118
6.4 Inkjet-printed gold ECG electrodes . . . 118
6.5 Stencil-printed nickel oxide thermistors . . . 122
6.6 Fabrication process for the wearable sensor patch (WSP) . . . 125
6.7 Real-time ECG signal monitoring with the WSP . . . 130
6.8 Improving printed gold to plated copper interface . . . 135
6.9 Battery lifetime of the WSP . . . 141
6.10 Chapter conclusions . . . 142

7 Conclusions & outlook **143**
7.1 Integrated bioelectronic and biophotonic bandage for wound monitoring . . . 144
7.2 Wearable multi-sensor platform for continuous health monitoring . . . 146
7.3 Printed large-area sensor array for structural health monitoring . . . 147
7.4 Flexible hybrid electronics for industrial and environmental monitoring . . . 148
7.5 Outlook . . . 148

List of Figures

1.1 Overview of a wearable sensor platform, where flexible sensors are utilized for real-time health monitoring . . . 2
1.2 System flow of biosensors and a graphical overview of this chapter . . . 3
1.3 Biosignals and sensing locations . . . 4
1.4 Stretchable graphene thermistors and characterization . . . 5
1.5 ECG using a flexible and stretchable sensor system . . . 8
1.6 heart rate (HR) monitoring using pressure sensors . . . 10
1.7 Wearable textile- and carbon nanomaterials-based respiration sensors . . . 12
1.8 Blood pressure wave measurements on the wrist and neck using a pressure sensitive transistor . . . 15
1.9 Pictorial overview of this thesis . . . 29

2.1 Printed electrodes for biopotential and bioimpedance measurements . . . 31
2.2 Fabrication process for manufacturing the printed electrode array . . . 33
2.3 Methods for removing the dielectric layer (Cytop) from the electrodes . . . 35
2.4 Topography coverage comparison between the flat array and the cutout array . 36
2.5 Time-dependent thermal deformation of polyethylene naphthalate (PEN), Teonex Q65FA Teijin-DuPont . . . 37
2.6 Electrical resistance of inkjet-printed gold lines for several sintering conditions . 38
2.7 Printed four-point probe structure and height profiles of the printed lines for the sintering study . . . 39
2.8 Topography analysis with atomic force microscopy (AFM) . . . 40
2.9 Cross-sectional morphology analysis with scanning electron microscopy (SEM) . 41
2.10 energy-dispersive X-ray spectroscopy (EDX) on printed traces . . . 41
2.11 Electrical reproducibility of the printed arrays across different designs . . . 44
2.12 Electrical impedance mapping of conformal surfaces using the printed array with flexure cuts . . . 45
2.13 A smart bandage for early detection of pressure ulcers . . . 47
2.14 Early detection of pressure-induced tissue damage . . . 48
2.15 Impedance maps identify mild, reversible pressure damage . . . 49
2.16 Printed ECG electrodes and characterization . . . 51
2.17 ECG signal comparison between printed electrodes and Ag/AgCl electrodes. Measurements are taken from the V_1 - V_2 location . . . 52
2.18 ECG signal recorded with printed electrodes from the V_3 - V_4 location . . . 53

2.19 ECG signal recorded with printed electrodes from the lower left rib cage 54
2.20 ECG signal recorded with printed electrodes from the V_5 - V_6 location 55
2.21 ECG signal recorded with printed electrodes from under the midline of the left rib cage, then from the back. Signals are not reliable at these locations 56
2.22 Flexible EMG recording system 58
2.23 Results from the flexible EMG recording system 58

3.1 Pulse oximetry with an organic optoelectronic sensor 63
3.2 OLED and OPD design and performance 66
3.3 OLED and OPD fabrication and physical device structures 67
3.4 Frequency response of various organic and inorganic light-emitting diode (LED) and photodiode (PD) configurations 68
3.5 PPG acquisition using combinations of inorganic and organic LEDs and PDs . . 69
3.6 Area scaling effects of OLEDs and OPDs, and reducing ambient noise by flexing the OPD around a finger phantom 69
3.7 Organic optoelectronic pulse oximetry system 70
3.8 Stability of the all-organic optoelectronic sensor 72

4.1 Reflectance oximeter sensor overview 75
4.2 Reflectance oximeter sensor design and placement on the wrist 76
4.3 PPG signal variation on the wrist 77
4.4 Assembly of the printed sensor 78
4.5 Pulsatile signal magnitudes for different sensor geometries 80
4.6 Performance comparison of different sensor geometries 81
4.7 The effect of an optical barrier in sensor performance 81
4.8 Process flow of the (**a**) TM and (**b**) IVW algorithms 82
4.9 HR detection using TM and IVW algorithms from a simulated dataset 84
4.10 The effect of signal-to-noise ratio (SNR) on the accuracy of HR estimation using TM and IVW algorithms 84
4.11 HR detection using TM and IVW algorithms from the printed multi-channel PPG sensor 86

5.1 Oximetry sensing locations and modes of oximetry 89
5.2 Overview and operation of the printed reflectance oximeter array (ROA) 91
5.3 Reflectance oximeter array assembly 92
5.4 Current Density vs. Total Flux for the OLEDs 93
5.5 Sensor placement and emitter-detector spacing (d) for reflectance oximetry . . . 98
5.6 Emitter-detector spacing (d) study data 99
5.7 The reflectance sensor mounting photos 100
5.8 Fabrication flow of the OLED and OPD arrays for the ROA 101
5.9 Photographs and performance parameters of the OPD and OLED arrays 102
5.10 Dynamic response of the OPDs at 680 nm, biased at -2V 103
5.11 System design for reflectance oximetry and single pixel reflection-mode pulse oximetry (reflection-mode pulse oximetry (SpO_2^r)) results 105
5.12 Control electronics and connections of the oximeter system 106

5.13 Graphical User Interface (GUI) for processing and visualizing the oximeter data 107
5.14 Single pixel reflection-mode pulse oximetry (SpO_2^r) results for a commercial and the printed reflectance probe . . . 108
5.15 Reflectance sensor temperatures on the forearm . . . 109
5.16 (**a**) Single pixel reflection-mode pulse oximetry (SpO_2^r) results with and without a 0.7 kPa external pressure. (**b,c**) Zoomed-in view of the PPG signal with and without the external pressure are shown in **b** and **c**, repectively. . . . 110
5.17 2D oxygen saturation monitoring with the ROA . . . 111
5.18 (**a**) Red and near-infrared (NIR) channels of the ROA signal, before and after inducing the ischemia. (**b**) Zoomed-in view of the signal during the pressure cuff-induced ischemia. The pulsatile PPG signal is absent because the blood flood is occluded. Here, reflection-mode pulse oximetry cannot be performed. (**c**) Zoomed-in view of the signal after releasing the pressure. Now, the pulsatile PPG signal is present because the blood flow is restored. In this case, reflection-mode pulse oximetry can be performed. . . . 112
5.19 2D contours maps of the red and NIR channels, and change in oxygen saturation (ΔSO_2) at every 30 *s* interval for the *in-vivo* oxygen saturation monitoring test with the ROA as shown in Fig. 5.17. . . . 113
5.20 ΔSO_2 monitoring for different durations of ischemia . . . 114

6.1 Proposed overview and system design of the wearable sensor patch (WSP) enabled by flexible hybrid electronics . . . 117
6.2 Surface energy optimizations for inkjet printing functional inks on Kapton® PI substrate . . . 119
6.3 Printing resolution of the printed gold ink on the plasma treated Kapton® PI substrate . . . 120
6.4 Electrical reproducibility and mechanical robustness testing of electrodes printed on Kapton® PI and the interface between the printed gold and gold plated copper pad . . . 121
6.5 Characterization and dynamic testing of the stencil-printed thermistors . . . 123
6.6 Optical and scanning electron microscope (SEM) images of the printed thermistor 126
6.7 Fabrication process for the WSP . . . 127
6.8 Fabrication frame and layout of the WSP . . . 128
6.9 Encapsulation process for the thermistor . . . 129
6.10 ECG recording with standard Ag/AgCl electrodes and printed gold electrodes . 130
6.11 Electrocardiography (ECG) signal and heart rate (HR) monitoring using the WSP 131
6.12 Post processing of ECG signal for noise reduction . . . 132
6.13 Post processing of ECG signal for heart rate (HR) detection . . . 133
6.14 Mechanical robustness testing of the WSP . . . 134
6.15 Micrographs of the gold/copper interface . . . 136
6.16 Critical surface tension characterization for various surfaces . . . 137
6.17 Nanoparticle ink wetting and spreading tests on different metallic surfaces . . . 138
6.18 Printing reliability improvement test vehicle (TV) and the use of nickel oxide (NiO) dams . . . 139
6.19 The TV array resistance after various manufacturing steps . . . 139

6.20 Comparison of gold ink printed on copper pads without and with gold-plating 140

7.1 An integrated bioelectronic and biophotonic wound sensing platform 145
7.2 An integrated flexible and wearable multi-sensor platform. Both vital signs and analytes in bodily fluids are used to provide an overall snapshot of a person's physiological state. 147
7.3 Large-area sensor array for structural health monitoring - the health of the infrastructure can be estimated through statistical analysis of the sensor data. . . . 148
7.4 Printed nickel oxide thermistor array for mapping the temperature of batteries. 149

List of Tables

1.1 Flexible thermistors and performance parameters. 6
1.2 Device fabrication techniques for wearable systems and devices. 20
1.3 Biosignals, sensing methods, and measurement parameters for vital signs monitoring. 22
1.4 Power requirements of wearable medical sensing system components. 24

4.1 HR calculated from a literature dataset [199] using template matching and inverse-variance weighting algorithms. 85

5.1 The focus and features of recently reported flexible oximeters. 90

Acknowledgments

Many individuals from a variety of institutions played instrumental roles producing the results presented in this dissertation. I enjoy working on interdisciplinary projects that bridge engineering, materials science, and biology – most of my doctoral projects were done in collaboration with researchers within and outside of our research group. I would like to sincerely acknowledge their support and help.

First and foremost, the biggest "thank-you" goes to my advisor, Prof. Ana Claudia Arias. Because of Ana, I got the opportunity to work in an emerging branch of physical electronics - flexible and printed electronics. I absolutely loved my Ph.D. experience. Ana gave me the freedom to explore new projects and guided me when I was straying off course. She was confident in my capabilities even when I was not. Her continuous support and mentorship made this dissertation possible. Ana's passion for research and honest concern for the success of the students makes her the best advisor one can get.

I was privileged to work with Prof. Michel Maharbiz, Prof. Jan Rabaey, and Prof. Liwei Lin - from being on my qualifying exam and dissertation committees, to guiding me throughout my doctoral research, their support was instrumental for me. They gave valuable insights into my research and transformed my views to observe the broader impact of research. I am a better researcher because of them.

I must acknowledge the invaluable suggestions, guidance, and support I got from Ramune Nagisetty at Intel Labs. For the better part of my doctoral work, I had the privilege of working with Ramune, her continuous guidance and support assisted me to grow both academically and professionally.

The work presented in this dissertation would not have been possible without the support from the funding sources - National Science Foundation (NSF), National Institutes of Health (NIH), Air Force Research Laboratory (AFRL), Systems on Nanoscale Information fabriCs (SONIC), one of the six SRC STARnet Centers, sponsored by MARCO and DARPA, Intel Corporation, and Cambridge Display Technology Limited (CDT). Furthermore, I am very grateful for the EECS Departmental Fellowship.

The most intriguing part of my doctoral work was the "oximeter" project. The fascinating progress we made in oximetry using organic optoelectronics would not have been possible without the contribution from the whole team - Adrien Pierre, Claire Lochner, Donggeon Han, Jonathan Ting, and Xingchun Wang. It was a challenging project, but working with this team made the project fun and exciting. I must acknowledge Nir Yaacobi-Gross, Chris Newsome, Richard Wilson, Gianluca Bovo, Simon King, and Martin Humphries at Cambridge Display Technology (CDT). From supplying materials to helpful technical discussions, CDT's support was vital throughout the project. I must acknowledge Juan Pablo Duarte Sepulveda for helping me with the oximeter testing setup. Chapters 3, 4, and 5 are based on the results from the oximeter project.

Another rewarding project I was fortunate to be part of was the "smart bandage" project. We had a huge team from UC Berkeley developing the bandage, while a team at UCSF carried out the clinical testing. I truly enjoyed the interdisciplinary nature of the project. I should acknowledge the team - Sarah Swisher, Monica Lin, Amy Liao, Elisabeth Leeflang, Felippe Pavinatto, Kaylee Mann, Agne Naujokas, Prof. David Young, Prof. Shuvo Roy, Prof. Michael R. Harrison, Prof. Vivek Subramanian, and Prof. Michel M. Maharbiz. This project made me

realize the impact translational medicine has - it is extremely important to design research so that it will eventually address a need that is currently unmet. We later applied the lessons from this project to design biopotential electrodes for electrocardiography and electromyography. Chapter 2 is based on the results from the "printed biopotential and bioimpedance electrodes" project.

Extensions of the electrodes project helped us to start exciting collaborations, where we explored the feasibility of printed electromyography electrodes. In collaboration with Ali Moin, Andy Zhou, Abbas Rahimi, Simone Benattiz, Alisha Menon, Senam Tamakloe, Fred Burghardt, Luca Beniniyz, and Prof. Jan Rabaey, we implemented the printed electrodes for electromyography signal acquisition. I am extremely grateful to the collaborators for utilizing our devices for medical sensing as well as human-machine interface systems. Results from these projects are described in Chapter 2.

Another exciting project in collaboration with Nano-Bio Materials Consortium (NBMC), a SEMI strategic association partner, was on the system-level implementation of printed sensors. I collaborated with Mohit Garg, Qiong Gui, Varun Soman, Madina Zabran, Steve Czarnecki, Prof. Mark Poliks, Prof. Zhanpeng Jin, Prof. Kanad Ghose, and James Turner from Binghamton University; Mark Schadt, Paul Hart, Robert Welte, Michael Shay, Konstantinos Papathomas, William Wilson, and Frank Egitto from i3 Electronics, Lockheed Martin, and American Semiconductor. In this project, I had the opportunity to work with personnel from both academia and industry. I would like to thank all the team members for their hard work and dedication, which allowed us to research above and beyond the applications of flexible hybrid electronics. Chapter 6 is based on the results from the "flexible hybrid electronics" project.

One of the biggest perks of being a graduate student at Berkeley is the opportunity to learn and work with many brilliant individuals. I must acknowledge past and present members of the Arias Research Group: Adrien Pierre, Claire Lochner, Donggeon Han, Jonathan Ting, Xingchun Wang, Natasha Yamamoto, Abhinav Gaikwad, Aminy Ostfeld, Felippe Pavinatto, Mahsa Sadeghi, Joseph Corea, Igal Deckman, Balthazar Lechêne, Margaret Payne, Alla Zamarayeva, Karthik Gopalan, Maruf Ahmed, Payton Goodrich, Carol Baumbauer, Xiaodong Wu, Juan Zhu, Tae Hoon Kim, Seiya Ono, Abhinav Koppu, and Jasmine Jan. In addition to our lab, I learned a lot about printed electronics from the members of the Subramanian Group: Will Scheideler, Gerd Grau, Muhammed Ahosan Ul Karim (Rumi), Seungjun Chung, Jake Sadie, and Steve Volkman. I should acknowledge Leeya Engel and Chengming Liu for our project on using printed electronics for hydrogel microactuators in microfluidics. Furthermore, I would like to acknowledge Prof. Ali Javey and Prof. Paul Wright for sharing lab space and resources to facilitate research. Moreover, my sincere thank-you goes to Prof. Miki Lustig and Shirley Salanio for providing valuable academic and professional guidance.

For almost six years, Cory 550 has been my second home. A resounding thanks to Natasha, Han, Ting, Balthazar, and Igal for making "550" a pleasant and fun place. Outside of the lab, I would like to thank the Bangladeshi community in Berkeley for being awesome!

This dissertation would not have been possible without the support and sacrifice of my parents: Dr. Md. Faiz Ahmad Khan and Rowshan Ara Faiz; my eldest brother, sister-in-law, niece and nephew: Dr. Yaseer Muhammad Tareq Khan, Dr. Nishat Fatema, Mahnaz Khan, and Tashfeen Khan; my elder brother, sister-in-law, and nephew: Yasser Md. Tahid Khan, Ranzeeba Nehrin, and Umair Khan; and my in-laws. I would like to dedicate this dissertation to my immediate and extended family members.

Finally, the biggest thank-you goes to my wife, Sifat Sharmeen Muin (Ishita), the love of my life. She was with me, literally every step of the way - she knows almost every figure I made; she helped me when I got stuck deriving equations; she proofread many of my papers. I can't imagine this dissertation without her continuous support and motivation. Doctoral research is hard. Because of Ishita, I enjoyed every moment of my Ph.D. journey, whether it was the lowest point when nothing in research made sense or the highest point when my papers got accepted. Thank you! Thank you so much, dear! Both of us are completing PhDs in engineering from Berkeley this semester - I can't express how proud I am of Ishita.

Berkeley has been a surreal experience. It is the most welcoming city in the US. The views of the bay from Berkeley are just breathtaking. Academically, the exceptional quality of the faculty and students never ceases to amaze me. I am truly grateful to the entire community for my amazing Ph.D. journey.

Yasser Khan
December, 2018
Berkeley, CA

List of Publications

Portions of this thesis have been drawn from the following publications:

- Yasser Khan, Aminy E. Ostfeld, Claire M. Lochner, Adrien Pierre, and Ana C. Arias. Monitoring of vital signs with flexible and wearable medical devices. **Advanced Materials**, 28(22):4373–4395, 2016. ISSN 1521-4095. doi: 10.1002/adma.201504366. URL http://onlinelibrary.wiley.com/doi/10.1002/adma.201504366/abstract

- Yasser Khan, Felippe J. Pavinatto, Monica C. Lin, Amy Liao, Sarah L. Swisher, Kaylee Mann, Vivek Subramanian, Michel M. Maharbiz, and Ana C. Arias. Inkjet-printed flexible gold electrode arrays for bioelectronic interfaces. **Advanced Functional Materials**, 26(7): 1004–1013, 2016. ISSN 1616-3028. doi: 10.1002/adfm.201503316. URL http://onlinelibrary.wiley.com/doi/10.1002/adfm.201503316/abstract

- Sarah L. Swisher, Monica C. Lin, Amy Liao, Elisabeth J. Leeflang, Yasser Khan, Felippe J. Pavinatto, Kaylee Mann, Agne Naujokas, David Young, Shuvo Roy, Michael R. Harrison, Ana C. Arias, Vivek Subramanian, and Michel M. Maharbiz. Impedance sensing device enables early detection of pressure ulcers in vivo. **Nature Communications**, 6:6575, 2015. doi: 10.1038/ncomms7575. URL http://www.nature.com/ncomms/2015/150317/ncomms7575/full/ncomms7575.html

- Claire M Lochner*, Yasser Khan*, Adrien Pierre*, and Ana C Arias. All-organic optoelectronic sensor for pulse oximetry. **Nature Communications**, 5:5745, 2014

- Yasser Khan*, Donggeon Han*, Jonathan Ting*, Maruf Ahmed*, Ramune Nagisetty, and Ana C. Arias. Organic multi-channel optoelectronic sensors for smart wristbands. 2019. Submitted

- Yasser Khan, Donggeon Han, Adrien Pierre, Jonathan Ting, Xingchun Wang, Claire M Lochner, Gianluca Bovo, Nir Yaacobi-Gross, Chris Newsome, Richard Wilson, et al. A flexible organic reflectance oximeter array. **Proceedings of the National Academy of Sciences**, 115(47):E11015–E11024, 2018

- Yasser Khan, Mohit Garg, Qiong Gui, Mark Schadt, Abhinav Gaikwad, Donggeon Han, Natasha A. D. Yamamoto, Paul Hart, Robert Welte, William Wilson, Steve Czarnecki, Mark Poliks, Zhanpeng Jin, Kanad Ghose, Frank Egitto, James Turner, and Ana C. Arias. Flexible hybrid electronics: Direct interfacing of soft and hard electronics for wearable health monitoring. **Advanced Functional Materials**, 26(47):8764–8775, 2016. ISSN 1616-3028. doi: 10.1002/adfm.201603763

- Varun Soman, Yasser Khan, Madina Zabran, Mark Schadt, Paul Hart, Michael Shay, Frank Egitto, Konstantinos Papathomas, Natasha A. D. Yamamoto, Donggeon Han, Ana C. Arias, Kanad Ghose, Mark D. Poliks, and James N. Turner. Reliability challenges in fabrication of flexible hybrid electronics for human performance monitors: A system level study. 2019. Submitted

Glossary

Hb deoxyhemoglobin. 62–64, 88, 89, 91, 93, 94, 96

HbO_2 oxyhemoglobin. 62–64, 88, 89, 91, 93–96

SpO_2^r reflection-mode pulse oximetry. v, vi, 94, 95, 97, 104, 105, 108, 110, 112, 114

SpO_2^t transmission-mode pulse oximetry. 89, 104, 105, 108, 112

ADC analog to digital converter. 21, 23, 24, 70, 71

AFE analog front end. 23, 71, 75, 78, 90, 103, 105, 106, 116, 117, 141

AFM atomic force microscopy. iv, 40

AgNWs silver nanowires. 6

CMOS complementary metaloxidesemiconductor. 25

CO_2 carbon dioxide. 33, 34, 42, 43

ECG electrocardiography. ii–vi, 2, 7–9, 22, 24, 26, 27, 30–32, 50–57, 116–118, 122, 126, 127, 130–135, 141, 142

ECoG electrocorticography. 2, 22

EDX energy-dispersive X-ray spectroscopy. iv, 41, 42

EL electroluminescence. 63

EMG electromyography. ii, v, 22, 26, 30–32, 57, 58

EQE external quantum efficiency. 62, 65, 73, 76, 77, 97, 100, 102

F8BT poly((9,9-dioctylfluorene-2,7-diyl)-alt-(2,1,3-benzothiadiazole-4,8-diyl)). 65

FDA food and drug administration. 2

FHE flexible hybrid electronics. 115, 116, 142

FPCB flexible printed circuit board. 27, 116, 118, 122, 125, 126, 142

HR heart rate. iv–vi, viii, 2–4, 7, 9, 10, 14, 22, 24, 25, 27, 50, 57, 74, 75, 82–86, 131–134

ICs integrated circuits. 2, 27, 29, 115–117, 125, 142

IoT internet of things. 27, 116, 148

ITO indium tin oxide. 65, 97, 101

IVW inverse-variance weighting. iii, v, 27, 82–86

LED light-emitting diode. v, 9, 17, 18, 61, 62, 68, 69, 71, 73, 74, 77, 78, 88

MAs motion artifacts. 74, 82, 85

MCU microcontroller. 21, 23, 78

MPU microprocessor. 21, 23

NiO nickel oxide. vi, 6, 7, 27, 122–124, 126, 135, 139–141, 148

NIR near-infrared. vi, 18, 27, 62, 64, 71, 73, 75–81, 88–94, 97, 98, 100–109, 111–113

NTC negative temperature coefficient. 6

O_2 oxygen. 34, 35, 50

OLED organic light-emitting diode. ii, iii, v, 18, 26, 27, 61–63, 65–71, 73, 75–79, 89, 91–94, 97, 100–107, 109, 111

OPD organic photodiode. iii, v, 18, 26, 27, 61–63, 65–71, 73, 75–79, 89, 91, 92, 97, 100–103, 105–107, 111

$PC_{71}BM$ [6,6]-phenyl C71-butyric acid methyl ester. 65

PD photodiode. v, 9, 17, 18, 61, 68, 69, 71, 73, 74, 77, 78, 88

PDMS polydimethylsiloxane. 13, 16, 17, 19

PEDOT:PSS Poly(3,4-ethylenedioxythiophene)-poly(styrenesulfonate). 6, 8, 9, 32, 65, 97, 100, 101

PEN polyethylene naphthalate. iv, 33, 34, 37, 50, 51, 59, 78, 97, 100, 101

PET polyethylene terephthalate. 37, 59

PI polyimide. iii, vi, 116, 118–123, 126–128, 135, 136, 140

PPG photoplethysmography. iii, v, vi, 9, 23, 25, 27, 68–71, 73–75, 77–79, 81–89, 93, 94, 96, 97, 104, 105, 108, 110, 112, 114

PSBR polystyrene-butadiene rubber. 122, 123, 126

PTB7 poly({4,8-bis[(2-ethylhexyl)oxy]benzo[1,2-*b*:4,5-b′]dithiophene-2,6-diyl} {3-fluoro-2-[(2-ethylhexyl)carbonyl]thieno[3,4-*b*]thiophenediyl}). 65

PTC positive temperature coefficient. 6

PVDF polyvinylidene fluoride. 14

RFID radio frequency identification. 16

ROA reflectance oximeter array. v, vi, 89, 91–94, 97, 100, 101, 103, 105, 107, 109, 111–114

SEM scanning electron microscopy. iv, vi, 40, 41, 122, 126

sEMG surface electromyography. 3, 4

SHM structural health monitoring. 28, 147

SNR signal-to-noise ratio. v, 74, 77, 79, 84, 85, 88, 89, 97, 114, 115

TBT poly((9,9-dioctylfluorene-2,7-diyl)-alt-(4,7-bis(3-hexylthiophene-5-yl)-2,1,3-benzothiadiazole)-2′,2′-diyl). 65

TFB poly(9,9-dioctylfluorene-*co*-n-(4-butylphenyl)-diphenylamine). 65

TFT thin film transistor. 16, 17, 22, 24, 25

TM template matching. iii, v, 27, 82–86

TV test vehicle. vi, 139–141

WSP wearable sensor patch. iii, vi, 27, 116–118, 122, 125, 127, 128, 130–132, 134, 135, 140–142

Chapter 1

Introduction

Healthcare, roughly one-fifth of the US economy, has seen tremendous improvements in the medical sciences and engineering innovations. While these advancements are improving in-hospital care, in-home care has been lagging behind. Wearable medical sensors have the potential to revolutionize healthcare: they encourage healthy living by providing individuals feedback on personal vital signs and enable facile implementation of both in-hospital and in-home health monitoring [1]. Consequently, wide implementation of these sensors can reduce prolonged hospital stays and cut avertible healthcare costs. In recent years, there has been an increased demand for wearable devices, as demonstrated by the growth of the wearable fitness market to $5 billion in 2015, which is higher by 25 percent from 2014 - this growth rate is expected to be sustained over the next 5 years [9]. Concurrently, there has been a significantly increased interest in monitoring stress and human performance during physically demanding tasks. Wearable medical devices, for improved in-home care, customized for patients with known health issues that can benefit from regular and even continuous monitoring, are desired. Currently, devices are being developed to monitor human vital signs continuously, as non-invasively and comfortably as possible. Regular monitoring of vital signs would help to establish an individual health baseline and alert users and medical professionals of abnormalities indicating that further medical attention and care may be necessary. Today, most of the wearable devices have a watch format and track activity levels. By incorporating vital signs sensors, these devices can be upgraded for both fitness monitoring and medical diagnostics.

Moving towards health monitoring devices that interface well with the skin and the body may help with the adoption of wearable medical devices and even improve the performance of fitness monitoring. Considerable efforts are taking place where new fabrication techniques and materials are being applied to sensors and electronics with the goal of demonstrating flexible and conformal electronic devices. The bulky and rigid nature of conventional silicon-based devices can impede their applications in epidermal and implantable medical sensing [10, 11]. Alternative materials, such as plastic and elastomeric substrates, used in these flexible devices are conformal by nature, lightweight, and therefore offer better interface with the human skin and soft tissue. Many sensors also use electronic and optoelectronic materials that are flexible by nature [3, 4, 12, 13] while other approaches look into transferring small and thin conventional devices onto flexible substrates [14, 15]. Meanwhile, silicon-based electronics provide

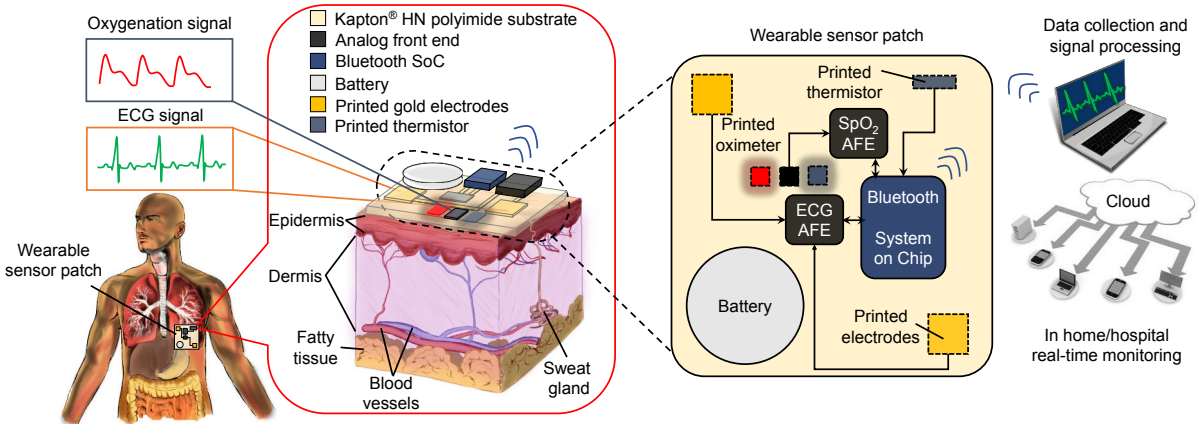

Figure 1.1. **Overview of a wearable sensor platform, where flexible sensors are utilized for real-time health monitoring**.

unparalleled performance in data processing and performance. Therefore, the ideal design for a comfortable wearable medical device would take a hybrid approach where new advanced flexible materials are used in the same fabrication platform as silicon integrated circuits (ICs). Such a hybrid approach can also take into consideration the diversity of shapes and sizes of the population, making medical devices better customized for individuals. Additionally, flexibility and a good fit to the body can also improve signal quality and reduce noise from the measurement [3, 4]. The main focus of this thesis is the design and system-level implementation of flexible and wearable medical sensors. A schematic illustration of a wearable sensor platform is shown in Fig. 1.1, where flexible sensors are used to collect biosignals such as temperature, HR, ECG, pulse oxygenation. The collected data is then transferred to a network for real-time in home or in-hospital monitoring.

In Chapter 1, we discuss different biosignals that can be non-invasively measured using wearable medical sensors. We survey the reported sensor systems, sensing mechanisms, sensor fabrication, power, and data processing requirements. Medical devices are designed to diagnose, prevent, and treat disease. According to the food and drug administration (FDA), a medical device should not achieve its purposes through chemical action within or on the body, and an agent which achieves its purpose through chemical action is termed as a drug [16]. Therefore, sensors ranging from a simple temperature sensor to an invasive electrocorticography (ECoG) sensor fall under the broader umbrella of medical devices. In this chapter, we limited our focus to non-invasive and wearable vital signs sensors. Vital signs are measurements of the body's most basic functions and are useful in assessing the physical state of a person.

In this chapter, we review several sensors that are flexible and could be used as wearable devices to monitor vital signs such as heart and respiration rate, temperature, blood pressure, pulse oxygenation, and blood glucose. An overview of the general working principle of each sensor is given together with examples of flexible sensors previously reported in the literature. General fabrication processes that allow flexibility are also reviewed together with schemes for data processing, transmission, and visualization. In Fig. 1.2, a visual summary of this

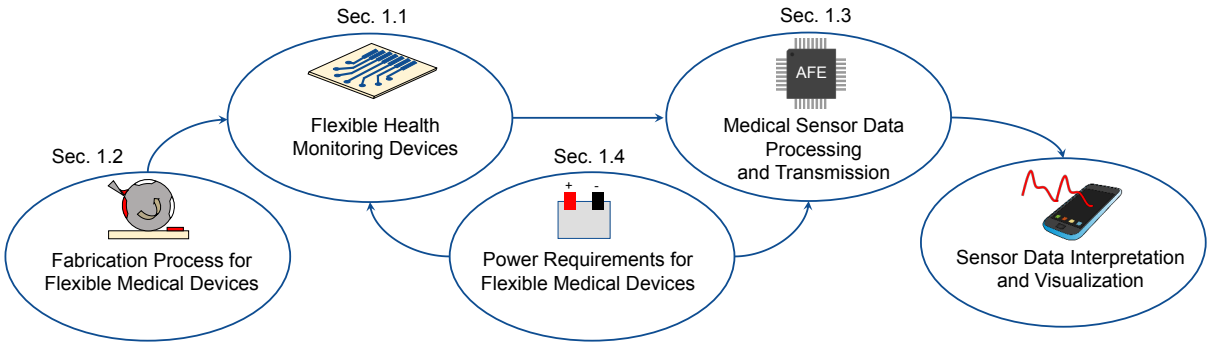

Figure 1.2. **System flow of biosensors and a graphical overview of this chapter**. Section 1.1 presents various biosensors designed to acquire biosignals. Section 1.2 discusses the fabrication processes reported in the literature for developing flexible medical devices. Section 1.3 introduces the process flow for biosignal acquisition, filtering, amplification, processing, and transmission to a host computer or portable device. Section 1.4 discusses the power requirements and methods of powering wearable biosensor systems.

chapter is given. In Section 1.1, flexible health monitoring devices are described. For each sensor, the underlying sensing principle, alternative sensing schemes, and the reported sensors in the literature are discussed. In Section 1.2, fabrication processes are reviewed. Section 1.3 describes the data processing and transmission requirements of the sensors, and also lists the measurement range and signal frequencies associated with different types of vital sign measurements. Finally, in Section 1.4, the power requirements of wearable electronics are discussed along with practical considerations such as choice of power source and storage in different sensing scenarios. Overall, in this chapter, we present all the major components in wearable biosensor systems and discuss the progress made in this field, as well as the challenges that lie ahead.

1.1 Flexible health monitoring devices

The four main vital signs routinely monitored by medical professionals are (1) Body temperature, (2) HR, (3) respiration rate, and (4) blood pressure [17]. (5) Pulse oxygenation (oxygenation of fresh arterial blood) and (6) blood glucose do not fall into the category of vital signs, yet these are widely used by medical professionals. Fig. 1.3 gives an overview of the biosignals and sensing locations. In Fig. 1.3a, biosignals are grouped according to the sensing location. For example, blood pressure measurements and bioelectronic measurements such as sEMG can be performed on the arm [18, 19], therefore these two biosignals are grouped under the red dot (Arm). Similarly, temperature, HR, pulse oxygenation, bioelectronic, and motion signals can be obtained from the wrist, therefore these are grouped under the green dot (Wrist). Other biosignals that can be extracted from the chest (orange dot), leg (yellow dot), ear (blue dot), and bodily fluids (black dot) are also shown in the figure. In Fig. 1.3b, biosignals are listed according to precedence. The same order is followed in this chapter, where we discuss

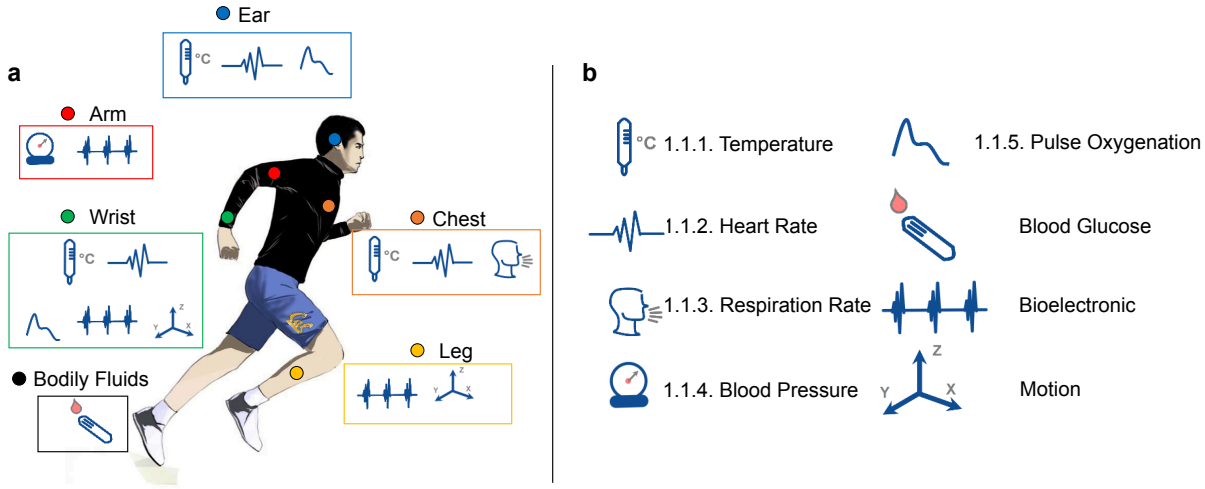

Figure 1.3. **Biosignals and sensing locations**. (**a**) Sensing locations for wearable medical devices. Here the biosignals are grouped according to the sensing location. Blood pressure measurements and bioelectronic measurements such as sEMG can be performed on the arm, therefore these two biosignals are grouped under the red dot (Arm). The wrist (green dot) can be used for obtaining a vast amount of biosignals - temperature, HR, pulse oxygenation, bioelectronic, and motion signals. Similar to the wrist, the chest (orange dot) is also a suitable biosensing location. Temperature, HR, and respiration rate can be extracted from the chest. The leg (yellow dot) can provide bioelectronic and motion signals. Electrochemical sensing can be performed on bodily fluids such as sweat and tear (black dot). Since bodily fluids can be obtained from different parts of the body, the sensing location is not marked. Additionally, these biosignals can be obtained from other sensing locations, for example, pulse oxygenation can be obtained from the fresh arterial blood of the finger, earlobe, or forehead. Here, we highlighted the sensing locations where the measurements can be done in a less obtrusive manner. (**b**) Biosignals and their corresponding sections in this chapter.

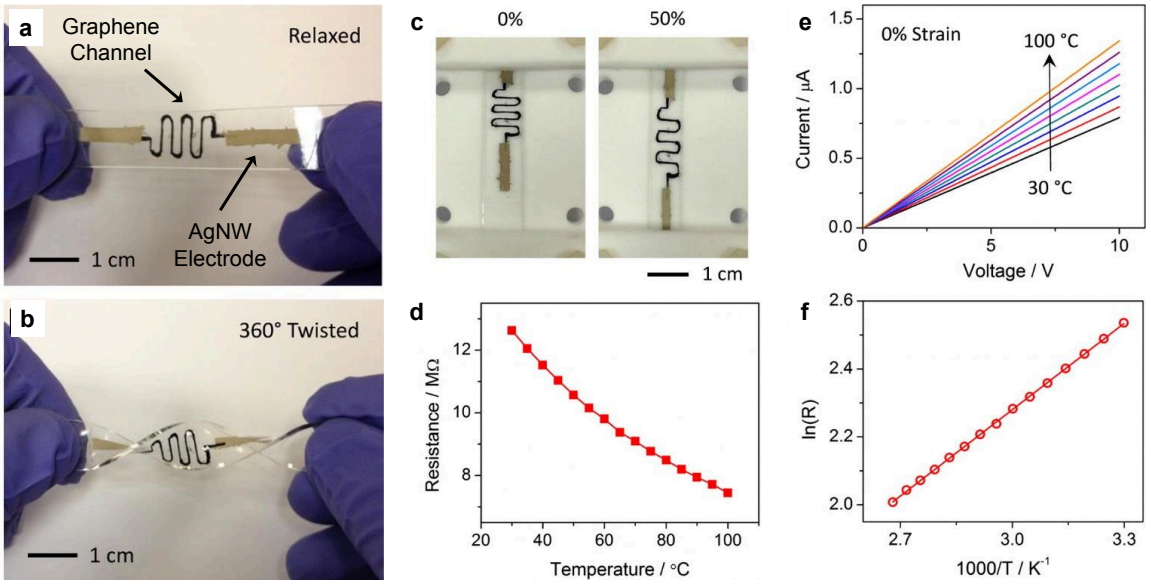

Figure 1.4. **Stretchable graphene thermistors and characterization**. (**a**, **b**) Images of the stretchable graphene thermistors at relaxed and twisted states. (**c**) Images of the stretchable graphene thermistor at 0 and 50% strains. (**d**) Resistance variation with temperature showing a nonlinear relationship. (**e**) IV curves of the thermistor at 0% strain in the temperature range of 30 to 100 °C. (**f**) Dependence of $ln(R)$ on $1000/T$ showing a linear relationship. Reproduced with permission [21]. Copyright 2015, American Chemical Society.

the biosignal, the sensing mechanisms, and the reported flexible and wearable biosensors in literature used for measuring the specific biosignal. Bioelectronic and motion signals are also shown in Fig. 1.3 because they can be used to extract important physiological information such as the stress level or movement of a person. However, considering the scope of this chapter, these two biosignals were omitted from the discussions.

1.1.1 Temperature

Body temperature provides an insight into the physiological state of a person. An elevated body temperature is an indication of infection or fever. On the other hand, a degraded body temperature signifies low blood flow due to circulatory shock. Therefore, body temperature is regarded as the first vital sign. While measuring body temperature, the effect of the measurement site needs to be taken into account because body temperature varies depending on the measurement site; for example, at room temperature (25 ° C), normal wrist temperature is around 32 ° C while the body-core temperature is around 37 ° C [20]. In wearable form factor, temperature sensors are usually placed on the arm or the chest, hence, recorded temperatures are less than the body-core temperature.

Body temperature can be measured using thermistors [21–24], thermoelectric effects [25], or via optical means [26]. However, the prominent method used in wearable sensors is the thermistor configuration. The resistance of thermistors varies according to the temperature. If

Table 1.1. Flexible thermistors and performance parameters.

Thermistor Material	β **(K)**	α **(% / K)**	**Ref.**
Multi-Walled CNTs*	112.49	-0.15	[22]
PEDOT:PSS† and CNT		-0.61	[23]
Graphene	835.72	-1.12	[21]
NiO	4262.70	-5.71	[24]

*Carbon Nanotubes

†Poly(3,4-ethylenedioxythiophene)-poly(styrenesulfonate)

the resistance increases with temperature increase, the sensor is positive temperature coefficient (PTC) type. Conversely, if the resistance decreases with temperature increase, the sensor is negative temperature coefficient (NTC) type. The general equation governing a thermistor is given below:

$$R_t = R_0 \exp \beta(\frac{1}{T} - \frac{1}{T_0}) \tag{1.1}$$

Here, R_t is the resistance at temperature T, R_0 is the resistance at T_0 (reference temperature), and β is the material constant for the thermistor. Equation 1.1 can be rewritten as:

$$\ln R_t = \ln R_0 + \beta(\frac{1}{T} - \frac{1}{T_0}) \tag{1.2}$$

Now, a linear relationship between $\ln(R_t)$ and $1/T$ is established. β represents the slope of the $ln(R_t)$ vs. $1/T$ plot, which is related to the Boltzmann relation ($\frac{E}{kT}$), where E is the bandgap of the thermistor material and k is the Boltzmann's constant. Generally, the sensitivity of the thermistor is quantified using β and the temperature coefficient of the thermistor, α, which can be found by differentiating Equation 1.1 with respect to T and dividing by R_t:

$$\alpha = \frac{1}{R_t}\frac{dR_t}{dT} = -\frac{\beta}{T^2}(\%/K) \tag{1.3}$$

Both β and α can be used to characterize the performance of the thermistor; β has the units of Kelvin while α represents the percentage change of resistance per degree Kelvin. The described working principle and performance quantification apply to most of the reported wearable thermistors. Depending on the thermistor material, β and α can vary significantly. Some of the reported thermistors in flexible and wearable form factor and their performance parameters are listed in Table 1.1. For these reports, the thermistor material is deposited and patterned on top of conductive electrodes.

Yan et al. used resistive graphene as the temperature sensing channels and highly conductive silver nanowires (AgNWs) as electrodes (shown in Fig. 1.4) [21]. Fabricated stretchable devices proved mechanically robust and demonstrated strain dependent resistance (Fig. 1.4b, c, and e). The thermistors demonstrated $\beta = 835.72K$ and $\alpha = -1.12\%/K$. Huang et al.

used NiO based thermistors, and demonstrated $\beta = 4262.70K$ and $\alpha = -5.71\%/K$. These performance parameters are comparable to commercially available thermistors [24]. Jeon et al. used nickel microparticle-filled binary polymer composites as the temperature sensor, where the polymers had a melting point in the range of 35 to 40 ° C [27]. When the material temperature reaches the melting point of the polymers, the particle-particle distance of the host nickel microparticles increases due to volume expansion of the polymers, which increases the thermistor resistance. This results in a huge β in the sensing temperature zone, hence, a low gain read circuit is used to read out the sensor data. While promising advances have been made in wearable temperature sensing, a few impediments still hinder accurate temperature measurements. Most reported thermistors show a strain dependence [21, 24], which is not ideal for wearable sensing because flexing or twisting the sensor can alter the resistance of the thermistor. Decoupling strain effects from temperature effects in thermistors still remains challenging. A hybrid approach of using a small rigid thermistor embedded in a flexible and stretchable matrix can be used to circumvent the strain dependence. The host flexible and stretchable matrix will provide the required compliance and the rigid thermistor will be minimally influenced by the induced strain. Another bottleneck in wearable temperature sensing is to accurately measure body-core temperature. Wearable sensors record skin temperature, which is a few ° C less than the core temperature of 37 ° C. Additionally, the skin temperature has a strong dependence on environmental temperature fluctuations. Boano et al. measured temperature shift of 2 to 3 ° C in skin temperature during indoor to outdoor movement using wearable temperature sensors [28]. On the other hand, the core temperature varies less than 1 ° C throughout the day. Although, the variation of core and skin temperature is dissimilar, it is possible to establish a relationship between the two, and estimate the core temperature from the skin temperature using reported models in the literature [29–31]. Additionally, evaporation of sweat results in a reduced relationship between core and skin temperature [32], as well as a degraded thermal contact between the skin and the sensor. Therefore, for accurately measuring the core temperature, all these impediments need to be addressed.

1.1.2 Heart rate

The primary function of the human heart is to pump oxygenated blood and nutrients to the body and remove carbon dioxide and other wastes. The sequence of cycling deoxygenated blood through the lungs and pumping newly oxygenated blood to the body through the aorta is called the cardiac cycle. The HR or pulse is the frequency of cardiac cycles, expressed as beats per minute (b.p.m.). The HR changes according to the body's need and is susceptible to alteration in the body's normal state. Any major change to the physical or mental state of a person usually changes the pulse. Therefore, HR is used as one of the vital signs to assess the physical and mental state of a person [17].

The HR can be measured manually from the radial artery at the wrist, from the carotid artery at the neck, or by listening directly to the heartbeat using a stethoscope. To measure the HR more accurately, electrical, optical, and strain sensors can be used. In the case of electrical measurement, skin electrodes are used to pick up the depolarization signal from the heart muscles. This technique is known as ECG. In addition to health monitoring, ECG is a useful diagnostic technique for assessing the cardiovascular system. Although ECG measurements are conventionally done using 12 leads, the signal can be picked up by using 2 electrodes

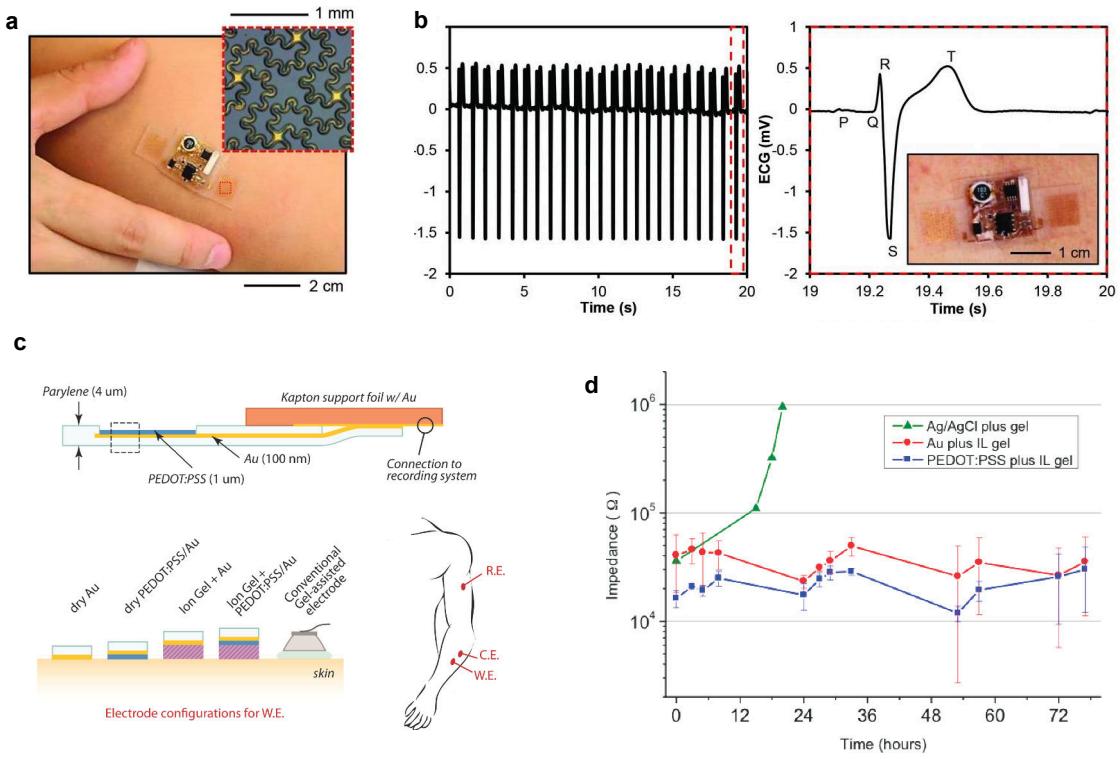

Figure 1.5. **ECG using a flexible and stretchable sensor system**. (**a**) Optical images of the sensor system on the forearm, with a pair of epidermal electrodes in self-similar serpentine mesh layouts (inset optical micrograph). (**b**) ECG acquired by using the device mounted on the sternum. A detailed view of the ECG signal shows the expected Q, R, and S waveforms. Reproduced with permission [33]. Copyright 2014, AAAS. (**c**) An ionic liquid gel-assisted ECG electrode. The different electrode configurations tested. Schematic of the electrode positions on a subject's arm. The working electrode and counter electrode were placed on the forearm, 5 cm away from each other. The reference electrode was placed on the arm, 30 cm away from the working electrode. (**d**) Electrode/skin impedance measured at 1 kHz for IL gel-assisted Au and PEDOT:PSS electrodes and commercial Ag/AgCl electrode with an aqueous gel. Reproduced with permission [34]. Copyright 2014, Wiley-VCH.

placed on the chest [35]. This allows the sensor designs in wearable form factor. However, the signal intensity drops as the spacing between the electrodes is reduced [36]. Xu et al. used 2 electrodes in a band-aid form factor as shown in Fig. 1.5a. The sensor system was composed of electrodes, circuits, and radios for wireless communication in a soft microfluidic assembly; as a result, the complete system was flexible and stretchable [33]. Fig. 1.5b shows the obtained ECG signal using the flexible system. Similar wearable ECG configuration is used with polymer [37], carbon nanotube [38], stretchable elastomer [39], and textile-based [40, 41] electrodes. Since the ECG signal is periodic, the HR can be obtained from the R wave-to-R wave (RR) interval of the ECG signal.

While the conventional gel-assisted Ag/AgCl electrodes remain the gold-standard for clinical use, these electrodes are cumbersome for use in wearables and result in skin irritation [44]. In wearable form factor, electrodes that operate without gels, adhesives, and even skin contact have been demonstrated [45, 46]. However, the performance of these electrodes remains below par. Leleux et al. used ionic liquid gels in conjunction with gold and PEDOT:PSS electrodes (Fig. 1.5c), and demonstrated stable operation up to three days without re-application of the gel (Fig. 1.5d) [34].

PPG is another powerful method for measuring the HR. The pulse signal can be obtained from the plethysmogram by using optical [4] and pressure [42, 43] sensors. With every heartbeat, the heart pumps oxygenated blood to the body and pulls back the deoxygenated blood; these actions distend the arteries and arterioles in the subcutaneous tissue. In the optical sensing method, which is known as PPG, a LED is used to illuminate the arteries, and depending on the blood volume the transmitted or reflected light intensities through and from the skin and tissue change. This signal is then obtained by using a PD. During the systolic phase (the phase of the heartbeat when the heart muscle contracts and pumps blood from the chambers into the arteries) the light absorption peaks due to a high volume of blood. The interval between two systolic peaks can be used to calculate the HR. The same principle applies for pressure sensors - the systolic peaks can be detected using pressure sensor placed on the radial artery [42] or the carotid artery [43]. Schwartz et al. used a pressure sensitive polymer transistor and picked up the pulse signal from the radial artery (Fig. 1.6a - c) [42]. Using the same pressure sensing technique, Nie et al. picked up the pulse signal from the carotid artery (Fig. 1.6 d - e). However, in this case, the sensor was a droplet-based capacitive pressure sensor [43].

Using the three sensing techniques: electrical, optical, and pressure, the HR can be measured accurately. The sensing method should be chosen according to the sensing location. For example, on the chest, ECG electrodes should be chosen over optical and pressure sensor. Similarly, on the wrist, optical or pressure sensors are preferable over ECG for HR sensing.

1.1.3 Respiration rate

Respiration rate is a critical vital sign because without adequate inflow of oxygen and removal of carbon dioxide, a patient is at risk of death or permanent injury. Furthermore, abnormal respiration rates are symptoms of many disorders such as sleep apnea, asthma, chronic obstructive pulmonary disease, and anemia [47–49].

To measure respiration rate, sensors can respond in various ways to the flow of breath, or to the expansion and contraction of the chest and abdomen during breathing. Numerous methods exist to transduce the expansion and contraction of the lungs into an electrical sig-

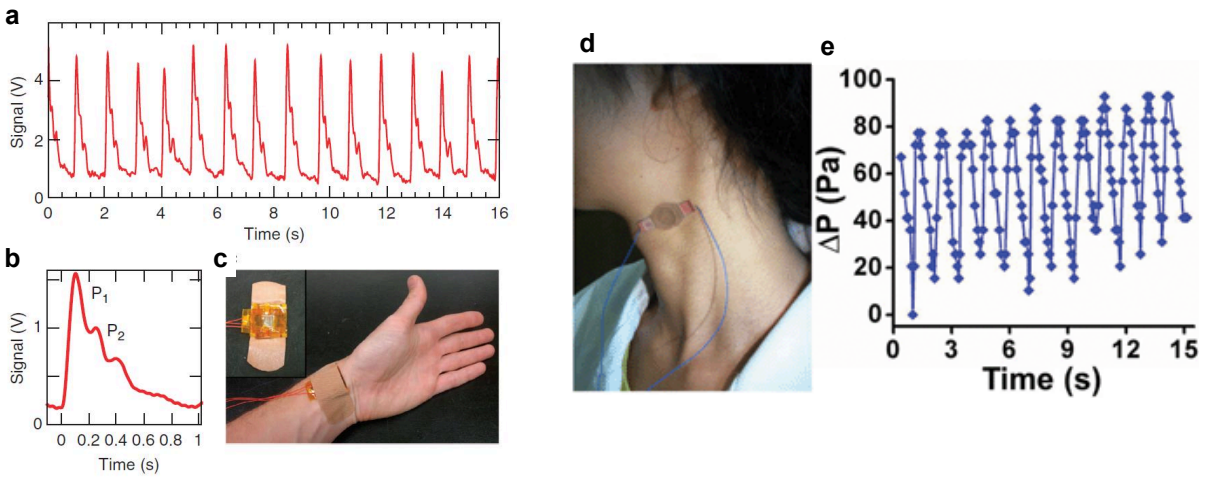

Figure 1.6. **HR monitoring using pressure sensors**. (**a-c**) Pulse wave of the radial artery measured with a pressure sensitive polymer transistor. (**a**) Real-time transient pulse signal. (**b**) Averaged signal from 16 periods (separate measurements). (**c**) Photo showing the placement of the sensor on the radial artery of a person. Reprinted by permission from Macmillan Publishers Ltd: Nature Communications [42], copyright (2013). (**d,e**) Monitoring pulse and blood pressure variation using a droplet-based pressure sensor. (**d**) The pressure sensor is applied on the skin surface above the carotid artery. (**e**) Blood pressure variations, as well as the pulse signal, are observed. Reproduced with permission [43]. Copyright 2012, Royal Society of Chemistry.

nal. In impedance plethysmography, electrodes are placed onto the body and the change in impedance between them reflects the change in lung volume during inhalation and exhalation [50]. Most wearable respiration sensors, however, physically expand and contract along with the lungs and employ some type of strain or pressure sensing to detect the volume change. A single solid piece of material can be used as a strain gauge by exploiting the Poisson effect: when tensile stress is applied to the material, its length increases in the direction of the stress and decreases in the direction perpendicular to the stress. If a conductive material is used, the resistance measured in the direction of the tension increases as a result. If a dielectric material is used instead, the capacitance measured perpendicular to the strain increases. Alternatively, when conductive materials are embedded or woven into a stretchable insulating matrix, the change in contact area between the conductors and the resulting change in resistance can be used to sense the strain. If a conductive material is formed into a loop around the body, the change in inductance as the body circumference changes can also be used to measure respiration. Alternatively, a compressible material can be used to sense pressure by sandwiching it between two stiffer materials wrapped tightly around the body. Another method is to use a looped optical fiber whose transmittance changes as the loops are stretched. Finally, while all of these techniques require applying a signal, either electrical or optical, to the sensor and measuring the response, piezoelectric or triboelectric sensors can generate an electric signal directly from applied pressure. All of these sensing mechanisms require the sensing element to be in close contact with the body so that the expansion and contraction of the torso during breathing is transmitted adequately to the sensor. It is, therefore, critical for the sensor to be as comfortable and conformable as possible.

To detect the flow of breath, sensors can be placed near the nose or mouth that respond to the changes in air temperature, humidity, pressure, or carbon dioxide concentration during respiration [51, 52]. Acoustic sensors on the neck can also be used to measure respiration rate [53, 54]. These types of sensors can be highly accurate and can more easily detect certain conditions than chest-based sensors, such as respiratory obstructions in which air stops flowing into the lungs despite continued motion of the chest [51, 55]. Strain sensors on the torso also tend to respond to other body motions in addition to respiration, such as walking, speaking, and arm movement [49, 55, 56], whereas sensors on the nose and throat are not susceptible to such motion artifacts. However, sensors on the nose and throat are likely to be more conspicuous and less comfortable than those on the torso. Thus, for general activity tracking purposes, where the wearer is not at high risk for respiratory problems, the strain and pressure sensors may still be the preferred choice. The downsides of these sensors can also be mitigated through signal processing and the use of multiple sensors in different locations, such as the chest and abdomen. For example, band-pass filters can be used to remove interference from body motion during speaking and walking [49]. Additionally, the difference in timing between expansions of the chest and abdomen can be used to detect a partial airway obstruction [57]. Many new wearable and stretchable strain or pressure sensors have therefore been developed for respiration monitoring purposes in the past several years, utilizing novel materials and designs for improved comfort and sensitivity.

A number of respiration rate sensors take advantage of conductive textile technology to build the sensing elements directly into the textile. Huang et al. [61] and Atalay et al. [49] knitted conductive fibers—carbon-coated and silver-coated, respectively—together with non-conductive fibers to form resistive strain sensing textiles. As the textile is stretched, the contact

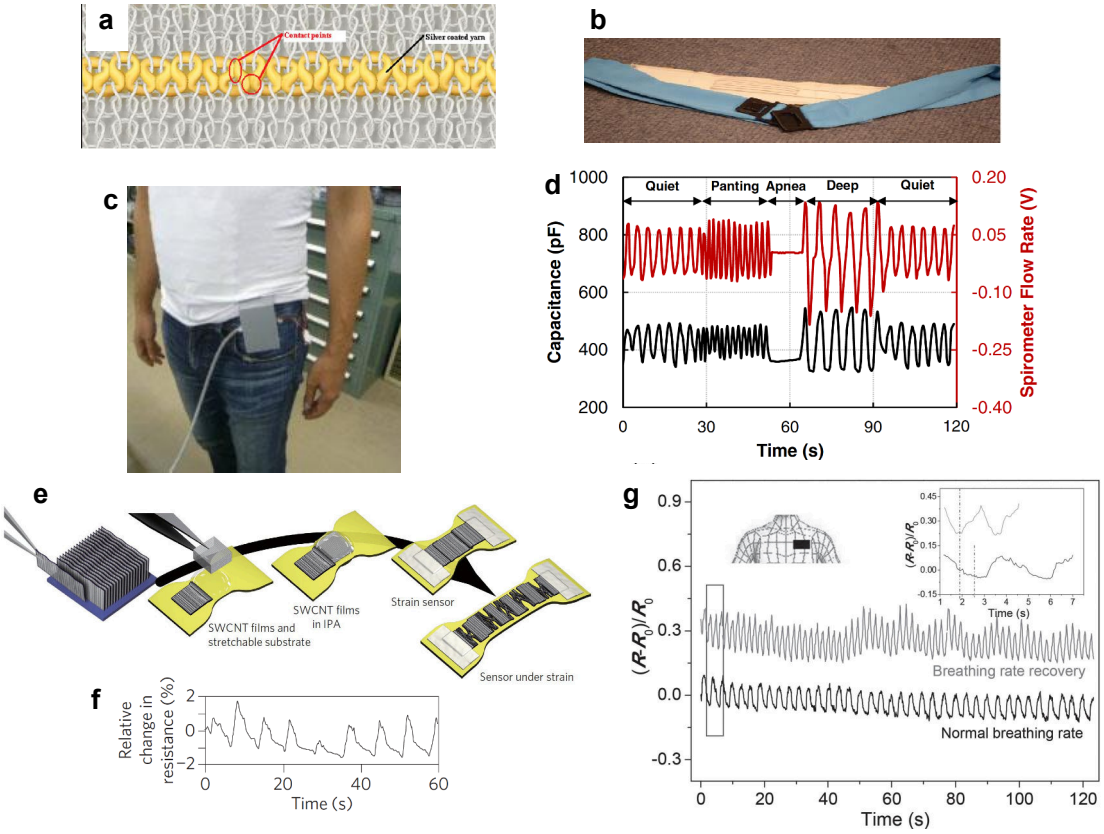

Figure 1.7. **Wearable textile- and carbon nanomaterials-based respiration sensors**. (**a**) Knitted resistive sensor, showing the silver coated yarn (yellow) woven into a non-conductive textile. Contact points between loops are highlighted in red; when the textile stretches the contact area is reduced, increasing the resistance. (**b**) Photograph of a belt containing the knitted resistive sensor. Reproduced with permission [49]. Copyright 2015, IEEE. (**c**) Respiration sensing t-shirt, with capacitive textile electrodes on front and back, along with a box for data acquisition electronics. (**d**) Capacitance signal between textile electrodes (black), compared to conventional spirometer flow rate (red), during different breathing patterns. Reproduced with permission [58]. Copyright 2013, The Japan Society of Applied Physics. Respiration sensing patches based on carbon nanomaterials. (**e**) Fabrication process diagram for aligned carbon nanotube strain sensor. (**f**) Respiration pattern measured with the strain sensor. Reproduced with permission [59]. Copyright 2011, Macmillan Publishers Ltd. (**g**) Measured change in resistance of graphene woven fabric strain sensor during normal breathing and exercise. Insets show the waveforms of a single breath cycle and the location of the sensor on the chest. Reproduced with permission [60]. Copyright 2014, Wiley-VCH.

area between the conductive fibers is reduced, and the resistance increases. Fig. 1.7a shows knitted loops of conductive fibers, highlighting the contact areas, and Fig. 1.7b shows a belt containing the resistive sensor [49]. Wijesiriwardana knitted copper wires into an elastomeric

textile to form an inductive loop; when wrapped around the torso the inductance of the loop changed in response to the expansion and contraction of the lungs [62]. Multiple textile-based pressure sensors have also been reported. In Hoffmann et al. [63] and Min et al. [48], a compressible textile or foam material is sandwiched between two conductive textile electrodes. When the chest expands, the pressure applied on the compressible textile reduces its thickness, increasing the capacitance between the electrodes. A process for fabricating resistive textile pressure sensors was developed by Li et al., in which cotton fibers were converted directly into conductive carbon by pyrolysis, and then infiltrated with an elastomer to form the pressure sensor [64]. This sensor was integrated into a conventional belt to measure respiration rate. Kundu et al. fabricated a potentially more comfortable alternative to the aforementioned belt-based sensors: a capacitive sensor embedded in a t-shirt [58]. In this design, textile electrodes were attached to the anterior and posterior sides of the shirt, as shown in Fig. 1.7c, and the capacitance between them was monitored. The effectiveness of this textile sensor is exemplified by a comparison with a conventional spirometer measurement, as shown in Fig. 1.7d. Guo et al. developed a shirt with resistive respiration sensing capability, by printing a carbon-filled silicone piezoresistive element onto the garment [47]. Both of these garments also included removable boxes carrying the data acquisition electronics. Non-textile sensing devices have been integrated into belts and garments as well, including sliding-plate capacitive strain sensors [56], crystalline conductive polymer film strain gauges [65], and optical fibers [66–68].

There are, however, some downsides to the textile-integrated sensors. First, there is an inherent tradeoff between comfort and sensitivity: to acquire a signal of sufficient quality, the garment or belt needs to be tight. The sensing textiles may therefore be uncomfortable, particularly if worn for extended periods of time, and may also require manufacturing of many different sizes. Furthermore, the sensing garment should be reused repeatedly and perhaps even washed, requiring the sensing elements to be extremely durable. Patch-type sensors, on the other hand, resembling an adhesive bandage, can potentially be smaller, less expensive, and more unobtrusive than the textile sensors, and can be disposable. Several patch strain sensors have recently been developed based on composites of carbon nanomaterials such as carbon nanotubes or graphene embedded in an elastomer matrix, which find applications in electronic skins and human motion detection in addition to respiration rate monitoring. Carbon nanomaterials have several properties that make them ideal for strain sensors, including exceptional flexibility, mechanical strength, and carrier mobility, enabling excellent sensitivity to both low and high strains as well as fast response time [59, 60, 69, 70]. Stretching the composite reduces the number of percolation conduction pathways as well as the contact area between the conductive particles, increasing the end-to-end resistance of the sensor. Yamada et al. fabricated films of aligned carbon nanotubes, which were attached to a polydimethylsiloxane (PDMS) support perpendicular to the direction of strain [59]. When the device was stretched, the carbon nanotube film separated into islands with gaps bridged by narrow nanotube bundles, and the overall film resistance could be correlated with the size of the islands and gaps and therefore the amount of strain. Fig. 1.7 shows the fabrication process for these sensors (e) and a representative respiration waveform (f). Wang et al. fabricated graphene woven fabrics using a copper mesh template and incorporated them into sensors using a combination of PDMS and medical tape as a stretchable substrate [60]. Stretching the graphene caused reversible crack formation, which decreased the number of current pathways and therefore increased the resistance. Waveforms of relative change in resistance are shown during normal breathing and

during exercise in Fig. 1.7g. Boland et al. infiltrated elastic bands with graphene flakes to form highly stretchable strain sensors [69]. The graphene flakes diffuse through the pores in the elastic band, resulting in a structure that exhibits good conduction between flakes but maintains the very high stretchability of the elastic band. Finally, Cai et al. used random networks of carbon nanotubes as stretchable and transparent electrodes for capacitive strain sensors [70]. These sensors employed a stretchable silicone dielectric, which experienced a decrease in thickness and increase in area following the Poisson effect under tension. Each of these sensors was integrated into an adhesive bandage placed onto the chest to monitor respiration, illustrated in the inset to Fig. 1.7g. Of these sensors, the graphene-infiltrated elastic bands showed the highest extensibility, 800%, and the largest relative signal strength during breathing, a resistance change of about 2x [69].

Finally, several self-powered wearable piezoelectric and triboelectric respiration sensors have been developed recently. Films of the piezoelectric material polyvinylidene fluoride (PVDF), which generates a voltage in response to changing mechanical deformation, have been integrated into multiple wearable respiration sensors [72]. Chiu et al. improved upon the flat film design by using a freely movable curved PVDF structure integrated into a sensor patch, achieving an improvement in signal amplitude of over twofold [73]. These types of sensors also respond to heartbeats, so signal processing is required to separate the respiration information from the HR information. In Yi et al., a triboelectric sensor was built using stretchable rubber and aluminum foil, which naturally experience electron transfer from the aluminum to the rubber when they are brought into contact [74]. Stretching the rubber reduces its charge density, causing a corresponding flow of electrons into the aluminum foil from the ground. This device was used to measure respiration rate by incorporating it into a band around the abdomen. While additional power may still be required to perform data processing and communication, utilizing a self-powered sensor can reduce the overall power requirements, allowing a smaller-capacity power source to be used.

1.1.4 Blood pressure

Blood pressure is one of the most important signs into the general health of a person. The two most significant numbers in blood pressure are the maxima (systolic) and minima (diastolic). A typical blood pressure measurement device is a sphygmomanometer, which consists of a pump connected to an inflatable cuff that is typically wrapped around the arm and a manometer to measure the pressure. The cuff pressure is initially inflated well above 200 mm Hg, cutting off blood circulation to the arm, the pressure is then decreased until blood starts to spurt into the blood vessel at the peak pressure of the pulse, known as the systolic pressure. Further reducing the pressure to the point where this turbulent blood flow stops is known as the diastolic pressure, the lowest pressure of the pulse. The turbulence of the blood flow may either be measured using the sounds heard through a stethoscope or the small oscillations in the pressure of the cuff (known as oscillometry). The blood pressure of a healthy person lies below 120/80 (systolic/diastolic); higher blood pressures are diagnosed as hypertension.

While the use of sphygmomanometers has become routine during clinical visits, these systems are limited by their stationary setup and expensiveness, making continuous long-term monitoring difficult. This creates many gaps through which asymptomatic cardiac conditions

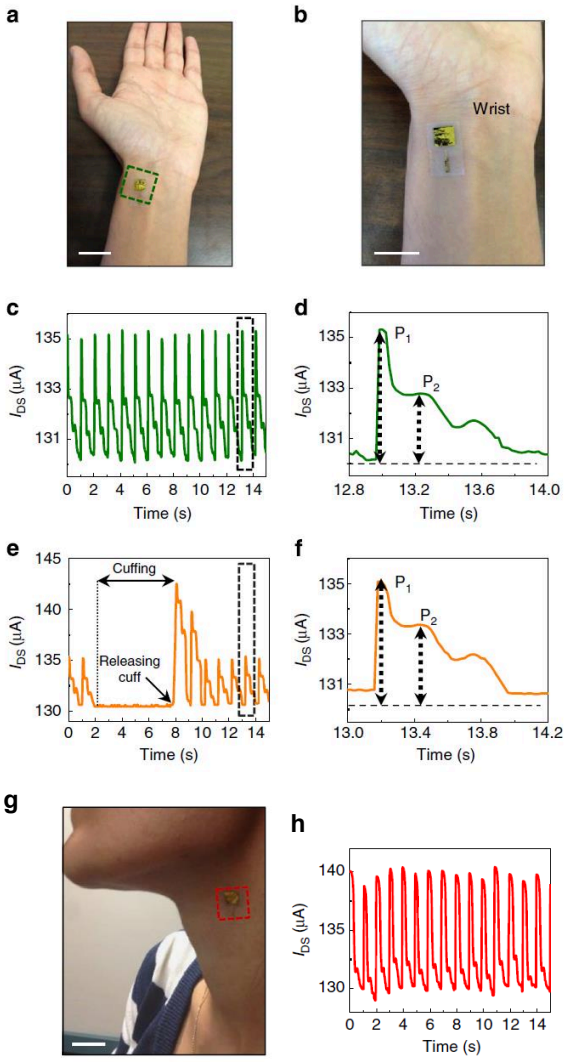

Figure 1.8. **Blood pressure wave measurements on the wrist and neck using a pressure sensitive transistor**. (**a**) Photograph of the sensor placed on a wrist (scale bar, 2 cm). (**b**) magnified view (scale bar, 1 cm). (**c**) I_{DS}–time plot for a sensor mounted on the wrist. (**d**) I_{DS}–time plot for data in the region indicated by the dashed box in **c**. (**e**) I_{DS}–time plot for the sensor while reading pressure on the wrist before, during and after application of pressure on the arm using a commercial pneumatic cuff. (**f**) I_{DS}–time plot for data in the region indicated by the dashed box in e. Photograph of a sensor placed on (**g**; scale bar, 1 cm) neck. (**h**) blood pressure from the neck. Reproduced with permission [71]. Copyright 2014, Macmillan Publishers Ltd.

may go undetected until a heart attack or stroke occurs [75]. Sphygmomanometers also lack the ability to monitor the pressure of the pulse waveform between the systolic and diastolic pressure, known as arterial tonometry, which is very useful for diagnosing cardiac conditions [76]. Additionally, the cuff size of sphygmomanometers must be chosen carefully for each individual or else a false value would be read.

The development of new material systems has led to the fabrication of highly sensitive strain sensors capable of measuring pulse pressure waveforms with ease [42, 71, 77–81]. These novel pressure sensors are typically in the form factor of capacitors, which use either a compressible dielectric to induce a change in capacitance or a piezoelectric dielectric to induce a voltage across the device. The signal from the capacitive elements are either amplified by an external instrument or a monolithically integrated device on the same substrate, typically a thin film transistor (TFT) [42, 71]. Alternatively, strain-dependent resistors may be fabricated and were commonly used in the early development of wearable pressure sensors [79, 82, 83]. However, these are no longer as common in literature, most likely as a result of the constant current that demands higher power consumption than their capacitive counterparts. Additionally, radio frequency identification (RFID) techniques have been used to detect arterial wall motion but require implanting of the device under the skin [84].

Compressible capacitive strain sensors consist of a elastic, but robust dielectric sandwiched between two flexible electrodes. As the dielectric is compressed from externally applied pressure, the capacitance of the device changes. The most common material of choice for the dielectric is PDMS owing to its biocompatibility, inexpensiveness and the extreme range of strain. Additionally, Mannsfeld et al. demonstrated in a seminal work that the sensitivity of planar PDMS can be improved by a factor of 30, decreasing the effective modulus of the material, and the relaxation time can be reduced to by a factor of 104, by molding the surface into microstructured pyramids [85]. These high sensitivities and fast relaxation times enabled a new set of devices that could measure blood pressure precisely enough for arterial tonometry. Further examining the effects of these microstructures, Tee et al. have shown that smaller sidewall angles and larger pyramid spacing led to a decrease in the effective modulus, improving sensitivity to 0.2 kPa^{-1} [86]. However, the attempt to measure pulse pressure was made difficult by the fact the pressure of the finger on the sensor was far greater than the pulse and by the nonlinearity of the sensor, with decreased sensitivity to the small pressure variations from the finger's pulse at high background pressures. The effective modulus of the PDMS dielectric may also be reduced by creating a porous film [87] and roughening the surface by casting PDMS on a rough substrate [79]. Wang et al. demonstrated that casting PDMS on an inherently microtextured substrate such as silk and depositing stretchable and conformal carbon nanotube conductors creates a pulse pressure sensor with a sensitivity of 1.8 kPa^{-1} [79]. In this design, the change in contact area between two carbon nanotube coated rough PDMS films, and the resulting change in resistance between them, allowed the pressure to be sensed. An ionic fluid may also be used as a dielectric, as reported by Li et al., with an electrical double layer acting as the main source of capacitance with a sensitivity of 0.45 kPa^{-1} [77]. The relaxation time was sufficiently fast to reliably measure arterial pulse pressure.

Piezoelectric materials are another go-to material set for creating strain-sensitive devices, and were used in early developments of strain sensors [82]. When a piezoelectric material is strained, a voltage signal is induced across the device. Dagdeviren et al. integrated such materials as the dielectric in an array of capacitors on an ultra-conformal substrate [71]. The

high sensitivity of the device made it possible to reliably measure pulse pressure in a variety of locations on the body (Fig. 1.8a, b, and g). The I_{DS}–time plots shown in Fig. 1.8c - f, and h, were correlated to the systolic and diastolic pressures. Additionally, the voltage induced from piezoelectric materials can also provide a current signal across a low-resistance device. Choong et al. combined a piezoelectric and a conductive polymer deposited on top of microstructured PDMS to create a device with a high sensitivity of 10.3 kPa^{-1} [80]. Piezoelectric materials can even be deposited over a surface of fibers, which not only are easily integrated with textiles but also sense pressure isotropically [78].

The system of a pulse pressure sensor is equally important as the sensor itself. Amplification in these systems is a necessity as a result of the substantially larger background pressure in comparison to the pulse pressure, and is facilitated through monolithic integration of an amplifier next to the sensor. Dagdeviren et al. achieved such integration by connecting their piezoelectric capacitors to a TFT deposited on the same substrate in a common source configuration [71]. Schwartz et al. approached this issue with the same amplification scheme but instead directly integrated their compressible capacitor as the gate dielectric for their TFT, resulting in very clear output signals well over 1V [42]. Another issue with pulse pressure sensing is placing the sensor in the area with the strongest signal. An addressable array of pressure sensors can be scanned to find the pixel with the strongest pulse signal, as demonstrated by Li et al., avoiding the need to precisely place a wearable sensor [77]. Additionally, having an array of high-resolution sensors would make it possible to measure pulse delay between different locations, an important but infrequently used technique to assess cardiac health [76].

Despite the plethora of sensors demonstrated to measure the pulse pressure, few reports attempted to correlate the measured signals to blood pressure [71, 80, 88]. Those that did determine blood pressure found highly non-linear relationships between systolic/diastolic pressures and the sensor output. A more rigorous study has yet to be done on the reliability of these sensors, which shows the use-to-use and person-to-person variability.

1.1.5 Pulse oxygenation

Oxygen saturation or oxygenation is the concentration of oxy-hemoglobin in the blood divided by the sum of the concentration of oxy- and deoxy-hemoglobin in the blood. Depending on the sensing location and method, oxygenation can be categorized into - tissue oxygenation (StO_2), venous oxygenation (SvO_2), and peripheral oxygenation (SpO_2). Among different oxygenation measurements, SpO_2 measurement is ubiquitous due to its non-invasive nature. If the signal is collected from the fresh pulsatile arterial blood, the measurement is termed as pulse oxygenation. Combined with a person's pulse, pulse oxygenation reflects a person's cardiovascular health. In a healthy adult, pulse oxygenation should be at least 95%. If it falls too low, below 80%, proper organ function is hindered [89]. SpO_2 is determined by an optical measurement where two LEDs operating at two different wavelengths alternatively shine light through or on the sensing location, which can be the finger, earlobe, forehead, or wrist. At a given time, the blood volume and the concentration of oxy-hemoglobin in the blood determine the intensity of the transmitted or reflected light through or from the tissue and skin. This optical signal is then collected by a PD. In the transmission mode, the PD is located at the opposite side of the tissue or skin to collect the transmitted light. Alternatively, in the reflection mode, the PD is located at the same side as the LEDs to collect the reflected light. This optical measurement

is based on the fact that the hemoglobin in the blood has a different absorptivity depending on whether or not it is bound to oxygen, and on the wavelength of light. The oxygenation is derived from the ratio of the PD signal upon excitation at each wavelength and the known molar absorptivity of oxy- and deoxy-hemoglobin at each wavelength [4, 89, 90].

In transmission pulse oximetry, one LED has a peak wavelength at which oxy-hemoglobin has a higher absorptivity than deoxy-hemoglobin, and the other LED has a peak wavelength at which oxy-hemoglobin has a lower absorptivity than deoxy-hemoglobin. The light from each LED is absorbed by blood, skin, and other tissues before it reaches the PD. The ratio of absorbed light at each wavelength, R_{os}, is derived from the ratio of transmitted light in accordance with Beer-Lambert's law as given by Equation 1.4. The transmitted light is given by the PD signal upon excitation at each wavelength.

$$R_{os} = \frac{A_{\lambda_1}}{A_{\lambda_2}} = \frac{ln(T_{n,\lambda_1})}{ln(T_{n,\lambda_2})} \tag{1.4}$$

The arterial oxygen saturation, S_aO_2, is then derived from R_{os} and the molar extinction coefficient of oxy-hemoglobin ($\varepsilon_{\lambda,HbO_2}$) and deoxy-hemoglobin ($\varepsilon_{\lambda,Hb}$) at each wavelength:

$$S_aO_2(R_{os}) = \frac{\varepsilon_{\lambda_1,Hb} - \varepsilon_{\lambda_2,Hb}R_{os}}{(\varepsilon_{\lambda_1,Hb} - \varepsilon_{\lambda_1,HbO_2}) + (\varepsilon_{\lambda_2,HbO_2} - \varepsilon_{\lambda_2,Hb})R_{os}} \tag{1.5}$$

Organic optoelectronics are a prime candidate for use in pulse oximetry because they are solution processable at low temperatures compatible with fabrication on flexible plastic substrates. Unlike the inorganic optoelectronics used in commercially available pulse oximeters, the flexible form factors of OLED and OPD allow for an oximeter that has a conformal fit to the human body [4, 91].

Bansal et al. demonstrated oximetry using OLED made from poly[2-(3',7'-dimethyloctyloxy)-5-methoxy-1,4-phenylenevinylene] or OC_1C_{10}-PPV (with peak emission in the red and tail in the NIR) and two OPDs made from $PTB7 : PC_{70}BM$ (with an un-filtered absorption maximum at 690 nm) to perform pulse oximetry using reflected light rather than transmitted light [91]. The OLED is placed in between the two OPDs, each with a different filter to allow the OPD to read light with a peak wavelength of 610 nm or 700 nm. The OLED and OPD were placed onto a subject's forearm with 20 mm spacing in order to probe the oxygen saturation of muscle tissue, and successfully showed the change in the concentration of oxy-hemoglobin in the tissue upon induction and termination of ischemia induced in the arm.

With a focus away from making the optoelectronics themselves flexible, Rothmaier et al. have shown a flexible and wearable pulse oximeter using inorganic light sources and detectors that are not form-fitting to the human body by creating a textile optical fiber glove to transmit the optical signals from the light source, through the fore-fingertip, and back to the detector [92]. Plastic optical fibers (POF) made from poly(methyl methacrylate) (PMMA) were woven or embroidered into polyester fibers. Their wearability while taking oxygenation measurements was demonstrated by integrating the optical fiber textile into the fore-fingertip of a glove in order to take pulse oximetry measurements. Organic and textile optoelectronics are extremely promising for novel implementations of pulse and tissue oximetry. While textile optoelectronics can be integrated into clothing, organic optoelectronics on flexible substrates can be adhered directly to the skin with a secure fit. Even in commercially available pulse oximeters, motion

artifacts and ambient light interference are known problems that hinder the measurement accuracy. By adhering the sensor closely to the skin and letting it flex and move with the skin, the noise from ambient light can be reduced as well as the impact of motion artifacts [4].

1.2 Fabrication process for flexible medical devices

A wide variety of fabrication methods is necessary in order to create all the components of a wearable health monitoring device. Conventional silicon-based microfabrication techniques are necessary for the sensor readouts, microprocessor, and communication. However, large area sensors and batteries are desirable in order to increase signal quality and operation time, respectively. Given the poor area-cost scalability of silicon processing [93], printing functional materials on inexpensive substrates is an attractive alternative to maintain desirable device performance while saving cost. Finally, the fabricated devices must be integrated onto a wearable substrate such as a textile, elastomer or patch.

Silicon processing is a necessity in order to form the workhorse silicon-based transistor processors that communicate and compute. The tremendous advances in computational speed and low power consumption of these devices following Moore's law make this technology completely unrivaled by any other processing technology. While these circuits are on fabricated on rigid silicon wafers, it is possible to transfer them to flexible and stretchable substrates that conform well to the body. The Rogers group has extensively demonstrated such transfer techniques for a variety of systems ranging from image sensors [94], wearable [14] and even implantable devices and systems [15, 95]. Transferring pre-fabricated devices on silicon can be done using several techniques. A packaged integrated circuit package may flip chip bonded or pick-and-placed onto an elastomeric substrate using a low-temperature solder[14] or adhesive printed electrodes[96] as shown in Table 1.2. Devices fabricated on a wafer may also be transferred directly onto an elastomeric substrate such as PDMS by performing a wet etch underneath the fabricated device to loosen the foundation [94]. A buried oxide layer on the wafer is needed in order to act as the detachment point for this transfer. The interconnects between these transferred devices can also be deposited and etched into shape with microfabrication techniques [14, 15, 94]. However, since the transferred wafer-based devices are fairly rigid and not stretchable, the interconnects must be able to accommodate the all the strain of the substrate to prevent other devices from fracturing. To achieve such a goal, the interconnects can either delaminate off the substrate [94], or be patterned into a serpentine configuration [14] to reduce the strain they experience. Sekitani et al. demonstrated that stretchable interconnects created from printable pastes can connect rigid devices transferred onto an elastomeric substrate [13].

Solution processable materials simplify fabrication and reduce cost by eliminating vacuum deposition, photolithography and etch steps used in microfabrication. Common solution processable materials include dielectrics, conductors and semiconductors used to make a wide variety of devices. These functional inks may be deposited on a variety of substrates, ranging from plastic to textiles, using scalable roll-to-roll compatible printing methods. Despite the limited performance of printed transistors, printing is ideal for sensors. Not only is cost reduced, but larger sensors can be more easily printed than microfabricated since the process is not limited by wafer throughput. Additionally the need for any transfer processes may be

Table 1.2. Device fabrication techniques for wearable systems and devices.

Method	**Scalability**	**Solution Viscosity**	**Deposition on Wearable Substrates**	**Roll-to-Roll Throughput**	**Ref.**
Microfabrication	Limited, expensive	NA	Need transfer process and bonding layer	Pick-and-place machines, 0.1 - 1 m/s	
Spin coating	Limited, wasteful	$<$ 1,000 cP	Plastic or elastomeric substrates	Not compatible	
Printing: Blade & slot-die coating	High, limited to one dimensional features	$<$100 cP	Plastic or elastomeric substrates	0.01 - 1 m/s	[97, 98]
Printing: Inkjet	Limited, good for sparse features	5-50 cP	Plastic or elastomeric substrates	0.01 - 0.1 m/s	[98]
Printing: Gravure and flexographic	High	10 - 1,000 cP	Plastic or elastomeric substrates	0.1 - 10 m/s	[99]
Printing: Screen and stencil	High	1,000 - 100,000 cP	Plastic, elastomeric or textile substrates	0.1 - 1 m/s	[98, 100]
Molding	Medium to high, depending on curing time	No requirement	Plastic, elastomeric or textile substrates	0.01 - 0.1 m/s	[101]

eliminated since the sensor may be printed on a wearable substrate. A vast range of wearable sensors such as temperature sensors [24], bioelectronic electrodes [12], biosensors [102], and electrochemical sensors [103, 104] have been demonstrated by printing solution-processable functional inks. The most common solution processing technique for low viscosity inks of <100 centipoise (cP) is spin coating. While this does produce a uniform film, it does not use ink parsimoniously and is difficult to scale to large areas [98]. A more efficient method of printing uniform films from low viscosity inks can be achieved by doctor blade coating [4], slot-die coating [98] and spray coating [105]. Patterning low viscosity inks may either be achieved via patterning the surface of a substrate to direct wetting [97] or inkjet printing [98]. Inkjet printing is well adept for depositing sparse, thin designs but becomes difficult for larger-sized features [3, 106, 107]. Gravure and flexographic printing require higher viscosity inks for reliable printing[98]. While formulating high viscosity inks necessitates the use of highly soluble solutes, features as small as five micron can be reliably printed at speeds approaching one meter per second[99]. Functional materials with a high paste-like viscosity (1,000-100,000 cP) can be deposited via screen printing and stencil printing[100, 108]. Molding is also compatible with roll-to-roll manufacturing, but the flow rate into the mold pattern and curing speed is a critical factor in determining the maximum throughput speed[101]. Solution processing can even be integrated with textile substrates, which are conformal and robust. However due to the high roughness and porosity of textiles, they are best suited for devices that require thick active layers such as batteries[109, 110].

The low power and high speed of silicon-based electronics coupled with the low cost area scalability, facile wearable substrate integration and high sensor performance of printable sensors means all wearable systems will be heterogeneous. Consequently it will be necessary to integrate the transfer process for silicon processors and printing of the sensors onto the same line to maximize efficacy. Additionally, proper printing techniques will need to be chosen which deposit the necessary film thicknesses to maximize energy storage in the batteries, minimize energy consumption by the sensors, and make the operating voltages between the silicon and printed-based devices compatible.

1.3 Medical sensor data processing and transmission

Sensors are essentially transducers - biosensors transduce biosignals to different kind of electrical signals, such as voltage, current, impedance, and capacitance. However, these electrical signals require preprocessing before they can be interpreted to a meaningful number or signal that can be used for medical monitoring or diagnostics. In this section the workflow of a complete biosensor system is discussed. Fabricated biosensors are often connected to an analog front end, where the analog electrical signal is filtered and amplified. A microcontroller (MCU) or microprocessor (MPU) then reads the signal after digitizing the analog signal using an analog to digital converter (ADC). Next, the data is processed using algorithms running on the MCU / MPU and finally sent out to a computer or portable device via wired or wireless interface for data interpretation and visualization.

While designing a biosensor system, the type of electrical signal generated by the biosensor, the measurement range, and the frequency of the signal should be taken into account. The measurement range determines the resolution required in the circuitry to resolve the de-

Table 1.3. Biosignals, sensing methods, and measurement parameters for vital signs monitoring.

Biosignal	**Biosensor / Measurement Method**	**Transduced Signal**	**Measurement Range and Paramater**	**Signal Frequency**	**Ref.**
Temperature	Thermistor / Thermoelectric / Optical	Resistance	32 - 40 ° C / 90 - 104 ° F	dc - 0.1 Hz	[27]
HR					
Electrocardiography (ECG)	Skin electrodes	Voltage	0.5 - 4 mV	.01 - 250 Hz	[35, 111]
Photoplethysmography	Optical	Photodiode Current	0.05 - 4 μA	.05 - 30 Hz	[90]
Respiration Rate	Strain gauge / Impedance	Resistance	2 - 50 breaths / min	0.1 - 10 Hz	[49, 59]
Blood Pressure	Pressure sensitive TFT	TFT Drain Current	10 - 400 mm Hg	dc - 50 Hz	[71]
Pulse Oxygenation	Optical	Photodiode Current	SpO_2 80 - 100 %	.05 - 30 Hz	[4, 90]
Glucose	Electrochemical	Current	Tear glucose conc. 0.05 - 1mM	dc - 0.1 Hz	[112]
Bioelectronic					
Electroencephalography (EEG)	Scalp electrodes	Voltage	5 - 300 μ V	dc - 150 Hz	[111]
Electrocorticography (ECoG)	Brain-surface electrodes	Voltage	10 - 5000 μ V	dc - 150 Hz	[111]
Electromyography (EMG)	Skin electodes	Voltage	0.1 - 5 mV	dc - 10 kHz	[111]
Galvanic skin response	Skin electodes	Impedance	1 - 500 kΩ	0.01 - 1 Hz	[111]
Electrooculography (EOG)	Contact electrodes	Voltage	50 - 3500 μ V	dc - 50 Hz	[111]

sired signal. For suppressing unwanted noise, the raw analog signal is filtered and only the desired part of the signal is amplified. Table 1.3 lists biosignals discussed in this chapter, the sensing mechanisms, the transduced electrical signal, measurement range, and signal frequencies. Since there are variations from person to person, a tolerance should be added to these parameters. In general, these design criteria apply to most of the biosensors.

Conventional biosensors generate a continuous time signal or analog signal. Non-invasively obtained biosignals tend to be small and contain noise. The main purpose of the analog front end (AFE) is to reduce the noise and bring up the signal to levels that can be read by the MCU / MPU. For most setups, the power line frequency (50 Hz or 60 Hz) and the associated harmonics need to be taken out using filters. A differential input scheme using differential amplifiers or instrumentation amplifiers can also be used to reduce ambient noise [36]. Next, depending on the frequency of interest (Table 1.3), high-pass, low-pass, or band-pass filters can be implemented to extract the desired signal [4, 35, 90]. After that, the signal is brought up to a level so that it can be read with ADCs; here the resolution of the ADC should be selected considering the signal range and signal to noise ratio (SNR). The digitized signal is processed by the MCU / MPU - the sampling frequency should be high enough to reduce aliasing. Finally, the processed data is sent out to a host computer or a portable device using wired or wireless interfaces. An additional design parameter is the power requirements of the biosensors and the circuitry, which is discussed in the next section.

1.4 Power requirements for flexible medical devices

Providing the required electrical power to flexible and wearable devices is one of the grand challenges in electronics today. While some self-powered sensing elements have recently been developed [25, 73, 74, 81, 113], most health monitoring devices require power to drive the sensing elements; examples include resistive strain and temperature sensing and optoelectronic measurements such as PPG. In addition to the demands of the sensor itself, power is required to analyze the data collected and to communicate or display the result. The basic requirement of power sources for these wearable health monitoring modules is to provide whatever power is needed, without disrupting the wearer's mobility or comfort. To avoid plugging wires into the module frequently, on-board energy storage or reliable energy harvesting with sufficient capacity must be present. These power sources should be located near the sensor module, to minimize wiring and the associated resistive losses, discomfort, and system complexity. Since large energy harvesting or storage capacity tends to require a large area or volume of material, it is beneficial for the power sources themselves to be flexible so that they do not limit the conformability or comfort of the system. In particular, the structure and mechanical properties of the power source would ideally be similar to those of the sensor itself (e.g. stretchable or woven textiles) so that the power source can withstand the same stresses and respond similarly. This section will discuss the power requirements for the various types of wearable health sensing components and the technologies available to provide the necessary power. Focus will be given to the limitations and opportunities of each power source technology, recent advances making them more suitable for wearable applications, and demonstrations of their potential in health monitoring systems.

The reported power requirements for various types of vital signs monitoring systems

Table 1.4. Power requirements of wearable medical sensing system components.

System	Component	Peak Current (mA)	Voltage (V)	Duty Cycle (%)	Average Power (μW)	Ref.
Temperature sensor	Resistive sensor	0.01	3	100	30	[114]
	ADC	1.2	3	0.001	3	
	Microcontroller	4	3	1	150	
	Bluetooth LE	18 (RX), 15 (TX)	3	0.05	60	
	Display	0.2	3	10	60	
Temperature sensor	Resistive sensor	0.001	10	-	-	[21]
HR sensor	Pressure sensitive TFT	<0.01	100	-	<1,000	[42]
ECG	Entire system	-	-	-	35,000	[33]
Pulse oximeter	Optoelectronic probe	-	3.7	50	1,760	[115]
	Optoelectronic probe (low power mode)	-	3.7	8	150	
	Microcontroller + Bluetooth LE	-	3.7	-	11,550	
	Microcontroller + Bluetooth LE (low power mode)	-	3.7	-	3	
Pulse oximeter	Organic optoelectronic probe	20	9	-	-	[4]
Glucose sensor	Entire system in contact lens	-	-	-	3	[112]
EEG	ASIC front end	0.02	3	-	-	[116]
	Entire system	-	3	-	800	

are given in Table 1.4. Although the current, voltage, and power consumption values vary greatly, there are some generalizations to be made. First, the power consumption of light-emitting devices (e.g. the optoelectronic probes used for PPG) is relatively high compared to resistive sensors. The peak current for wireless communication is also very high, although communicating data infrequently can reduce the average power consumption. Microcontrollers consume less power than wireless transmitters while operating, but must generally operate for longer time periods, particularly if significant computation is being done locally to avoid sending large amounts of data wirelessly.

Often, the duty cycle of the components can be adjusted to reduce power consumption, either by reducing the operating time of the component during each cycle or by increasing the time between uses of the component. For example, in their design of a solar-powered pulse oximeter, Dieffenderfer et al. included a low-power mode with lower duty cycle for cases when sufficient solar power is not available [115]. However, since monitoring health is of utmost importance, the duty cycle must be adjusted with care to ensure that the reliability of the sensing, data analysis or communication is not compromised. Also, although reducing the duty cycle reduces the average power, the peak current is typically not impacted. The power supply must therefore be designed to supply the peak current without a significant loss in efficiency, as well as supplying the average power for whatever duration is required between charging cycles.

Designing custom low-power data-processing circuits and wireless transmitters can also reduce power consumption, such as in the 3-μW glucose-sensing contact lens [112]. However, if a higher power is permissible, use of off-the-shelf components such as microcontrollers and radios can reduce cost and improve simplicity of the design and compatibility with legacy systems. Additionally, it is desirable to operate all components of a system at the same voltage to avoid additional circuitry to convert between voltages. This is typically in the 3-4 V range, as shown in the table, which is compatible with complementary metaloxidesemiconductor (CMOS) circuits and lithium-ion batteries. However, in the case of many thin-film and organic active electronic devices, particularly TFTs such as the pressure sensitive transistors for HR monitoring [42], the voltage requirement can be much greater than that of CMOS circuits. Some types of energy harvesters also produce voltages that are far outside this range or highly variable. In these cases, power electronics are necessary.

In some sensing mechanisms, a voltage or current is directly generated in response to a stimulus, allowing the sensor to be self-powered. Examples of self-powered sensors are the piezoelectric respiration and HR sensors [73, 81], triboelectric respiration and HR sensors [74, 113], and thermoelectric temperature sensors [25]. However, since requirements for data processing and communication are significant, a system with a self-powered sensing element is not necessarily able to be fully self-powered.

In conclusion, a plethora of flexible and wearable medical devices have been demonstrated with applications in vital signs monitoring, electronic skin, and epidermal and implantable medical sensing. Most of the reported devices utilize flexible, stretchable, and lightweight materials for fabricating the biosensors. The data processing and transmission requirements were met using silicon-based electronics. This scheme allowed the best use of both soft and hard electronics. In this chapter, we listed and discussed flexible and wearable vital monitoring devices, focusing on biosignals such as temperature, HR, respiration rate, blood pressure, pulse oxygenation, and blood glucose. We hope that this chapter will provide readers with the

underlying sensing principle, sensor fabrication, data processing and power requirements of these novel biosensors. We also hope this chapter will convince readers that with further improvement of the biosensors coupled with low-cost and large-area processing capabilities, the promise of soft bioelectronic and biophotonic sensors and its applications in monitoring vital signs monitoring is enormous.

1.5 Scope of this thesis

This thesis describes the design, fabrication and system-level implementation of the printed bioelectronic and biophotonic sensors for wearable health monitoring. The subsequent chapters will present sensing methodology, design criteria, fabrication, and applications of printed medical sensors. The main topics covered in this thesis are:

1. Chapter 2: Printed bioelectronic electrodes for bioimpedance spectroscopy, ECG, and EMG.
2. Chapters 3, 4, and 5: Printed biophotonic sensors for blood and tissue oximetry
3. Chapter 6: Integration of printed sensors to flexible hybrid electronics for wearable health monitoring

Chapter 2 presents the fabrication and low-temperature sintering ($\approx$ 200 °C) technique to fabricate gold electrodes. Bioelectronic interfaces require electrodes that are mechanically flexible and chemically inert. Flexibility allows pristine electrode contact to skin and tissue, and chemical inertness prevents electrodes from reacting with biological fluids and living tissues. Therefore, flexible gold electrodes are ideal for bioimpedance and biopotential measurements such as bioimpedance tomography, ECG, electroencephalography (EEG), and EMG. In this chapter, we present a manufacturing process to fabricate gold electrode arrays on plastic substrates. At low-temperature sintering conditions, lines of different widths demonstrate different sintering speeds. Therefore, the sintering condition is targeted towards the widest feature in the design layout. Manufactured electrodes show minimum feature size of 62μm and conductivity values of 5 x 10^6 Sm^{-1}. Utilizing the versatility of printing and plastic electronics processes, electrode arrays consisting of 31 electrodes with electrode to electrode spacing ranging from 2 mm to 7 mm are fabricated, and used for impedance mapping of conformal surfaces at 15 kHz. Overall, we show the fabrication process of an inkjet-printed gold electrode array that is electrically reproducible, mechanically robust, and promising for bioimpedance and biopotential measurements.

Chapter 3 presents an all-organic optoelectronic sensor for pulse oximetry. Pulse oximetry is a ubiquitous non-invasive medical sensing method for measuring pulse rate and arterial blood oxygenation. Conventional pulse oximeters use expensive optoelectronic components that restrict sensing locations to fingertips or earlobes due to their rigid form and area-scaling complexity. In this chapter, we present a pulse oximeter sensor based on organic materials, which are compatible with flexible substrates. Green (532nm) and red (626nm) OLEDs are used with an OPD sensitive at the aforementioned wavelengths. The sensors active layers are deposited from solution-processed materials via spin-coating and printing techniques. The all-organic optoelectronic oximeter sensor is interfaced with conventional electronics at 1kHz

and the acquired pulse rate and oxygenation are calibrated and compared with a commercially available oximeter. The organic sensor accurately measures pulse rate and oxygenation with errors of 1% and 2%, respectively.

Chapter 4 reports a systematic study of a reflectance oximeter sensor design in terms of component geometry, light emitter and detector spacing, and the use of an optical barrier between the emitter and the detector to maximize sensor performance. The reflection-mode sensor, which consists of light emitters and detectors, is a vital component of reflectance oximeters. In this chapter, printed red and NIR OLEDs and OPDs are used to design three sensor geometries: (1) Rectangular geometry, where square OLEDs are placed at either side of the OPD; (2) Bracket geometry, where the OLEDs are shaped as brackets and placed around the square OPD; (3) Circular geometry, where the OLEDs are shaped as block arcs and placed around the circular OPD. Utilizing the bracket geometry, we observe 39.7% and 18.2% improvement in PPG signal magnitude in the red and NIR channels compared to the rectangular geometry, respectively. Using the circular geometry, we observe 48.6% and 9.2% improvements in the red and NIR channels compared to the rectangular geometry. Furthermore, a wearable two-channel PPG sensor is utilized to add redundancy to the measurement. Finally, IVW and TM algorithms are implemented to improve the detection of HR from the multi-channel PPG signals.

Chapter 5 demonstrates a novel flexible and printed sensor array composed of OLEDs and OPDs, which senses reflected light from tissue to determine the oxygen saturation. Transmission-mode pulse oximetry, the optical method for determining oxygen saturation in blood, is limited to only tissues that can be transilluminated, such as the earlobes and the fingers. The existing sensor configuration provides only single point measurements, lacking 2D oxygenation mapping capability. In this chapter, we use the reflectance oximeter array beyond the conventional sensing locations using a novel sensor configuration. The sensor is implemented to measure oxygen saturation on the forehead with 1.1% mean error and to create 2D oxygenation maps of adult forearms under pressure-cuff-induced ischemia. In addition, we present mathematical models to determine oxygenation in the presence and absence of a pulsatile arterial blood signal. The mechanical flexibility, 2D oxygenation mapping capability, and the ability to place the sensor in various locations make the reflectance oximeter array promising for novel medical sensing applications such as monitoring of real-time chronic medical conditions as well as post-surgery recovery management of tissues, organs, and wounds.

Chapter 6 reports on interfacing of soft devices, i.e., sensors to silicon ICs for wearable health monitoring. The interfacing of soft and hard electronics is a key challenge for flexible hybrid electronics. Currently, a multi-substrate approach is employed, where soft and hard devices are fabricated or assembled on separate substrates, and bonded or interfaced using connectors - this hinders the flexibility of the device, and is prone to interconnect issues. In this chapter, utilizing a process flow compatible with flexible printed circuit board (FPCB) assembly process, a WSP is fabricated composed of inkjet-printed gold ECG electrodes and a stencil-printed NiO thermistor. The ECG electrodes provide 1 mV_{p-p} ECG signal at 4.7 cm electrode spacing and the thermistor is highly-sensitive at normal body temperatures, and demonstrates temperature coefficient, $\alpha \approx$ -5.84 % K^{-1} and material constant, $\beta \approx$ 4330 K. This sensor platform can be extended to a more sophisticated multi-sensor platform where sensors fabricated using solution processable functional inks can be interfaced to hard electronics for health and performance monitoring, as well as internet of things (IoT) applications.

Finally, Chapter 7 provides an overview of the future directions with printed bioelectronic and biophotonics sensors. In addition, discusses potential application scenarios of flexible hybrid electronics in medical/environment/agricultural/structural sensing. Particular attention is given to the topics listed below:

1. Integrated bioelectronic and biophotonic bandage for wound monitoring
2. Wearable multi-sensor platform for continuous health monitoring
3. Printed large-area sensor array for structural health monitoring (SHM)
4. Flexible hybrid electronics for industrial and environmental monitoring

A pictorial overview of the thesis is provided in Fig. 1.9.

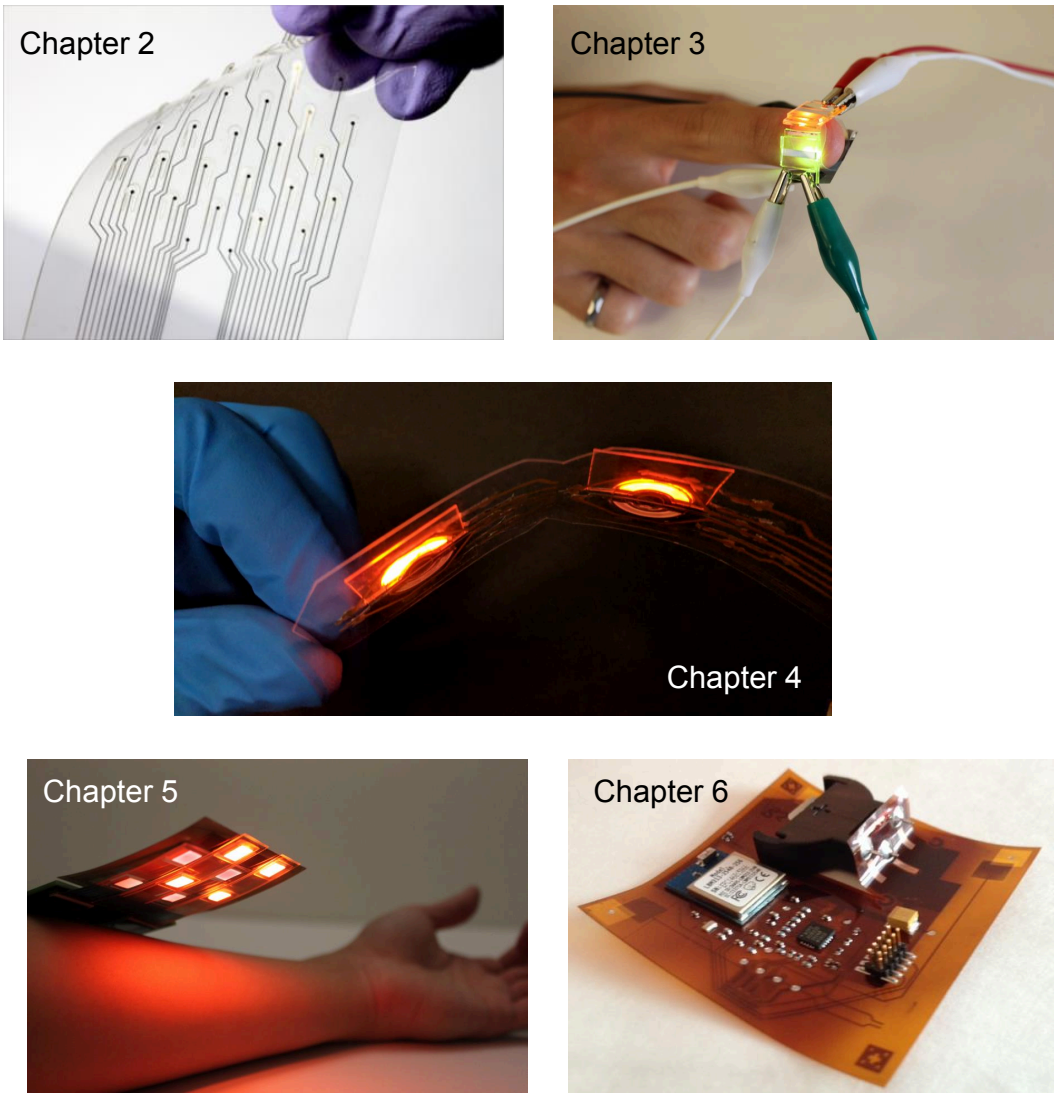

Figure 1.9. **Pictorial overview of this thesis**. Chapter 2 presents the fabrication and low-temperature sintering of printed gold electrodes for bioelectronic interfaces. Chapters 3 presents an all-organic optoelectronic sensor for pulse oximetry. Chapter 4 discusses the design, sensing methodology, fabrication of printed reflectance oximeters. Chapter 5 presents a flexible organic reflectance oximeter array, which is used for blood and tissue oximetry. Chapter 6 discusses a key enabling technology for flexible and printed sensors - flexible hybrid electronics, where soft sensors are interfaced with hard silicon-based ICs for wearable health monitoring.

Chapter 2

Printed biopotential and bioimpedance electrodes

2.1 Introduction

Bioelectronic electrodes are essential in electrophysiology, the scientific field that investigates the relationship between electricity and life. Since the advent of electrophysiology in 1783 marked by Luigi Galvani's experiment of electrical stimulation of a frog leg, electrodes have been used to transduce the body's ionic current to electronic current and vice versa [111]. These bioelectronic electrodes can be utilized for both bioimpedance and biopotential measurements (Fig. 2.1). In biopotential measurements, differential voltage measurements are done on skin and tissue (Fig. 2.1a,b). For example, in ECG, a set of electrodes are used to pick up the electrical depolarization signal of the heart that provides the cardiac rhythm of the patient [117] (Fig. 2.1b). Similar to ECG, electrodes can be used to pick up electrical signals produced by skeletal muscles, which is known as EMG (Fig. 2.1a). In the case of bioimpedance tomography, a small amount of alternating current is sourced through the tissue, and the resultant voltage signals are recorded using an array of electrodes (Fig. 2.1c). Then, various biological tissues are electrically differentiated depending on the complex impedance of the tissues. The contrast between two different types of tissues, for example, lean and fatty tissue can be picked up using this technique, and reconstructed graphically [118]. For bioimpedance and biopotential measurements, the interface between the electrode and the body is crucial, any disturbance at the interface creates unwanted noise artifacts or even invalidates the measurement [119]. Flexible electronics and optoelectronics are highly promising for creating high-fidelity bioelectronic and biophotonic interfaces [4, 90, 120, 121]. The elasticity of flexible electronics allows skin-like devices, which are bendable and stretchable [3, 122]. Hence, medical devices fabricated using flexible materials have the potential to interface better with the human body when compared to rigid electronics.

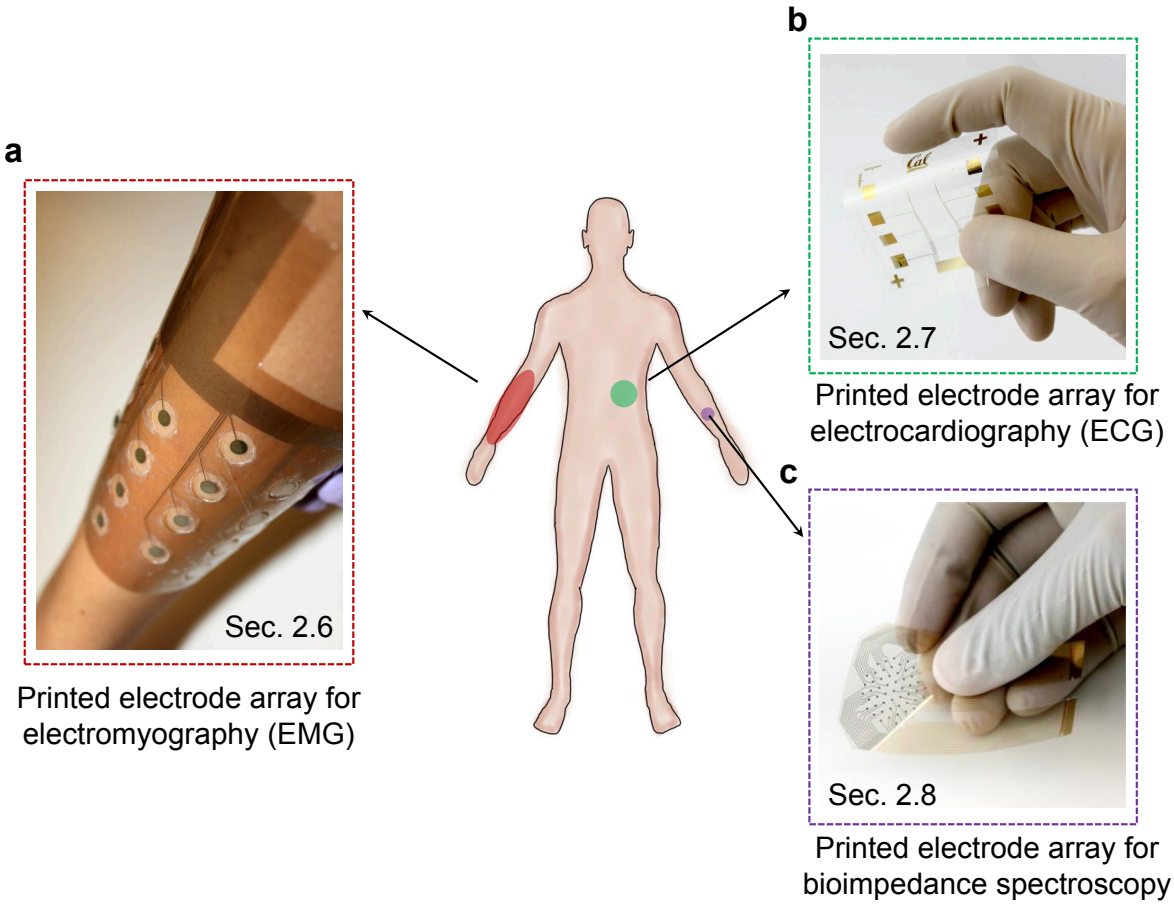

Figure 2.1. **Printed electrodes for biopotential and bioimpedance measurements**. (**a**) A printed electrode array is utilized on the arm to record EMG signal. Here, the electrode array covers a large area to sense biopotential signal from the arm muscles. (**b**) A printed electrode array is utilized on the lower-left ribcage to record ECG signal. The ECG electrodes are placed in a manner to maximize the ECG signal magnitude, which originates at the heart. The sensor placement locations are limited for ECG electrodes. (**c**) A printed electrode array is utilized for bioimpedance spectroscopy. Here, the array can be used to measure the complex impedance of tissues. The bioimpedance array can be placed on any part of the body to quantify the contrast among various types of tissues.

2.2 Printed electrodes for bioelectronic interfaces

Fabrication of flexible medical devices has heavily relied on processing techniques such as metal evaporation, atomic layer deposition, photolithography processes, and transfer printing [123, 124]. In contrast, printing methods, which use relatively inexpensive tools and mild processing conditions [123, 125] can also be used to fabricate flexible medical devices [3, 4]. Among other printing techniques, inkjet-printing is promising for fabricating bioelectronic electrodes because inkjet-printing is a non-contact, direct, additive printing method with minimal waste of materials. Additionally, inkjet-printing allows easily changeable layouts, which drastically reduce turn-around times for multiple design iterations.

Although the use of inkjet-printing to fabricate biosensors is well-described [102, 106, 126], the number of inkjet-printed flexible medical devices in literature is still limited. Jensen et al. utilized inkjet-printed gold nanoparticle electrochemical arrays on heat resistant polyimide Kapton substrate for immunodetection of a cancer biomarker protein [127]. Jalo et al. demonstrated inkjet-printed antennas on plastic substrates using silver nanoparticle ink, and optimized antenna design for Bluetooth signal transmission from the human body surface[128]. While silver can be used for interfacing sensors to electronics, silver reacts chemically to bodily fluids, which makes silver undesirable for direct body and skin interfaces [129]. Alternatively, organic conducting polymer, PEDOT:PSS can be used for fabricating high-performance bioelectronic electrodes [34]. That said, gold remains the metal of choice for fabricating electrodes for biomedical applications. Gold is a high work function metal, hence it demonstrates superior stability and inertness when in contact with aqueous media, biological fluids, or living tissues. To summarize, although bioelectronic electrodes can be fabricated in different ways by using conductive materials [12, 130–132], there is still a lack in the materials science literature of the description of robust and efficient inkjet-printed electrode arrays with applications in the biomedical field.

In this chapter, we report on the fabrication of inkjet-printed flexible gold electrode arrays on plastic substrates that can be used in wearable biomedical applications. These electrode arrays are printed using a gold nanoparticle ink, and the sintering conditions are adjusted to plastic-compatible temperatures around 200 °C. At low-temperature sintering conditions, lines of different widths demonstrate different sintering speeds. We observed that this is due to a diffusion-controlled mechanism of sintering, which depends on surfactant displacement and solvent evaporation. Therefore, the optimum sintering condition is targeted towards the widest feature in the design layout. To enhance mechanical compliance, laser-cut free-standing electrodes are used, which interface better to curved surfaces. Overall, in this chapter, practical considerations for inkjet-printing reproducible and robust flexible arrays are described, which can be used for bioimpedance and biopotential measurements such as bioimpedance tomography, ECG, electroencephalography (EEG), and EMG. Here we focus on the array fabrication, low-temperature sintering, and the methodology used for mapping impedance on conformal surfaces.

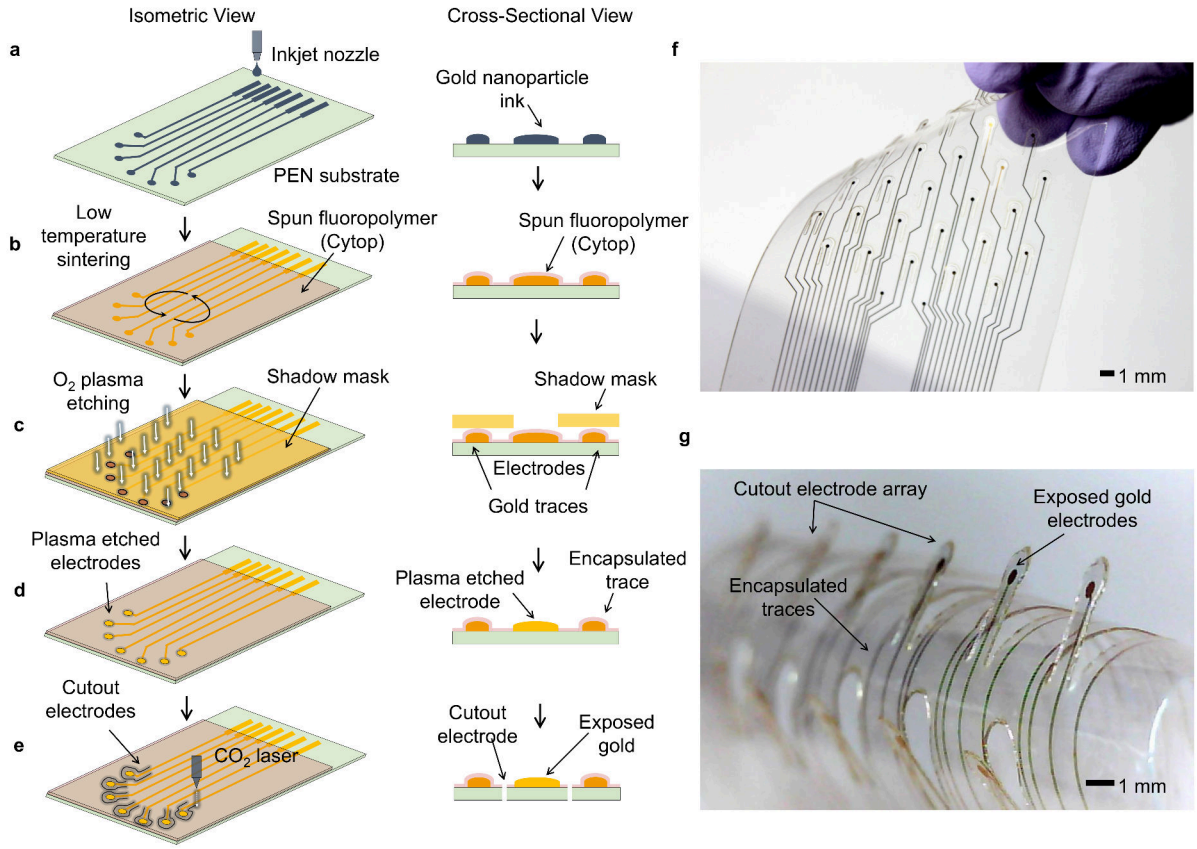

Figure 2.2. **Fabrication process for manufacturing the printed electrode array**. (**a-e**) Isometric views and corresponding cross-sectional views of the process steps are shown side by side. (**a**) Gold nanoparticle ink is inkjet printed on PEN substrate. (**b**) After low-temperature sintering, a thin (100 nm) dielectric layer of a fluoropolymer (Cytop) is spun to encapsulate the gold traces. (**c**) To expose the electrodes, oxygen (O_2) plasma etching is used in conjunction with a shadow mask. (**d**) Plasma etched electrodes are shown, which will be in contact with the sensed surface. At this point, traces are encapsulated and the electrodes are exposed, as shown in the cross-sectional view. (**e**) CO_2 laser is used to cut out freestanding electrodes. (**f**) Finished array after laser cutting electrodes. (**g**) Electrode array after bent to 5 mm radius - cutout electrodes extend like freestanding flaps, which aid in reaching into deeper parts of the sensed surface.

2.3 Flexible inkjet-printed gold electrode array

Inkjet-printing is promising for fabricating gold electrode arrays since it is a non-contact, digital, and additive printing method. In contrast to other printing methods such as screen printing, which uses high viscosity inks with surfactants, inkjet-printing uses low viscosity inks - this allows printing of high-purity materials with no binders [133]. Most common types of conductive ink used in inkjet-printing are metal micro and nanoparticle dispersions, metal precursor solutions, conducting polymer solutions, and nanocarbon material dispersions [134]. Because gold is highly stable and remains inert when in contact with biological fluids or living tissues, we employed gold nanoparticle ink for the array fabrication.

The flexible arrays are inkjet-printed on a 45 μm thick planarized PEN substrate: Teonex Q65FA Teijin-DuPont. The process steps are illustrated in Fig. 2.2a - e, where process steps and corresponding cross-sectional views are shown side by side. Gold nanoparticles are printed with 10 pL drops at 30 μm drop spacing. Less than 25 μm drop spacing created bulge instability, while higher than 35 μm drop spacing resulted in isolated drops, which did not merge to form continuous lines. The wet ink is then dried and sintered using the low-temperature sintering process. At low-temperature sintering conditions, sintering time depends on the ink volume of the printed features - the wider and more voluminous the line, the longer the sintering time. Therefore, the optimized sintering condition was targeted towards the widest features in the array, which are 350 μm pads. In the bioelectronic configuration, electrodes are used to extract voltage or current signal from skin or tissue, which is then carried by the traces to the external part of the circuit. Hence, the traces are electrically encapsulated, and the electrodes are kept open for direct electrical contact. A thin layer of a fluoropolymer (Cytop) is deposited using spin coating to encapsulate the traces (Fig. 2.2b). Since the encapsulation layer is thin (100 nm), it did not hinder the contact between the electrode and the sensed surface. In addition, Cytop proved quite robust to acids, alkaline, and organic solvents. Also, the hydrophobic nature of the thin Cytop coating properly encapsulated gold traces from bodily fluids.

O_2 plasma etching in conjunction with a shadow mask was used to create vias in the Cytop to expose the electrodes (Fig. 2.2c). The cross-sectional view in Fig. 2.2d shows the traces are covered with Cytop, and the electrodes are exposed. CO_2 laser cutting was also explored as an alternative to O_2 plasma etching to create vias. The CO_2 laser deposited sub-products of the degraded Cytop on the sidewalls while creating vias, creating bumps that are not desirable for electrode contacts (Fig. 2.3a,c). On the contrary, O_2 plasma created clean cuts (Fig. 2.3b,d,e). Therefore, for creating vias, O_2 plasma etching was chosen over CO_2 laser cutting. Finally, the CO_2 laser is used to cut around the electrodes to create freestanding flaps. Since these flaps are mechanically constrained from only one side, these demonstrated better compliance than uncut electrodes in reaching deeper parts of the sensed surfaces. For example, in a surface wound sensing scenario, the array needs to conform to a surface with cuts in the range of a few millimeters deep. The freestanding flaps can reach into cuts that are a few millimeter deep, while the uncut electrodes remain over the cut, resulting in no electrical contact.

A finished array is shown in Fig. 2.2f. The 45 μm thick PEN substrate is quite flexible. Also, the laser-cut freestanding electrodes enhance the conformity of the array. Fig. 2.2g shows a zoomed view of the free-standing electrodes. In this case, the array was bent to 5 mm radius of curvature. These cut-out flaps have better flexibility because they are confined to the substrate from just one direction.

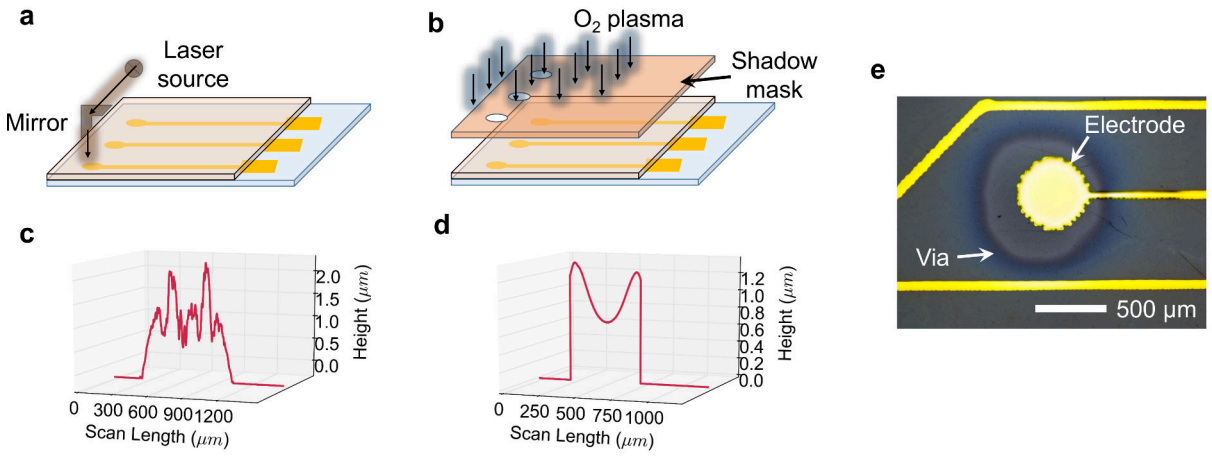

Figure 2.3. **Methods for removing the dielectric layer (Cytop) from the electrodes**. (**a**) Laser drilling to open via through the dielectric layer. (**b**) O_2 plasma etching using a shadow mask to selectively etch the dielectric layer. The surface profile of an electrode after (**c**) laser drilling and (**d**) plasma etching. (**e**) Micrograph of an electrode after plasma etching - etched area encircled by a dark Cytop layer, which is clearly visible; also the exposed electrode is shown.

For testing the efficacy of the cutout array over the flat array, both arrays are used to map a surface with different sensing depths as shown in Fig. 2.4. These topography mapping tests are designed to mimic biological surfaces that are few millimeters deep. Both the flat and the cutout array are placed over a metallic mesh, which is the sensed surface, and glass slides are placed on top of the mesh to emulate sensing depths ranging from 0.5 mm to 5 mm (Fig. 2.4a and b). Electrical resistance measurements from electrode pads to the metallic mesh are done using a multimeter to verify proper electrode to surface contact. Resistance values similar to the line resistances of the electrodes are considered as a 'successful' contact, and significantly higher resistance values are deemed as an 'unsuccessful' contact. The results are presented in the bar chart in Fig. 2.4c. The flat and the cutout array perform similarly with higher than 90% successful contacts for sensing depths of ranging 0.5 and 1 mm. For sensing depths higher than 1 mm the cutout array retains the performance, while the flat array performance degrades significantly. This is due to the fact that at higher sensing depths the array needs to bend up as shown in Fig. 2.4d and e, and electrodes that are confined to the substrate also bend up, which results in no contact between the electrode and the surface. Most of the electrodes at the edge of the step-height do not make contact for the flat array. At higher sensing depth (2 mm and beyond), the second layer of electrodes of the flat array starts to lift up, which is why successful contacts percentage drops to around 50%. On the other hand, the cutout array allows electrodes to move freely and make contact to the surface, therefore, a high-fidelity electrode to surface contact can be established (Fig. 2.4e). In Section 2.7, these electrodes are used for surface impedance mapping of convex and concave surfaces, which mimic surfaces to be sensed in biomedical applications.

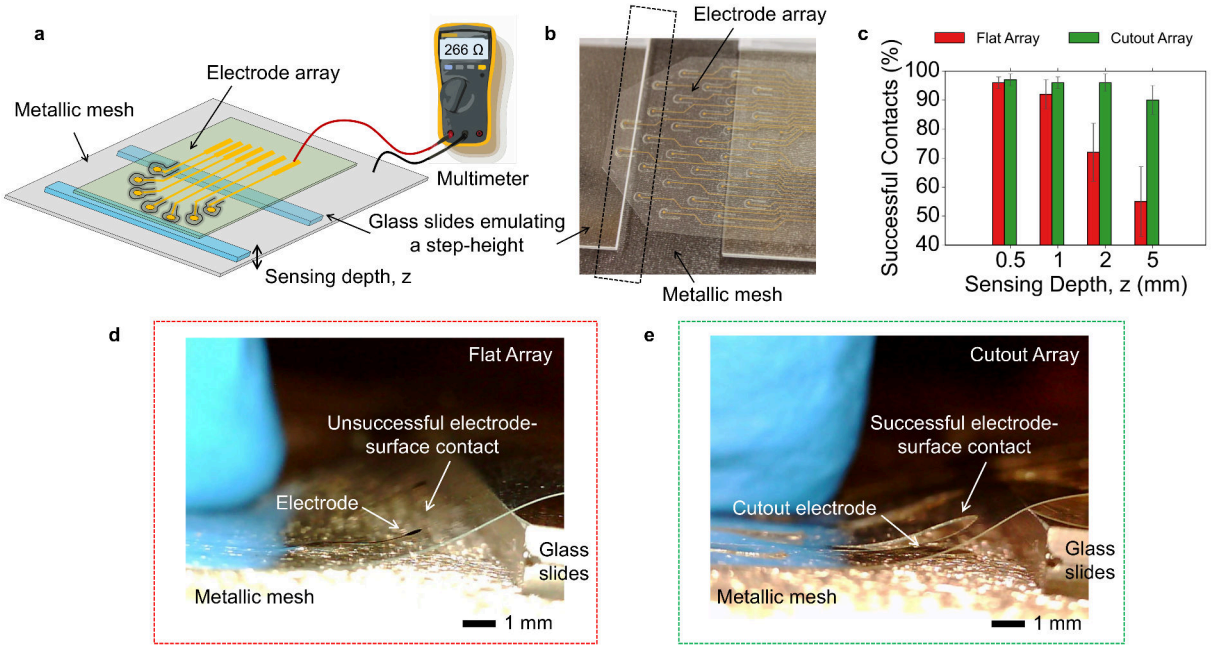

Figure 2.4. **Topography coverage comparison between the flat array and the cutout array**. (**a**) A schematic overview of the topography coverage test setup - the array is placed on a metallic mesh, and glass slides on top of the mesh emulate a step-height. Resistance measurements are done from the electrode pad to the metallic mesh to confirm electrode-surface contact. (**b**) Optical image of the setup - the electrode array, the metallic mesh, and the glass slides are shown. (**c**) A bar chart depicting the percentage of successful electrode-surface contacts by the flat and the cutout array for various sensing depths. Clearly, the cutout array (green bars) provides significant edge over the flat array (red bars) for sensing depths over 1 mm. The error bars represent data collected from five separate runs. (**d-e**) Close-up images collected from the dotted region in (**b**) (at the step-height) for the flat array and the cutout array, respectively. (**d**) Electrodes at the step-height in the flat array do not touch the surface of the metallic mesh because the 2 mm thick glass slides bend the whole array upward, resulting in an unsuccessful electrode-surface contact. (**e**) The cutout array also bends upward at the interface, however, the cutout electrodes are not confined to the array, therefore, the electrodes can make a conformal contact, resulting in a successful electrode-surface contact.

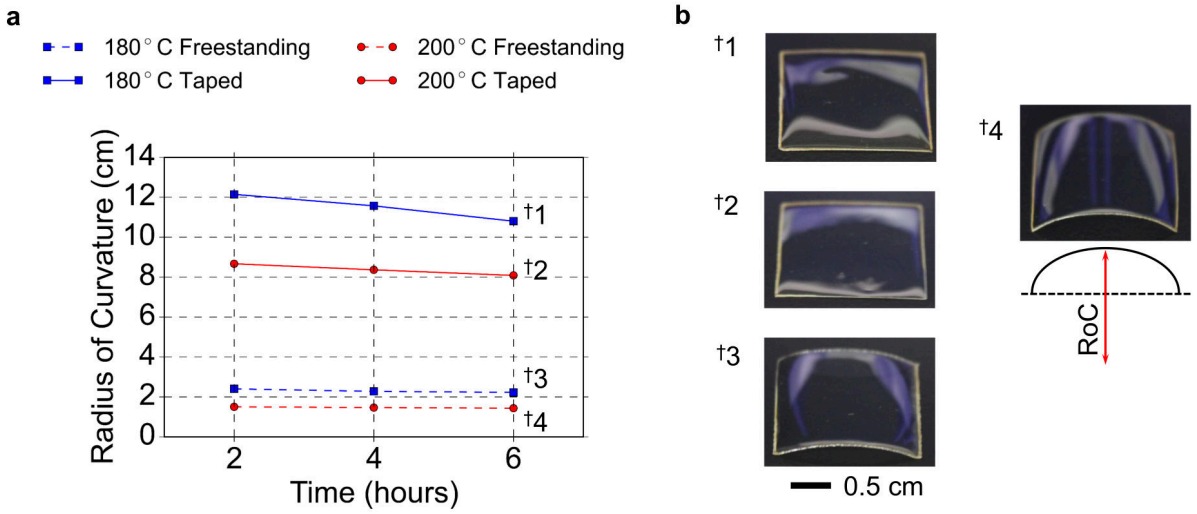

Figure 2.5. **Time-dependent thermal deformation of PEN, Teonex Q65FA Teijin-DuPont**. (**a**) Deformation Radius of Curvature (RoC) versus time plot for 2 cm x 2 cm pieces of PEN. Four different conditions were explored at 180 and 200 °C, where samples were left on top of the hotplate (Freestanding) and taped on top of the hotplate (Taped). (**b**) Optical images of the samples heat-treated for 6 hours, demonstrating thermal deformation ('†' symbols correspond to the heat-treatment conditions).

2.4 Plastic-compatible low-temperature sintering

Although gold is promising for bioelectronic electrode fabrication, processing inkjet-printed electrodes on plastic substrates is challenging. Gold nanoparticle ink requires high sintering temperatures, in the range of 250 °C, which is above the melting temperature of the most common plastics used in flexible electronics, such as polyethylene terephthalate (PET) and PEN. This high processing temperature is suitable for inorganic surfaces like silicon [135]. Moreover, PET and PEN undergo thermal deformation at temperatures higher than the glass transition temperature (T_g) [136]. A common practice in sintering lab-scale printed films to mitigate substrate deformation is to tape down films to the hotplate. Therefore, all the samples reported in this paper were sintered while taped down to the hotplate. A time-dependent thermal deformation plot of the heat-stabilized variant of PEN film is shown and discussed in Fig. 2.5. For printing gold on plastics, custom-made formulations with tailored particle sizes and surfactant chemical structures have to be synthesized [137–139]. Additionally, sintering studies in the literature focus on deposited films [140], while electrode arrays have traces, electrodes, and pads of different geometries and widths. Here, we performed low-temperature sintering of a gold nanoparticle ink and studied different printed geometry and the corresponding sintering characteristics.

To understand the relationship between printed trace linewidth and sintering conditions, traces with widths of 62 μm, 119 μm, and 176 μm were sintered at several combinations of sintering temperature and time, as shown Fig. 2.6a - c. The standard sintering condition for the gold nanoparticle ink is 250 °C for 1 hour, and resistivity of 5.6 x $10^{-8}\Omega$m is attained

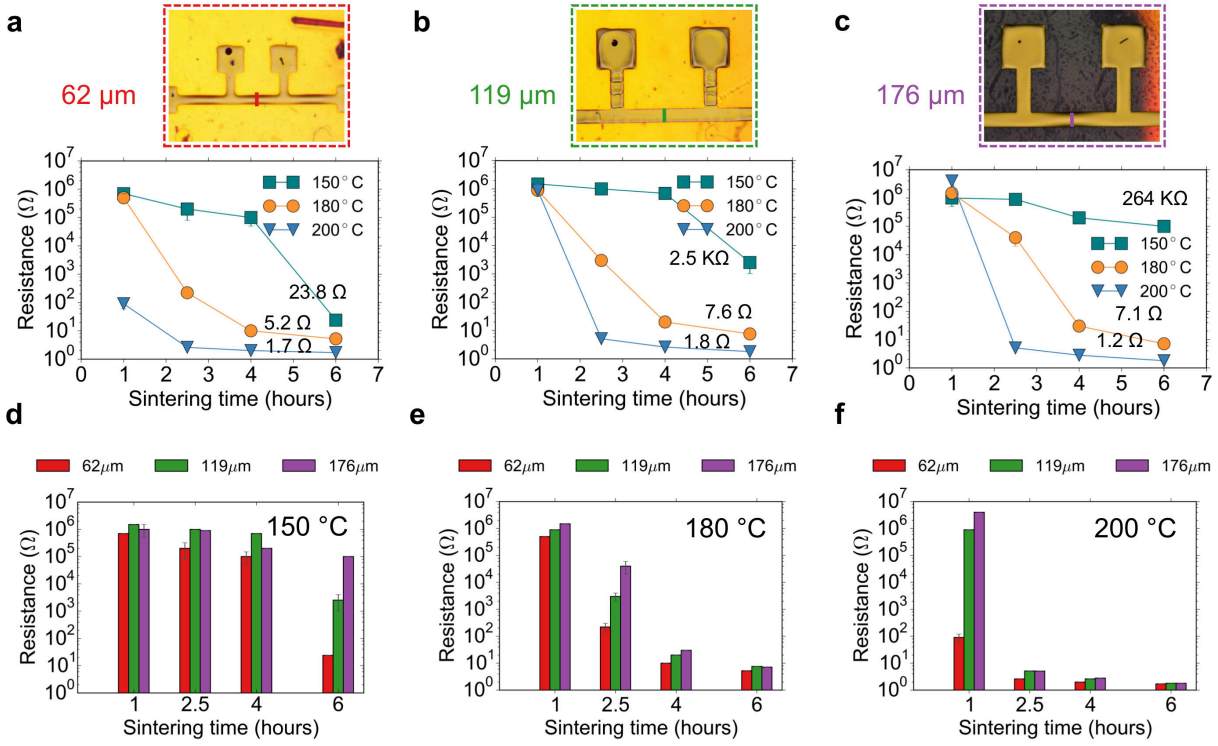

Figure 2.6. **Electrical resistance of inkjet-printed gold lines for several sintering conditions**. (**a-c**) Resistance versus sintering time plots for lines of three different widths (62 μm, 119 μm, and 176 μm) - shown in the insets (n = 3 for the error bars). These lines were sintered at 150 °C (cyan squares), 180 °C (orange circles), and 200 °C (blue inverted triangles). While the 62 μm lines in a) show similar resistance after 6 hours of sintering at all three sintering temperatures, the 176 μm lines in (**c**) remain highly resistive after 6 hours of sintering at 150 °C. (**d-f**) Resistance data grouped by sintering temperatures for better visualization. Red bars represent 62 μm lines, green bars represent 119 μm lines, and purple bars depict 176 μm lines. (**f**) A clear transition from high resistance to low resistance is seen for all three lines widths at 200 °C after 2.5 hours of sintering.

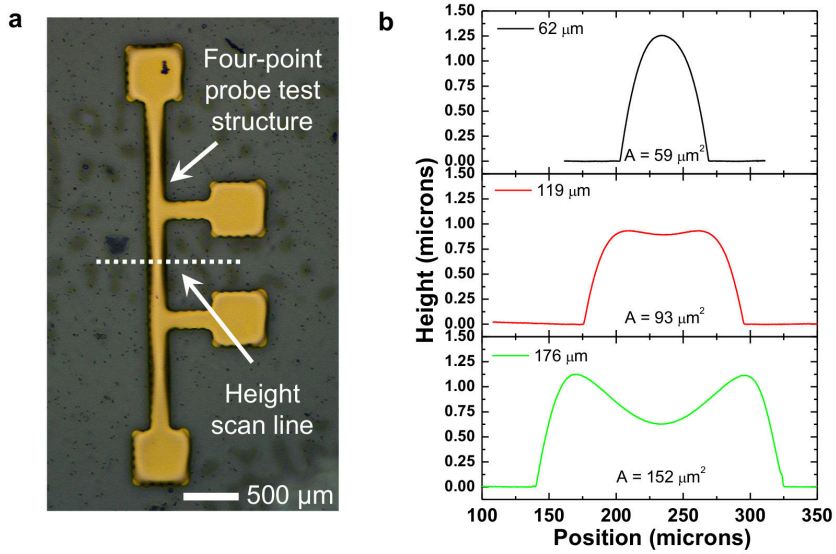

Figure 2.7. **Printed four-point probe structure and height profiles of the printed lines for the sintering study**. (**a**) Four-point probe structure used in the sintering study. (**b**) Surface profiles of the printed gold lines with the three different widths studied in this work.

for printed lines sintered at this condition. We show that it is possible to achieve resistivity values of similar magnitude if we use a lower temperature for a longer time. For instance, 2.0 x $10^{-7}\Omega$m was obtained for printed lines (176 μm wide) sintered at 200 °C for 6 hours. In general, the lower the temperature, the longer it takes to attain a level of low resistance, as expected.

The dependence of sintering speed on trace linewidth can be seen in Fig. 2.6a - c. This effect becomes apparent in Fig. 2.6d - f, where resistance values are plotted separately for each individual temperature studied, and each linewidth is represented by a color-coded bar. From the bar charts, a conclusion can be drawn that under low-temperature sintering conditions, wider lines take a longer time to sinter compared to the narrower lines. Therefore, if the sintering condition is not properly chosen, very heterogeneous electrical properties are expected in an electrode array with traces of varying width. For example, the narrower traces will be conductive while the wider pads will remain non-conductive. In our experiment, the 62 μm lines have an average resistance of 23.8 Ω after 6 hours at 150 °C (Fig. 2.6a), and 176 μm lines have an average resistance of 264 kΩ under the same conditions (Fig. 2.6c). In other words, for each sintering temperature there is a specific time for which the lines go through a transition regime after which they become conductive, and inside this transition zone resistance can vary orders of magnitude for lines of different width. For 62 μm lines, the transition time is 6 hours at 150 °C, 2.5 hours at 180 °C, and 1 hour at 200 °C.

Linewidths for our samples scale in a ratio of 1:2:3 and the cross-sectional area of such lines have roughly the same proportion (described in Fig. 2.7). As for any specific combination of temperature and time in our sintering procedure, thermal energy is delivered to the samples with a fixed rate, it is reasonable to affirm that the impact of the heat transfer will be more

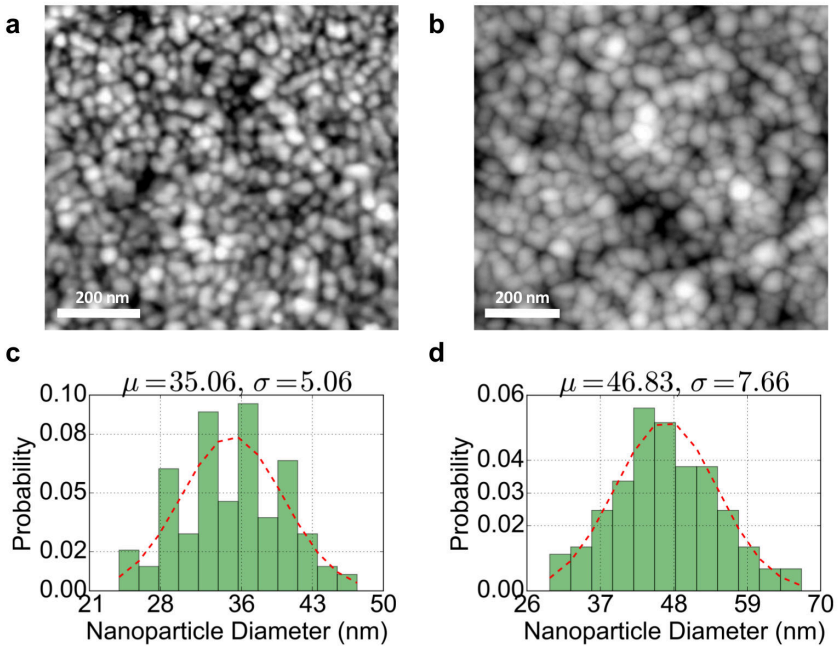

Figure 2.8. **Topography analysis with AFM**. (**a**) AFM image of a printed line sintered on a hot plate for 2.5 hours at 200 °C. (**b**) AFM image of a printed line sintered in an oven for 1 hour at 250 °C. The printed trace in **a** presents resistivity, ρ_a = 1.3 x $10^{-6}\Omega$ m, while printed trace line in **b** provides resistivity, ρ_b = 5.6 x $10^{-8}\Omega$ m. (**c-d**) The size distribution and average particle size of the printed lines in **a** and **b**, respectively. The size distribution was obtained by analyzing the AFM images of sintered lines. The particle sizes show a normal distribution with an average diameter of ranging from 35 to 47 nm.

intense for lines with less ink, and vice-versa. In other words, the wider (more voluminous) the line, the slower the effects of heating, and the lower the sintering speed.

2.5 Sintering mechanism

To study the underlying sintering process and the origin of the dependence of sintering speed on trace linewidth, topography and cross-sectional morphology of the sintered films were imaged with AFM and SEM. These images are shown in Fig. 2.8 and Fig. 2.9. All the printed structures in this report, regardless of different linewidths, presented a surface morphology displaying quasi-spherical, uniformly distributed particles with an average diameter of ranging from 35 to 47 nm, as depicted in Fig. 2.8. Such particle diameter is only slightly bigger than the original 12 nm diameter the nanoparticles had in the liquid ink. Using the sintering condition of 180 °C for 2.5 hours, we observed significant variation in conductivity for the three linewidths studied (Fig. 2.6e). Interestingly, SEM images of the three trace linewidths (sintered at 180 °C for 2.5 hours) show that particles have approximately the same average diameter mentioned above across all the film thickness (Fig. 2.9a - c). Therefore, it can

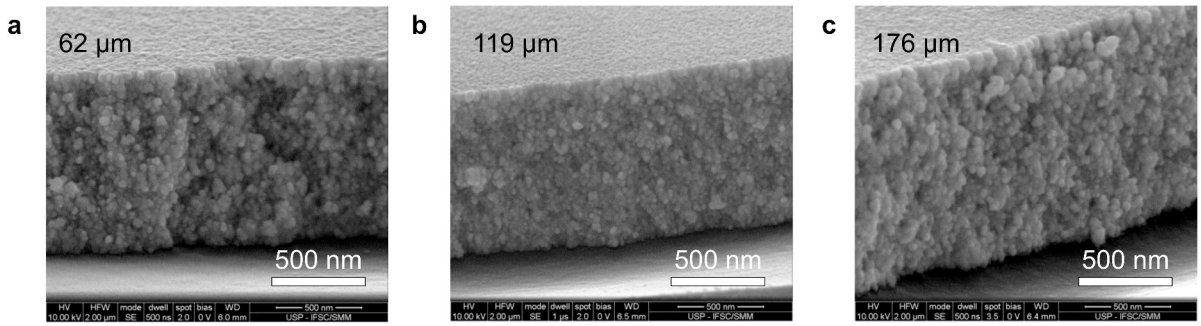

Figure 2.9. **Cross-sectional morphology analysis with SEM**. (**a-c**) are SEM images of the cross-sectional morphologies of the inkjet-printed gold lines. The printed lines were sintered on a hot plate for 2.5 hours at 180 °C. This sintering condition was chosen for the SEM analysis due to the reason that we observed significant variation in conductivity for the three linewidths sintered at 180 °C for 2.5 hours. Dimensions at the top left corner indicate the trace linewidth.

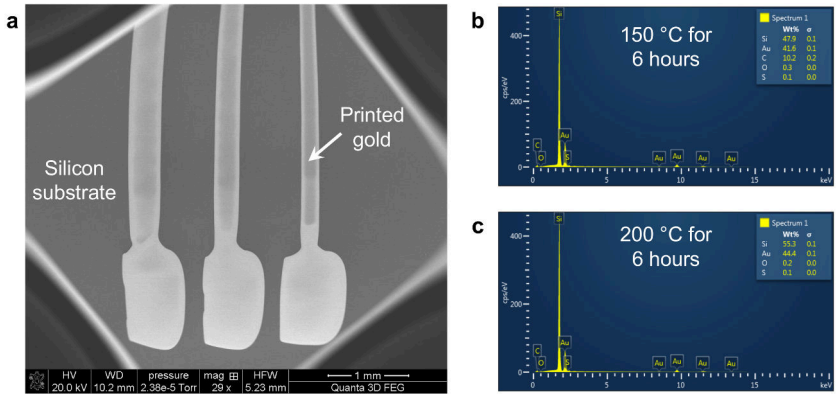

Figure 2.10. **EDX on printed traces**. (**a**) SEM showing printed traces on a silicon substrate and the arrow indicates the location from where EDX was collected. (**b**) and (**c**) EDX spectrum for lines sintered at 150 °C and 200 °C for 6 hours, respectively.

be inferred that the sintering stage in the low-temperature regime has a weak correlation with particle size.

The mechanism through which conducting traces are formed from metallic nanoparticle-based inks is already well comprehended, and involves a few steps: (a) ink drying, (b) surfactant melting and removal from around the particles, (c) particle coalescence, (d) crystallization, (e) necking, (f) Ostwald or digestive ripening, and finally (g) particle growth [141, 142]. Specifically in the earlier stages of the process, pre-sintering (or curing) events related to the surfactant molecules take place, which include melting of the organic layer and the formation of a superlattice in which the particles can make direct contact and a percolation path for electrons is formed [141, 143]. Fig. 2.8a shows a gold line sintered on a hotplate at 200 °C for 2.5 hours and Fig. 2.8b shows a gold line sintered at 250 °C for 1 hour in the oven (recommended by the ink manufacturer). Although some formation of necking and fused clusters of gold are observed in Fig. 2.8b, the particle size increased to average diameter of 47 nm compared to the particles in Fig. 2.8a, which had average diameter of 35 nm. However, there is a stark difference in resistivity between the two lines. The line sintered at a higher temperature and shorter time presents resistivity almost two orders of magnitude lower (ρ = 5.6 x $10^{-8}\Omega$ m) than the one sintered at lower temperature and longer time (ρ = 1.3 x $10^{-6}\Omega$ m). From these observations, we can conclude that for our nanoparticle ink, the sintering stage and line conductivity cannot be unequivocally deduced from particle size.

From the weak correlation between particle size and resistivity change in this study, we speculate that the increase in conductivity for the gold lines is primarily driven by a solvent and surfactant-related phenomenon. To verify the effect of solvents, we performed EDX on two lines sintered at 150 °C and 200 °C for 6 hours, and observed the ratio of carbon to gold peak, $I_{C/Au}$ (described in Fig. 2.10). For the line sintered at 150 °C, $I_{C/Au}$ was .25, and for the line sintered at 200 °C, $I_{C/Au}$ went below the detection limit of the instrument. We can conclude that at the lower sintering temperature trapped solvent resulted in high $I_{C/Au}$, while at 200 °C solvents were evaporated and the surfactants were displaced from the surfaces of the nanoparticles. Additionally, at this range of temperatures, typical surfactant molecules melt [142]. And with the longer sintering time nanoparticles can approach and merge, forming a percolation path and causing line resistance to decrease several orders of magnitude [142]. Such particle rearrangement, which eventually culminates in the formation of the already mentioned superlattice [143], usually happens in a matrix of molten surfactant and is a diffusion-controlled process. Thus, the dependence of sintering speed on trace linewidth observed here is due to the diffusion-based mechanism of sintering.

2.6 Electrical reproducibility and mechanical robustness of the printed array

While we printed multiple array layouts, in this report we focused on two specific array designs: (1) 31 electrodes arranged in a hexagonal pattern to cover approximately 16 cm^2 area (Fig. 2.11a). Here the electrodes have 150μm radii and are placed 7 mm apart, this sparse packing allows the flexure cuts using CO_2 laser. The laser cuts are around 200μm wide as shown in Fig. 2.11a inset. The cutout electrodes demonstrated higher mechanical compliance than the array without flexure cuts. (2) In this design, the sensing area is limited to 2 cm^2, and

the electrodes have 100μm radii and are placed 2 mm apart, using the same hexagonal packing (Fig. 2.11b). This design did not allow flexure cuts because the spot size of the CO_2 laser is over 200 μm, and cutting around the traces damaged the printed gold. Therefore, for creating reproducible printed arrays, we opted not to use flexure cut for the 100μm radii microelectrode array (Fig. 2.11b inset).

Sheet resistance (R_s) of the 31 electrodes of the two designs are shown in Fig. 2.11c and d. Both designs show R_s in the range of 0.28 to 0.36 Ω/sq, while the larger array demonstrates stricter packing in the histogram - 0.30 to 0.34 Ω/sq (Fig. 2.11c). A slight deviation in R_s in the microarray may have resulted from probe-electrode contact resistance (Fig. 2.11d). The traces are approximately 0.6 μm thick, which yields resistivity, ρ = 1.92 x $10^{-7}\Omega$ m. Here the low-temperature sintering process (200°C for 6 hours) was used. Printed features strongly adhere to the substrate and are stable to flexions as shown in Fig. 2.11e. The printed traces survived a simple tape test. Furthermore, we monitored the resistance of a printed line while bending to the radius of 5 mm and 10 mm, also twisting to an angle of 30°. For the bending test, the array was bent on cylinders with radius of 5 mm and 10 mm, and for the twisting test, the array was twisted to an angle of 30° while keeping one end anchored, as shown in the right schematic of Fig. 2.11e. There was no significant change in resistance during the bending and twist tests. Resistance data while bending remained stable, while the majority of the noise in the twisting test resulted from the contact resistance and instrumentations.

2.7 Electrical impedance mapping of two-dimensional surfaces using the printed array

The lightweight and flexible nature of the printed arrays provides a significant edge over conventional FR4 printed circuit boards in two-dimensional (2D) surface impedance mapping. We used the printed array to map out the surface impedance of various 2D surfaces. Since the array is tailored for biomedical applications, we tried to simulate different surfaces on which the array would be used. The instrumentation setup for the surface mapping in shown in Fig. 2.12a. The array is connected to a control board, which hosts a microcontroller and a set of multiplexers (MUXs) so that a connection can be made to two distinct electrodes for taking the impedance measurement. A computer program switches among the electrodes, then collects and transmits data for each selected pair. Using the collected impedance data, a 2D map is created by interpolating the data as shown in Fig. 2.12a. While various algorithms can be used for reconstructing the surface, nearest-neighbor interpolation demonstrated the best results.

Three different surfaces were chosen to test the efficacy of the array: (1) Flat surface (Fig. 2.12b), (2) Convex surface (Fig. 2.12c), and (3) Concave surface (Fig. 2.12d). Corresponding impedance maps are shown in Fig. 2.12e, f, and g. Images of the experimental setup are shown in Fig. 2.12b, c, and d. In the case of the flat surface, the array is placed on top of a metallic mesh and an insulating film shaped in the form of the letter "C" is placed in between the metallic mesh and the electrode array. Using the impedance meter and the control board impedance data was collected from the surface. Extracted data after the reconstruction is shown in Fig. 2.12e. Here, we show the phase data at 15 kHz. Since the current at 15 kHz strongly interacts will cell membranes, we chose this frequency.

Similar surface impedance data is collected from a convex surface with a 5 mm bending

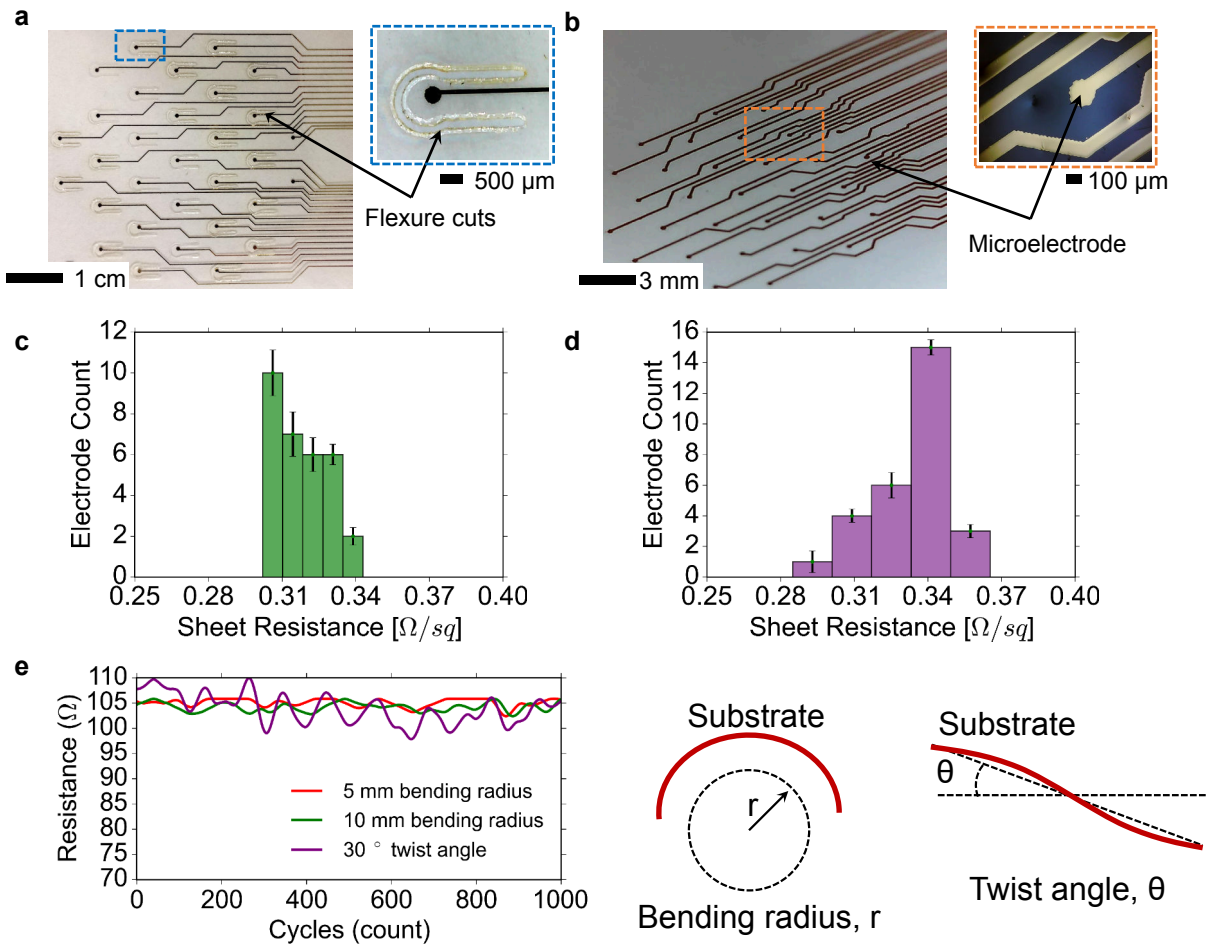

Figure 2.11. **Electrical reproducibility of the printed arrays across different designs**. (**a** and **b**) Two different array designs and micrographs. Corresponding sheet resistances, R_s of the arrays are shown, respectively, in (**c**) and (**d**). (**a**) A larger array with 31 electrodes covering 16 cm^2 area (electrode radii = 150 μm). Electrodes are packed in a hexagonal fashion with 7 mm spacing. Flexure cuts are visible, which are around 200 μm wide (blue inset). (**b**) Microelectrode array with 31 electrodes covering 2 cm^2 area. The 100μm radii electrodes are densely packed with 2 mm spacing. (**c** and **d**) Sheet resistance of the larger and the microarray. Error bars signify data from 5 arrays for each design and standard deviation of the data sets. From the histograms, it can be inferred that the larger array shows strict packing in terms of R_s, however both designs show relatively close mean R_s: 0.30 Ω/sq for the larger array and 0.34 Ω/sq for the microarray. (**e**) The mechanical robustness of the printed arrays. Bending and twisting tests are performed on the printed traces. The arrays are bent to 5mm (red line) and 10mm (green line), and torsionally loaded to 30 ° angle of twist (purple line). Most of the noise in the measurements resulted from the contact resistance and instrumentations. The schematics on the right shows the conventions used for the bending and twisting tests.

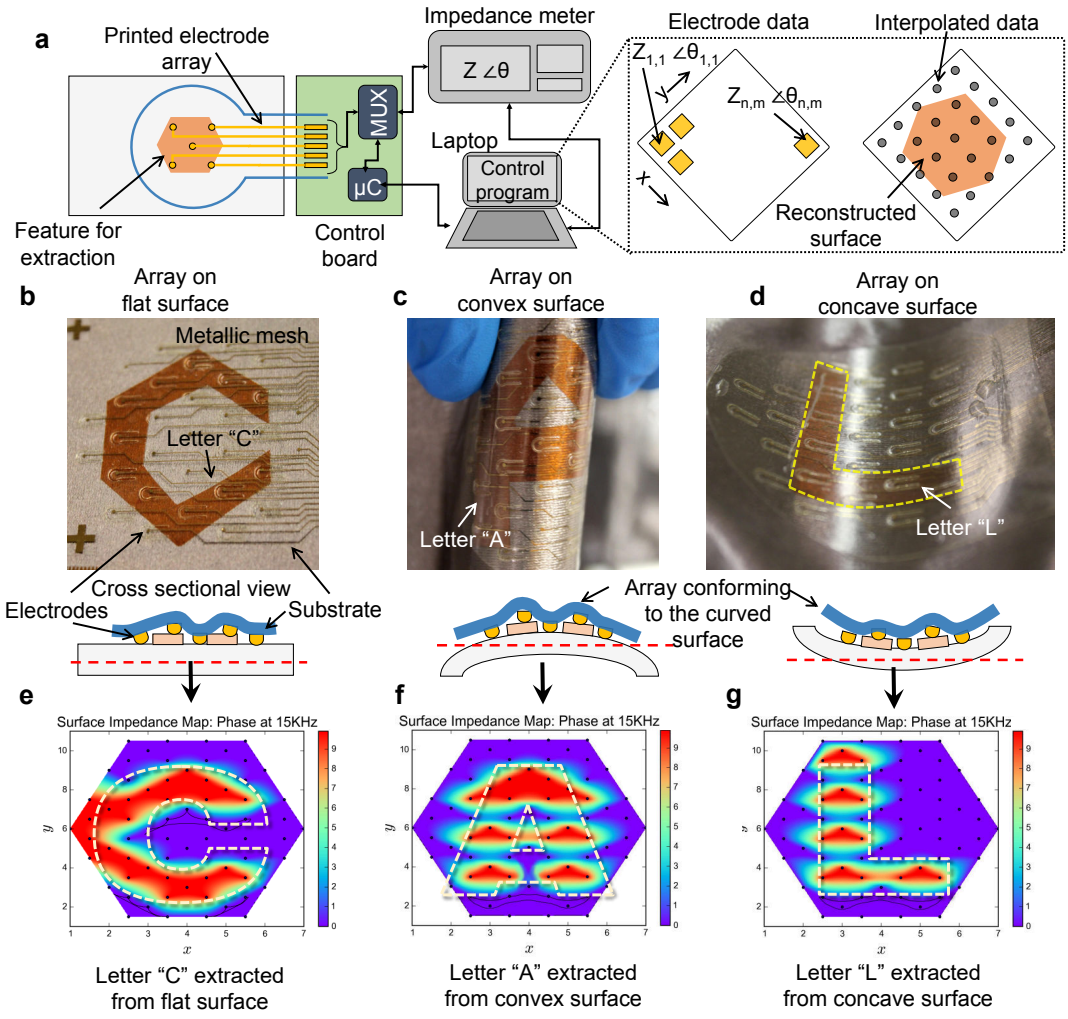

Figure 2.12. **Electrical impedance mapping of conformal surfaces using the printed array with flexure cuts**. (**a**) Impedance mapping setup: the printed array is connected to a control board, where a set of multiplexers (MUXs) switch connections among electrodes, and the signal is fed to an impedance meter. A control program reads the data collected by the impedance meter and spatially maps the impedance of the sensed surface. (**b-d**) An array is used to spatially map surface impedance of flat and curved surfaces. (**b**) The array is placed on a flat conductive surface and used to map the letter ″C″ made out of an insulating material. (**e**) The contrast between the metal and the insulator is electrically mapped out from the flat surface. (**c** and **f**) The array is placed on a 5 mm convex surface, and used to map the letter ″A″ - the array conforms to the curved surface and the impedance map shows the letter ″A″ electrically extracted from the convex surface. (**d** and **g**) The array is used to map a concave surface. The letter ″L″ is shown in the impedance map. For all the impedance measurements, phase at 15 kHz is used.

radius. The printed array conforms to the curved surface as shown in the cross-sectional image Fig. 2.12c. In this case, the letter "A" was imaged, and the phase data at 15 kHz is shown in Fig. 2.12f, which reconstructs the letter "A". For the last test case, the array was placed on a concave surface. Here, the freestanding electrodes got bent to the curved edges of the sensed surface, therefore contact to the surface proved robust, and the imaged letter "L" (Fig. 2.12d), was reconstructed effectively (Fig. 2.12g). In addition to mapping conformal surfaces, we used our electrode array to map out pressure ulcers from irregular surfaces such as wounded skin [3, 144]. Also, electrodes prepared with the same methodology showed to be stable in aqueous solution and under application of an electric field [106, 145].

2.8 A smart bandage for early detection of pressure ulcers

Chronic skin wounds, a silent epidemic, results in an estimated US$25 billion cost every year. Lack of a standardized method for wound sensing and monitoring is affecting over 2.5 million patients just in the United States each year [146]. Almost a third of the dermatological health budget in the US is spent on treating chronic skin wounds [147]. An elegant solution to this problem can be realized using flexible printed bioelectronics. The scope of flexible electronics stretches beyond electronic gadgets and has the potential to revolutionize both in-hospital and in-home health monitoring. Flexible electronics for medical sensing is advantageous over conventional electronics because flexible electronics can efficiently extract biomedical signals from conformal surfaces without compromising signal quality.

We used printed electrode array, similar to the one described in the previous section, to map surface wounds. In patients who are bedridden for a long amount of time, pressure builds up at a localized area on the skin, that results in lack of blood circulation, and eventually tissue damage (Fig. 2.13a). A pressure ulcer develops that is invisible to the naked eye at an early stage. Currently, no sensor can detect such damage. We used our electrode array to non-invasively map the pressure-induced tissue damage as shown in Fig. 2.13b. We used the sensor array to measure bioimpedance of the skin (Fig. 2.13c), and observed that impedance measurements of tissues correlate better tissue health with more reactive impedance values. And damaged tissue due to pressure, demonstrated less reactive impedance values. Impedance was robustly correlated with tissue health across multiple animal samples, in a rat model. The flexible electrode array provided a significant edge over conventional rigid printed circuit boards by conforming to the skin and reaching deep into the wound.

The choice of frequency to was determined by the electrical model of impedance spectroscopy (Fig. 2.13d). Cells float in a conductive liquid called extracellular fluid. Cell membranes can be modeled as dielectric barriers between the conductive extracellular and intracellular fluids. The high-frequency current ($>$1 MHz) passes without much interaction, thus carries small information about the cell membranes, same goes for low-frequency current ($<$ 5 kHz), which goes through the extracellular fluid. At 15 kHz strong interaction with the membranes yields significant information about the cell membranes. Therefore, we used impedance measurements at 15 kHz for determining a damage threshold [3].

In a rat model, we used magnets to induce tissue damage (Fig. 2.14). The damage can be classified in the following categories: (1) Irreversible damage, which was detected both visually and electrically (Fig. 2.14a); (2) Reversible damage, which was detected electrically but not visu-

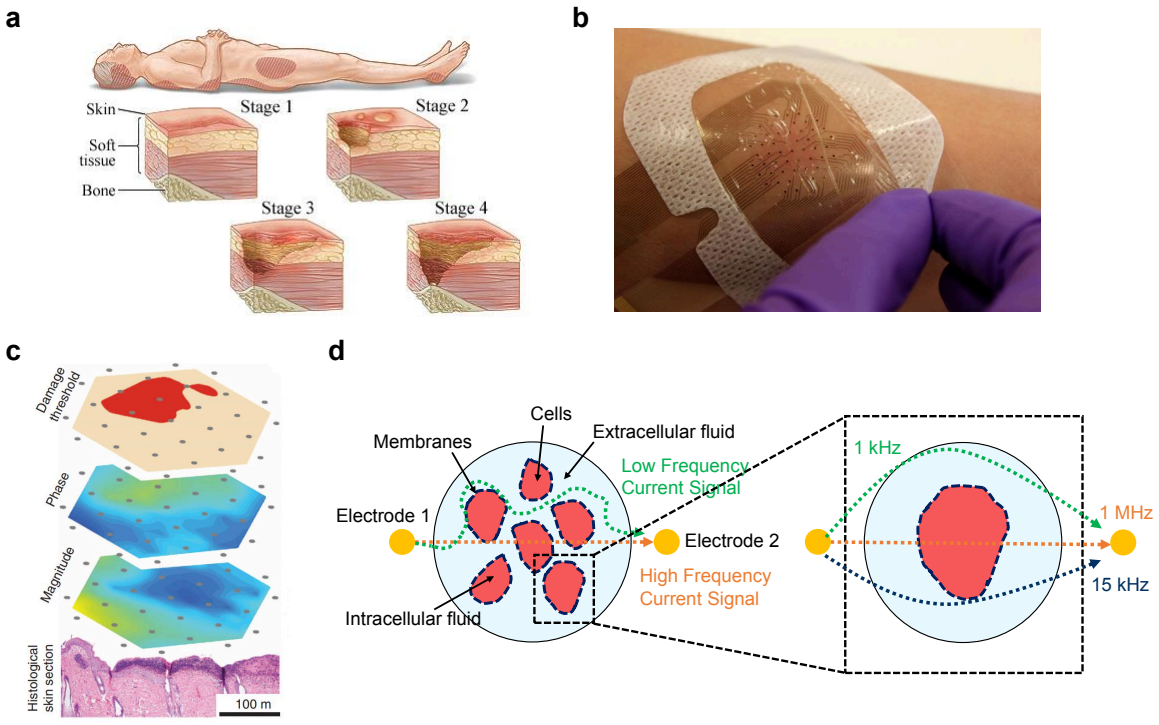

Figure 2.13. **A smart bandage for early detection of pressure ulcers**. (**a**) Different stages of ulcer formation. Over time, due to pressure build-up and loss of blood circulation, a skin ulcer develops. (**b**) Smart electronic bandage for early detection of pressure ulcers. (**c**) Magnitude and phase of the bioimpedance are used to create a damage threshold parameter, which electronically detects ulcer formation. The results are confirmed by histology analysis. (**d**) The electrical model of impedance spectroscopy. Cells float in a conductive liquid called extracellular fluid. Cell membranes can be compared to dielectric barriers between the conductive extracellular and intracellular fluids. High-frequency current (>1 MHz) passes without much interaction, thus carries small information about the cell membranes, same goes for low-frequency current (< 5 kHz), which goes through the extracellular fluid. At 15 kHz strong interaction with the membranes yields significant information about the cell membranes.

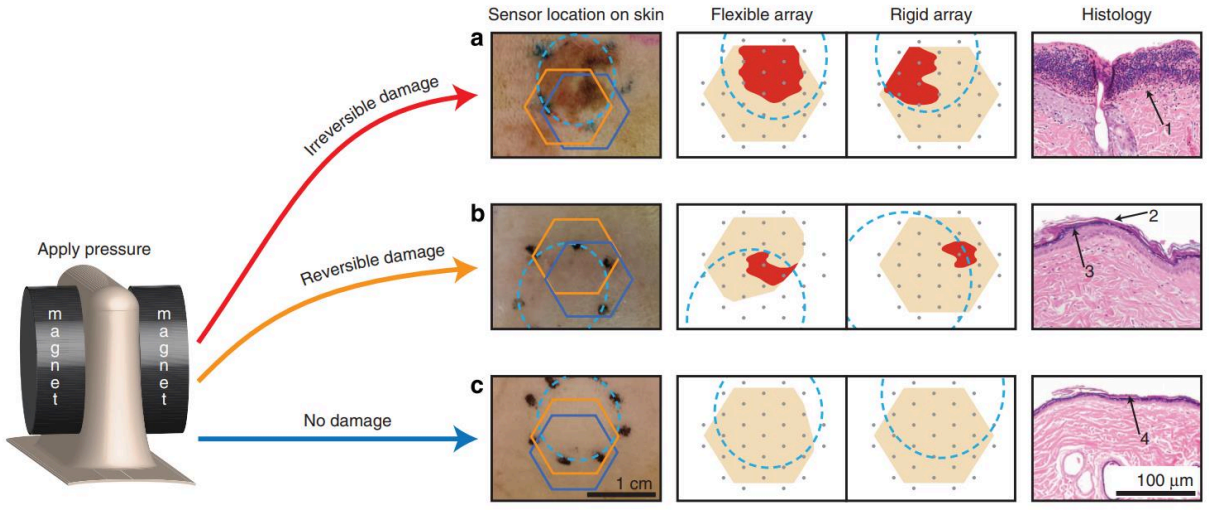

Figure 2.14. **Early detection of pressure-induced tissue damage**. Magnets were used to create a pressure ulcer model on rats in vivo. The damage can be classified in the following categories: (**a**) Irreversible damage, which was detected both visually and electrically; (**b**) Reversible damage, which was detected electrically but not visually; and (**c**) No damage, where the damage was not detected visually or electrically. Histological analysis indicated loss of epidermis (1) and ulceration when there was irreversible tissue damage, hyperkeratosis (2) and hypergranulosis (3) when the damage was measurable but reversible, and focal hyperkeratosis (4) in the scenario where no damage is detected. Representative wound images with sensor locations indicated, damage parameter maps obtained from those wounds using flexible and rigid sensor arrays, and histology results are shown for each scenario. Dashed light blue circles indicate where the pressure was applied to the skin, orange and dark blue hexagons indicate the location of the flexible and rigid arrays on the wound, respectively, and grey dots represent the electrodes. Scale bars, 1 cm (for wound photos) and 100 mm (for histology images). [3]

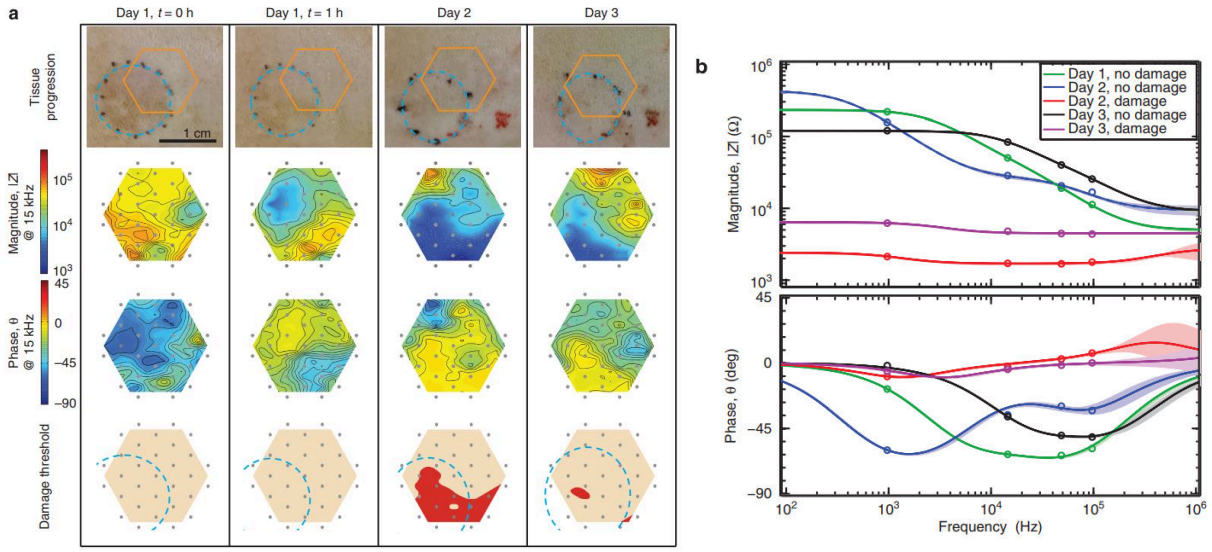

Figure 2.15. **Impedance maps identify mild, reversible pressure damage**. (**a**) The progression of reversible pressure damage created with a 1-h ischemia cycle is shown on days 13. Dashed grey circles indicate where the pressure was applied and dots represent the placement of the electrodes. Slight discoloration of the skin is observed immediately after removing the magnets, but no ulcer develops. Impedance magnitude and phase were measured with the rigid printed circuit board array. Damage is detected electrically on day 2 even with no visible evidence of the pressure damage, demonstrating the early detection capability of the device. (The small abrasion to the right of the measured area was irritation from hair removal.) Only a small region of damage remains on day 3. Scale bar (1 cm) applies to all wound photos. (**b**) A Bode diagram showing the impedance magnitude and phase versus frequency of No damage and Damage regions on days 13. A representative electrode pair was selected from each region. The circle markers indicate the measured data values, whereas the lines and the shaded regions indicate the estimated transfer function and the 95% fit confidence interval, respectively. [3]

ally (Fig. 2.14b); and (3) No damage, where the damage was not detected visually or electrically (Fig. 2.14c). The electrical detection was based on impedance measurements. A threshold was set for the measurements taken at 15 kHz. The irreversible damage was detected both visually and electrically. Reversible damage was detected electrically but not visually as shown in Fig. 2.15. Healthy tissue demonstrates capacitive behavior under impedance spectroscopy. When the cell membrane gets damages the impedance signature shows a shift towards a resistive behavior - decrease in impedance magnitude, and phase toward zero. Hence, demonstrate the cells are getting damaged. With a damage threshold, this change in impedance can be used for classifying tissue whether it is damaged or not. Thus these results demonstrate the feasibility of an electronic “smart bandage” for early detection of pressure ulcers.

2.9 Printed ECG electrodes

ECG records the electrical signals of the heart. ECG is used to monitor HR, cardiac cycles, and heart problems. It is one of the most used non-invasive medical test, which provides quick results. In the previous section, we use our printed electrodes to monitor bioimpedance of tissues. The similar manufacturing process can be used to fabricate ECG electrodes on plastic substrates as shown in Fig. 2.16a and b. Here, the electrode-to-electrode spacing is higher (7 cm). We followed a fabrication process similar to the bioimpedance electrodes, where the highest temperature in this process is 200 °C, which is close to the glass transition temperature of the PEN substrate. The annealing step fuses gold nanoparticles yielding conductive lines and electrodes. Then an amorphous fluoropolymer (Cytop) was spin coated onto the substrate surfaces to encapsulate the conductive features, followed by a 150 °C bake for 30 min. O_2 plasma etching opened the electrodes and connection tabs. A finished sensor photo is shown in Fig. 2.16a. Since the ECG signal may vary depending on placement on the body, 4 electrodes were placed along two sides of the substrate this will aid the system software to optimize a pair of electrodes that yield the maximum signal strength.

For manufacturing consistency, it is essential that the batch-to-batch variability in conductivity be as small as possible. Reproducibility of the process was verified using electrical resistance data. Printed features demonstrated the conductivity of 8.0×10^4 S cm^{-1}, which is ≈20% of gold's bulk conductivity (Fig. 2.16c and d). We observed a low standard of deviations of the mean in the sheet resistance from batch to batch. Four-point probe method was used to measure the sheet resistance.

Our printed sensor electrodes performed similarly to standard Ag/AgCl electrodes. Fig. 2.17 shows a comparison between our ECG electrodes printed on PEN and standard clinical Ag/AgCl electrodes. The noise levels in the signals using our printed electrodes were mainly due to the interconnections between the sensor and the recording unit. The Ag/AgCl electrodes were placed at the standard clinical positions of V_1 and V_2. The resultant signals are shown on the left panel of Fig. 2.17. ECG traces using our electrodes are shown on the right panel of Fig. 2.17. These traces have average peak heights varying from 0.4 to 0.55 mV compared to the Ag/AgCl electrodes that had an average peak height of 0.6 mV. The upper trace is for nodes 4 & 8 on our sensor and shows the same waveform as that observed with the Ag/AgCl electrodes. Nodes 4 & 8 most closely correspond with the location of the Ag/AgCl electrodes and are thus the best direct comparison of the two electrodes. Traces from the other printed electrode combinations, nodes 1 & 4 and 4 & 5, are shown in the lower two figures (Fig. 2.17, right). Average peak heights are again comparable with values of 0.55 mV and 0.4 mV respectively. These results show that multiple locations can be used to recorded signals capable of producing HR and HR variation data. This capability could be exploited to compensate for the loss of signal due to intermittent contact of a particular electrode.

Fig. 2.18 shows the ECG traces using our printed electrodes for the electrocardiographic V_3 and V_4 region. Again the average peak heights varied from 0.4 to 0.6 mV and showed clearly defined peaks at regular intervals. Interestingly, nodes 4 & 5 demonstrated the largest peak heights while 4 & 8 were at the greatest distance from each other. This body region which is flatter than the V_1 and V_2 region and subject to somewhat less stretching demonstrate peaks with high fidelity that are certainly capable of defining hear rate and HR variation.

Fig. 2.19 shows ECG traces using our printed electrodes and a commercial recording unit

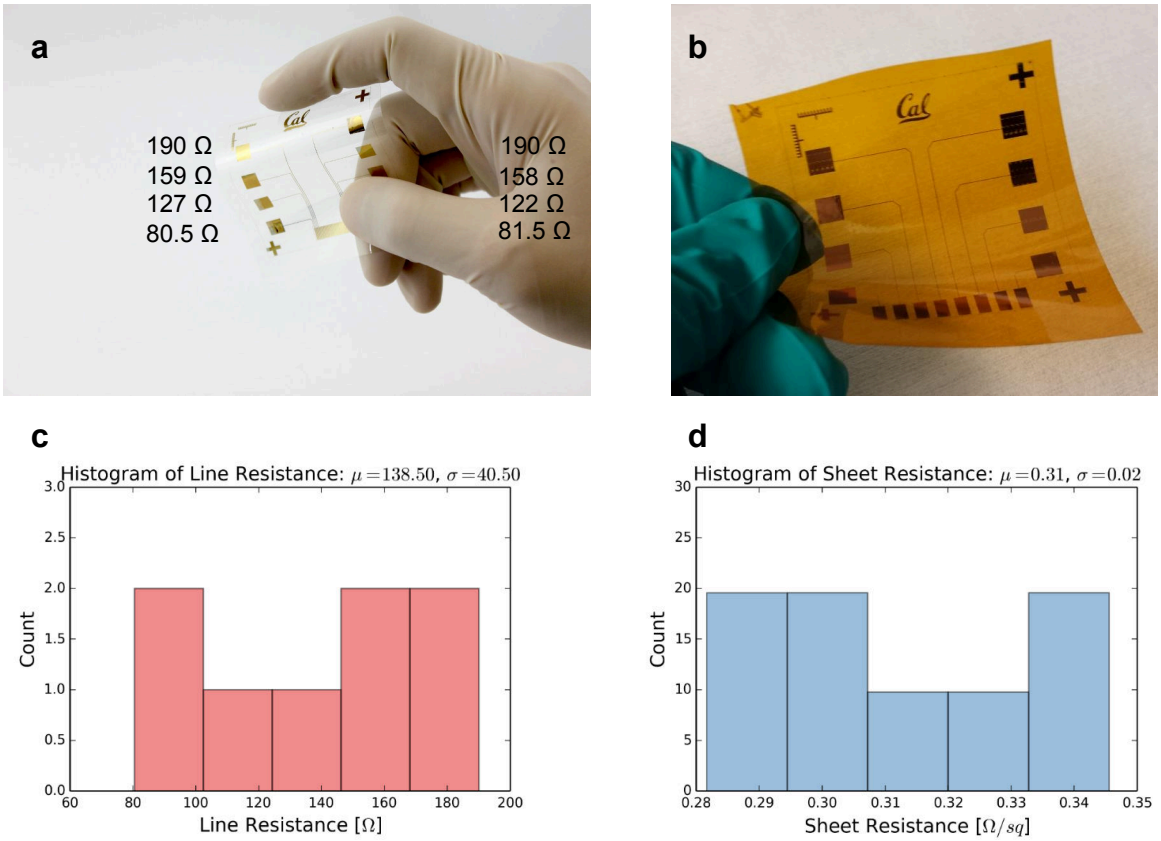

Figure 2.16. **Printed ECG electrodes and characterization**. (**a** and **b**) Eight electrodes are printed on a 5 cm × 5 cm planarized PEN substrate, and on Kapton PI substrate, respectively. (**c** and **d**) Line and sheet resistance of the printed electrodes on PEN.

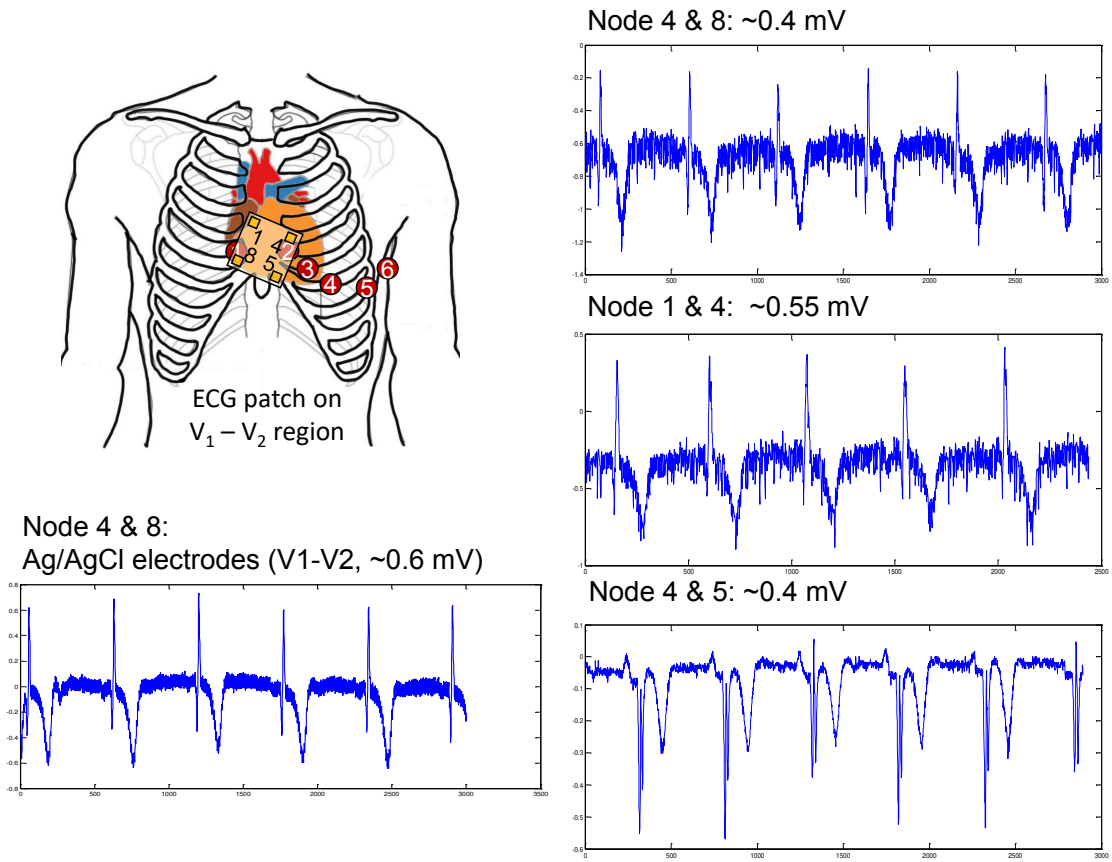

Figure 2.17. **ECG signal comparison between printed electrodes and Ag/AgCl electrodes. Measurements are taken from the V_1 - V_2 location**.

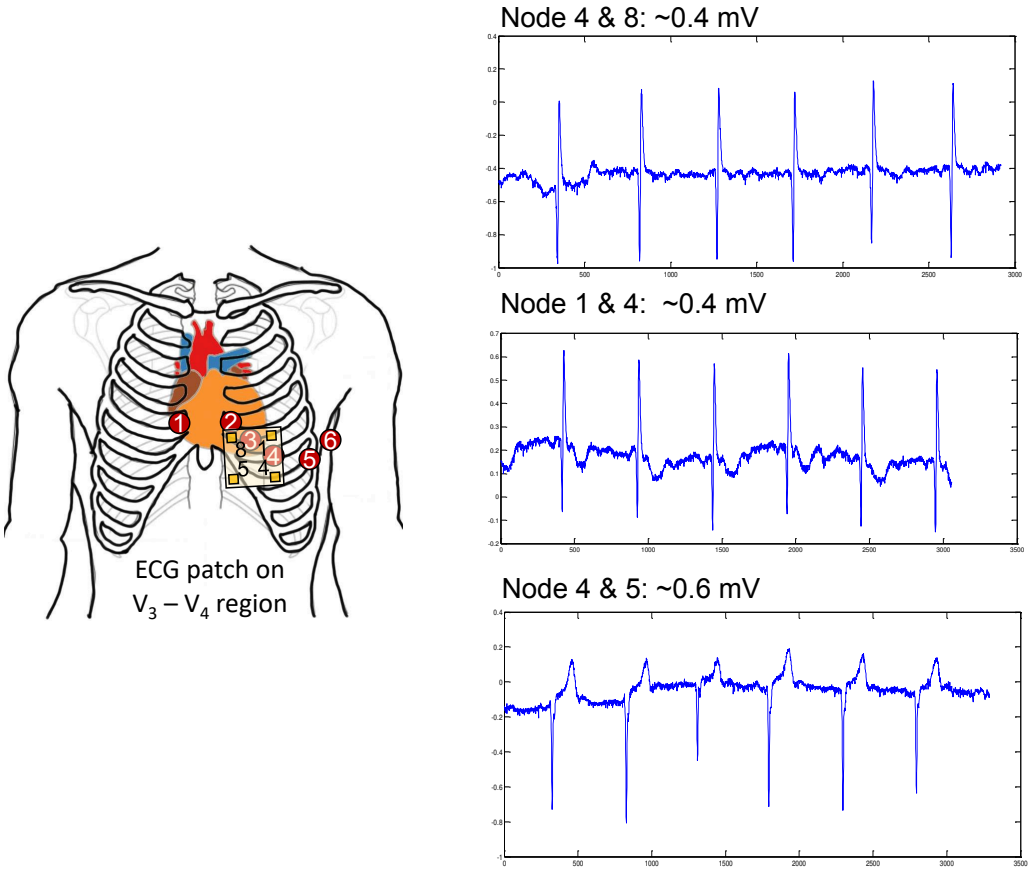

Figure 2.18. **ECG signal recorded with printed electrodes from the V_3 - V_4 location.**

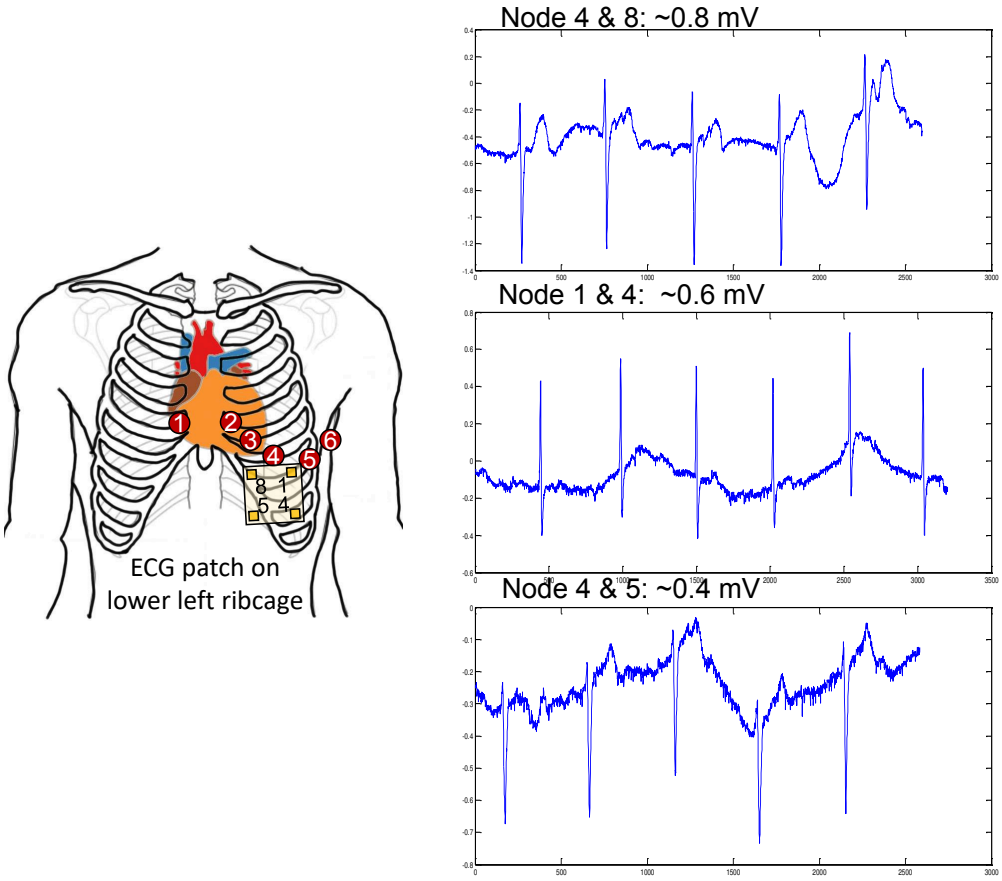

Figure 2.19. **ECG signal recorded with printed electrodes from the lower left rib cage**.

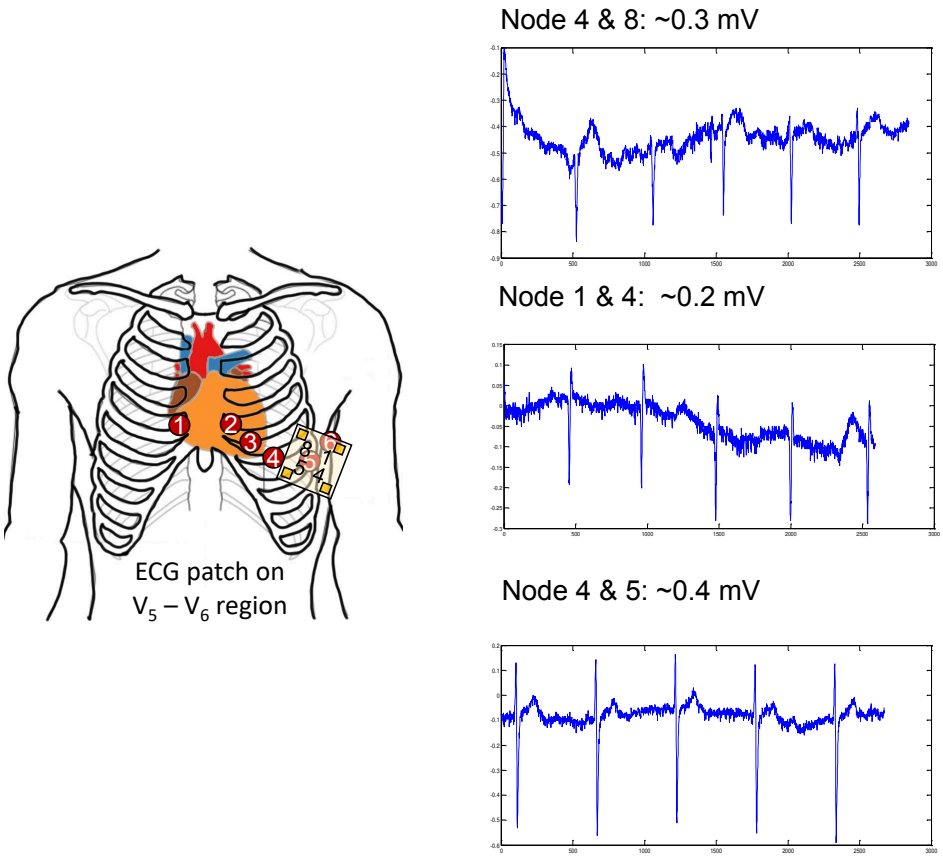

Figure 2.20. **ECG signal recorded with printed electrodes from the V_5 - V_6 location.**

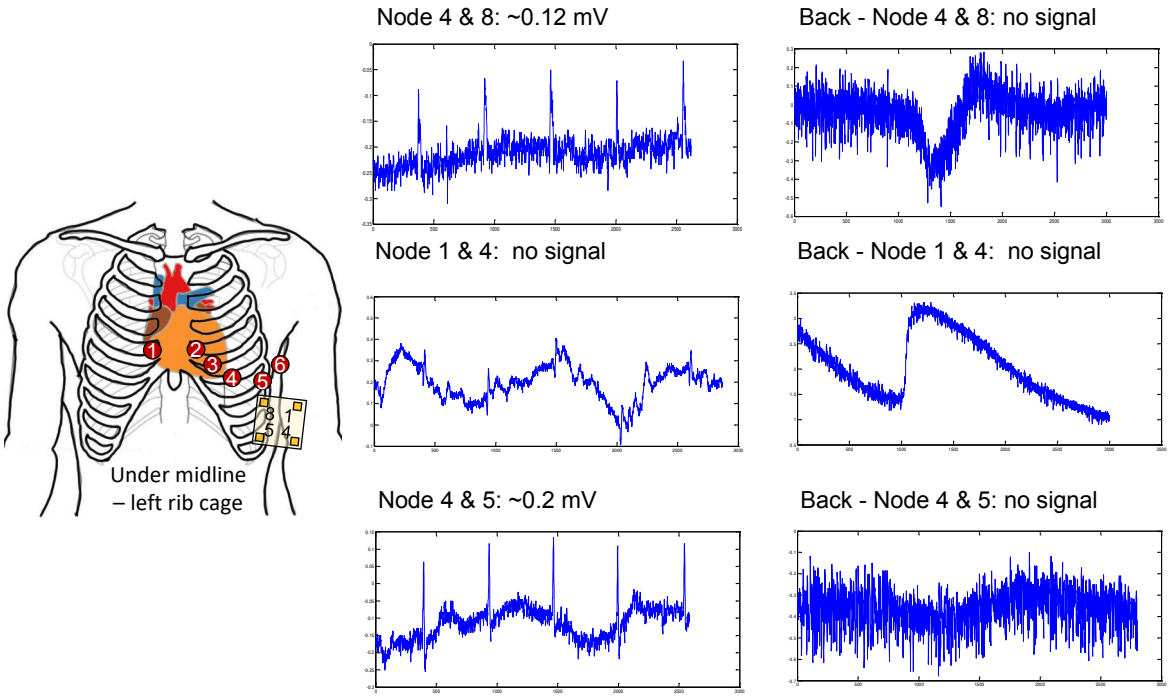

Figure 2.21. **ECG signal recorded with printed electrodes from under the midline of the left rib cage, then from the back. Signals are not reliable at these locations.**

for the lower left rib cage as shown. The traces show an overall slowly varying baseline not previously observed, but still have high fidelity peaks with average heights varying from 0.4 to 0.8 mV. With nodes 4 & 8 recording the highest peak heights of all our measurements. Again the peaks appear at regular intervals and are more than sufficient for calculating HR and HR variation. The traces again show another potential body location for sensor placement.

Fig. 2.20 shows traces recorded in the electrocardiographic V_5 and V_6 region with reduced average peak heights of 0.2 to 0.4 mV. The traces show a slowly varying baseline, but the peaks remain well defined and HR and HR variation could be calculated from them. This body region has more curvature than most of the other regions that may limit its usefulness as a potential sensor location.

Two body regions even further from the heart, the lower rib cage under the midline and the lower back were also evaluated. Fig. 2.21 shows that poor ECG signals or just noise recorded from both regions. Overall, the traces in Fig. 2.17 - 2.20 show extremely good waveform fidelity and very low noise. In fact, the noise level is lower than that of the commercial unit recording from standard Ag/AgCl electrodes. These results demonstrate the feasibility of using the printed electrodes for recording ECG signal with high-fidelity. The ECG recordings above demonstrate that out sensor is equivalent to the standard clinical Ag/AgCl electrodes and that our circuit is superior to that of the commercial reference unit used on our laboratory. We have also demonstrated that there are several body regions with different curvatures that can be used with our sensor to record ECG signals, and that the signals are of sufficient fidelity to easily calculate HR and HR variation.

2.10 Printed EMG electrodes

Another biopotential signal that can be non-invasively detected by an array of electrodes is ECG. EMG is a clinical technique for evaluating and detecting the electrical activity produced by skeletal muscles. EMG records the electric potential generated by muscle cells, which are electrically or neurologically activated. This signal can be used to detect movement, activation level, recruitment order, or muscle abnormalities. In this section, we demonstrate the use of printed electrodes in a EMG-based gesture recognition for human-machine interaction (HMI) (Fig. 2.22). Since this is an on-going project, here, we show the design of a printed EMG array. The results from this project will be reported in a later publication. Two types of electrodes are currently being evaluated: (1) Photolithographically defined gold-plated copper electrodes (Fig. 2.22a) and (2) Printed gold electrodes (Fig. 2.22c). The EMG system is composed of the flexible electrodes array and a custom wireless device for 64-channel signal acquisition and streaming. We use brain-inspired high-dimensional (HD) computing for processing EMG features in one-shot learning [148].

The EMG signal is recorded from photolithographically defined 4×16 gold-plated copper electrode array all referenced to a single Ag/AgCl patch electrode placed on the elbow. Since the obtained signal is a mixture of the EMG potentials and time-varying offset and noise, but the desired feature is the envelope of the high-frequency EMG. Therefore, a preprocessing step is needed before using the HD classifier.

We obtained EMG gesture data from three healthy, adult male subjects. Each subject participated in three data acquisition sessions across different days, where the electrode array

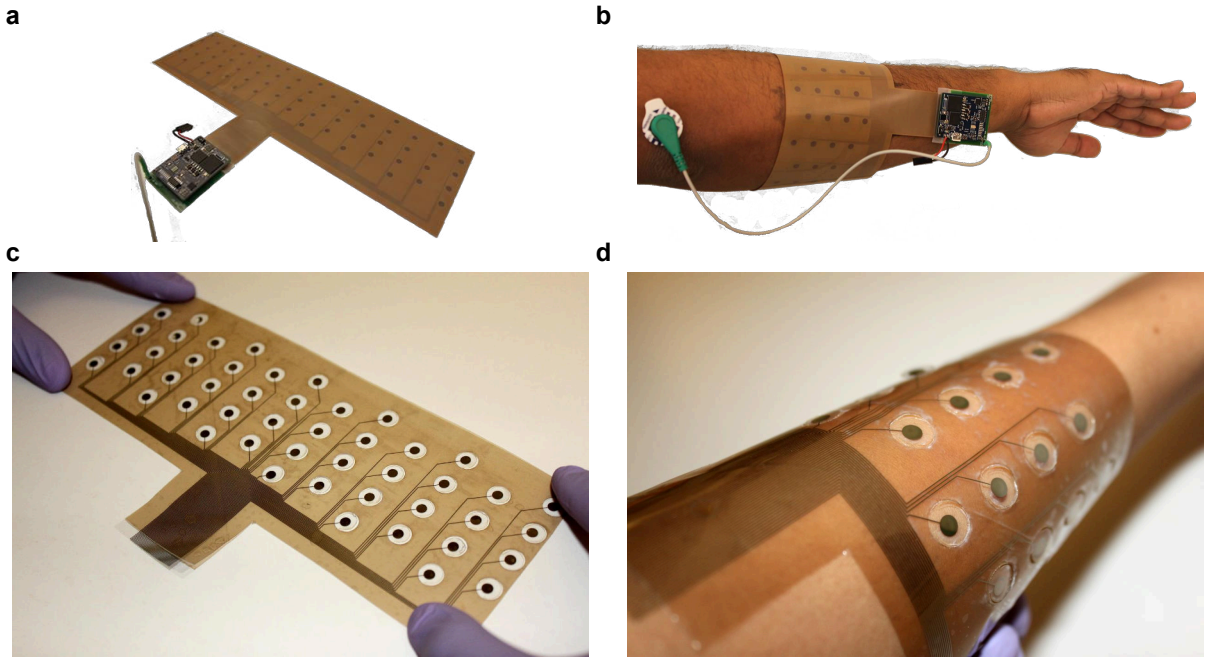

Figure 2.22. **Flexible EMG recording system**. (**a**) Photolithographically defined 4 × 16 gold-plated copper electrode array with attached wireless biosignal acquisition device. (**b**) The electrode array is positioned on the arm. (**c**) Inkjet-printed 4 × 16 gold electrodes array. (**d**) The gold electrode array is positioned on the arm.

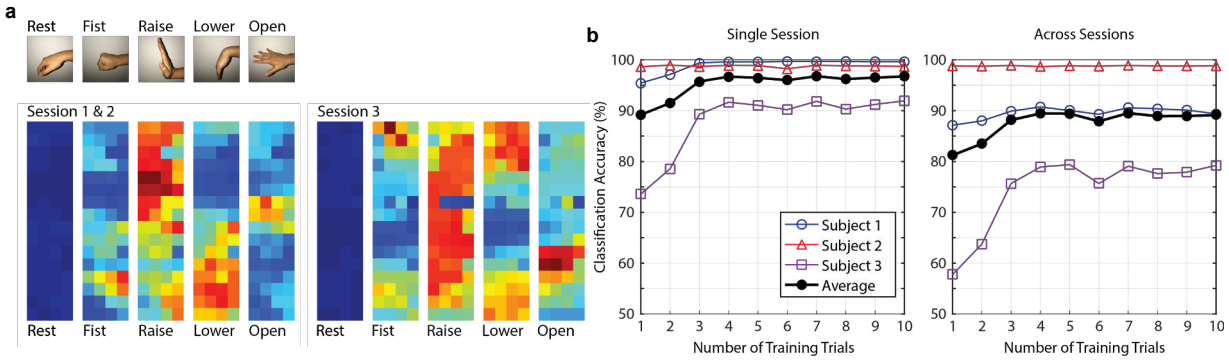

Figure 2.23. **Results from the flexible EMG recording system**. (**a**) Dataset gestures with the associated normalized activity maps for different sessions (Subject 1 shown). Pixels correspond to electrode positions in the array. (**b**) Classification accuracy for different number of training trials.

was reapplied with fresh hydrogel tape for each session. For sessions 1 and 2, the array was placed in approximately the same position each time. Session 3 data were recorded with the array in a different orientation 1 week after sessions 1 and 2. Each data set contained ten trials of four hard gestures (fist, raise, lower, open) (Fig. 2.23a) held for 5 seconds each in different sequences. Each sequence began and ended with rest, which we treated as a fifth gesture. Centered 3-second segments of each 5-second gesture were labeled for inclusion in the testing and training sets. Preprocessed features for each gesture were averaged and arranged in matrices for visualization as heat maps of muscular activity. The classification accuracy averaged over all three subjects for training set sizes from 1 to 10 trials is shown in Fig. 2.23b. Maximum performance (96:64%) is achieved when training on only 3 trials, and training on a single trial can deliver acceptable accuracy (89:19%) for true one-shot learning. While the data presented here is from the photolithographically defined 4×16 gold-plated copper electrode array, in our on-going work, we see a similar performance for the inkjet-printed 4×12 gold electrodes array. Another variant of the printed array is a screen-printed 4×12 silver electrode array. The results from the printed arrays will be reported in a later publication.

Overall, here, we demonstrated a flexible high-density electrode array that can provide large area coverage and dense electrode spacing. Hence, illustrate the feasibility of reliable and robust gesture recognition system.

2.11 Chapter conclusions

A gold electrode array fabricated on plastic substrates addresses both mechanical compliance and chemical inertness requirements of bioimpedance and biopotential electrodes. However, sintering temperatures in the range of 250 °C of gold nanoparticle ink is a big manufacturing impediment towards fabricating printed electrodes on common plastic substrates such as PET and PEN. In this chapter, design and low-temperature sintering techniques are demonstrated for gold electrodes. A crucial observation of the study was that melting and removing surfactants from the surfaces of the nanoparticles, and reducing solvent content from the bulk film plays a significant role in enhancing conductivity of printed films. In addition, the grain size of sintered films is important, however, conductivity cannot be unequivocally deduced from surface particle growth. To attain conductive lines, both sintering temperature and transferred thermal energy are important. Also, at low-temperature sintering conditions, sintering speed depends on the width of printed lines. With longer sintering times, conductivity as high as 5 x 10^6 Sm^{-1} can be reached at sintering temperatures of 200 °C.

Utilizing the versatility of the process flow, electrode arrays of various sizes and shapes were designed and fabricated on plastic substrates. Electrode arrays consisting of 31 electrodes with electrode to electrode spacing ranging from 2 mm to 7 mm are fabricated, and used for impedance mapping of conformal surfaces at 15 kHz. Since inkjet printing was used for fabricating the arrays, the turnaround time from design to design was quite low compared to the process flows that rely on vacuum processing techniques. Minimum feature size of 62 μm was reproducibly printed with sheet resistance of 0.30 Ω/sq for 0.6 μm thick lines. Additionally, laser-cut free-standing electrodes were created to enhance conformity of the array, which enhanced contact to conformal surfaces. Finally, these arrays were used for surface impedance mapping of different two-dimensional surfaces.

In summary, here we demonstrated flexible gold electrode array fabrication, low-temperature sintering, and the methodology used for mapping impedance on conformal surfaces. These gold electrodes are utilized for both bioimpedance and biopotential measurements. Taking advantage of the low-cost and large-area manufacturing techniques, these efficient and affordable electrode arrays can be used in novel in-home and in-hospital medical sensing applications.

Chapter 3

Printed transmission-mode oximeter

3.1 Introduction

Oximetry, the technique for determining oxygen saturation, optically measures the light absorption of oxygenated and deoxygenated blood and tissue at two different wavelengths. Conventional pulse oximeters non-invasively measure human pulse rate and arterial blood oxygen saturation with an optoelectronic sensor composed of two inorganic LEDs with different peak emission wavelengths and a single inorganic PD [149, 150]. The LEDs are placed on one side of a finger and the light transmitted through the tissue is subsequently sensed by the PD which is placed on the opposite side of the finger. Sequential sampling of the transmitted light provides information on the ratio of oxygenated and deoxygenated hemoglobin in the blood. This ratio and a calibration curve are used to compute arterial blood oxygen saturation. Currently, the application of commercially available pulse oximeters is limited by the bulk, rigidity, and high large-area scaling cost of conventional inorganic based optoelectronics. In this chapter, we show a pulse oximeter sensor composed of OLEDs [151, 152] and a flexible OPD [153]. We successfully demonstrate that the organic optoelectronic sensor provides accurate measurement capability and we anticipate that our application of solution processable organic optoelectronics in pulse oximetry will enable low-cost, disposable, and wearable medical devices.

Wearable medical sensors have the potential to play an essential role in the reduction of health care costs: they encourage healthy living by providing individuals feedback on personal vital signs and enable the facile implementation of both in-hospital and in-home professional health monitoring. Consequently, wide implementation of these sensors can reduce prolonged hospital stays and cut avertible costs [154]. Recent reports show ample wearable sensors capable of measuring pressure [42, 155], biopotential and bioimpedance [33, 39], pulse rate [156], and temperature [157, 158] in real time. These sensors are developed in wearable and flexible form-factors using organic [42, 158, 159], inorganic [157, 160, 161], and hybrid organic-inorganic [33, 155, 160] materials.

Organic semiconductors developed for OLEDs and OPDs have been primarily applied to display and photovoltaic technologies [162, 163]. This is due to their potential for large-area

roll-to-roll manufacturing at large volumes which is enabled by solution processing and the use of flexible substrates [164]. These attributes also make organic optoelectronics very attractive for medical sensors, where flexibility combined with large areas can result in an improvement of the overall sensor performance. In the past 10 years, a lot of resources were used to improve the stability of organic semiconductors in order to meet the lifetime requirements of displays and photovoltaics [165, 166]. When compared to the above markets, disposable medical sensors have less stringent lifetime requirements on the materials, since these devices would be used only for a few days as opposed to years.

Organic optoelectronics have previously been used to perform pulse measurements [167–169]. Here, we report a sensor composed solely of organic optoelectronics that measures both human pulse and arterial blood oxygenation. We anticipate that our results will inspire system level integration of organic-inorganic electronics, where the large-area, low-cost and mechanical flexibility of organic sensors will be combined with the computational efficiency of inorganic electronics. A schematic view of the sensor is given in Fig. 3.1a, where two OLED arrays and two OPDs are placed on opposite sides of a finger.

3.2 Pulse and oxygenation with red and green OLEDs

In contrast to commercially available inorganic oximetry sensors, which use red and NIR LEDs, we use red and green OLEDs. Incident light from the OLEDs is attenuated by pulsating arterial blood, non-pulsating arterial blood, venous blood, and other tissue as depicted in Fig. 3.1b. When sampled with the OPD, light absorption in the finger peaks in systole (the heart's contraction phase) due to a large amount of fresh arterial blood. During diastole (the heart's relaxation phase), the reverse flow of arterial blood to the heart chambers reduces blood volume in the sensing location, which results in a minima in light absorption. This continuous change in arterial blood volume translates to a pulsating signal - the human pulse. The DC signal resulting from the non-pulsating arterial blood, venous blood, and tissue, is subtracted from the pulsating signal to give the amount of light absorbed by the oxygenated and deoxygenated hemoglobin in the pulsating arterial blood. HbO_2 and Hb have different absorptivities at red and green wavelengths, as highlighted on the absorptivity of oxygenated and deoxygenated hemoglobin plotted in Fig. 3.1c. The difference in the molar extinction coefficient of oxygenated and deoxygenated hemoglobin at the green wavelength is comparable to the difference at NIR wavelengths (800-1000 nm) used in conventional pulse oximeters. In addition, solution-processable NIR OLED materials are not stable in air and show overall lower efficiencies [170, 171]. Thus we elected to use green OLEDs instead of NIR OLEDs.

Using red and green OLEDs and an OPD sensitive at visible wavelengths (the OLEDs' emission spectra and the OPD's external quantum efficiency (EQE) as a function of incident light wavelength are plotted in Fig. 3.1d), blood oxygen saturation (SO_2) is quantified according to Eq. 3.1. Here, C_{HbO_2} and C_{Hb} are the concentration of HbO_2 and Hb, respectively.

$$SO_2 = \frac{C_{HbO_2}}{C_{HbO_2} + C_{Hb}} \tag{3.1}$$

In transmission mode pulse oximetry, light from LEDs is directed into the top of the finger and the transmitted light is sensed at the bottom of the finger with a photodetector.

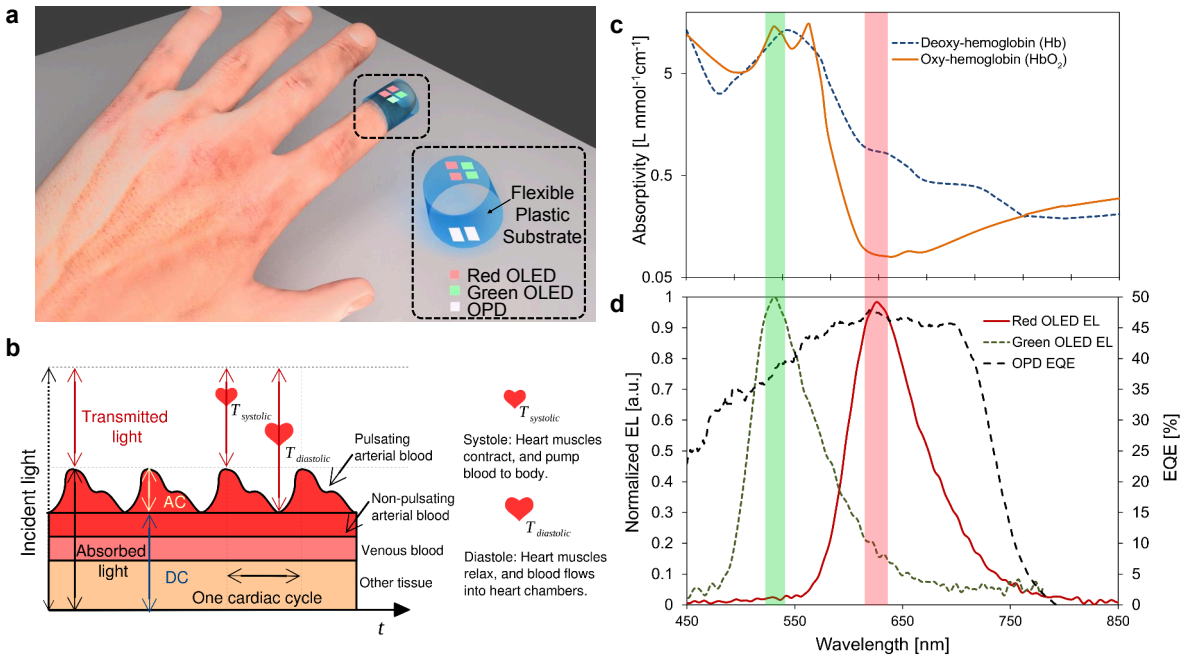

Figure 3.1. **Pulse oximetry with an organic optoelectronic sensor**. (**a**) Pulse oximetry sensor composed of two OLED arrays and two OPDs. (**b**) A schematic illustration of a model for the pulse oximeter's light transmission path through pulsating arterial blood, non-pulsating arterial blood, venous blood, and other tissues over several cardiac cycles. The AC and DC components of the blood and tissue are designated, as well as the peak and trough of transmitted light during diastole ($T_{diastolic}$) and systole ($T_{systolic}$), respectively. (**c**) Absorptivity of oxygenated (orange solid line) and deoxygenated (blue dashed line) hemoglobin in arterial blood as a function of wavelength. The wavelengths corresponding to the peak OLED EL spectra are highlighted to show that there is a difference in Hb and HbO_2 absorptivity at the wavelengths of interest. (**d**) OPD external quantum efficiency (black dashed line) at short circuit, and EL spectra of red (red solid line) and green (green dashed line) OLEDs.

Beer-Lambert's law states that the intensity of light traveling through a medium decreases exponentially with distance. Transmission T is given by,

$$T = I_0 \exp(-\varepsilon C d) \tag{3.2}$$

Here, I_0 is the incident light intensity, ε is the molar absorptivity with units of L $mM^{-1}cm^{-1}$, C is the concentration of the absorbent medium, and d is the optical path length through the medium.

The absorbance, A, is now defined as,

$$A = -\ln \frac{T}{I_0} = \varepsilon C d \tag{3.3}$$

Now if we consider attenuation in skin, tissue, and bones – represented with the subscript DC, and attenuation in HbO_2 and Hb – represented with the subscripts HbO_2 and Hb, the following equations represent transmission at diastole and systole:

$$T_{high,dia} = I_0 \exp(-\varepsilon_{DC} C_{DC} d_{DC}) \exp(-(\varepsilon_{HbO_2} C_{HbO_2} + \varepsilon_{Hb} C_{Hb}) d_{dia}) \tag{3.4}$$

$$T_{low,sys} = I_0 \exp(-\varepsilon_{DC} C_{DC} d_{DC}) \exp(-(\varepsilon_{HbO_2} C_{HbO_2} + \varepsilon_{Hb} C_{Hb}) d_{sys}) \tag{3.5}$$

Light has to pass through an additional optical path Δd at systole, therefore $d_{sys} = d_{dia} + \Delta d$. Additionally, a normalization step ($T_{normalized} = T/T_{high,dia}$) is required to determine the normalized systolic transmission.

Now Eq. 3.3 can be rewritten by superpositioning absorbance of HbO_2 and HbO at a specific wavelength,

$$A = (\varepsilon_{HbO_2} S_a O_2 + \varepsilon_{Hb}(1 - S_a O_2))(C_{HbO_2} + C_{Hb}) \Delta d \tag{3.6}$$

The ratio of the absorbance at red (rd) and green (gr) light can be found using the following equation,

$$R_{os} = \frac{A_{rd}}{A_{gr}} = \frac{(\varepsilon_{rd,HbO_2} S_a O_2 + \varepsilon_{rd,Hb}(1 - S_a O_2))(C_{HbO_2} + C_{Hb}) \Delta d}{(\varepsilon_{gr,HbO_2} S_a O_2 + \varepsilon_{gr,Hb}(1 - S_a O_2))(C_{HbO_2} + C_{Hb}) \Delta d} \tag{3.7}$$

Finally, arterial oxygen saturation ($S_a O_2$) can be calculated using Eq. 3.8. Here, $\varepsilon_{rd,Hb}$ and $\varepsilon_{gr,Hb}$ are the molar absorptivity of Hb at red (λ = 626 nm) and green (λ = 532 nm) wavelengths. Similarly, ε_{rd,HbO_2} and ε_{gr,HbO_2} are the molar absorptivity of HbO_2 at red (λ = 626 nm) and green (λ = 532 nm) wavelengths.

$$S_a O_2(R_{os}) = \frac{\varepsilon_{rd,Hb} - \varepsilon_{gr,Hb} R_{os}}{(\varepsilon_{rd,Hb} - \varepsilon_{rd,HbO_2}) + (\varepsilon_{gr,HbO_2} - \varepsilon_{gr,Hb}) R_{os}} \tag{3.8}$$

However, empirical correction is required to overcome limitations of Beer-Lambert's Law in scattering tissue (versus a glass cuvette). We experimentally obtained the 11% offset in the calibration curves for the combination of "red and NIR" light vs. the combination of "red and green" light.

3.3 Organic optoelectronic oximeter components

OLED and OPD performance are both paramount to the oximeter measurement quality. The most important performance parameters are the irradiance of the OLEDs (Fig. 3.2b), and the EQE at short circuit of the OPD (Fig. 3.1d and 3.2d). As the OLEDs operating voltage increases, irradiance increases at the expense of efficiency [172], as shown by the lower slope of irradiance than current as a function of applied voltage in Fig. 3.2b. For a pulse oximeter, this is an acceptable trade-off because higher irradiance from the OLEDs yields a strong measurement signal.

We have selected polyfluorene derivatives as the emissive layer in our OLEDs due to their environmental stability, relatively high efficiencies, and self-assembling bulk-heterojunctions that can be tuned to emit at different wavelengths of the light spectrum [152]. The green OLEDs were fabricated from a blend of poly(9,9-dioctylfluorene-*co*-n-(4-butylphenyl)-diphenylamine) (TFB) and poly((9,9-dioctylfluorene-2,7-diyl)-alt-(2,1,3-benzothiadiazole-4,8-diyl)) (F8BT).

In these devices, electrons are injected into the F8BT phase of phase-separated bulk-heterojunction active layer while holes are injected into the TFB phase, forming excitons at the interfaces between the two phases and recombining in the lower energy F8BT phase for green emission [173]. The emission spectrum of a representative device is shown in Fig. 3.1d. The red OLED was fabricated from a tri-blend blend of TFB, F8BT, and poly((9,9-dioctylfluorene-2,7-diyl)-alt-(4,7-bis(3-hexylthiophene-5-yl)-2,1,3-benzothiadiazole)-2′,2′-diyl) (TBT) with an emission peak of 626 nm as shown in Fig. 3.1d. The energy structure of the full stack used in the fabrication of OLEDs, where indium tin oxide (ITO)/PEDOT:PSS is used as the anode, TFB as an electron blocking layer [174], and LiF/Al as the cathode, is shown in Fig. 3.2a. The layers are deposited using spin coating (Fig. 3.3a), while the cathode is deposited using thermal evaporation. The physical structure of the device is provided in Fig. 3.3c. The red OLED operates similarly to the green, with the additional step of excitonic transfer via Förster energy transfer [175] to the semiconductor with the lowest energy gap in the tri-blend, TBT, where radiative recombination occurs. The irradiance at 9 V for both types of OLEDs, green and red, was measured to be 20.1 mW cm^{-2} and 5.83 mW cm^{-2}, respectively.

The ideal OPD for oximetry should exhibit stable operation under ambient conditions with high EQE at the peak OLED emission wavelengths (532 nm and 626 nm). A high EQE ensures the highest possible short circuit current, from which the pulse and oxygenation values are derived. poly({4,8-bis[(2-ethylhexyl)oxy]benzo[1,2-*b*:4,5-b′]dithiophene-2,6-diyl} {3-fluoro-2-[(2-ethylhexyl)carbonyl]thieno[3,4-*b*]thiophenediyl}) (PTB7) mixed with [6,6]-phenyl C71-butyric acid methyl ester ($PC_{71}BM$) is a stable donor:acceptor bulk heterojunction OPD system which yields EQE as high as 80% for spin-coated devices [153]. The transparent electrode and active layer of the OPD are printed on a plastic substrate using a surface tension assisted blade coating technique recently developed and reported by Pierre et al. [97] (Fig. 3.3b). Fig. 3.2c shows the energy band structure of our device including the transparent electrode (a high conductivity/high work function PEDOT:PSS bilayer) and an Al cathode. The physical device structure of the OPD is shown in Fig. 3.3d. The EQE at 532 nm and 626 nm is 38% and 47% respectively at short circuit condition, as shown in Fig. 3.1d, and the leakage current of about 1 nA cm^{-2} at 2 V applied reverse bias is shown in Fig. 3.2d together with the photocurrent when the device is illuminated with a 355μW cm^{-2} light source at 640 nm.

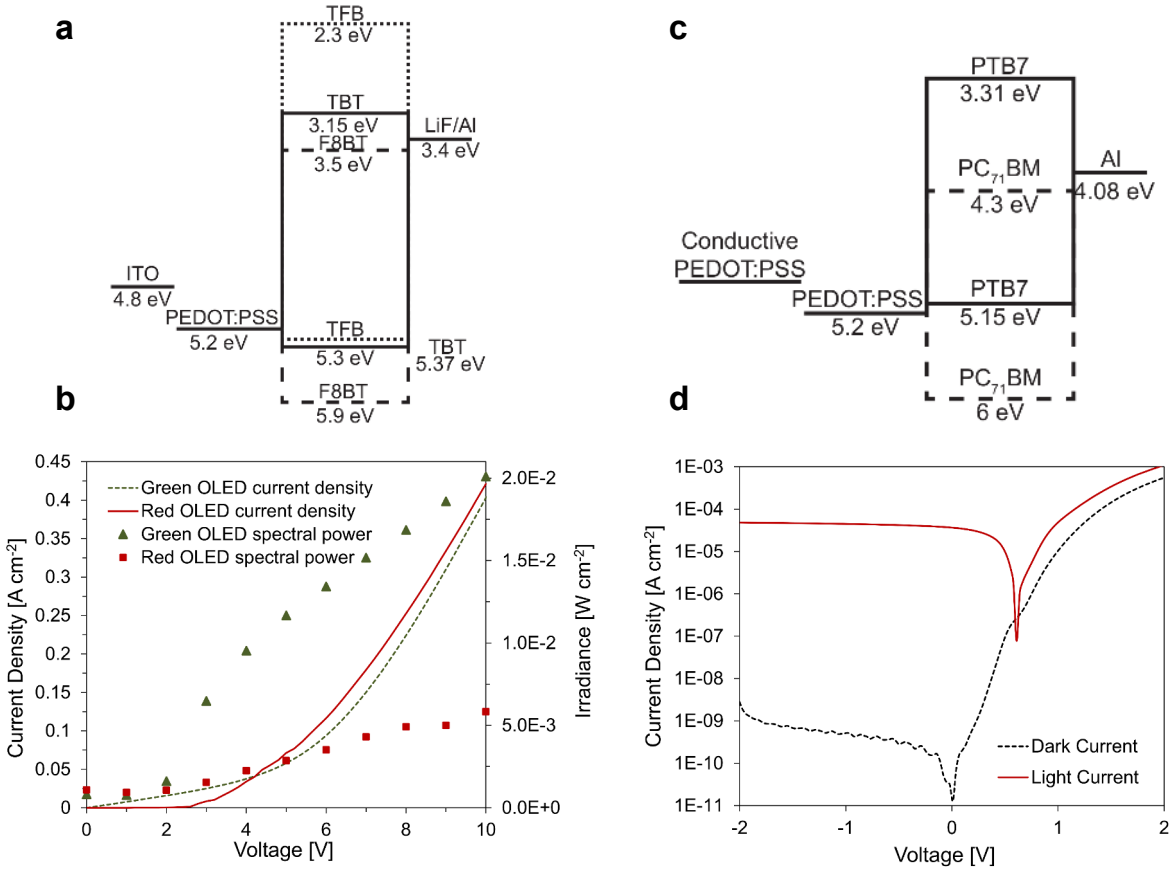

Figure 3.2. **OLED and OPD design and performance**. (**a**) OLED energy structure. (**b**) Current density of red (red solid line) and green (green dashed line) OLEDs and irradiance of red (red squares) and green (green triangles) OLEDs as a function of applied voltage. (**c**) OPD energy structure. (**d**) Light current (red solid line) with excitation from a 640 nm, $355 \mu W cm^{-2}$ light source and dark current (black dashed line) as a function of applied voltage.

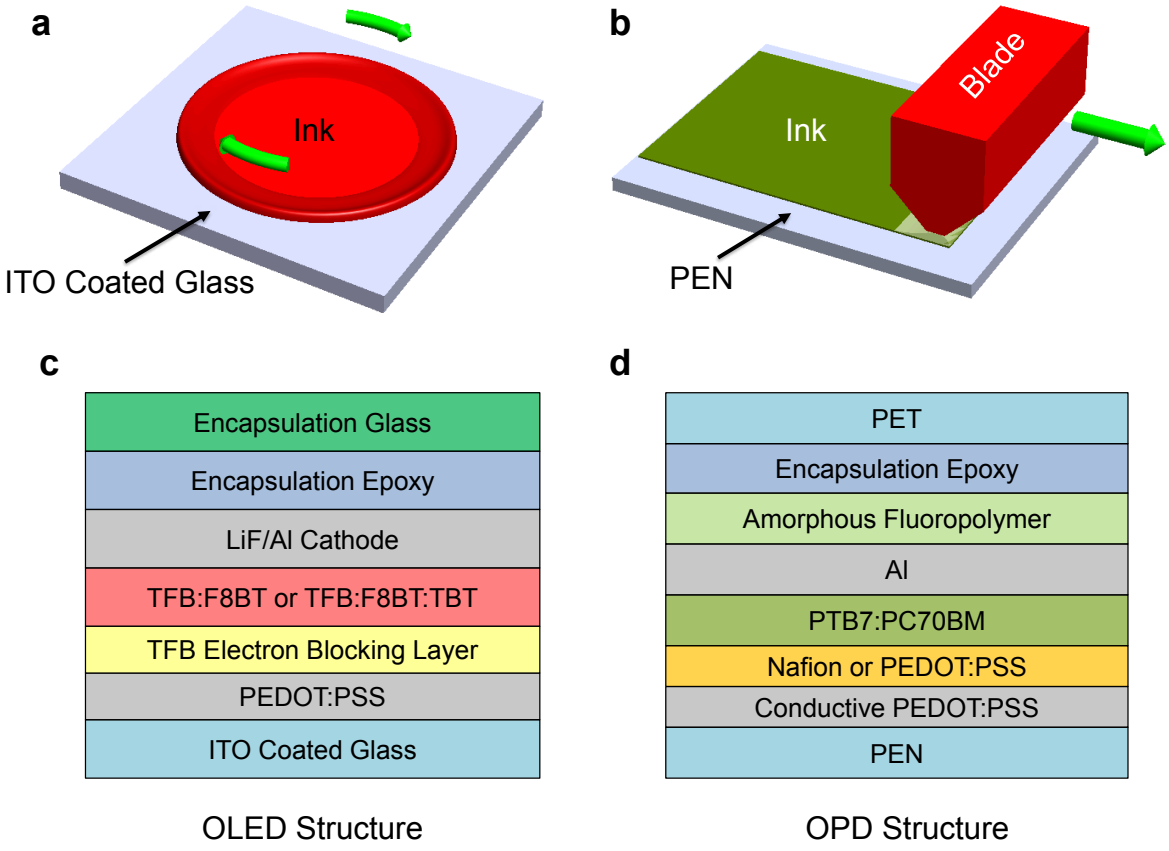

Figure 3.3. **OLED and OPD fabrication and physical device structures**. (**a**) The OLEDs are fabricated on a glass substrate using spin coating. (**b**) The OPDs are fabricated using blade coating on a PEN substrate. (**c,d**) The physical structures of the OLEDs and OPDs, respectively.

Despite the low reverse bias leakage current shown in Fig. 3.2d, we chose to bias the OPD at 0 V, the short-circuit condition, in order to sense low photocurrent levels. The frequency response of both the OPD and OLEDs was also characterized, since oximetry is usually performed at 1 kHz. The 3 dB cut-off was found to be at frequencies higher than 10 kHz for the all-organic optoelectronic sensor, which is significantly higher than the operational frequency required for oximetry (Fig. 3.4). Notably, the frequency performance of the OPD is not hampered at short-circuit because the shunt capacitance of organic PDs decreases negligibly with reverse bias, unlike inorganic PDs [176].

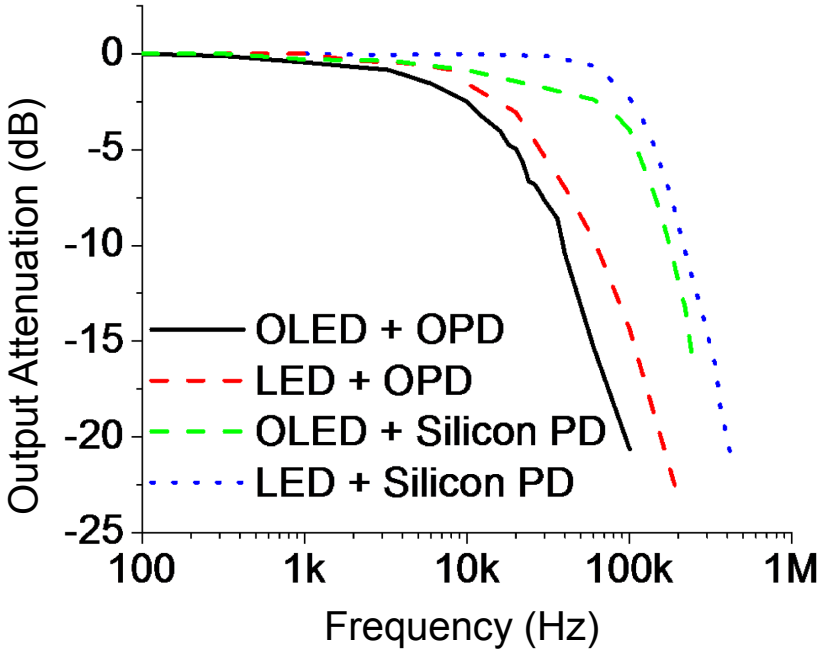

Figure 3.4. **Frequency response of various organic and inorganic LED and PD configurations.** The inorganic LED and PD showed the best response with a 3dB cutoff greater than 100 kHz. For the all organic combination with OLED and OPD, 10 KHz cutoff was obtained, which is significantly higher than the 1 kHz operation of the oximeter. Green (λ = 532 nm) LEDs and OLEDs were used with a 5 V peak to peak sinusoidal signal and a DC offset of 2.5V.

We observed that the OLED irradiance for both red and green wavelengths is sufficient for the transmission of light through the finger and the signal acquired by the organic photodetector is sufficiently high for resolving the pulsating PPG signal shown in Fig. 3.1b. The pulse waveforms (two cardiac cycles) generated with a combination of organic and inorganic devices are shown in Fig. 3.5. The PPG obtained when a human finger is illuminated by inorganic LEDs and the transmitted light is measured with an OPD is shown in Fig. 3.5a. When the same measurement is performed using OLEDs and a conventional Si PD (Fig. 3.5b) the magnitude of the PPG signal is reduced from 26 mVp-p to 16 mVp-p for the green and 16 mVp-p to 6 mVp-p for the red due to the lower optical power of the organic LEDs compared to their inorganic equivalent device. Finally both OLEDs and an OPD are used to obtain a PPG under

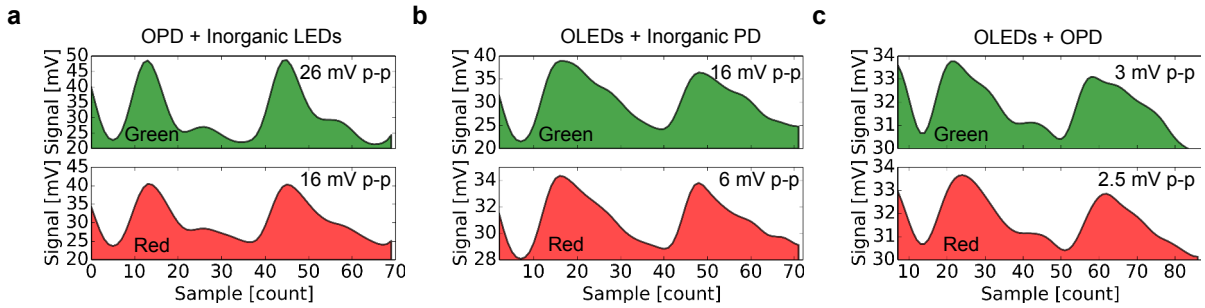

Figure 3.5. **PPG acquisition using combinations of inorganic and organic LEDs and PDs**. (**a**) PPG signal acquired using inorganic red and green LEDs and an OPD. Green and red PPG signal amplitudes of 26 mVp-p and 16 mVp-p were obtained, respectively. (**b**) PPG Signal acquired using OLEDs and silicon PD - absence of lensing epoxy and reduced irradiance of the OLEDs bring down signal magnitude to 16 mVp-p and 6 mVp-p for green and red excitation. (**c**) PPG signal acquired using OLEDs and OPD; although signal magnitudes are reduced to 3 mVp-p and 2.5 mVp-p, the signal is sufficient for resolving the PPG waveform and provide light absorbance ratio information for arterial blood oxygenation calculation.

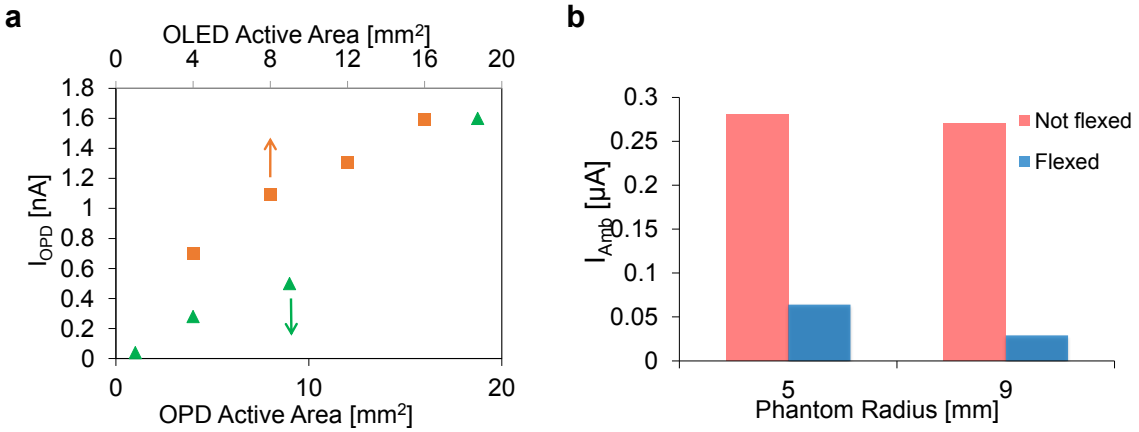

Figure 3.6. **Area scaling effects of OLEDs and OPDs, and reducing ambient noise by flexing the OPD around a finger phantom**. (**a**) OPD current (I_{OPD}) was observed for different OLED and OPD active areas. As expected, higher photo-current resulted with area scaling of the OLEDs and OPDs. (**b**) OPDs were flexed around 5 mm and 9 mm radius phantoms representative of small and large human fingers. 79% and 93% reduction in ambient noise were observed for the OPDs flexed around the phantoms, respectively.

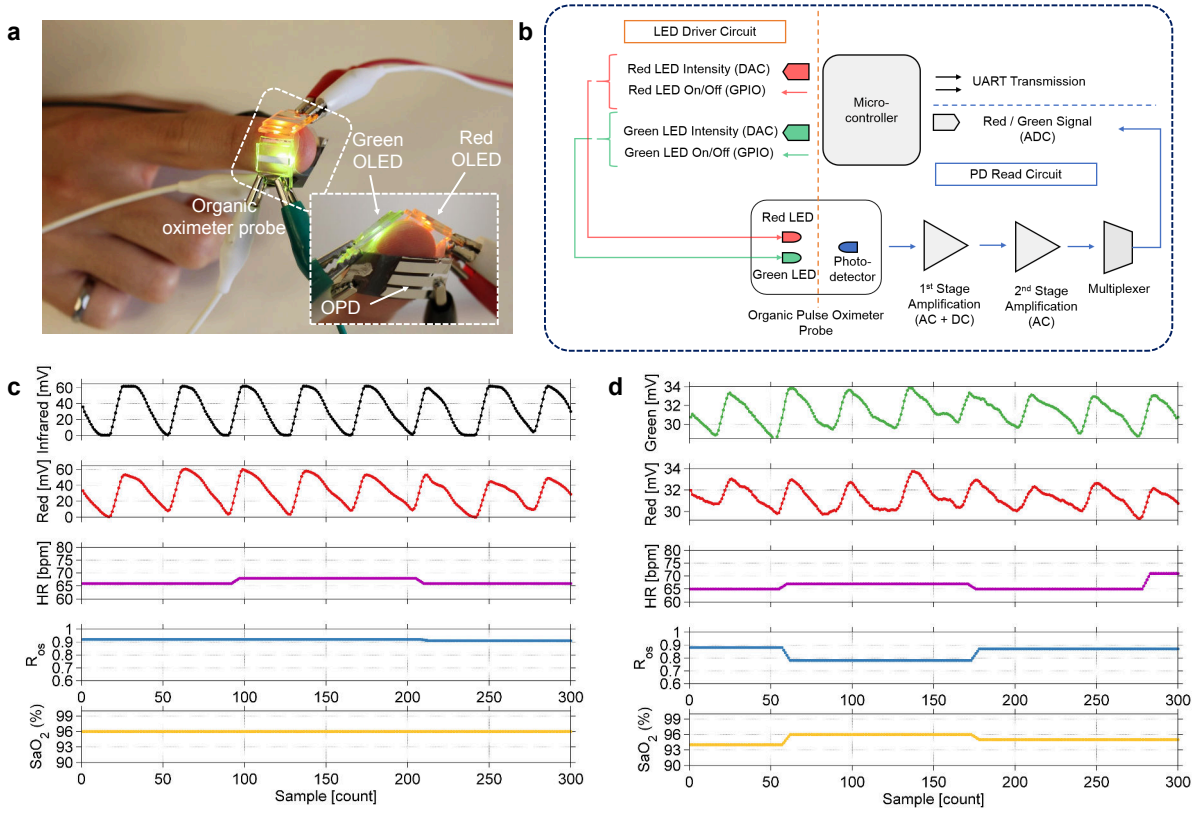

Figure 3.7. **Organic optoelectronic pulse oximetry system**. (**a**) Red and green OLEDs are placed on subject's finger and transmitted light is collected with one OPD pixel placed below the finger. (**b**) Hardware block diagram for the system setup - a microcontroller acts as the data acquisition and processing unit. OLEDs are triggered and controlled using general-purpose input/output port (GPIO) and digital-to-analog converter (DAC) pins, and the OPD signal is recorded using the ADC of the microcontroller. A two-stage amplifier between the OPD and ADC removes the DC part from the PPG signal and amplifies the pulsating PPG signal. (**c,d**) Simultaneous oximetry measurements with a commercially available inorganic oximeter probe and the organic oximeter probe, respectively. The PPG signal was obtained using red and infrared light for the commercially available probe (**c**), and using red and green light for the organic probe (**d**). Heart rate (HR) (magenta line in **c** and **d**) was obtained by timing the systolic peaks in the PPG signals. The ratio of the transmitted light at two wavelengths (R_{os}) (blue line in **c** and **d**) is converted to arterial blood oxygen saturation (S_aO_2) (yellow line in **c** and **d**) using Beer-Lambert's Law in conjunction with an empirical correction.

the same experimental conditions (Fig. 3.5c), yielding signal magnitudes of 3 mVp-p for the green and 2.5 mVp-p for the red. It is clear that the magnitude of the signal is substantially reduced with the introduction of organic-based devices, but the PPG obtained at red and green wavelengths yield similar shapes for all device combinations shown in Fig. 3.5, which will result in similar pulse and arterial oxygenation values. The lower signal magnitude shown by the organic probe is compensated for by increasing the area of devices, resulting in higher photocurrents which directly translate into higher PPG signals, as shown in Fig. 3.6a.

3.4 System design for an organic optoelectronic pulse oximeter

The organic pulse oximetry sensor composed of two red and green OLED arrays and an OPD (Fig. 3.7a) is interfaced with a microcontroller which drives the OLEDs, measures the OPD signal, and transfers the data to a computer for analysis (Fig. 3.7b). The obtained signal from the OPD passes through an AFE where the PPG signal is filtered and amplified. The pulsating part of the signal yields heart rate and oxygenation according to an empirical correction to Eq. 3.8. The accuracy of the organic optoelectronic sensor is characterized and calibrated by comparing pulse and oxygenation measurements taken simultaneously by the organic optoelectronic sensor and a commercially available pulse oximeter. The resultant pulse waveforms, pulse value, ratio of absorbed light, and arterial blood oxygen saturation from the red and NIR LEDs in the inorganic oximeter and the red and green OLEDs in the organic oximeter are shown in Fig. 3.7c and 3.7d, respectively. The OLEDs are powered by a 9 V battery and the OPD is biased at 0 V. The AC component of the signal (Fig. 3.1b) is essential for visualizing cardiac rhythm and computing arterial blood oxygen saturation. The OPD read-out circuit consists of two internal operational amplifiers (op-amps) (Fig. 3.7b) in which the first stage amplifies the whole PPG signal from the PD. The second stage only amplifies the pulsating part of the signal and is read by an ADC. With two-stage amplification, we obtained a 50-60 mVp-p PPG signal for the inorganic probe (Fig. 3.7c) and a 3-4 mVp-p PPG signal for the organic probe (Fig. 3.7d). The heart rate and ratio of transmitted light at two wavelengths (Fig. 3.7c and d) was calculated directly from the PPG signals and the arterial blood oxygen saturation was derived from the ratio of transmitted light, as discussed previously. The calculated heart rate and oxygenation derived from the PPG signals from the inorganic and organic probes are both 65-70 bpm and 94-96%, respectively (Fig. 3.7c and d). We observed 1% error for pulse rate and 2% error for oxygenation when comparing the organic optoelectronic sensor to the inorganic sensor.

Motion artifacts are one possible source of error in pulse oximetry measurements. Motion-induced errors can be minimized with signal processing algorithms that can be found in literature [177, 178]. In this work, we focus mainly on organic optoelectronic probe design and development, motion artifact characterization and mitigation algorithms can be implemented to further improve sensor performance.

3.5 Chapter conclusions

The novel combination of red and green OLEDs, as opposed to a red and NIR LED pair, is successfully implemented in pulse oximetry because the difference in the absorptivity of

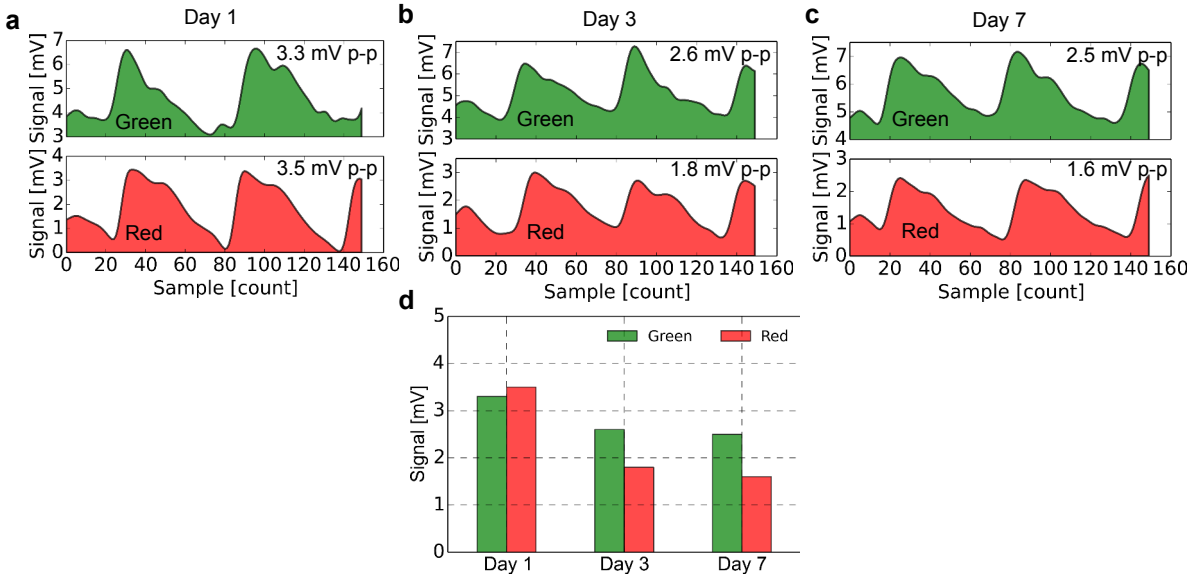

Figure 3.8. **Stability of the all-organic optoelectronic sensor.** (**a,b,c**) Recorded signal intensities on day 1, 3, and 7 respectively after fabrication of the sensor. (**d**) Bar chart showing the degradation in signal intensity over seven day time period. Decline in performance is mainly due to encapsulation failure of the organic optoelectronics.

oxygenated and deoxygenated hemoglobin at the green wavelength is comparable to the difference at NIR wavelengths [179]. Green LEDs have not been used conventionally in transmission oximetry because shorter wavelengths are more efficiently absorbed by the blood. However, the higher irradiance of the green OLEDs (Fig. 3.2b) compensates for any absorption losses in non-pulsating blood and tissue, as can be inferred from the higher green signal amplitudes in Fig. 3.7 compared to the red signal amplitudes. We employed an empirical correction to calculate arterial blood oxygenation from the ratio of transmitted green and red light, a scheme widely used for correcting for the deviation from Beer-Lambert's Law (which doesn't account for the scattering that occurs in human tissue) in red and NIR pulse oximetry measurements.

Aside from maximizing OPD EQE and short circuit photocurrent and OLED irradiance, the OPD's short circuit current resulting from ambient light should be minimized in order to achieve the best pulse oximetry signal, as parasitic photodetector current is a contributor to conventional pulse oximetry failure [180]. The effects of ambient light on the OPD's short circuit current were measured using two finger phantoms with radii of 9 mm and 5 mm, representative of the wide range of human finger sizes. Flexing the PD around the finger phantom, as opposed to taking the measurement with the PD placed flat, non-flexed, against the phantom, significantly reduces the parasitic short circuit current produced by ambient light. Under typical room lighting conditions of 72-76$\mu W cm^{-2}$, flexing the OPD around the 9 mm and 5 mm radii phantoms reduced the parasitic current from 270 nA to 20 nA and 280 nA to 60 nA, respectively (Fig. 3.6b). The ability of the flexible OPD to conform around the human body therefore improves the pulse oximeter's versatility.

The long-term stability of the organic optoelectronic pulse oximeter, like most organic optoelectronics, is limited by the robustness of the encapsulation technology employed in its fabrication [181, 182]. It has been shown that lifetime of organic optoelectronics can be significantly improved using robust encapsulation and packaging. With our encapsulation process, we see a 24% signal intensity decrease in the green and a 54% decrease in the red PPG signal over a seven-day time frame. Fig. 3.8 shows a decline in signal intensity, however the PPG signal shapes are intact.

The organic optoelectronic pulse oximetry sensor described here demonstrates the potential for the application of organic electronics to thrive in the medical device field. The large-area scalability, inexpensive processing and flexibility of organic optoelectronics will allow medical sensors to be made in new shapes and sizes, diversifying possible sensing locations on the human body, enabling medical professionals to better monitor their patients' care.

Chapter 4

Printed reflection-mode oximeter

4.1 Introduction

In the human body, cardiac rhythm changes the blood volume passing through the arteries, which generates a pulsatile signal that can be optically measured using a light source and a detector; this optical sensing technique is known as PPG. Generally, the PPG signal is used for calculating HR by utilizing only one light source, and for measuring oxygen saturation (S_pO_2) by employing two light sources. Pulse oximeters measure S_pO_2 of blood by using PPG signals at two distinct wavelengths where light absorption in oxygenated and deoxygenated blood is different [183]. PPG and oximetry can be performed in both transmission and reflection mode. Conventionally, transmission-mode pulse oximeter sensors composed of solid-state LEDs and PDs are used to measure S_pO_2 at the extremities of the body where light can easily penetrate thin regions of tissue, such as the earlobes and the fingertips. However, this method of measuring S_pO_2 presents a few limitations - (i) Transmission-mode oximetry has limited sensing locations [6], and (ii) Solid-state LEDs and PDs do not conform well to the skin, therefore, reduce the SNR [4].

Over the past few years, flexible and wearable sensors are getting significant attention in both academic research and industry due to their skin conformable form factors [184–192]. Consequently, flexible optical sensors are extensively studied for PPG and oximetry as they enhance SNR and provide design versatility [4, 6, 193–195]. Sensor fabrication and sensing methodology remain a strong focus of recent reports. However, the reflectance oximeter sensor design, which is a crucial component of reflection-mode PPG and oximetry, is not well-reported in the literature. In addition, wearable reflection-mode PPG sensors and oximeters are prone to different kinds of noises, such as motion artifacts (MAs), thermal noise, and electromagnetic interference [196]. Thermal noise and electromagnetic interference are high-frequency noise and can be eliminated through filtering. MAs, however, are challenging to remove from the PPG signals. Adaptive filtering [197–199] and comparing PPG signal to a reference accelerometer signal [199, 200] are popular techniques for reducing MAs. Multi-channel PPG signals can also be utilized to extract HR and oxygenation information from channels that are less affected by MAs [201, 202]. The multi-channel PPG approach does not require additional hardware

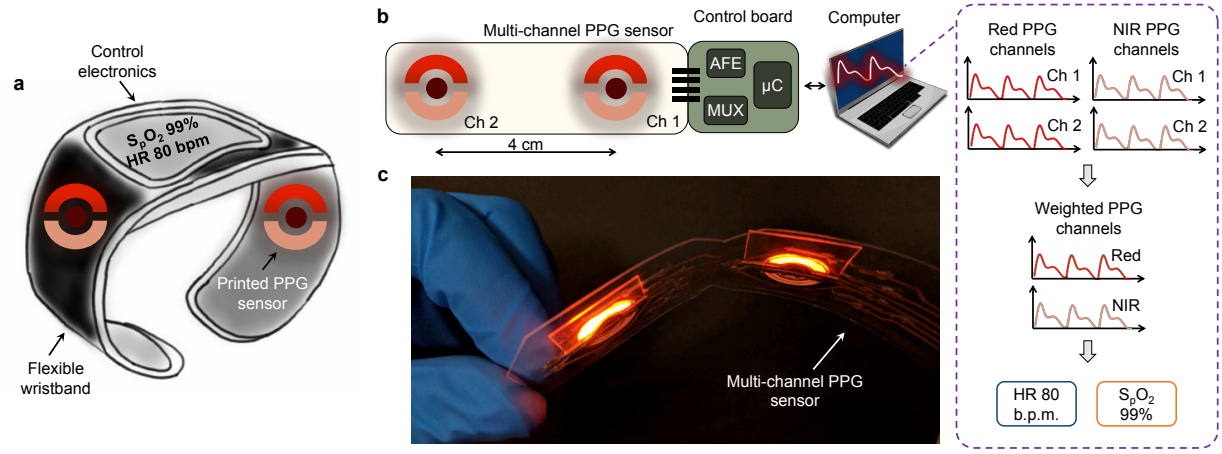

Figure 4.1. **Reflectance oximeter sensor overview**. (**a**) Schematic illustration of a wearable two-channel PPG sensor, where the PPG sensor pixels are mounted on the wristband. (**b**) Setup for the multi-channel PPG sensor. Two circular sensors are spaced 4 cm apart to collect data from the ulnar artery (Ch 1) and radial artery (Ch 2). The sensor pixels are driven using an AFE, while multiplexers are used to switch between the pixels. Both red and NIR PPG signals are collected and processed for extracting HR and pulse oxygenation data. (**c**) Photographs of the multi-pixel reflectance oximeter sensor bent to a radius of curvature of 5 cm.

blocks or a reference signal.

In this chapter, we systematically study the reflectance oximeter sensor design in terms of device geometry, light emitter and detector spacing, and the use of an optical barrier between the emitter and the detector to maximize sensor performance. Additionally, we utilize a printed, flexible, and two-channel reflectance oximeter to collect PPG signals using red and NIR OLEDs and OPDs. We implement inverse-variance weighting and template matching algorithms to improve the detection of HR from the multi-channel PPG signals. Overall, we report sensor design, optimization, and implementation of a two-channel organic optoelectronic sensor which is promising for wearable reflection-mode PPG and oximetry.

4.2 Reflectance oximeter sensor geometries and operation

A schematic illustration of a two-channel wrist-worn reflectance PPG sensor is shown in Fig. 4.1a. The multi-channel PPG sensor is designed using two circular sensors to collect PPG signals from the radial and the ulnar arteries (Fig. 4.1b). The sensor is interfaced to multiplexers that switch between the pixels and connects to an AFE. The AFE sequentially drives the OLEDs and reads out the OPD signals. Both red and NIR PPG signals are collected using the two pixels. Since most wearable PPG sensors are wrist-worn, we utilize the two-channel PPG sensor for on-wrist measurements. The underside of the wrist, especially on the radial and ulnar arteries, provide the best PPG signal magnitudes. One pixel (Ch 1) is placed on the ulnar artery, while the other pixel (Ch 2) is placed on the radial artery. A photograph of

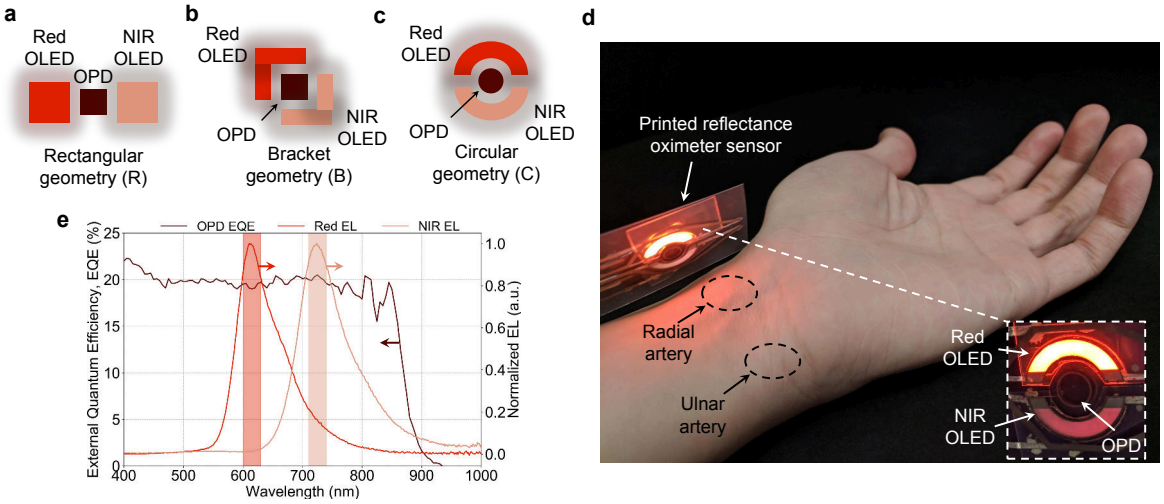

Figure 4.2. **Reflectance oximeter sensor design and placement on the wrist**. (**a-c**) Different sensor geometries with the same component areas. (**a**) Rectangular geometry (R), where the OLEDs are placed at either side of the OPD. (**b**) Bracket geometry (B), where the OLEDs are shaped as brackets and placed around the square OPD. (**c**) Circular geometry (C), where the OLEDs are shaped as block arcs and placed around the circular OPD. (**d**) Photograph of the printed reflectance oximeter sensor placed on the underside of the wrist. The radial and ulnar artery sensing locations are marked to show sensor placement locations. The inset shows a circular sensor with red and NIR OLEDs on the top and the bottom side of the OPD, respectively. (**e**) Normalized Electroluminescence (EL) of the red (red line) and NIR (peach line) OLEDs and EQE of the OPD (brick line). The OPD shows similar EQE at both red and NIR wavelengths.

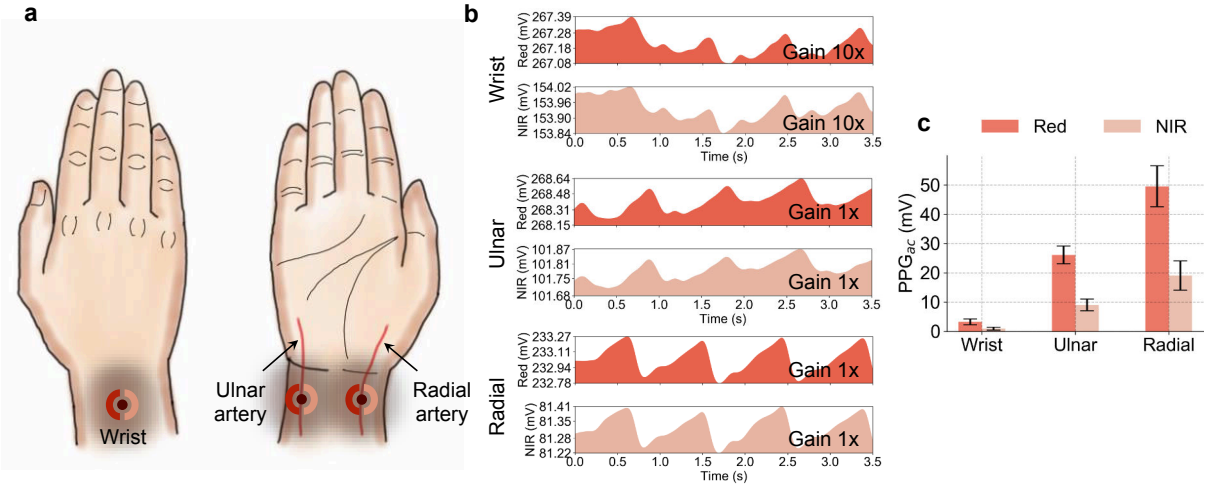

Figure 4.3. **PPG signal variation on the wrist**. (**a**) Three sensor placement locations are shown - (i) On top of the wrist, (ii) on top of the ulnar artery, and (iii) on top of the radial artery. (**b**) PPG signals from the wrist, ulnar and radial arteries are shown. Red color for the red channels and peach color for the NIR channels. Since the signal on the wrist is weak, a 10x gain setting is used to resolve the pulsatile PPG signal. (**c**) PPG signal magnitudes at the wrist, ulnar and radial arteries. The error bars represent data from 3 separate trials.

the multi-pixel sensor is shown in Fig. 4.1c, where the sensor is bent to a radius of curvature of 5 cm to resemble bending on the wrist.

Reflection-mode sensors require light emitters and detectors assembled on a substrate or a circuit board. Traditionally, red and NIR LEDs are placed on either side of the PD to assemble the sensor. The designs of commercially available optoelectronic sensors are limited in shape - typically rectangular, which do not provide much versatility to vary the sensor geometry. On the other hand, printed optoelectronics can be fabricated in various shapes and sizes [203]. In this work, we explore three different sensor geometries as shown in Fig. 4.2a-c: (1) Rectangular geometry (R), where the OLEDs are placed at either side of the OPD; (2) Bracket geometry (B), where the OLEDs are shaped as brackets and placed around the square OPD; (3) Circular geometry (C), where the OLEDs are shaped as block arcs and placed around the circular OPD. The rectangular sensor design is chosen to represent conventional sensors that use side-by-side optoelectronics placement. The bracket and the circular sensor geometries are non-traditional geometries chosen to improve PPG SNR. Fig. 4.2d shows the sensor placement on the underside of the arm. Radial and ulnar arteries are marked to show sensor placement. All sensors are composed of printed red and NIR OLEDs with emission peaks at 630 and 725 nm respectively, and OPDs with EQE of ~20% at the aforementioned wavelengths (Fig. 4.2e).

PPG signal magnitudes vary appreciably based on the sensor placement locations on the wrist. We explored three sensing locations: (i) On top of the wrist, (ii) on top of the ulnar artery, and (iii) on top of the radial artery and recorded PPG signals (Fig. 4.3a and b). While the radial artery provided the cleanest signal (49.50 mV for red and 19.08 mV for NIR), the pulsatile PPG signal on top of the wrist was the weakest (Fig. 4.3c). At the ulnar artery an

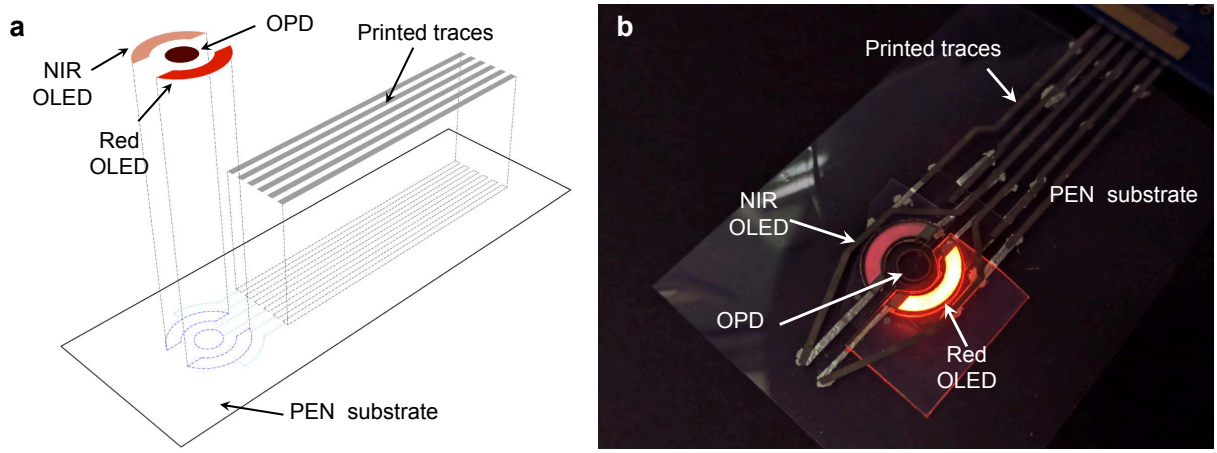

Figure 4.4. **Assembly of the printed sensor**. (**a**) Schematic depicting the sensor assembly. PEN is used as the base substrate. Inkjet-printed silver traces are used to connect the optoelectronic sensor to the control electronics. Red and NIR OLEDs and the OPD are then connected to complete the sensor. (**b**) Photograph of the assembled sensor.

order of magnitude improvement (26.12 mV for red and 9.02 mV for NIR) in PPG signal is observed over the wrist (3.24 mV for red and 0.94 mV for NIR). Therefore, we used our sensor on the underside of the wrist for both single and multi-channel measurements.

4.3 Sensor assembly and calibration

A base PEN substrate is used to assemble the reflectance sensor. Inkjet-printed silver traces are used to route connections from the optoelectronics to the control electronics that consists of an AFE and an MCU with a universal serial bus (USB) interface to a computer. The OLEDs and the OPD are printed on separate plastic substrates and then assembled on the PEN substrate with silver traces as shown in Fig. 4.4a. The photograph of the assembled sensor with the OLEDs and the OPD is shown in Fig. 4.4b. Since we are comparing different sensor geometries, a two-step calibration is used to account for the batch-to-batch device variability of the OLEDs and the OPDs. A calibration platform composed of a silicon PD and a red LED is used to calibrate the assembled sensor. In the first step, the OLEDs are calibrated using the silicon PD by operating the OLEDs at a fixed current and recording the PD current. The OLEDs of the assembled sensor are turned on sequentially to measure their intensities using the silicon PD. Each OLED is then calibrated to the maximum current measured in a batch of devices, $\kappa_{OLED} = \frac{max(I_{SiPD})}{I_{SiPD}}$. In the second step, the OPDs are calibrated by recording the OPD current while running the solid-state red LED at a fixed drive current. The red LED of the calibration platform is turned on and the OLEDs are turned off for calibrating the OPDs. The fabricated OPD detects light from the red LED and the measured photocurrent is recorded. Similar to the OLEDs, each OPD is then calibrated to the maximum OPD current measured in a batch of devices, $\kappa_{OPD} = \frac{max(I_{OPD})}{I_{OPD}}$. The obtained values are then used together with the measured PPG signal to calculate the calibrated signal magnitude. The calibration equation is

given below, which is used to compare sensor performances for the three different geometries.

$$PPG_{cal} = \kappa_{OLED} \cdot \kappa_{OPD} \cdot PPG_{meas}[mV] \tag{4.1}$$

4.4 Performance comparison among different sensor geometries

After the calibration step, a fair comparison among the three different geometries can be performed. Additionally, we evaluate another important design parameter, emitter-detector spacing, d. Fig. 4.5 a-c show the photographs of the rectangular, bracket, and circular sensors with an emitter-detector spacing of 2, 4, and 6 mm, which are labeled as R2, R4, R6, B2, B4, B6, C2, C4, and C6. These labels are used in Fig. 4.5d to show pulsatile PPG signal magnitude, PPG_{cal} based on Eq. 4.1.

The rectangular sensor consists of OLEDs and an OPD that are all square-shaped which are placed side-by-side. Since the OLEDs do not surround OPD from the top and the bottom, this scheme is susceptible to ambient light, which contributes to the noise of the measurement. Also, a significant amount of light coming out from the left edge of the red OLED and the right edge of the NIR OLED do not contribute to the measurement, hence, gets lost. Ideally, a perimeter light source that surrounds the OPD would be the best. The two new schemes, the bracket, and the circular designs, where the light sources encompass the perimeter of the OPD enhance measurement SNR. As shown in Fig. 4.5d, all three designs show an exponential decay with increasing d. Due to the perimeter lighting and better light collection by the OPD, both bracket and circular geometries outperform the rectangular design in terms of pulsatile PPG signal magnitude. While comparing the bracket and circular design, we observe a negligible difference in PPG_{cal}.

For a direct comparison of the different geometries, we kept the emitter-detector spacing constant at 2 mm, and kept the device area of the OLEDs and the OPDs same for all three geometries as shown in Fig. 4.6a. The OPD areas are kept fixed at 16 mm^2 and the OLED areas are kept fixed at 28 mm^2. The PPG waveforms for the different geometries are shown in Fig. 4.6b. Utilizing the bracket geometry, we observe 39.7% and 18.2% improvements in PPG signal magnitude in the red and NIR channels, respectively over the rectangular geometry. For the circular geometry, we observe 48.6 % and 9.2% improvements in the red and NIR channels, respectively over the rectangular geometry. The bracket and the circular design show almost similar performance in the PPG_{cal} (Fig. 4.6c). Additionally, the two new designs bring down the overall length of the sensor from 18.6 mm for the rectangular geometry to 12 mm for the bracket and 13.2 mm for the circular geometry.

In reflectance PPG and oximetry, the light coming back from the arteries contributes to the signal, while the light scattered from the skin surface contributes to noise. Therefore, blocking the light scattered from the skin surface enhances SNR. We incorporated the light blocking feature in our design by utilizing an optical barrier between the OLEDs and OPD. Black tape is cut into the shape that fits the area between the OLEDs and the OPD and is used to block scattered light. Fig. 4.7a shows the schematic of the sensor. With the blocking layer, we observe 26.5 % improvement in PPG_{cal} in the red channel, and while PPG_{cal} remained almost the same in NIR. Red light scatters more on the skin surface than the NIR. Therefore, more red

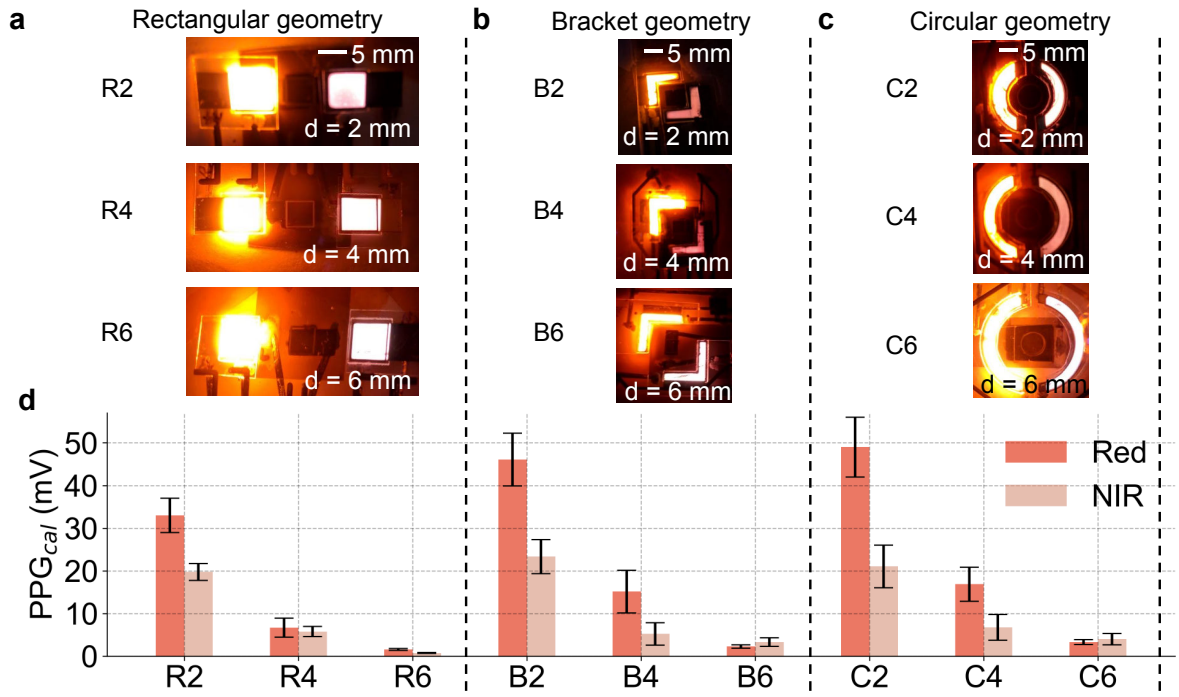

Figure 4.5. **Pulsatile signal magnitudes for different sensor geometries**. (**a**) Photographs of the rectangular sensors with emitter-detector spacing, d = 2, 4, 6 mm. The devices are labeled as R2, R4, and R6. (**b-c**) Similar to **a**, photographs of the bracket and circular sensors with emitter-detector spacing, d = 2, 4, 6 mm. The devices are labeled as B2, B4, B6, C2, C4, and C6. (**d**) The pulsatile signal magnitudes for all rectangular, bracket and circular sensors. Red-colored bars represent data for the red channel, while the peach-colored bars represent data from NIR channel. The error bars represent data from 3 separate trials.

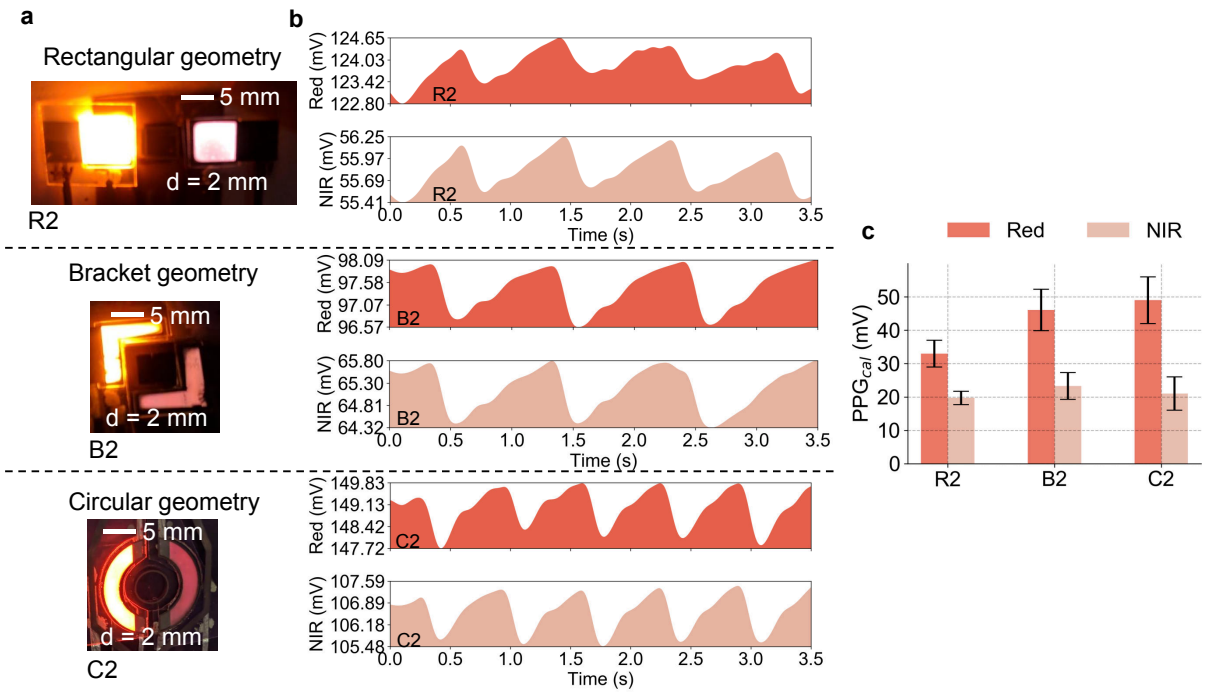

Figure 4.6. **Performance comparison of different sensor geometries**. (**a**) Photographs of the rectangular, bracket and circular sensors with an emitter-detector spacing of 2 mm. (**b**) PPG signals from the red and NIR channels for the sensors shown in **a**. (**c**) The pulsatile signal magnitudes for the smallest rectangular, bracket and circular sensors. Red-colored bars represent data for the red channel, while the peach-colored bars represent data from NIR channel. The error bars represent data from 3 separate trials.

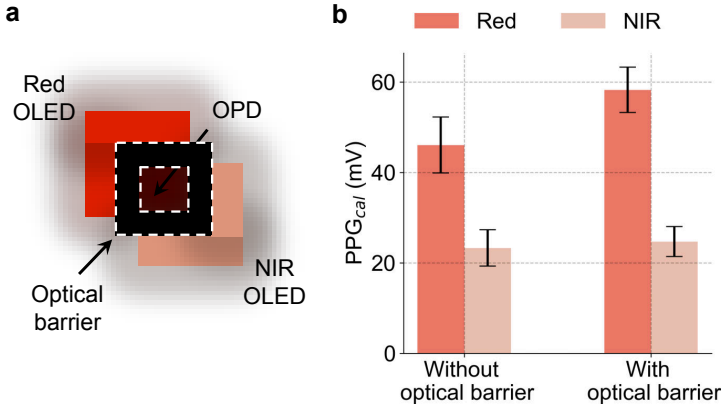

Figure 4.7. **The effect of an optical barrier in sensor performance**. (**a**) Schematic of a reflectance oximeter sensor, where an optical barrier is placed in between the emitters and the detector. (**b**) The pulsatile signal magnitudes of the red and NIR channels without and with the optical barrier. The error bars represent data from 3 separate trials.

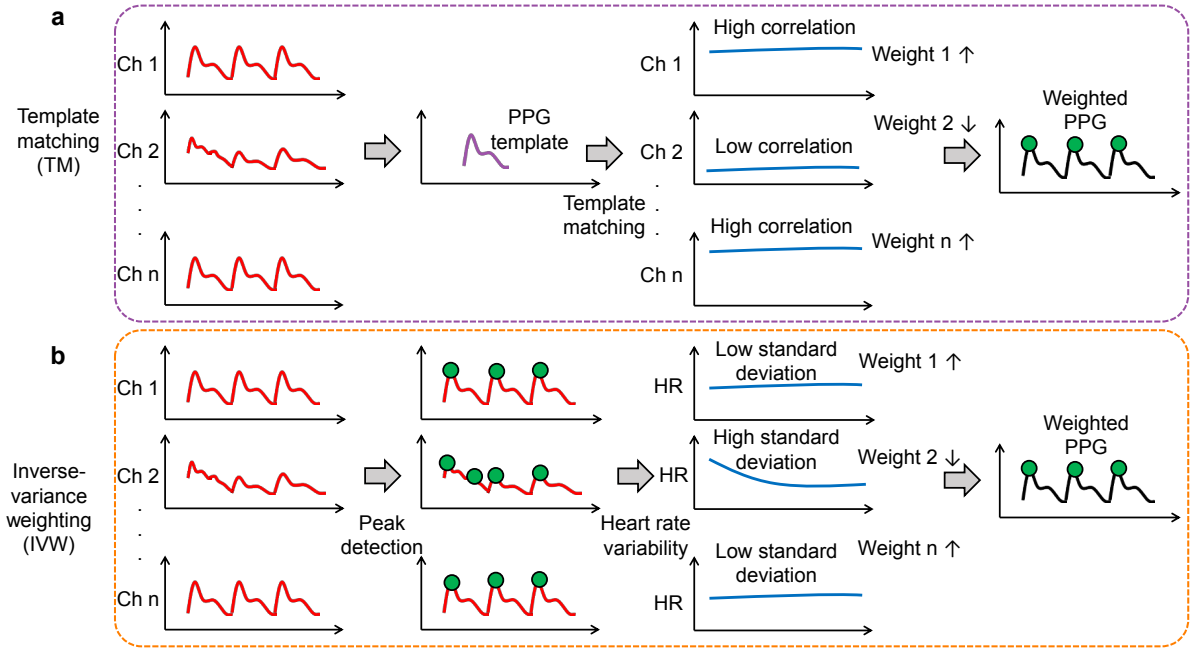

Figure 4.8. Process flow of the (**a**) TTM and (**b**) IVW algorithms.

light scattered by skin surface gets blocked by the optical barrier, resulting in an improved red PPG_{cal} (Fig. 4.7b).

4.5 Multi-channel PPG sensor operation and data processing

Wearable PPG sensors are susceptible to thermal noise, electromagnetic interference, and MAs. While thermal noise and electromagnetic interference can be reduced with filtering, reducing MAs requires additional hardware and software processing. Adaptive filtering is a popular technique for addressing MAs in PPG signals [197–199]. Another approach is to simultaneously record PPG and a reference signal such as an accelerometer signal and apply hybrid algorithms to determine HR and pulse oxygenation [199, 200]. Multi-channel PPG acquisition and processing can also be used to reduce MAs by utilizing channels that are lightly influenced by MAs [201, 202]. Multiple PPG channels add redundancy to the measurement for signal quality assessment, which is vital for properly extracting HR and pulse oxygenation values. To process multi-channel data, we implemented two algorithms: (1) TM with an ideal PPG signal, and (2) IVW. The efficacy of both methods in acquiring high-quality PPG signal, and extracting HR are examined. The process flow of the template matching and inverse-variance weighting algorithms are shown in Fig. 4.8a and b, respectively.

Both TM and IVW algorithms are used to obtain a weighted PPG signal from multi-channel PPG. The equation for obtaining the weighted PPG is given in Eq. 4.2.

$$PPG_w = \frac{W_1 \times PPG_1 + W_2 \times PPG_2 + ... + W_n \times PPG_n}{W_1 + W_2 + ... + W_n} \tag{4.2}$$

Here, PPG_w is the weighted PPG from all channels, W_i is the weight for channel i determined by either of the two methods discussed in following subsections and PPG_i is the PPG signal from channel i.

4.5.1 TM with an ideal PPG signal

Template matching is a popular data processing techniques in biomedical signal processing. TM has been widely used in processing electroencephalography (EEG), electrocardiography (ECG), and PPG data [204–206]. We use an ideal PPG template to determine the fidelity of the signal from each channel. The ideal template can be obtained from experimental data [207] or by modeling [208]. A small window is acquired from each channel after filtering. Then, troughs are detected to find the pulses in each window. Next, the correlation coefficient of each pulse with the ideal template is calculated. If the correlation coefficient is positive, the correlation coefficient is used as a weight to calculate the weighted average of the two signals. If the correlation coefficient for a pulse is negative, the pulse is ignored, i.e., the weight for that pulse in that channel is set to zero. Thus, using this method, the weight W_i's in Eq. 4.2 can be given by Eq. 4.3.

$$\begin{aligned} W_i &= \rho_i, \text{ if } \rho_i \geq 0, \\ &= 0, \text{ if } \rho_i < 0 \end{aligned} \tag{4.3}$$

Here, ρ_i is the correlation coefficient between a pulse in channel i and the PPG template. HR and oxygenation values are determined from the weighted signal. The process flow for TM is presented in Fig. 4.8a.

4.5.2 IVW based on HR

In inverse-variance weighting algorithm, W_i, weight for channel i in Eq. 4.2 are assigned based on the standard deviation of HR variability in a specific time window. First, peaks and troughs of the signal from each window are determined. Then, the HR is calculated from the distances in between peaks or troughs. The channel with higher standard deviation in HR is assigned lower weight, because, in a small time-window of PPG signal, HR should not change too drastically. The weight assignment, in this case, is described by Eq. 4.4.

$$W_i = \frac{1}{\sigma_i} \tag{4.4}$$

Here, σ_i is the standard deviation of HR in channel i. After assigning the weight, the weighted average of the signals (PPG_w) is computed and the HR and other features are extracted from the signal. The process flow is presented in Fig. 4.8b.

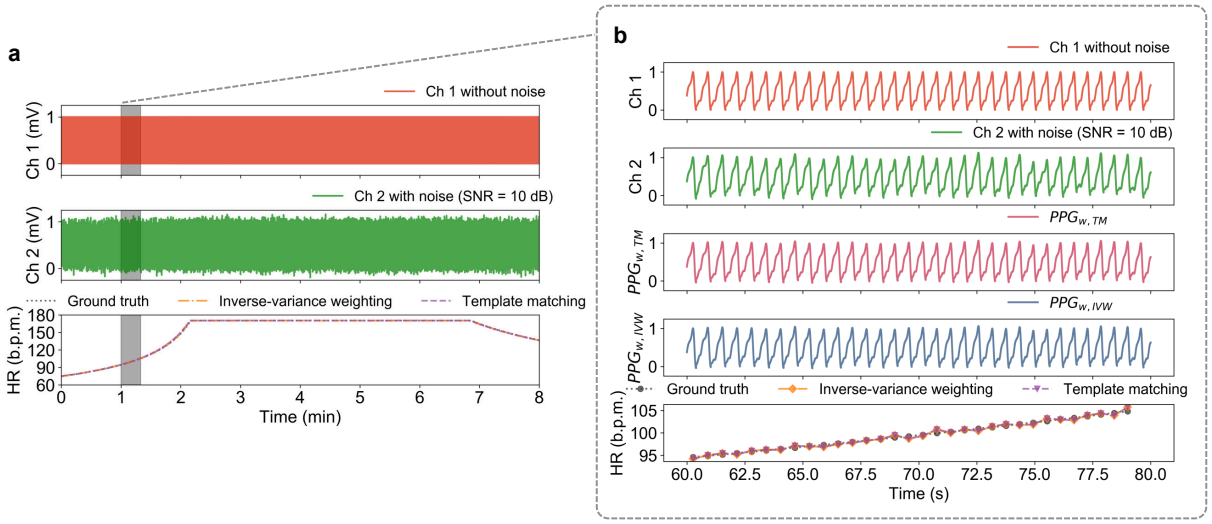

Figure 4.9. **HR detection using TM and IVW algorithms from a simulated dataset**. (**a**) 8 min long pristine PPG signal (Ch 1, top panel) and a PPG signal with 10 dB SNR (Ch 2, middle panel) are used as the multi-channel PPG data. Calculated HR from Ch 1 and Ch 2 using TM and IVW algorithms and the ground truth are shown in the bottom panel. (**b**) Zoomed-in data from 60 to 80 s of **a** - Ch 1, Ch 2, weighted PPG signal using TM and IVW algorithms, and calculated HR are shown.

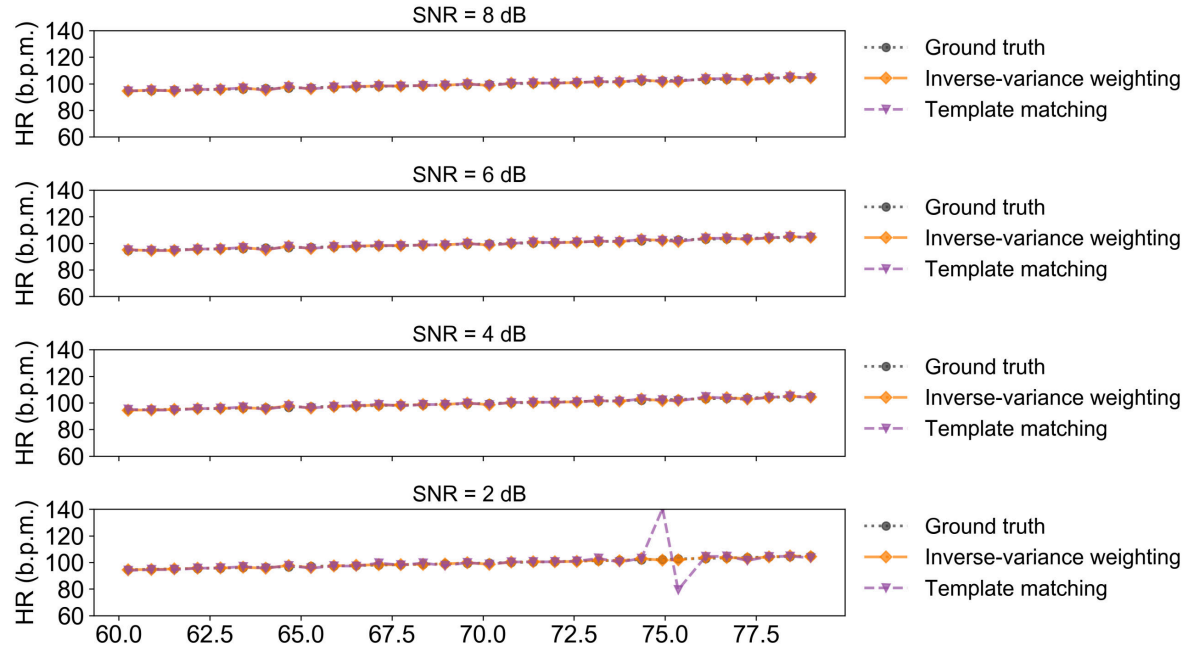

Figure 4.10. **The effect of SNR on the accuracy of HR estimation using TM and IVW algorithms**.

4.5.3 Implementation of TM and IVW algorithms on a simulated PPG dataset

To test the efficacy of the TM and IVW algorithms, a simulated dataset is used to determine HR variability over time. The simulated dataset is designed to represent HR variability while performing an exercise (Fig. 4.9a). Here, Ch 1 is a simulated PPG data, where the HR goes up in the first few minutes, stays constant and then goes down slowly. This PPG signal represents the change in PPG during real-time exercise. Ch 2 is the same PPG signal with a low-frequency noise added to it. Slow and fast variations of HR are utilized. In the fast variation case, HR is varied from 71 beats per min (b.p.m.) to 200 b.p.m. in 20 s. Both TM and IVW algorithms successfully reconstructed the PPG signals and determine HR accurately. In the slow variation case, HR was varied from 95 to 105 b.p.m. in 20 s (Fig. 4.9b), and both the algorithms successfully determined HR in this test case also.

The effect of noise on the accuracy of determining HR using TM and IVW algorithms is examined by adding noise of frequency below 5 Hz to one of the channels. This frequency range of noise is chosen because noise with a frequency above 5 Hz can be removed from the signal using a low-pass filter (LPF). The effect of SNR is shown in Fig. 4.10. The SNR is varied and as long as the SNR is above 3 dB, both algorithms accurately detect HR. However, at SNR less than 3 dB, the TM algorithm fails to predict HR accurately.

In addition to the simulated dataset, we used three sets of PPG dual channel data reported by Zhang et al. [199] to test the efficacy of the TM and IVW algorithms. The results are summarized in Table 4.1. For the datasets, I and III the HR calculated using both methods are close to the ground truth HR, i.e., within 2 b.p.m. However, in dataset II, both channels are severely affected by MAs, so the calculated HRs are further away from ground truth HR. For accurate detection of HR, at least one of the channels should be minimally affected by MAs so that the PPG pulses are recognizable.

Table 4.1. HR calculated from a literature dataset [199] using template matching and inverse-variance weighting algorithms.

Dataset	HR from Template Matching (b.p.m.)	HR from Inverse-Variance Weighting (b.p.m.)	HR from Ground Truth (b.p.m.)
I	74.26	74.26	74.34
II	64.66	64.66	68.73
III	72.12	72.12	74.53

4.6 Implementation of TM and IVW algorithms on the printed multi-channel PPG sensor data

After validating the TM and IVW algorithms on the simulated and literature datasets, we employed both methods for processing the data collected by the printed multi-channel PPG sensor. The sensor is placed on the underside of the wrist, where Ch 1 collects data from the ulnar artery and Ch 2 collects data from the radial artery (Fig. 4.11a and b, top two panels). The weighed PPG signals generated by TM and IVW algorithms are shown in panel 3 and 4 of Fig. 4.11b. Here, the signal magnitude of Ch 1 is weaker compared to Ch 2. Therefore, HR

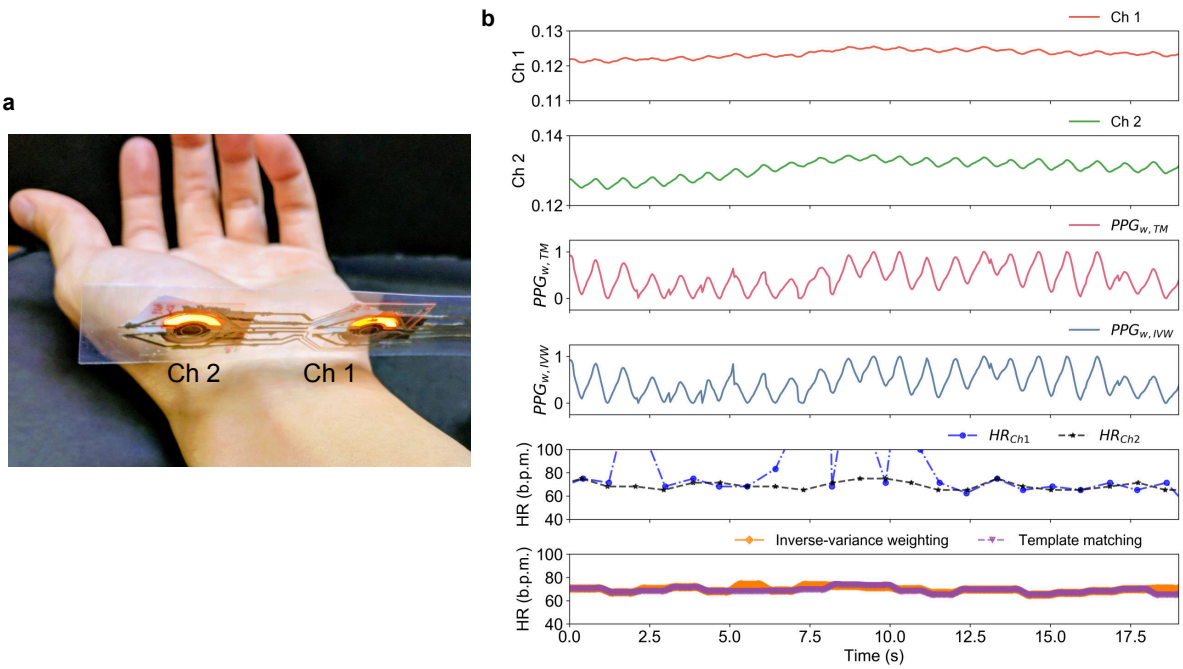

Figure 4.11. **HR detection using TM and IVW algorithms from the printed multi-channel PPG sensor**. (**a**) The printed sensor is placed on the underside of the wrist. (**b**) Ch 1 and Ch 2 are PPG data collected from the ulnar and the radial arteries, respectively. $PPG_{w,TM}$ and $PPG_{w,IVW}$ are the weighed PPG signals generated by TM and IVW algorithms. HR_{Ch1} and HR_{Ch2} are calculated HR by using Ch 1 and Ch 2 PPG data. The bottom panel shows calculated HR by TM and IVW algorithms.

calculated using only using Ch 1 PPG signal demonstrates significant variation (panel 5 of Fig. 4.11b). After implementing TM and IVW algorithms, accurate detection of HR is observed for both the algorithms (bottom panel of Fig. 4.11b), demonstrating the feasibility of using these two methods for wearable PPG sensors and oximeters.

4.7 Chapter conclusions

By utilizing the versatility of printed electronics, optoelectronic sensors for PPG and oximetry are fabricated in different shapes and sizes. In this work, we utilized non-conventional geometries such as bracket and circular designs to improve sensor performance. The new sensor geometries demonstrated a clear improvement over the conventional rectangular sensor design. Moreover, we used a wearable two-channel PPG sensor to add redundancy to the measurement and demonstrated the effectiveness of inverse-variance weighting and template matching algorithms to improve the detection of HR from the multi-channel PPG signals. The new sensor geometries not only improved the PPG signal magnitudes but also decreased the overall sensor length and reduced power consumption. These sensor designs coupled with multi-channel redundancy can be incorporated into wrist-worn devices, making them

extremely promising for wearable reflectance PPG and oximetry.

Chapter 5

Printed reflection-mode oximeter array

5.1 Introduction

Hemoglobin, a protein molecule in the blood, transports oxygen from the lungs to the body's tissues. Oximeters determine oxygen saturation (SO_2) in tissues by optically quantifying the concentration of HbO_2 and Hb [183]. Pulse oximetry, the most ubiquitous non-invasive method of oximetry, performs this ratiometric optical measurement on pulsatile arterial blood via PPG at two different wavelengths [209]. Pulse oximeters use optoelectronic sensors composed of LEDs and PDs and operate at red and NIR wavelengths, where the molar absorptivity of HbO_2 and Hb are significantly different. While both transmitted and reflected light can be used for pulse oximetry, in transmission-mode pulse oximetry ($S_pO_2^t$), the LEDs shine through the tissue and the transmitted light is collected using the PD on the opposite side (Fig. 5.1) - this restricts sensing locations to only tissues that can be transilluminated, such as the earlobes and the fingers, and the feet for neonates. On the contrary, reflection-mode pulse oximetry ($S_pO_2^r$) uses LEDs and PDs on the same side of the tissue (Fig. 5.1), which allows for diverse sensing locations, such as the forehead, forearm, abdomen, and leg. Additionally, $S_pO_2^r$ provides two-dimensional (2D) oxygenation mapping capability with an array of sensors, whereas only single point measurements can be performed with $S_pO_2^t$.

Recent progress in flexible and stretchable sensors has made them extremely promising for medical sensing and diagnostics because they enhance SNR by establishing a conformal sensor-skin interface [184–186, 210–215]. Consequently, novel flexible sensors utilizing organic and inorganic optoelectronics for transmission and reflection-mode pulse oximetry show a higher SNR due to a reduction in ambient noise [4, 91, 193–195, 216, 217]. Lochner et al. demonstrated $S_pO_2^t$ on the finger using an all-organic optoelectronic sensor [4]. Yokota et al. demonstrated $S_pO_2^r$ on the fingertips using an ultraflexible photonic skin [193]. Kim et al. utilized a wireless optoelectronic system to monitor blood flow and tissue oxygenation [194]. The focus and features of recently reported flexible oximeters are summarized in Table 5.1. Noninvasive 2D oxygenation mapping capability has the potential to transform real-time and post-surgery management and monitoring of wounds, tissues, and organs [218–221]. An *in-vivo* spatial oxygenation mapping device can aid in assessing tissue damage and injury

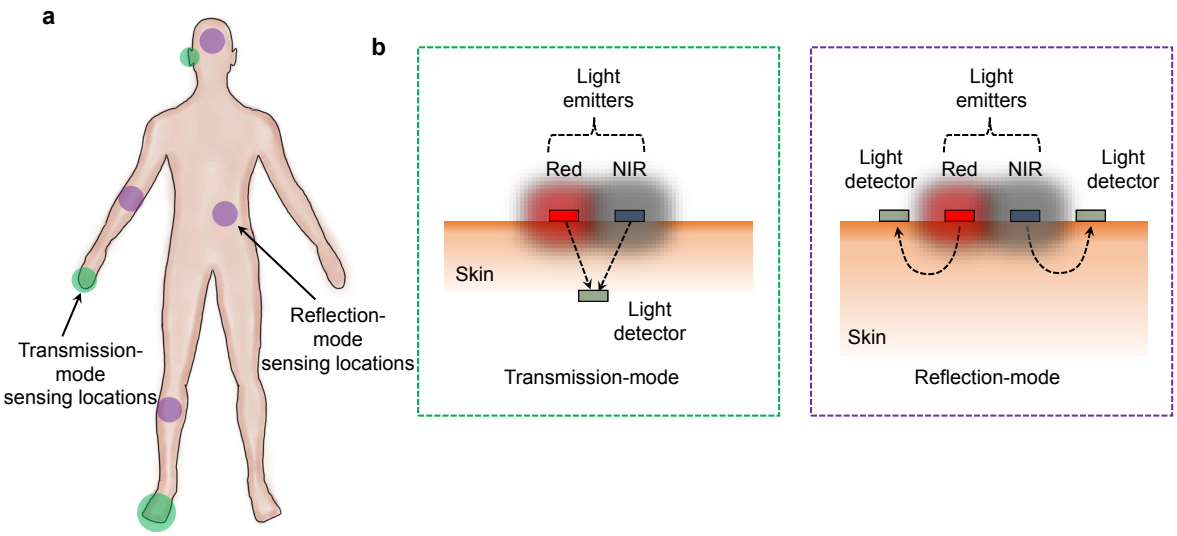

Figure 5.1. **Oximetry sensing locations and modes of oximetry**. (**a**) Sensing locations on the body. Transmission-mode pulse oximetry (SpO_2^t) sensing locations: fingers, earlobes, and feet (for neonates) are highlighted in green. SpO_2^t can be done on tissues that can be transilluminated. On the other hand, leveraging the sensor design, reflection-mode oximetry can be done at other locations such as the forehead, forearm, abdomen, leg, etc (highlighted in purple). (**b**) Two different modes of oximetry: transmission-mode and reflection-mode. In the transmission mode, the light emitters and the light detector are placed at the opposite end of the tissue, and the transmitted light is used for signal interpretation. In the reflection mode, the light emitters and the light detectors are placed on the same side of the tissue, and the reflected light is used for signal interpretation.

susceptibility. One such application scenario, where a flexible optoelectronic sensor array is used to map 2D oxygenation of a skin graft, is illustrated in Fig. 5.2a. To date, a flexible optoelectronic sensor capable of spatial mapping of oxygenation has not been demonstrated.

Here, we report a ROA, a flexible and printed electronic system realized by printing and integrating arrays of organic optoelectronics with conventional silicon integrated circuits for blood and tissue oximetry. The ROA is composed of 4 red and 4 NIR printed OLEDs and 8 OPDs (Fig. 5.2b and c). We use red (612 nm) and NIR (725 nm) OLEDs, where the molar absorptivity of HbO_2 and Hb are significantly different (Fig. 5.2d). The OPD and OLED arrays are fabricated on separate substrates and then assembled together to form the ROA (Fig. 5.3). Since organic optoelectronics and printing techniques such as blade coating and screen printing are utilized to fabricate the sensor on flexible plastic substrates, the sensor array is comfortable to wear and increases the SNR by establishing a high-fidelity sensor-skin interface. We implement the reflectance oximeter to measure $S_pO_2^r$ on the forehead with 1.1% mean error compared to commercial transmission-mode pulse oximeters. In the case of a medical shock, low blood perfusion, or organ injury, the pulsatile arterial blood signal of PPG becomes too

Table 5.1. The focus and features of recently reported flexible oximeters.

	Sensor material	Pulse oximetry	Reflectance oximetry	Operation wavelenghts (nm)			E - D spacing study / Spacing	Mechanical flexibility	Software control of AFE	Spatial mapping (2D array)
				Green	Red	NIR				
This work	**Organic**	**Ref. mode**	**Yes**	–	612	725	**Yes - 5 mm**	**Flexible**	**Yes**	**Yes**
Kim et al. [194]	Inorganic	**Ref. mode**	Rel. Meas.	–	625	950	No - 6 mm	**Flexible**	No	No
Yokota et al. [193]	**Organic**	**Ref. mode**	No	517	609	–	No	**Ultra-flexible**	No	No
Kim et al. [216]	Inorganic	**Ref. mode**	No	–	625	950	No - 2 mm	Flexible	No	No
Han et al. [195]	**Organic**	**Ref. mode**	No	520	611		No	Partial	**Yes**	No
Bansal et al. [91]	**Organic**	No	Rel. Meas.	–	610	700	**Yes - 20 mm**	**Flexible**	No	No
Lochner et al. [4]	**Organic**	Trans. mode	No	532	626	–	–	Partial	No	No

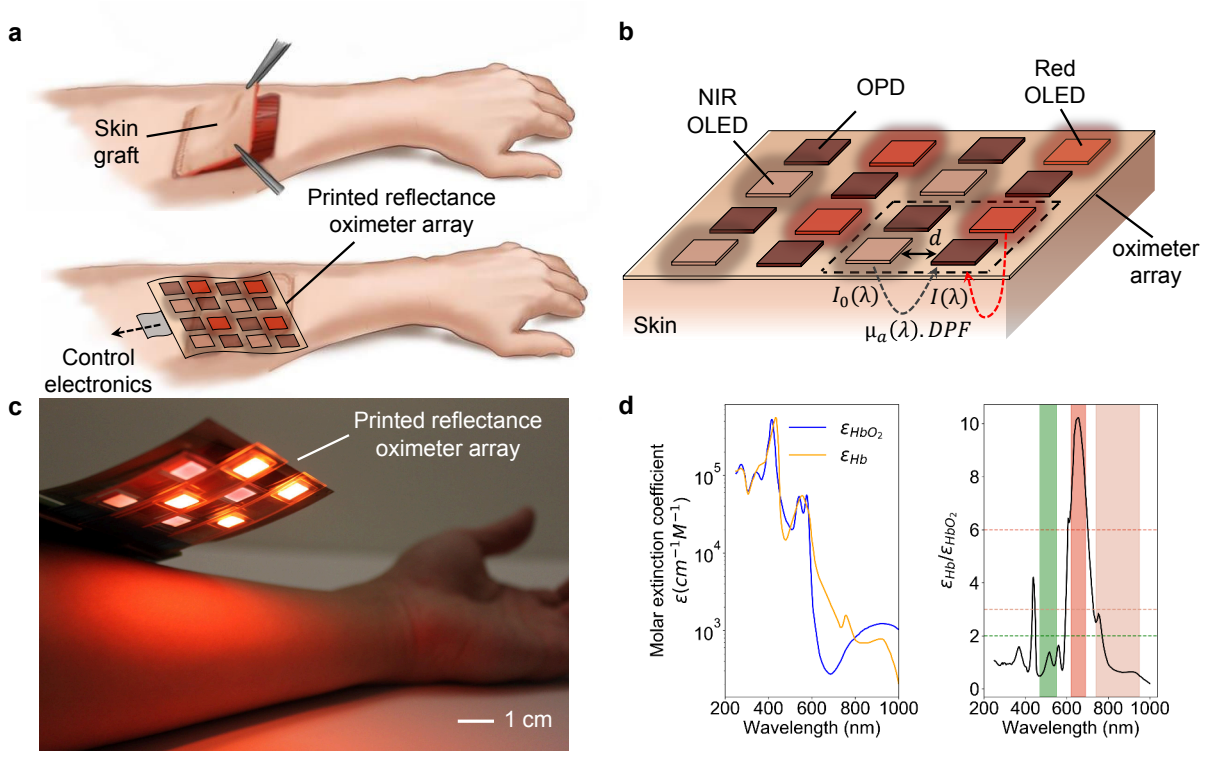

Figure 5.2. **Overview and operation of the printed ROA.** (**a**) Schematic of an application scenario of the ROA - 2D oxygenation mapping of a skin graft on the forearm. After surgery, the ROA is placed on the skin graft to map oxygenation of the reconstructed skin. (**b**) ROA sensor configuration. Red and NIR OLED arrays composed of 2×2 pixels each are placed side by side, where the pixels are arranged in a checkerboard pattern. The OPD array composed of 8 pixels is placed on top of the OLED arrays. The OLEDs are used as light emitters - $I_0(\lambda)$ is the incident light intensity. OPDs are used to collect the diffused reflected light, $I(\lambda)$. The OLEDs and OPDs are spaced at d cm (emitter-detector spacing). $\mu_a(\lambda)$ is the absorption coefficient of the sensed tissue, which depends on the specific absorption coefficients and concentration of HbO_2 and Hb, and DPF is the differential pathlength factor. (**c**) Photo of the ROA on top of a person's forearm. (**d**) The molar extinction coefficients of HbO_2 and Hb and the ratio of the molar extinction coefficients of Hb and HbO_2. Three regions are shown: (1) green ($\varepsilon_{Hb}/\varepsilon_{HbO_2} < 2$), (2) red ($\varepsilon_{Hb}/\varepsilon_{HbO_2} > 6$), and (3) NIR ($\varepsilon_{Hb}/\varepsilon_{HbO_2} < 3$). Either of the combinations of "red and green" or "red and NIR" can be used for oximetry.

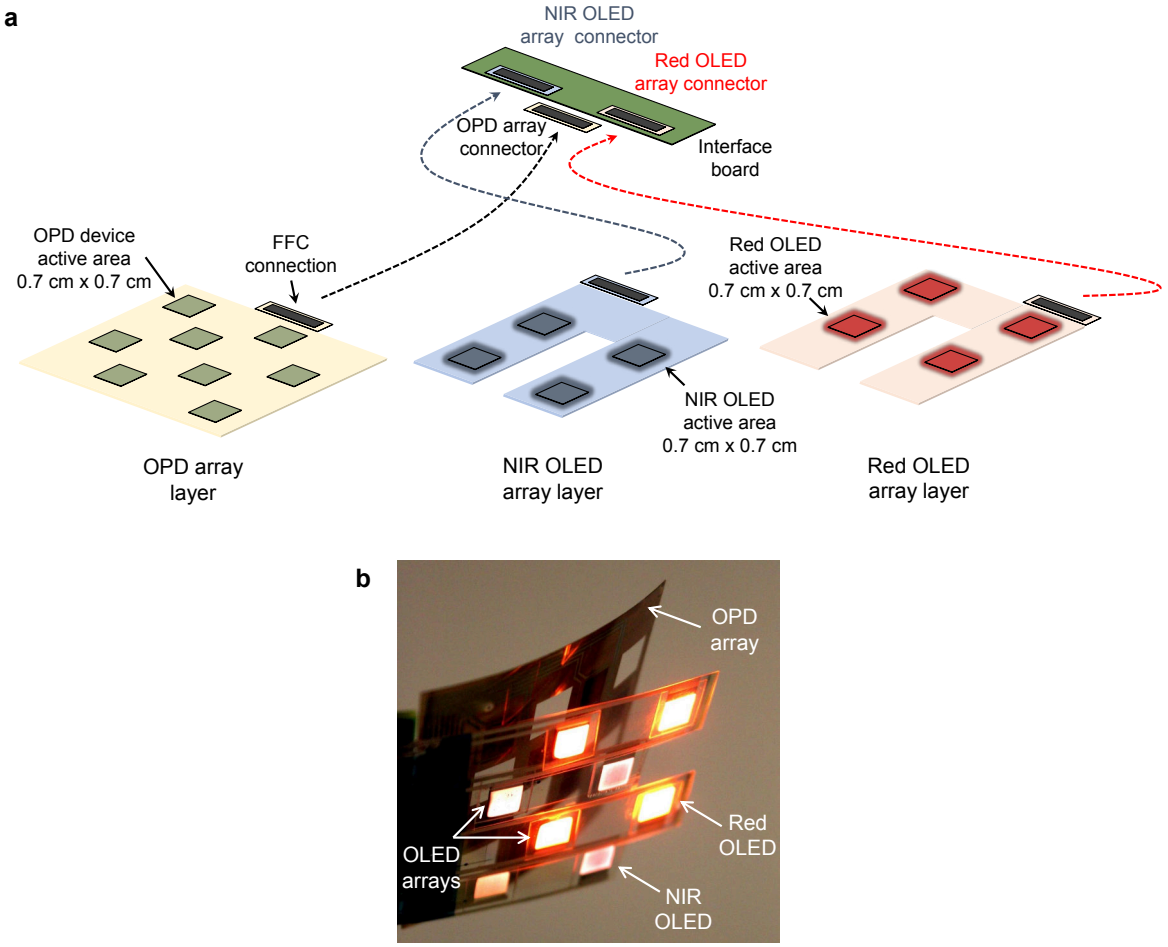

Figure 5.3. **Reflectance oximeter array assembly**. (**a**) Three layers of optoelectronics - (1) OPD array layer, (2) NIR OLED array layer, and (3) Red OLED array layer are fabricated on separate substrates. These layers are then stacked on one another: OPD array layer, NIR OLED array layer, and red OLED array layer, respectively and connected to the control electronics via flat flex cable (FFC) connectors. The layers are laser-cut so that one layer does not obstruct the other layer's optical path. With 0.7 × 0.7 cm active area for both OLEDs and OPDs, and 0.5 cm spacing between the OLEDs and OPDs, the dimension of the complete ROA is 4.3 cm in both length and width. (**b**) Photograph of the reflectance oximeter array assembly.

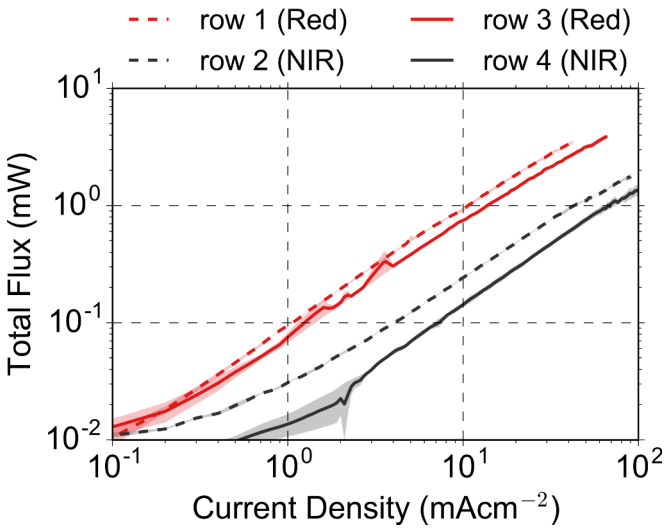

Figure 5.4. **Current Density vs. Total Flux for the OLEDs**. Total flux for OLEDs is shown according to the row position. At the operating condition of 10 $mAcm^{-2}$, the red OLEDs provide 0.9 mW of flux, while the NIR OLEDs provide 0.2 mW of flux.

weak to be used for pulse oximetry [222]. For the aforementioned cases and locations on the body with a low pulsatile PPG signal, we demonstrate a method to determine oxygenation in the absence of a pulsatile arterial blood signal. Also, the array implementation of the ROA allows us to create a 2D mapping of oxygenation of an area rather than a single point. By utilizing the array, we spatially map oxygenation values of a volunteer's forearm under normal and ischemic conditions. In addition, we discuss the sensor design, signal requirements, sensor fabrication, and the measurement methodology of the ROA. We believe the tools and devices developed in this work can be used for novel medical sensing applications such as *in-vivo* 2D mapping of oxygenation of tissues, wounds, skin grafts, or transplanted organs.

5.2 Analytical models for reflectance oximetry

Oximeters utilize the property that the molar extinction coefficients of HbO_2 and Hb vary appreciably over the visible and NIR spectrum (Fig. 5.2d). If two regions in the spectrum are chosen so that in one region, Hb has a higher absorptivity than HbO_2, and in the other region, Hb has a lower absorptivity than HbO_2, a ratiometric measurement can be performed to obtain the concentration of HbO_2 and Hb. Oxygen saturation in reflection-mode can be expressed as the ratio of the concentrations of oxygenated blood over the sum of the concentrations of oxygenated (C_{HbO_2}) and deoxygenated (C_{Hb}) blood.

$$SpO_2^r = \frac{C_{HbO_2}}{C_{HbO_2} + C_{Hb}} \tag{5.1}$$

In Fig. 5.2d, three regions are shown: (1) green ($\varepsilon_{Hb}/\varepsilon_{HbO_2} < 2$), (2) red ($\varepsilon_{Hb}/\varepsilon_{HbO_2} > 6$),

and (3) NIR ($\varepsilon_{Hb}/\varepsilon_{HbO_2} < 3$). Therefore, the combinations of "red and green" or "red and NIR" can be used for oximetry because of the contrast in molar extinction coefficients. Since the PPG signal magnitude for NIR is higher than the visible spectrum because light attenuation in tissue for NIR is much less than the visible spectrum, we use red and NIR OLEDs. In addition, the optical flux requirement for oximetry is less stringent for NIR than visible colors - the NIR OLEDs used in the ROA provide 0.2 mW of flux, compared to the 0.9 mW of flux of the red OLEDs at the operating condition of 10 mA cm^{-2} (Fig. 5.4). As discussed earlier, the operation of non-invasive reflectance oximetry can be grouped into two modes: (i) Reflection-mode pulse oximetry (SpO_2^r), when a pulsatile PPG signal is present, and (ii) Reflectance oximetry, when the pulsatile PPG signal is absent.

(i) Reflection-mode pulse oximetry (SpO_2^r)

In the case of SpO_2^r, a modified Beer-Lambert's law can be used to model the light propagation in tissue as shown in Fig. 5.2b and the equation below:

$$I(\lambda) = I_0(\lambda)e^{-\mu_a\cdot(\lambda)\cdot d\cdot DPF(\lambda)} \tag{5.2}$$

Where $I(\lambda)$ is the measured diffused reflected light intensity, $I_0(\lambda)$ is the incident light intensity, $\mu_a(\lambda)$ is the absorption coefficient of the sensed tissue, d is the distance between the light emitter and detector, and $DPF(\lambda)$ is the differential pathlength factor (DPF), which accounts for the multiple scattering of light in tissue.

The absorbance, A, can be defined as,

$$A(\lambda) = -\ln\frac{I(\lambda)}{I_0(\lambda)} = \mu_a(\lambda)\cdot d\cdot DPF(\lambda) \tag{5.3}$$

Now if we consider attenuation in skin, tissue, and bones – represented with the subscript dc, and attenuation in oxygenated and deoxygenated blood – represented with the subscripts HbO_2 and Hb, the following equations represent measured light intensities at diastole and systole of the cardiac cycle:

$$I_{high,dia}(\lambda) = I_0(\lambda)e^{-\mu_{a,dc}(\lambda)\cdot d_{dc}\cdot DPF(\lambda)}\cdot e^{-(\varepsilon_{HbO_2}(\lambda)C_{HbO_2}+\varepsilon_{Hb}(\lambda)C_{Hb})\cdot d_{dia}\cdot DPF(\lambda)} \tag{5.4}$$

$$I_{low,sys}(\lambda) = I_0(\lambda)e^{-\mu_{a,dc}(\lambda)\cdot d_{dc}\cdot DPF(\lambda)}\cdot e^{-(\varepsilon_{HbO_2}(\lambda)C_{HbO_2}+\varepsilon_{Hb}(\lambda)C_{Hb})\cdot d_{sys}\cdot DPF(\lambda)} \tag{5.5}$$

Light has to pass through an additional optical path Δd at systole, therefore $d_{sys} = d_{dia} + \Delta d$. Additionally, a normalization step ($I_{normalized} = I/I_{high,dia}$) is required to determine the normalized systolic intensity. Now Eq. 5.5 can be rewritten,

$$I_{norm}(\lambda) = \frac{I(\lambda)}{I_{high,dia}(\lambda)} \tag{5.6}$$

$$I_{norm,sys}(\lambda) = e^{-(\varepsilon_{HbO_2}(\lambda)C_{HbO_2}+\varepsilon_{Hb}(\lambda)C_{Hb})\cdot\Delta d\cdot DPF(\lambda)} \tag{5.7}$$

R_{os} is the ratio of absorbances in two different wavelengths,

$$R_{os} = \frac{A_{\lambda_1}}{A_{\lambda_2}} = \frac{\ln I_{norm,sys,\lambda_1}}{\ln I_{norm,sys,\lambda_2}} \tag{5.8}$$

Now, rearranging Eq. 5.1,

$$C_{HbO_2} = SpO_2^r(C_{HbO_2} + C_{Hb}) \tag{5.9}$$
$$C_{Hb} = (1 - SpO_2^r)(C_{HbO_2} + C_{Hb}) \tag{5.10}$$

After the normalizing step described in Eq. 5.6, absorbance, A, can be written as,

$$A(\lambda) = (\varepsilon_{HbO_2}(\lambda)C_{HbO_2} + \varepsilon_{Hb}(\lambda)C_{Hb}) \cdot \Delta d \cdot DPF(\lambda) \tag{5.11}$$

Inserting concentrations of oxygenated and deoxygenated blood,

$$A(\lambda) = (\varepsilon_{HbO_2}(\lambda)SpO_2^r(C_{HbO_2} + C_{Hb}) + \varepsilon_{Hb}(\lambda)(1 - SpO_2^r)(C_{HbO_2} + C_{Hb})) \cdot \Delta d \cdot DPF(\lambda) \tag{5.12}$$
$$= (\varepsilon_{HbO_2}(\lambda)SpO_2^r + \varepsilon_{Hb}(\lambda)(1 - SpO_2^r))(C_{HbO_2} + C_{Hb}) \cdot \Delta d \cdot DPF(\lambda) \tag{5.13}$$

The ratio of the absorbances at the two different wavelengths can be found using the following equation,

$$R_{os} = \frac{A_{\lambda_1}}{A_{\lambda_2}} = \frac{(\varepsilon_{\lambda_1,HbO_2}SpO_2^r + \varepsilon_{\lambda_1,Hb}(1 - SpO_2^r))(C_{HbO_2} + C_{Hb}) \cdot \Delta d \cdot DPF_{\lambda_1}}{(\varepsilon_{\lambda_2,HbO_2}SpO_2^r + \varepsilon_{\lambda_2,Hb}(1 - SpO_2^r))(C_{HbO_2} + C_{Hb}) \cdot \Delta d \cdot DPF_{\lambda_2}} \tag{5.14}$$
$$= \frac{A_{\lambda_1}}{A_{\lambda_2}} = \frac{(\varepsilon_{\lambda_1,HbO_2}SpO_2^r + \varepsilon_{\lambda_1,Hb}(1 - SpO_2^r)) \cdot DPF_{\lambda_1}}{(\varepsilon_{\lambda_2,HbO_2}SpO_2^r + \varepsilon_{\lambda_2,Hb}(1 - SpO_2^r)) \cdot DPF_{\lambda_2}} \tag{5.15}$$

Finally, oxygen saturation, SpO_2^r can be calculated using Eq. (5.16).

$$SpO_2^r(R'_{os}) = \frac{\varepsilon_{\lambda_1,Hb} - \varepsilon_{\lambda_2,Hb}R'_{os}}{(\varepsilon_{\lambda_1,Hb} - \varepsilon_{\lambda_1,HbO_2}) + (\varepsilon_{\lambda_2,HbO_2} - \varepsilon_{\lambda_2,Hb})R'_{os}} \tag{5.16}$$

Here, $\varepsilon_{\lambda,HbO_2}$ and $\varepsilon_{\lambda,Hb}$ are the molar extinction coefficient of HbO_2 and deoxyhemoglobin at each wavelength. $R'_{os} = \frac{R_{os}}{\frac{DPF_{\lambda_1}}{DPF_{\lambda_2}}}$, where $R_{os} = \frac{AC_{\lambda_1}/DC_{\lambda_1}}{AC_{\lambda_2}/DC_{\lambda_2}}$, is the ratio of pulsatile (ac) to stationary (dc) signals at the two wavelengths, and $DPF(\lambda)$ accounts for the multiple scattering in the reflection mode. Similar to the transmission-mode pulse oximetry, R'_{os} can be used with a calibration curve to provide SpO_2^r.

(ii) Reflectance oximetry

PPG signal from pulsatile arterial blood is essential for pulse oximetry. Therefore, in the case of low perfusion or in the absence of pulsatile arterial blood signal, pulse oximetry in both transmission and reflection mode cannot be performed. In these scenarios, Eq. 5.2 can be rewritten to measure the time-varying light intensity attenuation, $\Delta I(\lambda)$ in blood and tissue. Here, $\Delta\mu_a$ expresses the change in absorption during the measurement.

$$\Delta I(\lambda) = I_0(\lambda)e^{-\Delta\mu_a\cdot(\lambda)\cdot d\cdot DPF(\lambda)} \tag{5.17}$$

Now, $\Delta\mu_a(\lambda)$ can be expressed as the sum of the specific absorption coefficients $\varepsilon_{HbO_2}(\lambda)$, $\varepsilon_{Hb}(\lambda)$, of HbO_2 and Hb, times the concentrations, C_{HbO_2} and C_{Hb}:

$$\Delta\mu_a(\lambda) = \varepsilon_{HbO_2}(\lambda)\cdot\Delta C_{HbO_2} + \varepsilon_{Hb}(\lambda)\cdot\Delta C_{Hb} \tag{5.18}$$

Rewriting Eq. (5.17),

$$\varepsilon_{HbO_2}(\lambda)\cdot\Delta C_{HbO_2} + \varepsilon_{Hb}(\lambda)\cdot\Delta C_{Hb} = \frac{\ln\frac{I_0(\lambda)}{\Delta I(\lambda)}}{d\cdot DPF(\lambda)} \tag{5.19}$$

Since there are two wavelength channels, a system of linear equations can be established:

$$\begin{aligned}
\varepsilon_{HbO_2}(\lambda_1)\cdot\Delta C_{HbO_2} + \varepsilon_{Hb}(\lambda_1)\cdot\Delta C_{Hb} &= \frac{\ln\frac{I_0(\lambda_1)}{\Delta I(\lambda_1)}}{d\cdot DPF(\lambda_1)} \\
\varepsilon_{HbO_2}(\lambda_2)\cdot\Delta C_{HbO_2} + \varepsilon_{Hb}(\lambda_2)\cdot\Delta C_{Hb} &= \frac{\ln\frac{I_0(\lambda_2)}{\Delta I(\lambda_2)}}{d\cdot DPF(\lambda_2)} \\
\begin{bmatrix}\varepsilon_{HbO_2}(\lambda_1) & \varepsilon_{Hb}(\lambda_1)\\ \varepsilon_{HbO_2}(\lambda_2) & \varepsilon_{Hb}(\lambda_2)\end{bmatrix}\cdot\begin{bmatrix}\Delta C_{HbO_2}\\ \Delta C_{Hb}\end{bmatrix} &= \begin{bmatrix}\frac{\ln\frac{I_0(\lambda_1)}{\Delta I(\lambda_1)}}{d\cdot DPF(\lambda_1)}\\ \frac{\ln\frac{I_0(\lambda_2)}{\Delta I(\lambda_2)}}{d\cdot DPF(\lambda_2)}\end{bmatrix}
\end{aligned} \tag{5.20}$$

In Eq. 5.20, the molar extinction coefficients and $DPF(\lambda)$ can be obtained from the literature [183, 223]. Since change in the concentration of HbO_2 (ΔC_{HbO_2}) and Hb (ΔC_{Hb}) can be calculated, the change in oxygen saturation (ΔSO_2) can be determined for the transient measurement.

5.3 Reflectance oximeter design and placement on the body

Emitter-detector spacing (d) is an important design parameter for reflectance oximetry. To find the optimal d, we utilize a reflection-mode sensor board and measured the effect of

d on PPG ac and dc signals at the 8 locations of the body as depicted in Fig. 5.5a and b. The schematic of the sensor, containing three rings of four PDs spaced at 0.5, 0.8, and 1.1 cm away from the red and NIR LEDs at the center, is shown in Fig. 5.5c. Both ac and dc signal magnitude drops exponentially with increasing d. Fig. 5.5d and e show ac and dc signals for $d = 0.5, 0.8$, and $1.1\ cm$ recorded on the wrist. When placed at $d < 0.5cm$, the dc signal saturates the PD. This issue can be mitigated by putting an optical barrier between the LED and the PD to reduce direct coupling of light from the LED to the PD. While $d = 0.5cm$ provided us the best SNR, d can be different for other sensor designs. For a single pixel reflectance sensor, a minimum optical flux should be maintained to resolve the pulsatile PPG signal. We measured that this minimum flux is $\approx$ 0.2 mW for NIR and $\approx$ 0.6 mW for red light. Once the minimum optical flux is ensured, the emitter-detector spacing (d) can be reduced so that the light detected from the arteries (Signal) is distinguishable from the light scattered by the skin surface (Noise). Overall, the optical flux output of the LEDs, EQE of the PD, and active area of the LEDs and the PD influence the optimum d for a reflection-mode sensor. All of the mentioned strategies for reducing d can be utilized for scaling down the pixel-to-pixel spacing of the ROA, which will reduce the array size while providing an adequate signal level to quantify the light absorption in blood and tissue.

An approach similar to obtaining the optimal d is employed to find the optimal sensing location for SpO_2^r - we place the reflection-mode sensor at 8 different location of the body as depicted in Fig. 5.5a and b. Fig. 5.5a shows the pulsatile (ac) signal magnitude for red (Red_{ac}) and NIR (NIR_{ac}) channels with an emitter-detector spacing, $d = 0.5\ cm$. A high ac and a low dc signal are desirable for PPG measurements. The forehead provides the strongest peak-peak ac signal current - 20 nA for red and 60 nA for NIR, making it the most suitable location for SpO_2^r. The signal strength drops roughly by half on the wrists. Although we observed a clear degradation of the ac signal on the ribcage and the legs, heart rate and oxygenation values could be extracted from the measured signal. Similar to the ac signal, the forehead provides the highest dc signal, while the ribcage demonstrates the lowest dc signal magnitude. Fig. 5.6 provides the full dataset of the ac and dc measurements at the 8 sensing locations for 5 subjects. The reflectance sensor is mounted on the skin using an adhesive foam dressing. The sensor mounting photos are shown in Fig. 5.7.

5.4 OLED and OPD array fabrication and characterization

We printed the organic optoelectronics of the ROA on separate substrates and then assembled to form the sensor array. With 0.7 $\times$ 0.7 cm active area for both OLEDs and OPDs, and 0.5 cm spacing between the OLEDs and OPDs, the dimension of the complete ROA is 4.3 cm in both length and width. The OLED arrays are fabricated on top of PEN substrates with patterned ITO (Indium Tin Oxide) for contacts. A surface energy pattering (SEP) step is then performed that creates hydrophilic regions where PEDOT:PSS is blade coated, which is discussed in detail by Han et al. [195, 203] (Fig. 5.8a left panel). The interlayer and the emission layer are deposited using subsequent blade-coating steps (Fig. 5.8b left panel). Then, the dielectric and the silver traces are printed using a screen printer (Fig. 5.8c left panel). The purpose of printing the dielectric is to prevent shorts between the underlying ITO strips to the silver traces. Finally, thermal evaporation is used to deposit calcium/aluminum to finish the

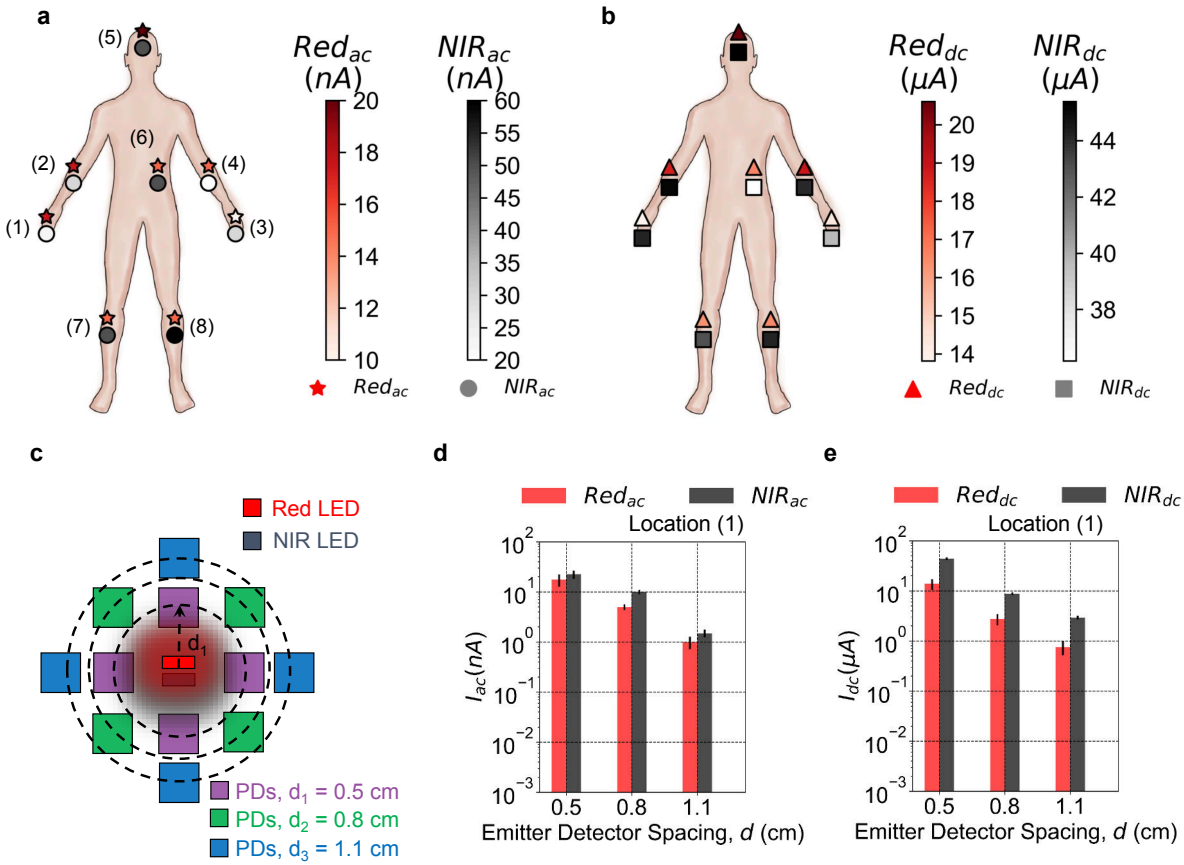

Figure 5.5. **Sensor placement and emitter-detector spacing (d) for reflectance oximetry**. (**a**) Pulsatile (ac) signal magnitude for red and NIR channels, where d = 0.5 cm. Sensor placement locations on the body are indexed from 1-8, while the fill color of the markers ($\star$ for red and $\circ$ for NIR) shows the signal current at each location. (**b**) Similar to **a**, stationary (dc) signal magnitude for red ($\triangle$) and NIR ($\square$) channels. (**c**) Schematic showing the setup for the emitter-detector spacing study - rings of four PDs spaced 0.5, 0.8, and 1.1 cm away from the LEDs at the center are used to obtain the signal. (**d-e**) ac and dc signal magnitudes recorded using the sensor board on the wrist. **d** shows the ac signal magnitude, and **e** shows the dc signal magnitude for d = 0.5, 0.8, and 1.1 cm. Data is collected from 5 subjects in 3 separate runs, error bars show the standard deviation of the data.

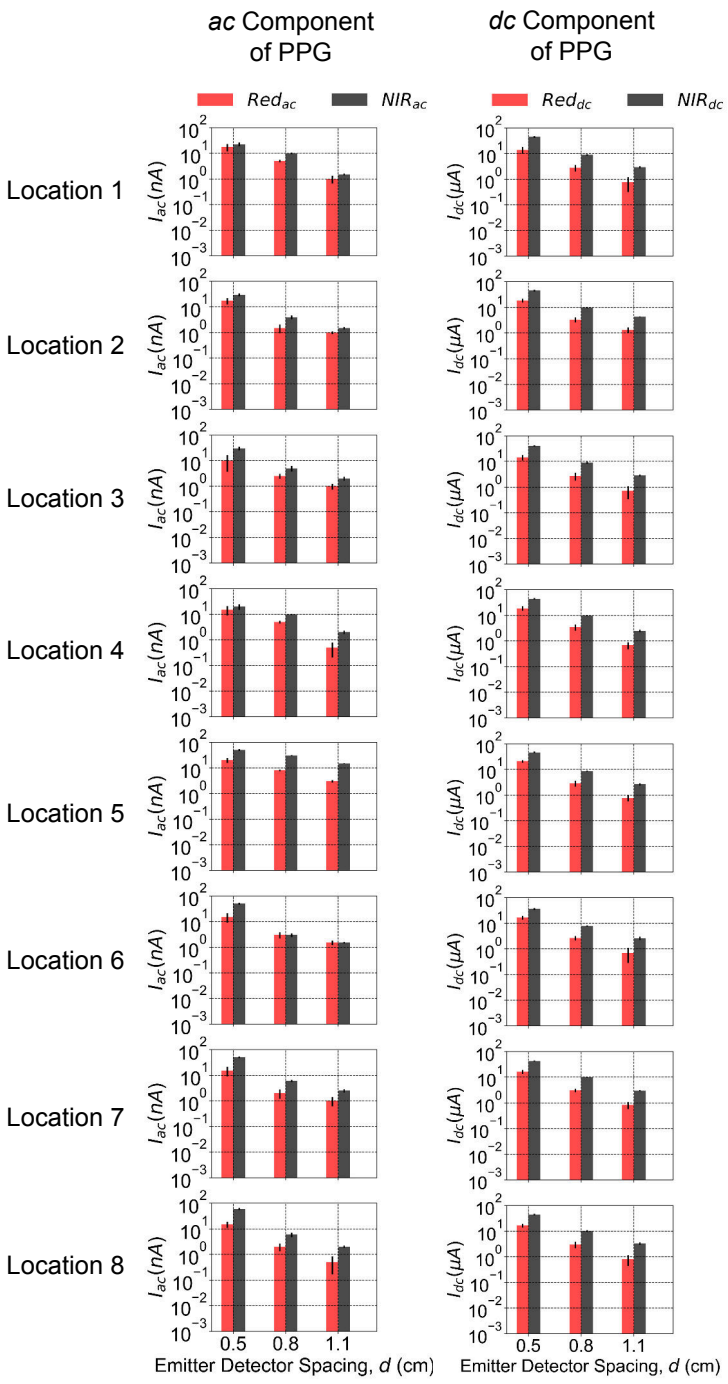

Figure 5.6. Emitter-detector spacing (d) study data. *ac* and *dc* signal magnitudes recorded using the sensor board at 8 locations as shown in Fig. 5.5**a** and **b**. The left panel shows the *ac* signal magnitudes, and the right panel shows the *dc* signal magnitudes for d = 0.5, 0.8, and 1.1 cm. Data is collected from 5 subjects in 3 separate runs, error bars show the standard deviation of the data.

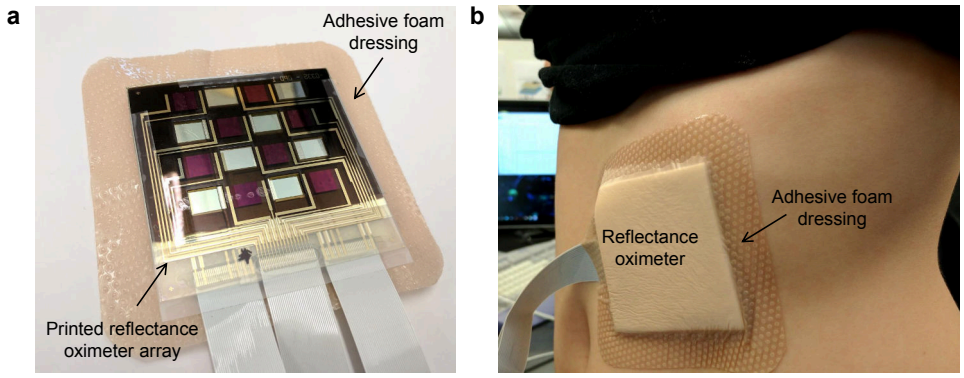

Figure 5.7. **The reflectance sensor mounting photos**. (**a**) Reflectance oximeter array assembly on an adhesive foam dressing. (**b**) The sensor is mounted on a volunteer's lower left rib cage.

fabrication of OLED arrays (Fig. 5.8d left panel). Each OLED pixel is encapsulated with UV curable epoxy and a plastic film. The OLED device stack is shown in Fig. 5.8g. The same process steps apply for both red and NIR OLEDs, only the active materials are different.

The OPD array is fabricated on a planarized PEN substrate. A PEDOT:PSS anode is blade coated using SEP technique as shown in Fig. 5.8a right panel. SEP process for OPDs is previously described by Pierre et al. [97, 100]. A patterned anode is necessary because, without patterning, a large parasitic capacitance is formed between the PEDOT:PSS layer and the body, which obscures the signal in noise. The active layer is then blade coated (Fig. 5.8b right panel). Next, silver traces are screen printed to connect the anodes and cathodes of each pixel to external circuitry as shown in Fig. 5.8c right panel. Finally, an aluminum cathode is evaporated to complete the device stack, which is shown in Fig. 5.8h.

The OPD and OLED arrays are shown in Fig. 5.9a and b, respectively. The OPD array comprises 8 OPD pixels, where each OPD row contains 2 OPD pixels. Brown markers from darker to lighter shades are used to label row 1-4 of the OPD array. The same markers are used to present the performance characteristics of the OPD pixels. As for the 2×2 red and NIR OLED arrays, row 1 and 3 contains the four red OLED pixels, and row 2 and 4 contains the four NIR OLED pixels. The ROA is formed by stacking the OLED and OPD arrays. The arrays are assembled as such that emitter-detector spacing of 0.5 cm is maintained.

The performance parameters of the OPD array are shown in Fig. 5.9c-e. The shade of brown lines indicates the row position of the pixels in the array as shown in Fig. 5.9a. An average EQE of 30% is observed across the absorption spectrum (Fig. 5.9d) with dark currents of a few nA cm^{-2} (Fig. 5.9c). The cutoff frequency is measured at over 5 kHz for OPDs as shown in Fig. 5.9e. Since the operation frequency of the pulse oximeters is generally less than 1 kHz, this bandwidth is sufficient for oximetry. The linear dynamic response of the OPDs is shown in Fig. 5.10.

The OLEDs show turn-on voltages at around 3V as designated in the J-V characteristics in Fig. 5.9f. The OLEDs are operated at 10 mA cm^{-2} for oximetry, where the red OLEDs provide 0.9 mW of flux, while the NIR OLEDs provide 0.2 mW of flux. The EQE values at

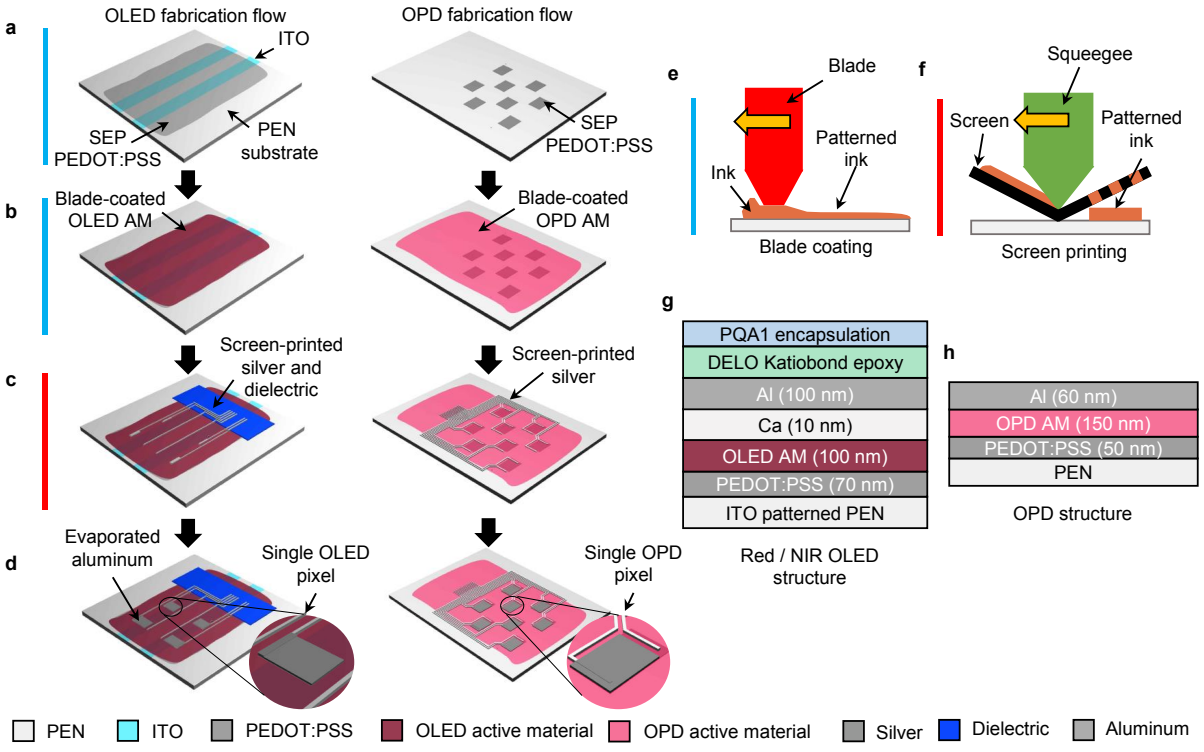

Figure 5.8. **Fabrication flow of the OLED and OPD arrays for the ROA**. (**a-d**) The OLED and OPD array fabrication steps are shown side by side. For the OLED array, only one color consisting of four pixels is shown for simplicity - the same fabrication steps are used for red and NIR OLEDs. For the OPD array, the complete array consists of 8 pixels. (**a**) PEDOT:PSS is blade-coated using surface energy pattering (SEP) on ITO patterned PEN for the OLEDs, and on a planarized PEN for the OPDs. (**b**) Active layers are blade-coated - brick color indicates OLED active material and pink color indicates OPD active material. (**c**) Silver traces are screen-printed on both OLEDs and OPDs. The OLEDs require an additional dielectric layer (blue) to prevent shorting of the anode to the cathode. (**d**) Aluminum cathode is evaporated, which defines the active area of the pixel. A zoomed-in view of the individual pixels is shown in the insets of **d**. (**e,f**) The deposition techniques: blade coating and screen printing are schematically shown and the color bars on the left side of the fabrication steps in **a-c** indicates the deposition technique used for that respective layer - sky blue for blade coating and red for screen printing. (**g,h**) Device structure of the OLED and the OPD, respectively.

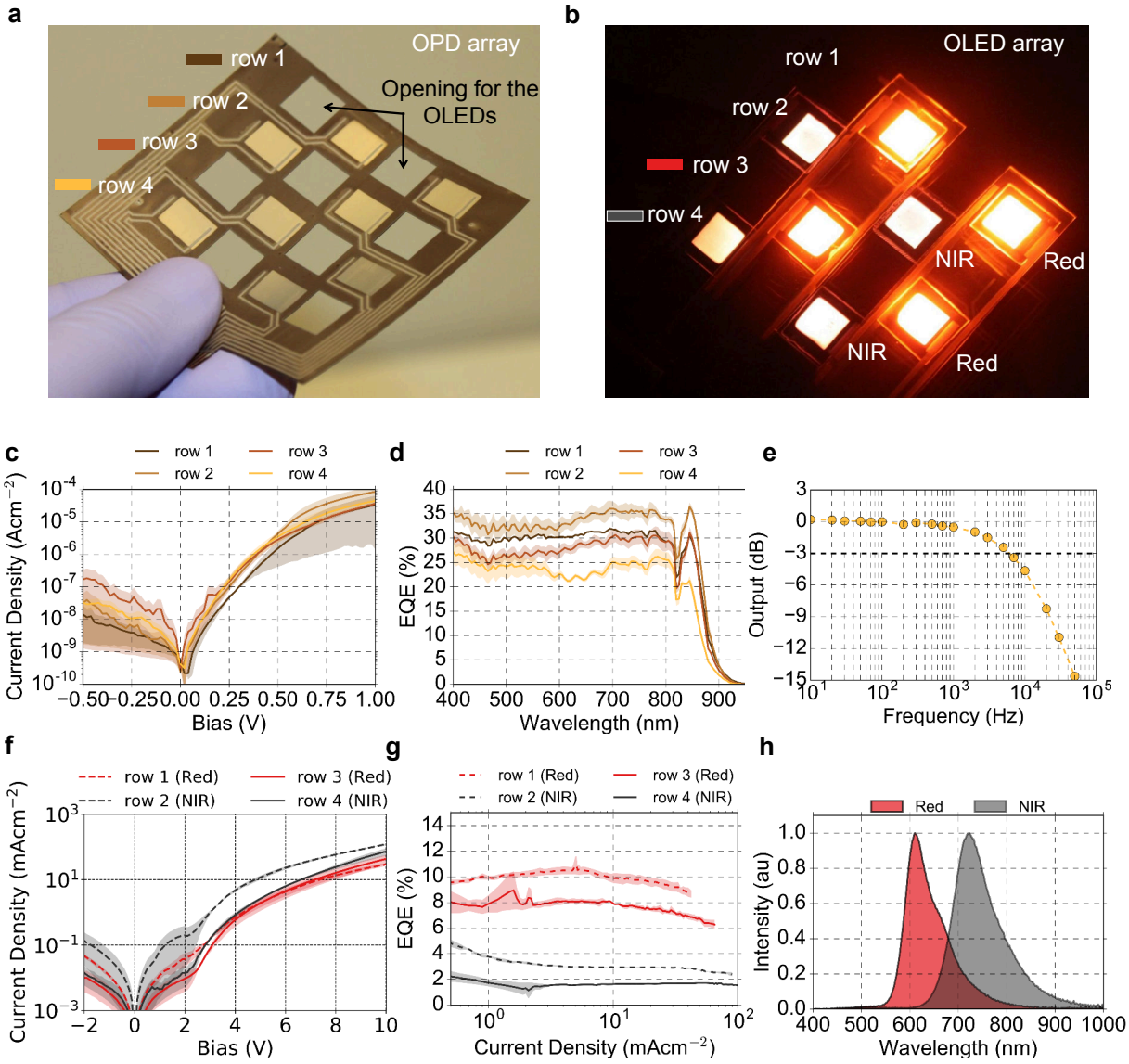

Figure 5.9. **Photographs and performance parameters of the OPD and OLED arrays**. (**a**) OPD array composed of 8 pixels - 2 pixels in each row. The rows are marked using different shades of brown markers, which represents the legends of performance data presented in the panels **c,d**. (**b**) Red and NIR OLED arrays - 2 × 2 red OLED array in row 1 and 3, and 2 × 2 NIR OLED array in row 2 and 4. The rows are marked using red and gray markers, which represents the legends of performance data presented in the panels **f,g**. (**c**) Current density vs voltage bias (*JV*) plot for the OPD array. Here each trace represents mean of the data in that row, while the shaded region shows the range of the data. (**d**) EQE of the OPD pixels in the array as denoted by row position in accordance with the colors in **a**. (**e**) The frequency response of an OPD pixel. The 3 dB cutoff is at over 5 kHz. (**f**) *JV* characteristics of the red and NIR OLED arrays as denoted by row position in accordance with the colors in **b**. (**g**) EQE as a function of current density of OLED arrays. (**h**) Emission spectra of the red and NIR OLED arrays.

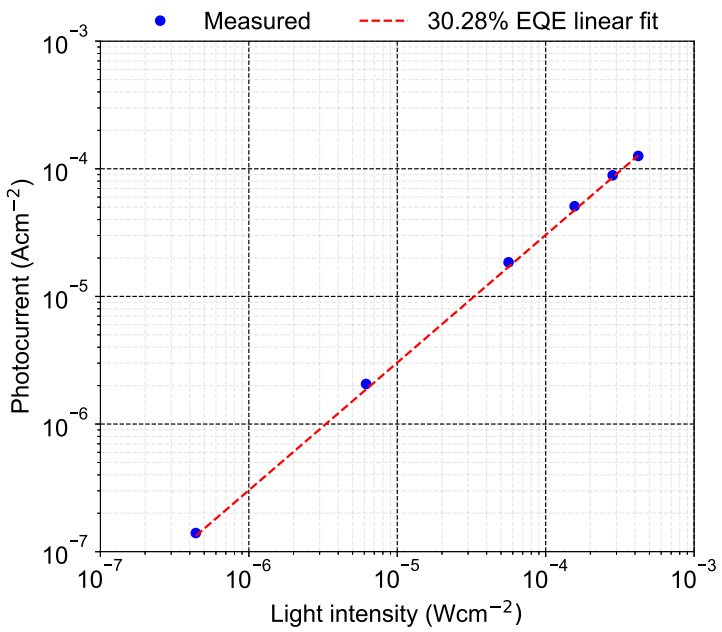

Figure 5.10. **Dynamic response of the OPDs at 680 nm, biased at -2V**.

operating conditions are ∼8-10% for red OLEDs and ∼2-3% for NIR OLEDs (Fig. 5.9g). The OLEDs demonstrate a change in performance parameters depending on the row position due to the decrease in active layer thickness in the blade coating direction, this variability can be mitigated by continuously feeding ink in front of the blade coater [195, 224]. The variability in the OLED and OPD performance can be accommodated by taking a calibration measurement before using the array for oximetry. The emission spectrum of the OLEDs is shown in Fig. 5.9h, where the red OLED has a peak emission at 612 nm and the NIR OLED has a peak emission at 725 nm.

5.5 System setup and single pixel reflection-mode pulse oximetry

The full system implementation requires addressing individual pixels of the oximeter. Therefore, the hardware and software for the ROA are designed to support both single pixel and array measurements (Fig. 5.11a). The printed ROA is interfaced with the control electronics using FFC (Flexible Flat Cable) connectors. Each pixel of the ROA is composed of one red and one NIR OLED, and two OPDs. Signals from the red and NIR channels are read out sequentially using the two OPDs, and the average of the OPDs are used for signal processing. Using this format, the 4×4 device (OLEDs and OPDs) array provides 3×3 readout pixels. The pixels are selected using analog switches. An AFE sequentially drives the OLEDs and reads out the OPD signal. The AFE is controlled by a microcontroller. Software control of the AFE allows flexibility in choosing OLED driving parameters, and also gives access to the variable OPD gain circuitry. A photograph of the control electronics is shown in Fig. 5.12, and the photographs of the software's Graphical User Interface (GUI) is shown in Fig. 5.13.

To test the reflectance oximeter in the single-pixel mode, we employed a setup where oxygenation of a volunteer can be changed by varying the oxygen concentration of the inhaled air (Fig. 5.11b). An altitude simulator is used to change the oxygen concentration of the air the volunteer breathes in via a facemask. Depending on the oxygen concentration of the air, the volunteer's oxygenation changes. This change in oxygenation is then picked up by a commercial finger probe sensor and using the reflection-mode sensor on the forehead. Calculated oxygen saturation using the commercial probe (SpO_2^t) and the reflectance probe (SpO_2^r) are shown in Fig. 5.11 c and d. We varied the inhaled oxygen concentration (O_2%) from 21% to 15% over a period of 8 min. During the first 30 s, a baseline oxygen concentration of 21% was set, then reduced to 17.5% at $t = 30\ s$; after keeping O_2% at 17.5% for 120 s, O_2% was further reduced to 15% at $t = 150\ s$ and was kept at that level for 150 s. Then O_2% was brought back to the baseline of 21%.

For the transmission-mode probe, oxygen saturation (SpO_2^t) drops from 96% to 90.5%, then comes back up to 94.5%. For the reflection-mode probe on the forehead, oxygen saturation (SpO_2^r) changes from 98% to 90.4%, then comes back up to 93.5%. We observed 1.1% mean error between SpO_2^t and SpO_2^r over the period of 8 min. The PPG signals for both transmission and reflection-mode probes at $240\ s < t < 245\ s$ are shown in Fig. 5.11e and f. PPG signal peaks and calculated heart rate from the PPG peaks show almost identical results for both SpO_2^t and SpO_2^r. Here, an error of 0.85% is seen between SpO_2^t and SpO_2^r, which falls within the 1-2% error margin that is inherent to pulse oximetry.

The pulse arrival time at the forehead and the fingers are different, the delay is on the order of 50 ms [225], which may slightly affect the pulse oxygenation calculations. Therefore, for a more direct comparison between the transmission and reflection-mode pulse oximetry, we collected pulse oximetry data in both transmission and reflection mode from the fingers of the same hand as shown in Fig. 5.14. In this experiment, the printed reflectance probe is placed under one finger and the commercial transmission-mode finger probe is worn on another finger. The commercial and reflectance finger probes provide almost identical SpO_2 variation with different concentrations of the inhaled oxygen. We observed a mean error of 0.41% between the commercial transmission-mode finger probe and the printed reflectance oximeter.

To investigate the temperature effects of the reflectance sensor, we operated the OLEDs of the device at different drive conditions and recorded the corresponding temperatures of the sensor on a volunteer's forearm (Fig. 5.15). We observed a negligible change in the temperature - the sensor temperature remained within $32 \pm 0.5^{\circ}C$ under the different OLED drive voltages from 0 to 9V. Moreover, to study the effect of an external pressure on the reflectance sensor, we collected reflection-mode signal with and without a 0.7 kPa external pressure (Fig. 5.16a). With the external pressure, the signal baseline changes for both red and NIR channels, and the PPG ac signal magnitude improves for the red channel (Fig. 5.16b) compared to PPG ac signal without an external pressure (Fig. 5.16c). However, for pulse oximetry calculations, the ratio of pulsatile (ac) to stationary (dc) signals at the two wavelengths is used, which remains almost same: $R'_{os} = 0.65$ with external pressure, and $R'_{os} = 0.67$ without external pressure.

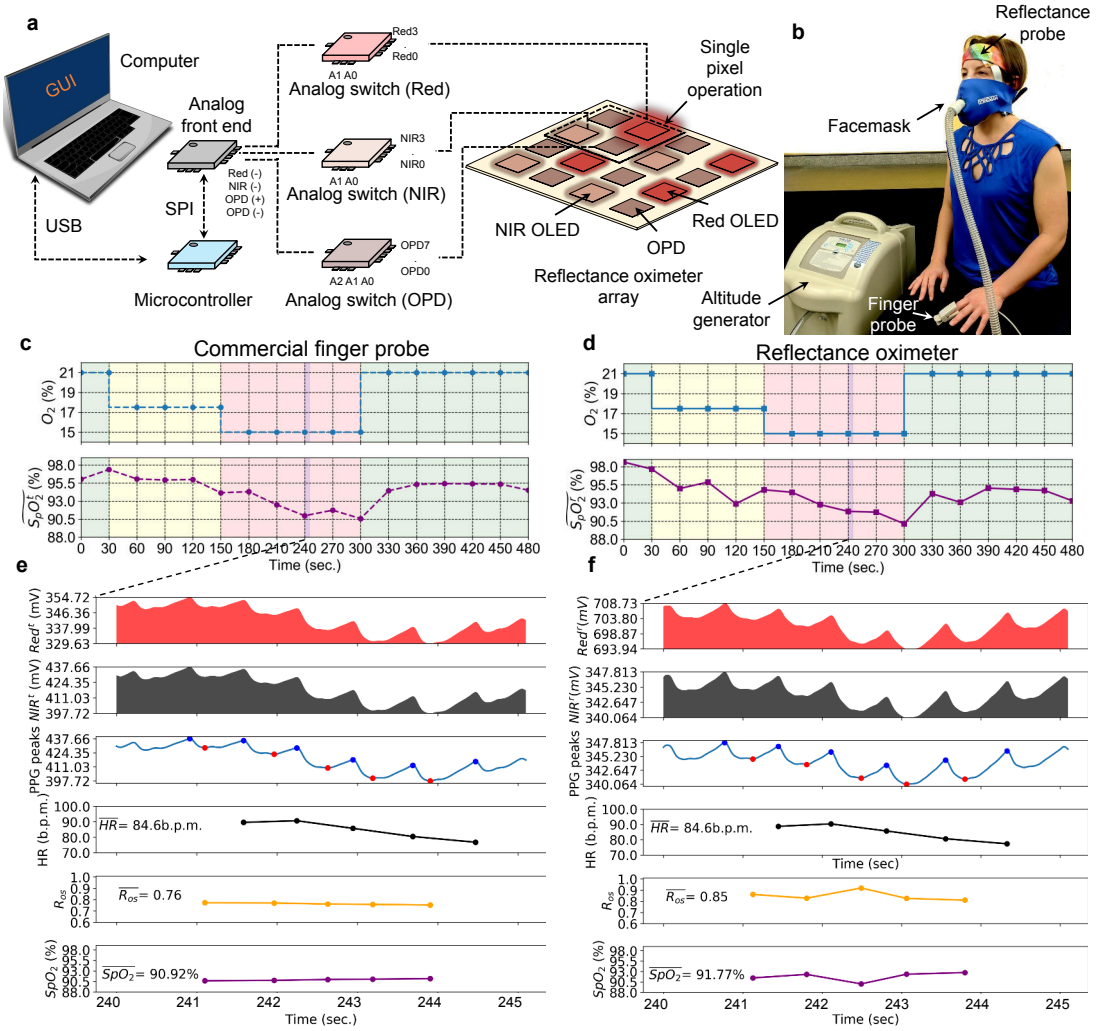

Figure 5.11. **System design for reflectance oximetry and single pixel reflection-mode pulse oximetry (SpO_2^r) results**. (**a**) Reflectance oximeter system design. Each pixel of the ROA (one red and one NIR OLED, and two OPDs) is connected to an AFE using analog switches, for both single pixel and array operation. The AFE drives the OLEDs and reads out the OPD signal. The AFE is controlled using an Arduino Due microcontroller. The data is then collected using a Universal Serial Bus (USB) interface, and processed using a custom software. (**b**) Setup for changing oxygen saturation of human volunteers - an altitude simulator varies the oxygen content of the air the volunteer breathes in via a facemask. The SpO_2 is recorded using a commercial probe on the finger and the reflectance oximeter on the forehead. (**c,d**) Results from the commercial transmission-mode finger probe oximeter (SpO_2^t) and the reflectance oximeter (SpO_2^r), where the oxygen concentration is changed from 21% to 15%. The oxygen concentration of the air (top panel, blue trace) and calculated oxygen saturation using SpO_2^t and SpO_2^r (bottom panel, purple trace). (**e,f**) Zoomed-in data for the SpO_2^t in **c** and SpO_2^r in **d** during 240 $s < t <$ 245 s show the red channel, NIR channel, PPG peaks, heart rate, R_{os}, and SpO_2.

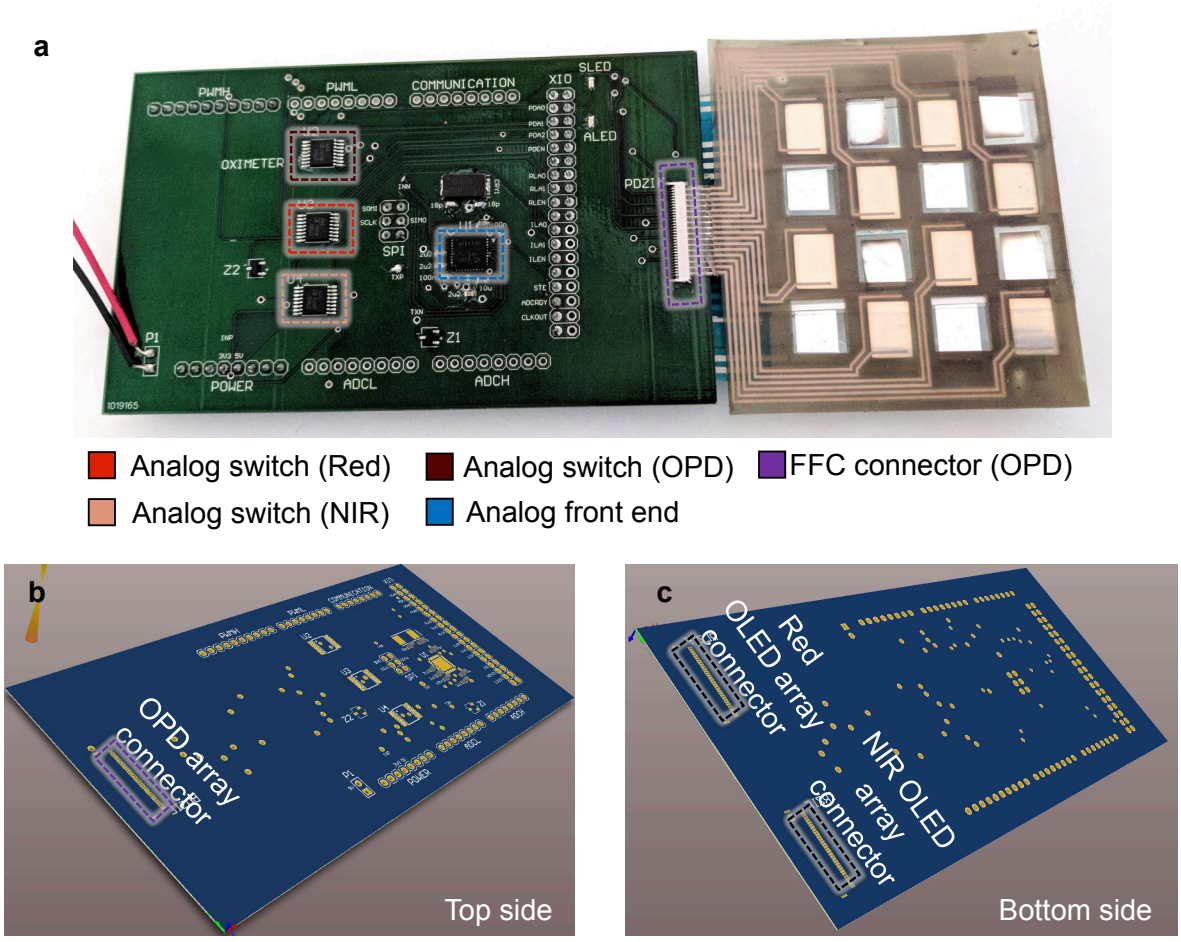

Figure 5.12. **Control electronics and connections of the oximeter system**. (**a**) The red and NIR OLED arrays and the OPD array are connected to the control electronics using FFC connectors. These connections then go through three analog switches to the analog front end (AFE 4490). The AFE connects to an Arduino Due microcontroller over Serial Peripheral Interface (SPI) bus, which provides software control of the oximeter array. (**b**) The top side of the control board, which shows the OPD array connector. (**c**) The bottom side of the control board, which shows the red and NIR OLED array connectors.

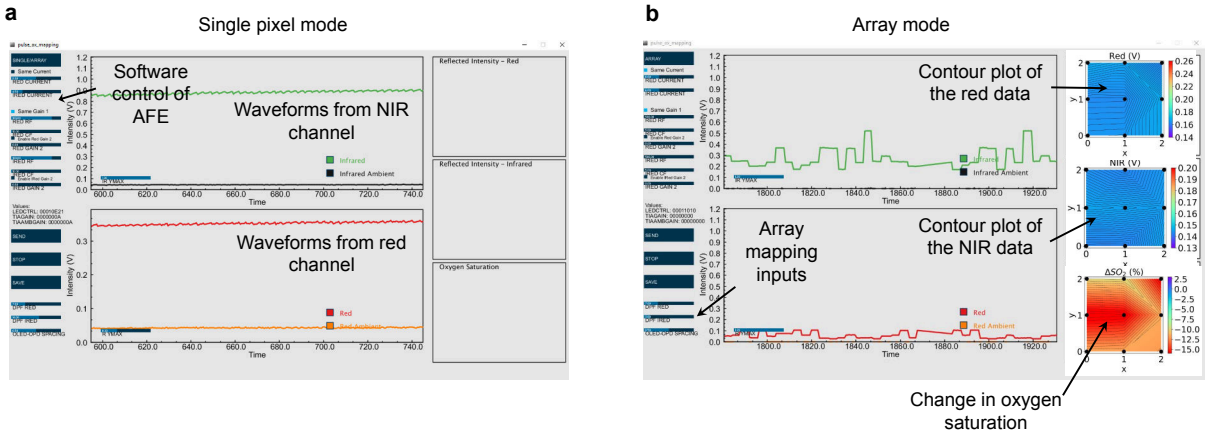

Figure 5.13. **Graphical User Interface (GUI) for processing and visualizing the oximeter data**. (**a**) In the single pixel mode, data is collected from a single red and NIR channel, and the waveforms and the background signals are plotted in real-time. The GUI allows software control to tune the OLED drive current and the OPD gain circuitry. (**b**) In the array mode, data is collected from the complete array. Contour maps of the red and NIR channels are plotted, in addition to the 2D map of change in oxygen saturation, ΔSO_2.

5.6 *in-vivo* 2D oxygen saturation monitoring

The pulse oximetry model is applicable when there is a pulsatile arterial blood signal. In the absence of a pulsatile arterial blood signal, we use the modified model (Eq. 5.20) to monitor local changes in tissue oxygenation of a volunteer's arm under normal and ischemic conditions. By restricting blood supply to the arm with a pressure cuff, we induce temporary ischemia to the arm by inflating the pressure cuff to 50 mmHg over the systolic pressure. We use the ROA to monitor the change in oxygen saturation (ΔSO_2) under normal condition and under pressure cuff induced ischemia with the ROA. The measurement setup is shown in Fig. 5.17a, where the ROA is used to measure ΔSO_2 on the forearm, while the pressure cuff is utilized to control blood supply to the arm, subsequently changing ΔSO_2 of the sensed tissue. Under normal condition, there is a pulsatile arterial blood signal (Fig. 5.18), which can be used with the pulse oximetry model. However, when the blood supply is restricted, only reflectance oximetry can be performed to measure ΔSO_2.

The 4×4 OLED and OPD devices provides 3×3 oximeter pixels. These pixels are indexed pixel 1 - 9, (Px1 - Px9) and are shown in Fig. 5.17b. A raster scan from Px1 to Px9 is used to collect data from the tissue. We used raster scanning speeds ranging from 100 ms Px^{-1} to 1 s Px^{-1}. Within this range, we did not observe analog-to-digital converter (ADC) channel leaking. For each pixel, samples are collected at 500 Hz, then the collected data is averaged. At a sampling rate faster than 50 ms Px^{-1}, we observed ADC channel leaking. The limiting factors to achieve a faster scanning speed are the 3 dB cut-off of the OPDs, the resistance and capacitance associated with each channel, and the settling time of the analog switches. After collecting data from all 9 pixels, 2D contour maps of red and NIR channels and ΔSO_2

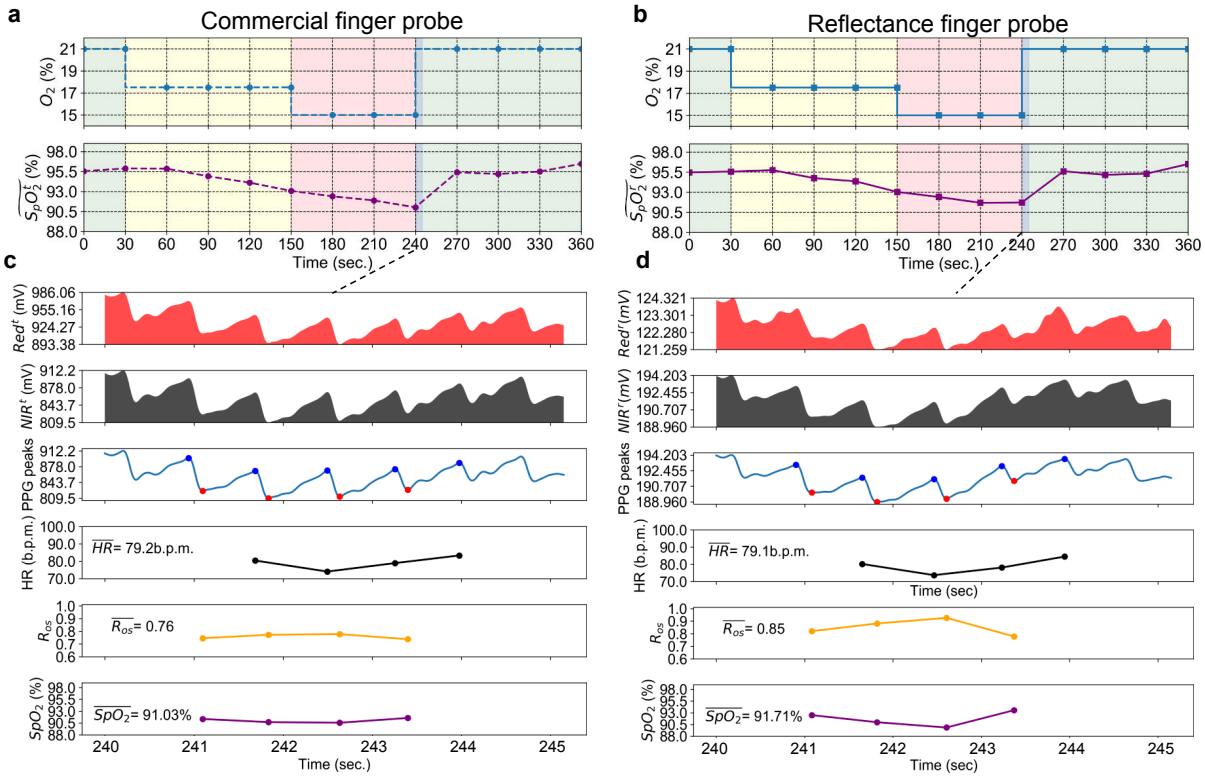

Figure 5.14. **Single pixel reflection-mode pulse oximetry (SpO_2^r) results for a commercial and the printed reflectance probe**. An altitude simulator varies the oxygen content of the air the volunteer breathes in via a facemask. The SpO_2 is recorded using a commercial probe on one finger and the reflectance oximeter on another finger of the same hand. (**a,b**) Results from the commercial transmission-mode finger probe oximeter (SpO_2^t) and the reflectance oximeter (SpO_2^r), where the oxygen concentration is changed from 21% to 15%. The oxygen concentration of the air (top panel, blue trace) and calculated oxygen saturation using SpO_2^t and SpO_2^r (bottom panel, purple trace). (**c,d**) Zoomed-in data for the SpO_2^t in **a** and SpO_2^r in **b** during 240 $s < t <$ 245 s show the red channel, NIR channel, PPG peaks, heart rate, R_{os}, and SpO_2.

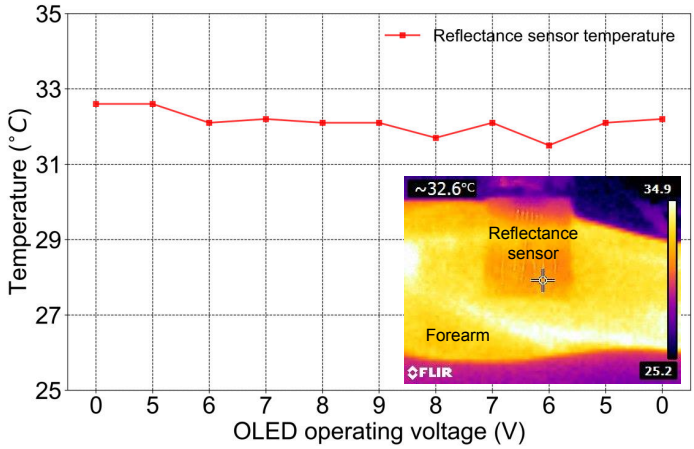

Figure 5.15. **Reflectance sensor temperatures on the forearm**. The sensor OLEDs are operated using drive voltages from 0 to 9V, and the temperature of the reflectance sensor is recorded. The temperature remains within $32 \pm 0.5^{\circ}C$ under the different drive conditions. The inset shows the thermal photo of the measurement setup. A thermal camera is used to record the sensor temperatures.

are created. For the *in-vivo* 2D oxygen saturation monitoring test, data during the first 30 s are collected under normal condition and is considered the baseline. The pressure cuff is then used to induce ischemia, therefore the signal amplitude in the red and NIR signal channels gradually decreases. Once the pressure is released the signals overshoot, going over the baseline (Fig. 5.17c). Fig. 5.17d shows the 2D maps of red and NIR signal channels, and ΔSO_2 during the test under normal condition ($t = 0\ s$), under ischemia ($t = 60, 120\ s$), and after releasing the pressure cuff ($t = 180, 240, 300\ s$). Since this is a transient measurement, ΔSO_2 remains at the baseline ($\Delta SO_2 = 0\%$) at $t = 0\ s$, under ischemia ΔSO_2 drops to -9.3 % at $t = 150\ s$, after releasing the pressure-cuff ΔSO_2 increases to +8.4 % at $t = 180\ s$, and comes back to the baseline +0.7 % at $t = 300\ s$. The 2D contours maps at every 30 s interval is provided in Fig. 5.19. We also monitored how different durations of ischemia effect ΔSO_2. Fig. 5.20 provides ΔSO_2 monitoring for 1, 2, and 2.5 min of ischemia, and ΔSO_2 drops to -6%, -9.5%, and -11.3%, respectively during these experiments. The results obtained in these tests agree with the studies reported in the literature on pressure cuff induced ischemia [219, 223, 226, 227].

In the 2D oxygenation mapping experiments, we monitored tissue oxygenation of the forearm with and without a pressure cuff induced ischemia. When blood supply to the arm is occluded using the pressure cuff, oxygenated blood cannot circulate to the forearm, which results in a drop in tissue oxygenation. We recorded this change in oxygenation using the ROA. With the status quo, i.e., transmission-mode pulse oximetry, this change in oxygenation cannot be observed, because when blood circulation is cut-off, the pulsatile arterial blood signal disappears, which is essential to calculate the pulse oxygenation using transmission-mode pulse oximetry. The ROA can measure the change in SO_2. Moreover, with the 2D mapping capability, the ROA can monitor oxygenation of an area rather than a single point, which is promising for monitoring oxygenation of tissues, wounds, and newly transplanted organs. In addition, the

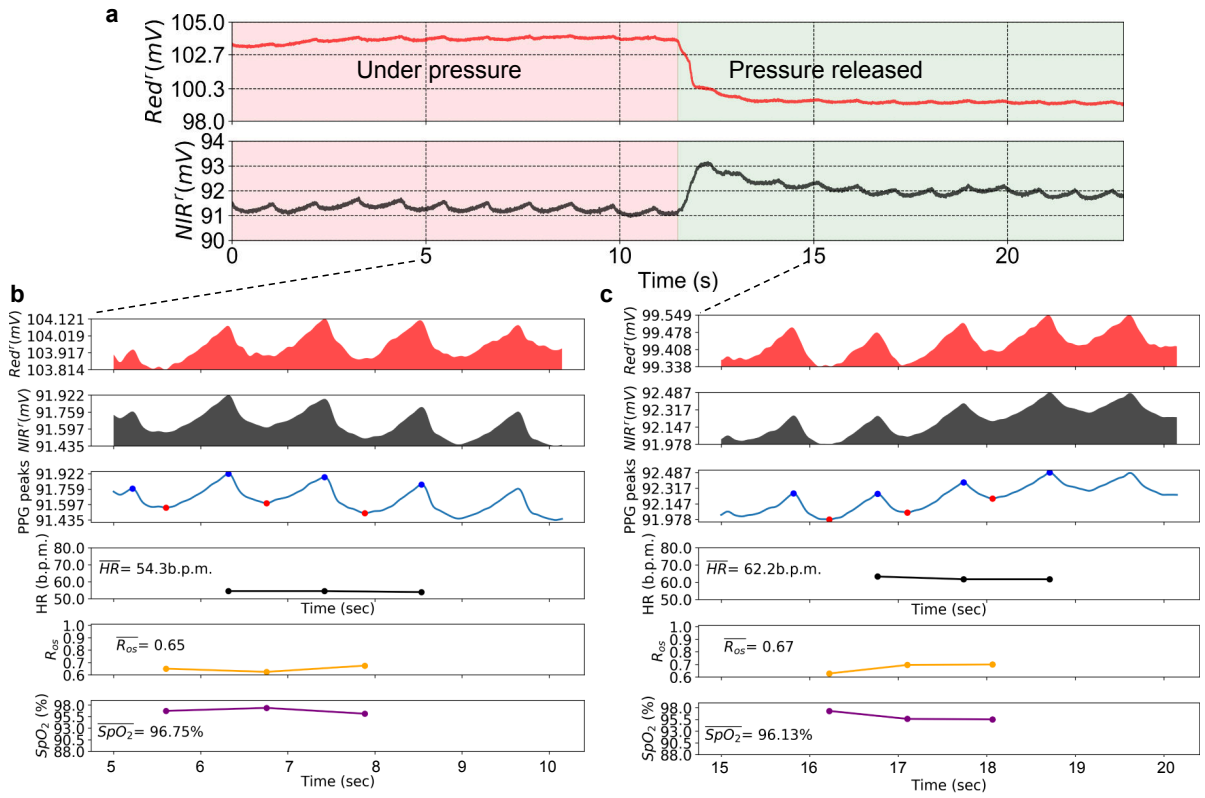

Figure 5.16. (**a**) Single pixel reflection-mode pulse oximetry (SpO_2^r) results with and without a 0.7 kPa external pressure. (**b,c**) Zoomed-in view of the PPG signal with and without the external pressure are shown in **b** and **c**, repectively.

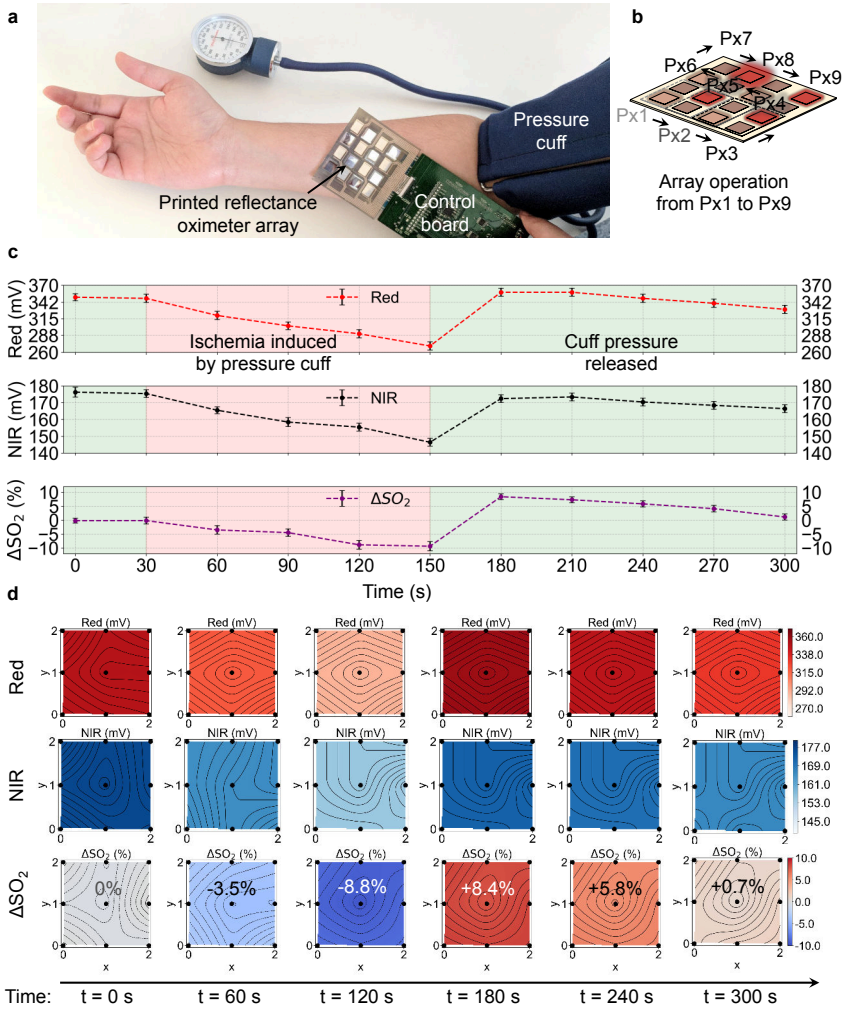

Figure 5.17. ***in-vivo* 2D oxygen saturation monitoring with the ROA**. (**a**) The ROA is placed on a volunteer's forearm to monitor the change in oxygen saturation (ΔSO_2). Blood supply to the forearm is controlled by a pressure cuff. The 4×4 devices of the ROA provide 3×3 oximeter pixels. (**b**) Oximeter pixel switching during the array operation. Each pixel is composed of one red and one NIR OLED, and two OPDs. A raster scan from Pixel1 (Px1) to Pixel9 (Px9) is used to collect data from the tissue. (**c**) ΔSO_2 for pressure-cuff induced ischemia for a recording of 300 s. Red, NIR, and ΔSO_2 data are shown using red, black, and purple dotted lines (dotted lines represent the means of the 9 oximeter pixels, errorbars represent the standard deviation of the data). Using the pressure cuff, blood supply to the forearm is occluded and restored. In the first 30 s, a baseline reading with no ischemia is taken. The pressure cuff is then inflated to 50 mmHg over the systolic pressure at $30\ s < t < 150\ s$, and released at $t = 150\ s$. ΔSO_2 varies from 0 % under normal condition to - 9.3 % ($t = 150\ s$) under ischemia, and to + 8.4 % ($t = 180\ s$) right after releasing the pressure cuff. (**d**) 2D contour maps of red, NIR, and ΔSO_2 under normal condition ($t = 0\ s$), under ischemia ($t = 60, 120s$), and after releasing the pressure cuff ($t = 180, 240, 300\ s$).

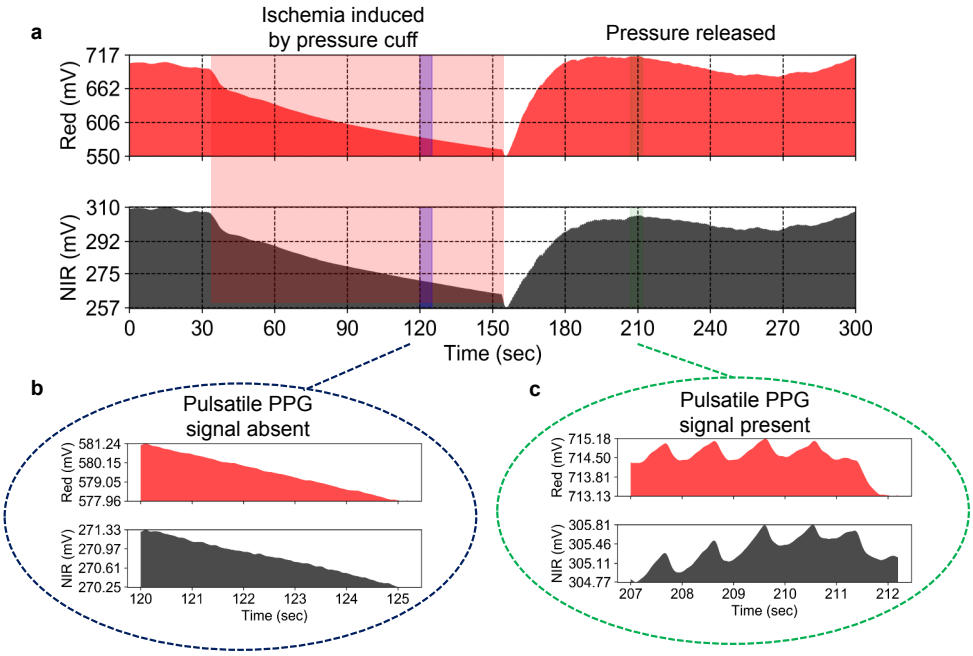

Figure 5.18. (**a**) Red and NIR channels of the ROA signal, before and after inducing the ischemia. (**b**) Zoomed-in view of the signal during the pressure cuff-induced ischemia. The pulsatile PPG signal is absent because the blood flood is occluded. Here, reflection-mode pulse oximetry cannot be performed. (**c**) Zoomed-in view of the signal after releasing the pressure. Now, the pulsatile PPG signal is present because the blood flow is restored. In this case, reflection-mode pulse oximetry can be performed.

ROA can be integrated to a multi-modal near-infrared spectroscopy (NIRS) system, where the ROA is interfaced to printed electromyography (EMG) or electrocardiography (ECG) electrodes on a flexible substrate to provide a lightweight, comfortable, and wearable sensor platform for muscle assessment during a persons normal activities and exercise [187, 228, 229].

5.7 Chapter conclusions

Existing techniques for measuring oxygen concentration in blood heavily rely on non-invasive transmission-mode pulse oximetry (SpO_2^t), which present two fundamental limitations: (1) Sensing locations are limited to only tissues that can be transilluminated; and (2) Only single point measurements can be performed with SpO_2^t due to the sensor configuration. Here, we presented a novel flexible and printed electronic system realized by printing and integrating arrays of organic optoelectronics for measuring oxygen saturation in the reflection mode. Two different modes of oximeter operations are discussed - (i) Reflection-mode pulse oximetry (SpO_2^r), when pulsatile PPG signal is present, and (ii) Reflectance oximetry, when pulsatile PPG signal is absent. Additionally, we explored the sensor design and placement of the sensor on the body. The forehead provided the strongest pulsatile signal. By using

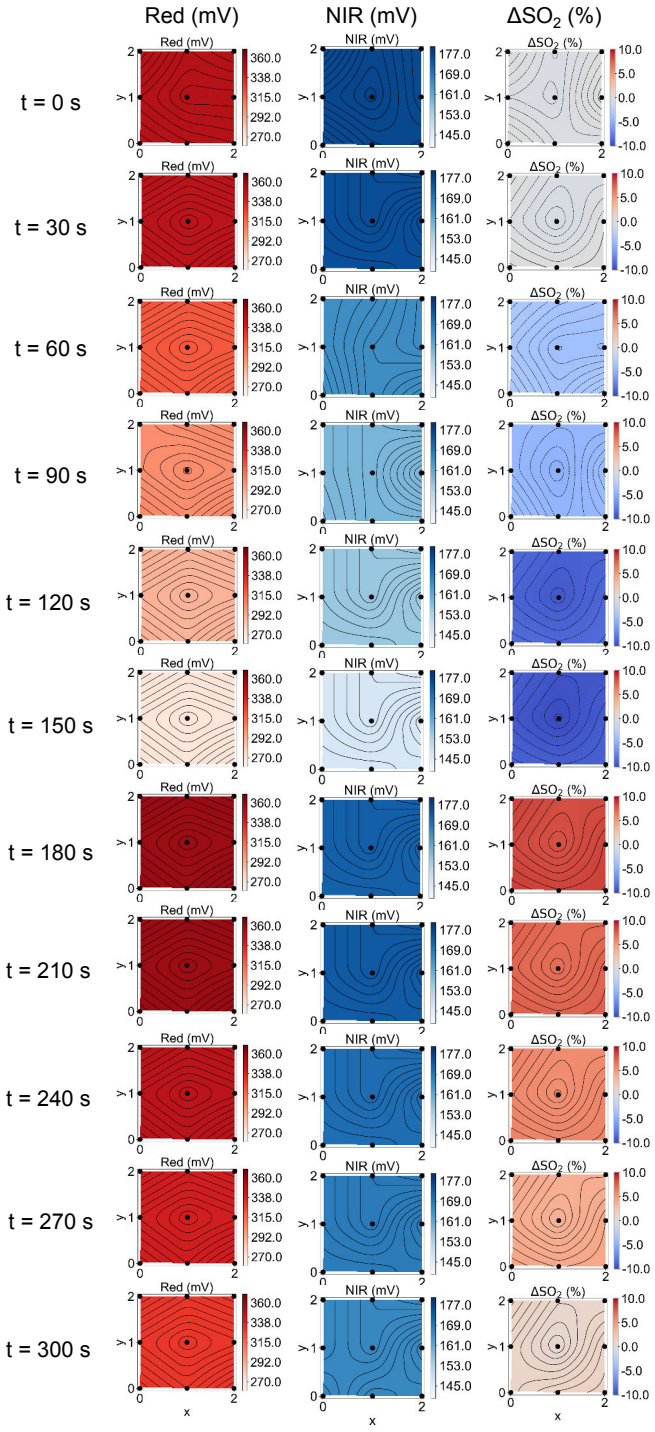

Figure 5.19. 2D contours maps of the red and NIR channels, and change in oxygen saturation (ΔSO_2) at every 30 *s* interval for the *in-vivo* oxygen saturation monitoring test with the ROA as shown in Fig. 5.17.

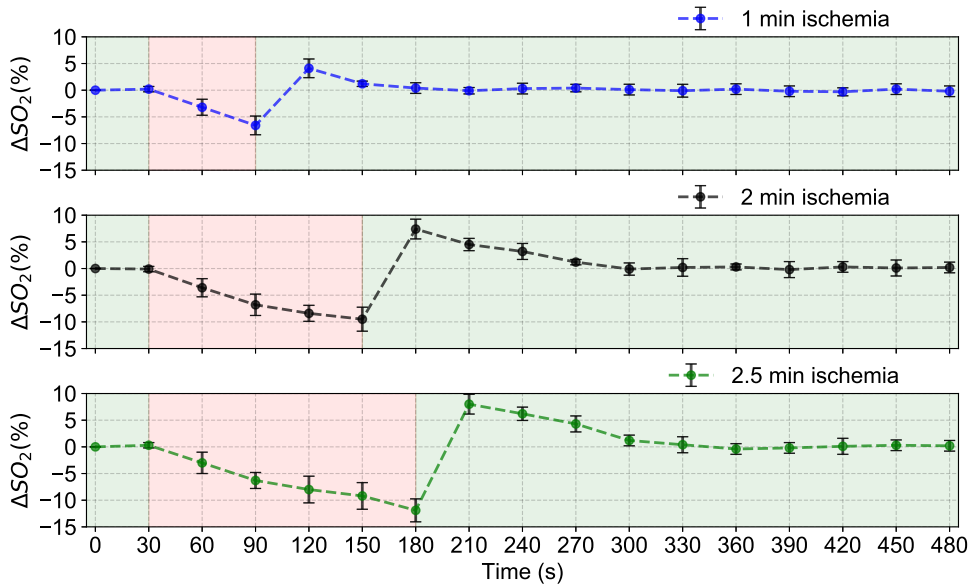

Figure 5.20. ΔSO_2 **monitoring for different durations of ischemia**. 1, 2, and 2.5 min of ischemia are used and ΔSO_2 drops to -6%, -9.5%, and -11.3%, respectively in these experiments.

the reflectance oximeter, we monitored oxygen saturation of a volunteer on the forehead and successfully measured SpO_2^r with a mean error of 1.1%. The use of an altitude simulator to change the oxygen concentration, verified the efficacy of the reflectance oximeter under both hypoxia and normal condition. Finally, in the case of a medical shock, low blood perfusion, or locations on the body with a low PPG signal, we demonstrate a method to determine ΔSO_2 in the absence of a pulsatile blood signal. The ROA was used to spatially map oxygenation values of a volunteer's forearm under normal and ischemic conditions.

Flexible organic and inorganic optoelectronics enhance the SNR of oximetry by reducing the ambient noise signal. Our demonstration of the ROA in this chapter increases the sensing locations of oximetry and enables measuring oxygenation in the absence of pulsatile arterial blood signal. Additionally, the use of printing techniques such as blade coating and screen printing to fabricate the sensor on flexible plastic substrates makes the sensor both comfortable to wear and efficient at extracting high-quality biosignal. This work presented an unprecedented level of control and integration in printed electronics systems. We hope that our demonstration of the flexible reflection oximeter array with 2D spatial mapping capability will encourage novel sensing schemes and aid in medical sensing applications such as 2D mapping of oxygenation in tissues, skin grafts, wounds, and transplanted organs.

Chapter 6

Flexible hybrid electronics for wearable health monitoring

6.1 Introduction

Recent thrust towards wearable medical devices has encouraged a myriad of efficient skin-like sensors that are extremely promising for medical monitoring [4, 193, 212, 230–233], imaging [234], and diagnostics [3]. The soft form factor of these sensors allows pristine sensor interfaces to human skin, which significantly improves the signal to noise ratio (SNR) [2, 3, 234]. In addition, these sensors are configurable and can be fabricated in different sizes and shapes that better suit the diverse human population. However, these flexible sensors require rigid silicon-based integrated circuits (ICs) for data processing and communications [185, 235, 236]. Although the tremendous mechanical mismatch of hard electronics and the soft human skin hinders sensor-skin interface, silicon ICs provide unparalleled computational performance at lower power than their flexible counterparts based on organic/inorganic materials [237, 238]. Therefore, a hybrid solution with soft and hard electronics is well-suited, where flexible devices are used for soft bio-interfaces and hard electronics are used for computation, signal processing, and data transmission.

Printed sensors provide a distinct advantage over rigid sensors at establishing high-fidelity sensor-skin interfaces due to their inherently flexible material systems and form factors. Hence, these sensors are suitable for monitoring vital signs as well as analytes in bodily fluids [1, 239, 240]. flexible hybrid electronics (FHE) is a fundamental enabling technology for system-level implementation of these novel printed and flexible devices. FHE bring together soft and hard electronics into a single platform, where the soft devices are used for conformal sensor interfaces, and the hard silicon-based devices provide the computational backbone and compatibility with existing electronic systems and standards. FHE comprise of (1) soft sensors or devices for conformal interfaces, (2) hard silicon-based electronics for computations, (3) interface between the soft and hard electronics, and (4) power source and driver electronics [192, 241]. Since soft electronics use novel materials and substrates, a multitude of deposition techniques is used for fabricating these devices [93, 122]. Therefore, integrating devices, sensors, and

ICs fabricated using vastly dissimilar technologies is a key challenge for FHE. Currently, a multi-substrate approach is employed where sensors and devices are fabricated on one flexible substrate, and then, interfaced to another flexible printed circuit board (FPCB) that hosts the rigid electronics using bonding or connectors [3, 155, 212]. This approach of interfacing is prone to alignment and interconnect issues.

In this chapter, we report on an interfacing scheme, where sensors are directly printed on flexible Kapton® PI substrate that hosts the silicon ICs and rigid passive components. This fabrication flow is completely compatible with the assembly-line process utilized in the FPCB industry and minimizes interconnect complexities. Using the direct printing technique, we fabricated a wearable sensor patch (WSP) capable of measuring electrocardiography (ECG) signal and skin temperature. The ECG electrodes are inkjet-printed using gold nanoparticle ink. Since the surface energy of bare Kapton® PI is not optimized for inkjet printing, we employed a series of surface energy modifications using tetrafluoromethane (CF_4) and oxygen (O_2) plasma. After the plasma treatments, we achieved high-quality inkjet-printed electrodes, which are reproducible and robust. The thermistor is fabricated by stencil-printing nickel oxide nanoparticle ink. The thermistor demonstrates temperature coefficient, $\alpha \approx$ -5.84 % K^{-1} and material constant, $\beta \approx$ 4330 K. Moreover, the sensitivity range of the thermistor covers the normal human skin temperature range of 32 - 37 °C. We anticipate that our results can be extended to a more sophisticated multi-sensor platform where sensors fabricated using other solution processable functional inks can be interfaced to hard electronics for health and performance monitoring, as well as internet of things (IoT) applications.

6.2 Wearable sensor patch

The WSP shown in Fig. 6.1a is an example of FHE implementation, where sensors fabricated by printing techniques are integrated with conventional electronics into a flexible sensing platform. The sensor patch utilizes a pair of printed gold electrodes for sensing ECG signal and a printed nickel oxide thermistor for measuring skin temperature. The complete system is being assembled on a Kapton® PI substrate, where the printed sensors are interfaced to silicon ICs, i.e., an analog front end (AFE), a Bluetooth System on Chip (SoC), and other hard passive components.

The WSP is being fabricated and assembled on a 5.08 cm x 5.08 cm, 50 μm thick flexible Kapton® PI substrate as shown in Fig. 6.1b. The area is chosen to balance the need for a large ECG electrode spacing with the desire to minimize area for wearer's comfort. This dimension ensures the wearable form factor and allows 4.7 cm spacing between the ECG electrodes. Gold printed electrodes are used for acquiring the ECG signal. An AFE amplifies and filters the signal before sending to a host computer via Bluetooth SoC. Filtering and amplification can also be done using discrete components in conjunction with the Bluetooth SoC, however, the AFE approach reduces the number of required discrete components. The skin temperature is recorded using a stencil-printed nickel oxide, negative temperature coefficient (NTC) thermistor. The thermistor is used in a voltage divider network, where the voltage across the thermistor varies according to the temperature, which is digitized and recorded using an analog to digital converter (ADC) of the Bluetooth SoC. The complete system is powered by a coin cell battery of 220 mAh capacity. While flexible thin-film batteries were considered, the capac-

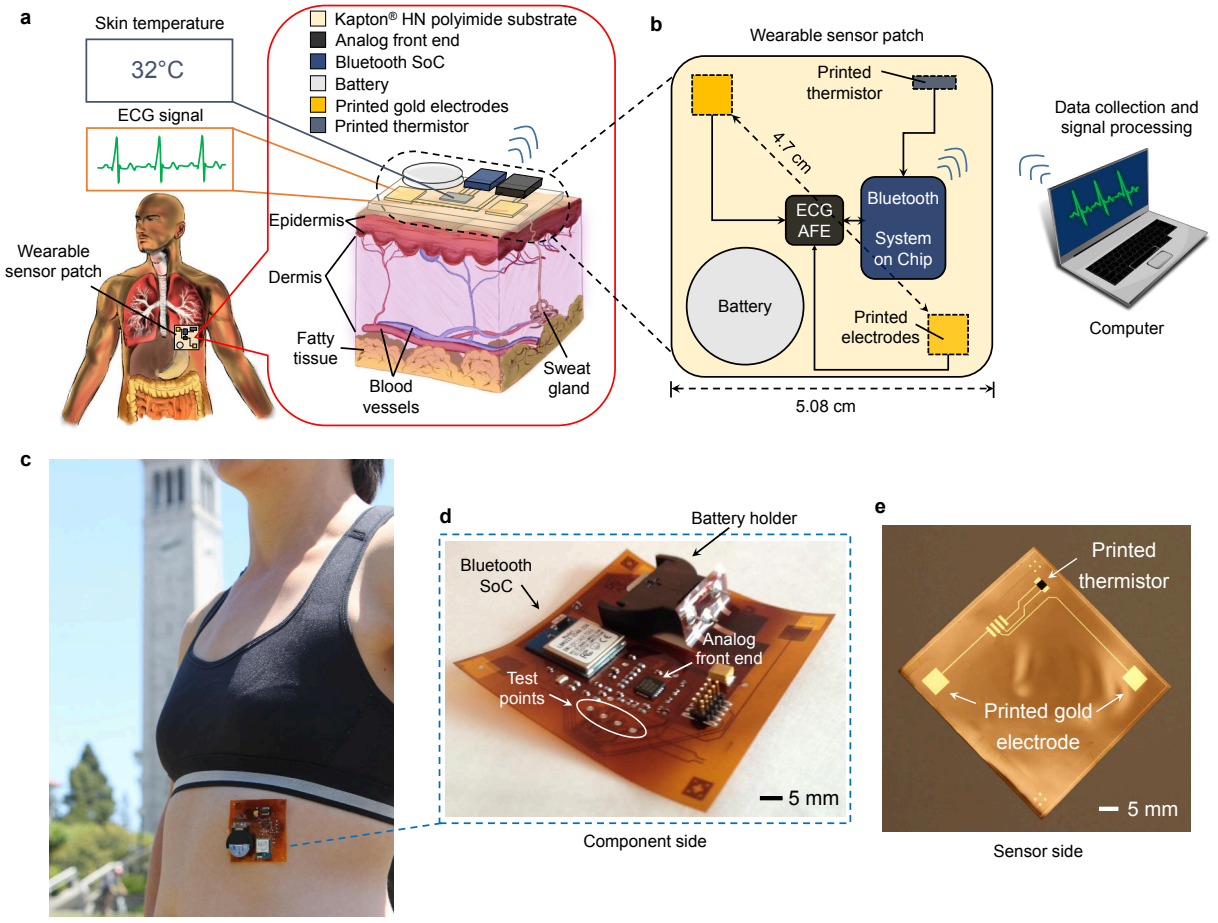

Figure 6.1. **Proposed overview and system design of the wearable sensor patch (WSP) enabled by flexible hybrid electronics.** (**a**) Schematic of the sensor patch placed on a subject's lower left rib cage. Skin temperature is read using a stencil-printed thermistor while the electrocardiography (ECG) signal is acquired using inkjet-printed gold electrodes. The electrodes and the thermistor are interfaced to silicon-based ICs for data acquisition, processing, and transmission. (**b**) System design of the sensor patch. The ECG signal is obtained using an analog front end (AFE). The data is then processed and transmitted using a Bluetooth System on Chip (SoC) to a host computer. The thermistor data is read using a voltage divider network, where the voltage drop across the thermistor is sensed using an analog to digital converter (ADC) of the SoC. After data transmission, both ECG and thermistor data are displayed on a host computer. (**c**) Photograph of the WSP mounted on a person's lower left rib cage. The sensor side faces down towards the skin, and the component side faces up. (**d**) Photograph of the component side of the patch. The battery holder, the Bluetooth SoC, AFE, and the test points are shown. (**e**) Photograph of the sensor side of the patch (before component assembly). The printed gold ECG electrodes and the thermistor are shown.

ity requirement of the battery proved challenging for the thin-film batteries. Additionally, the patch is intended for disposable use, therefore, a coin cell battery was chosen over rechargeable thin-film batteries.

6.3 Single-substrate integration by direct printing of sensors on Kapton PI substrate

The substrates conventionally used in printed electronics such as polyethylene terephthalate (PET) and polyethylene naphthalate (PEN) deform and melt at temperatures over 200 °C. However, FPCB process flow commonly requires processing temperature over 200 °C for electronic component assembly via solder reflow. Consequently, for integrating printed electronics to FPCBs, printed devices are typically processed on PET or PEN, and then attached to FPCBs using a low-temperature bonding process or by connectors. On the contrary, we employ a single-substrate approach and fabricate the WSP on a single Kapton® PI substrate with the printed sensors on one side and attach the electronic components on the other side. This approach simplifies the manufacturing protocol by using a single substrate, and obviates the bonding process that may not form a robust connection in the final device.

6.4 Inkjet-printed gold ECG electrodes

The surface energy of Kapton® PI that is used for FPCB is significantly higher than what is required for inkjet printing. Therefore, inkjet printing on Kapton® PI is challenging. During inkjet printing, the nanoparticle ink experiences both cohesion and adhesion forces on the substrate. These forces equilibrate and the contact angle (θ) between the droplet and the substrate provides an inverse relation to the surface energy of the substrate. To obtain reliable inkjet-printed features, appropriate surface energy is crucial.

Untreated Kapton® PI shows a contact angle in the range of 45-55° (Fig. 6.2a). Contact angles lower than 70° causes the ink to spread as schematically shown in the printing tests of Fig. 6.2a - the printed ink spreads at impact, and continues to spread further as shown in the micrographs at t = 0 and 60 s. To bring the surface energy down to a printable range, we treated the Kapton® PI surface with CF_4 plasma. This treatment lowers the Kapton® PI surface energy substantially as evidenced by the large increase in contact angle to over 90° (Fig. 6.2b). However, with this low surface energy, ink-substrate adhesion forces are weaker than particle-particle cohesive forces. Hence, printed ink rapidly dewets from the surface as shown schematically and with optical micrographs in Fig. 6.2b. A pad and an angled trace are printed, but the ink pulls back from the initial drop location and results in broken printed circuit traces. Therefore, forming the intended features becomes increasingly difficult. A second treatment step with an O_2 plasma increases surface energy to bring the contact angle into the printable zone. Fig. 6.2c shows contact angles in the range of 80 - 88°. The surface energy associated with this contact angle has been found to be ideal for inkjet printing our gold nanoparticle ink. We obtained high-quality printed pads and traces with complex bends using the CF_4 and O_2 plasma treatments. The prints show good feature definitions, and these optimization steps are used for printing the ECG electrodes of the WSP. While it is possible to use only CF_4 plasma for

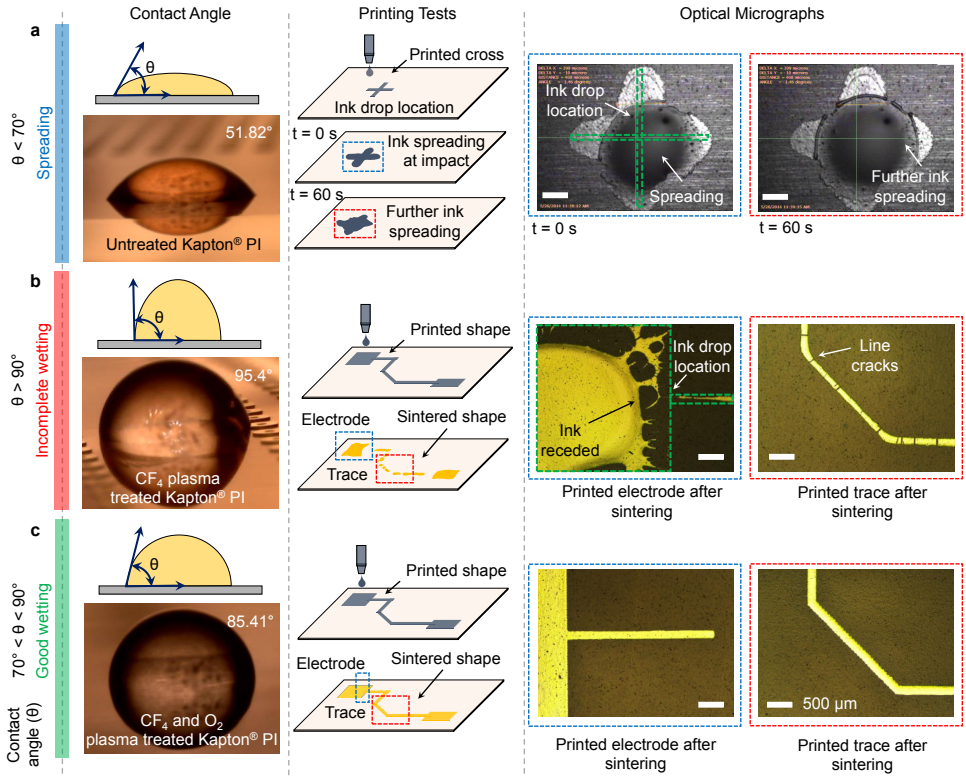

Figure 6.2. **Surface energy optimizations for inkjet printing functional inks on Kapton® PI substrate.** Blue, red, and green colored rows show deionized (DI) water contact angle (θ) schematically and obtained from a goniometer, inkjet printing trials, and optical micrographs of printed structures on Kapton® PI surfaces that show ink spreading, incomplete wetting, and good wetting, respectively. The scale bars in the micrographs represent 500 μm. (**a**) Printing tests on untreated Kapton® PI that shows uncontrolled spreading of ink. The high surface energy of untreated Kapton® PI generates a contact angle less than 70 °, which results in ink spreading as shown in the schematic of the "printed cross" and spreading of the ink (middle panel of **a**). The cross does not hold shape at impact, and the ink spreads further as shown by the micrograph that is taken 60 s after printing (right panel of **a**). (**b**) Printing tests on CF_4 plasma treated Kapton® PI that shows incomplete wetting of printed ink. To reduce the surface energy, the surface was fluorinated with CF_4 plasma treatment, hence, the contact angle goes above 90 °. At this high contact angle, the printed ink recedes due to high cohesive forces within the ink, resulting in agglomeration of ink and dewetting clusters. The middle panel shows the schematic of a printed pad and an angled trace. Ink dewetting and line cracking are observed after sintering the gold nanoparticle ink. Micrographs of the pad and trace are shown in the right panel of **b**. Receding and agglomerating ink created discontinuities in the sintered shapes. (**c**) Printing tests on CF_4 and O_2 plasma treated Kapton® PI that shows good wetting of printed ink. After the O_2 plasma treatment, the contact angle comes down to the printable range, 70 ° $< \theta <$ 90°. In this case, high-quality printing is observed, as demonstrated by the micrographs of the printed pad and the angled trace in the right panel of **c**.

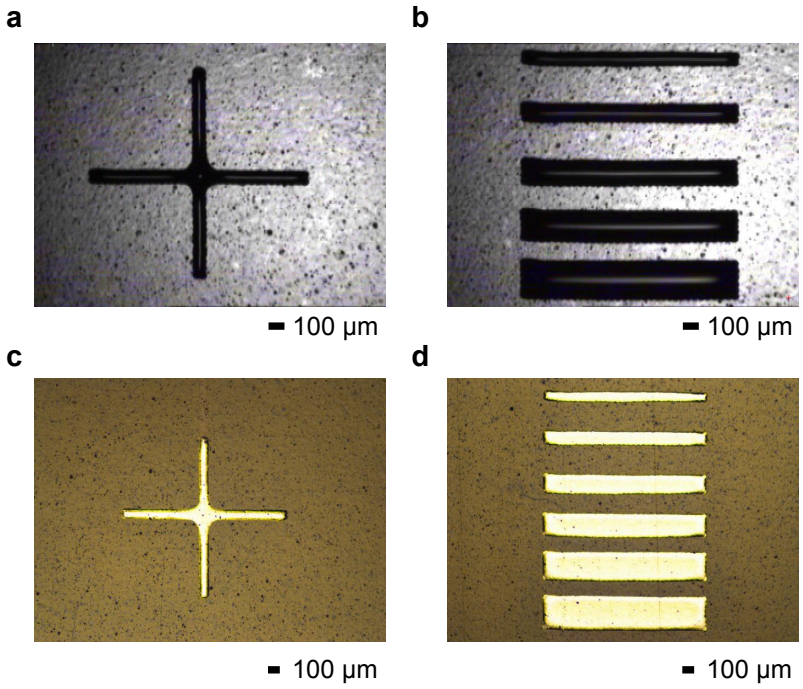

Figure 6.3. **Printing resolution of the printed gold ink on the plasma treated Kapton® PI substrate.** (**a, b**) Printed cross and lines with increasing width. The cross and the top line in **b** are printed by placing two horizontal lines spaced 30 μm apart, which yields 70 μm minimum linewidth. While it is possible to use lines that are single-drop wide, two-drops wide lines are much more reproducible and reliable. Lines 2 - 5 (from the top) in **b** are 3 - 6 drops wide. (**c, d**) Microscope images of the sintered cross and lines with increasing width. Sintered shapes demonstrate <5% shrinkage.

the surface energy optimization, CF_4 plasma did not allow sufficient control to reproducibly tune the surface energy. Therefore, O_2 plasma is used in conjunction with CF_4 plasma for finer control and higher reproducibility to adjust the surface energy. For the combination of our printed gold ink and the plasma treated Kapton® PI substrate, we obtain $70\mu m$ resolution as shown in Fig. 6.3.

The electrical reproducibility of the printed gold electrodes was verified by using line and sheet resistance tests on electrodes of varying lengths. The length of the electrodes e1, e2, e3, and e4 are 5.2, 3.7, 2.6, and 1.4 cm (electrodes e1 and e4 are shown in Fig. 6.4a as an example). The line and sheet resistance are presented in Fig. 6.4b using red and green bars, respectively. The mean line resistance of the electrodes goes down from 132 Ω in e1 to 47 Ω in e4, as the trace length is reduced. The mean sheet resistance varies from .26 Ωsq^{-1} in e1 to .32 Ωsq^{-1} in e4. The printed features demonstrate conductivity of 7.14 x 10^6 S m^{-1}, which is 16% of gold's bulk conductivity and agrees with our previous report on printed electrodes on PEN substrates [2]. The printing resolution is governed by the wetting of the printed ink on the substrate.

In our direct interfacing approach, the sensors are connected to the hard electronics by

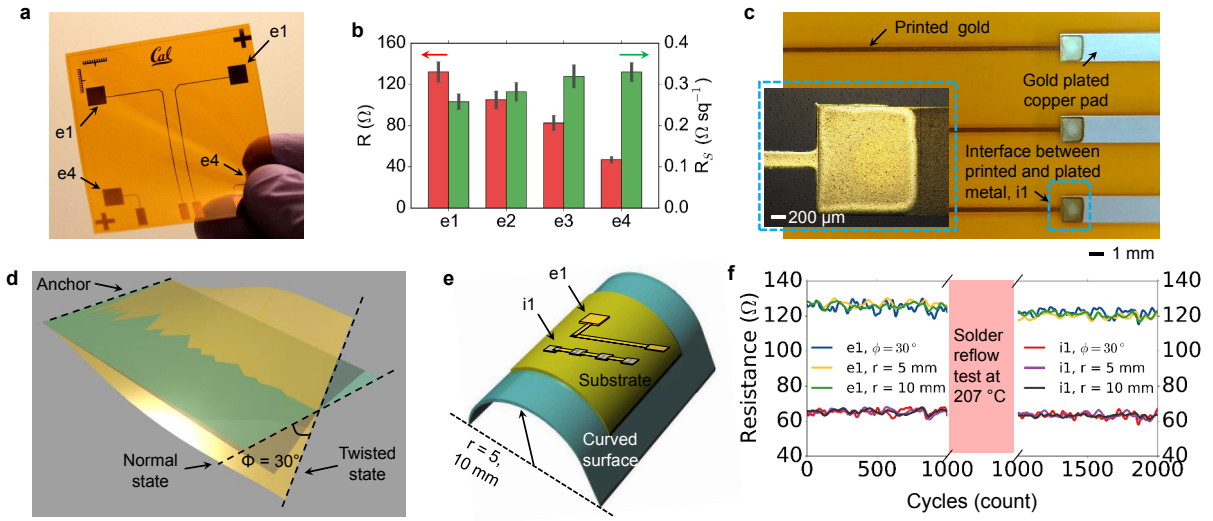

Figure 6.4. **Electrical reproducibility and mechanical robustness testing of electrodes printed on Kapton® PI and the interface between the printed gold and gold plated copper pad.** (**a**) Photograph of printed electrodes of varying trace lengths. Four different trace lengths are used that are indicated by e1, e2, e3, and e4 (e1 and e4 are shown in the photograph as an example). (**b**) Line (R) and sheet resistance (R_S) of the electrodes (the bar chart data is collected from 10 electrodes of the same length, the error bars represent the standard deviation of the data). (**c**) Photograph of the interface between the printed gold and gold plated copper pad. The blue inset shows a micrograph of the interface. (**d**) Schematic illustration of the torsion testing setup. The printed device is anchored at two ends, the other two ends are twisted in opposing directions. Twist angle of ϕ = 30 ° is used for the twist cycles. (**e**) Schematic illustration of the bend testing setup. The printed devices are subjected to bending radii of 10 and 5 mm. (**f**) Mechanical robustness testing results. The resistance of a printed trace (e1) that is bent to 10 mm (green) and 5 mm (yellow) bending radius, and twisted to 30 ° twist angle (blue). Similarly, the resistance of a line consisting of 6 printed/plated gold interfaces (i1) that is bent to 10 mm (black) and 5 mm (purple) bending radius, and twisted to 30 ° twist angle (red). The first 1000 cycles of bending and twisting are done before the solder reflow test, then the printed devices are run through a solder reflow oven at 207 °C. The second 1000 cycles of bending and twisting are done after the solder reflow test. Noise in resistance measurements arose from instrumentation and wire-pad contact resistance variations.

printing on top of the plated metal pads. Therefore, the interface between the printed gold and gold plated copper pad as shown in Fig. 6.4c needs to be electrically and mechanically pristine. While both bare copper and gold plated copper can be used on the FPCB side, oxidation of copper negatively impacts the contact. Since gold plated copper pads do not suffer from oxidation, they provide a much cleaner interface for the printed gold.

The mechanical robustness of the printed lines and the interfaces is another key concern because the WSP needs to survive flexural wear and tear experienced when worn by a human. Therefore, to test the mechanical robustness, we torsionally loaded sensors with a 30° angle of twist (ϕ) and subjected to bending radii of 10 and 5 mm. The schematic in Fig. 6.4d shows the conventions used in the twisting test - two ends of the substrate are anchored while the other two ends are twisted in opposing directions. Similarly, the schematic in Fig. 6.4e shows the conventions used for the bend testing. The printed electrode (e1) and the interface (line consisting of 6 printed/plated gold interfaces, i1) are mechanically cycled for 2000 cycles and negligible change in the electrical resistance is observed (Fig. 6.4f). At the very end of the manufacturing flow of the WSP, a solder reflow step is done, where the assembled sensor platform is subjected to a temperature profile with a maximum of 207 °C, and the process is discussed in the fabrication section. Hence, we performed the bend and twist testing before and after a simulated solder reflow step to gauge the effect of high temperature of the fabrication flow. The electrical and mechanical properties of the printed traces remained intact after the solder reflow test, as seen by the negligible change in electrical resistance of the traces under test. Thus, our processes for ECG electrodes and interconnects are reproducible and robust, i.e., the printed electrodes and traces can be fabricated with adequate precision and sufficiently low resistance (50 - 150 Ω), so that they will not affect the ECG waveforms nor will they impact the circuit design.

6.5 Stencil-printed nickel oxide thermistors

The material system used for the thermistor is composed of nickel oxide (NiO) nanoparticles mixed with a polystyrene-butadiene rubber (PSBR) binder. In a thermistor formed by NiO and PSBR, the number of charge carriers in the conduction band of NiO increases with increasing temperature, resulting in a decrease in the resistivity, while PSBR holds the nanoparticles to form the thermistor. Since PSBR is viscid, stencil printing is chosen over inkjet printing. We fabricated the thermistors by stencil printing the NiO/PSBR composite on top of gold electrodes. An array of fabricated thermistors on Kapton® PI substrates is shown in Fig. 6.5a. The optimized ink demonstrates strong adhesion to the substrate, which is verified using the standard tape test. Optical and scanning electron microscope (SEM) images of the printed thermistor are provided in Fig. 6.6.

For reliably measuring human body temperature, good temperature sensitivity from 32 to 42°C is extremely important. The resistance versus temperature plot is shown in Fig. 6.5b. We observed high sensitivity at normal human body temperatures. The resistance at 30° C ($R_{t@30}$) of the thermistors depends on the geometry of the thermistors. Our initial design, which had 800 μm electrode gap underneath the thermistor, resulted in thermistors with $R_{t@30} > 5$ MΩ. However, to use the thermistors in the WSP, the $R_{t@30}$ of the thermistors needs to be a few hundred KΩ to a MΩ, for reliable operation of the thermistor circuitry. We reduced the $R_{t@30}$

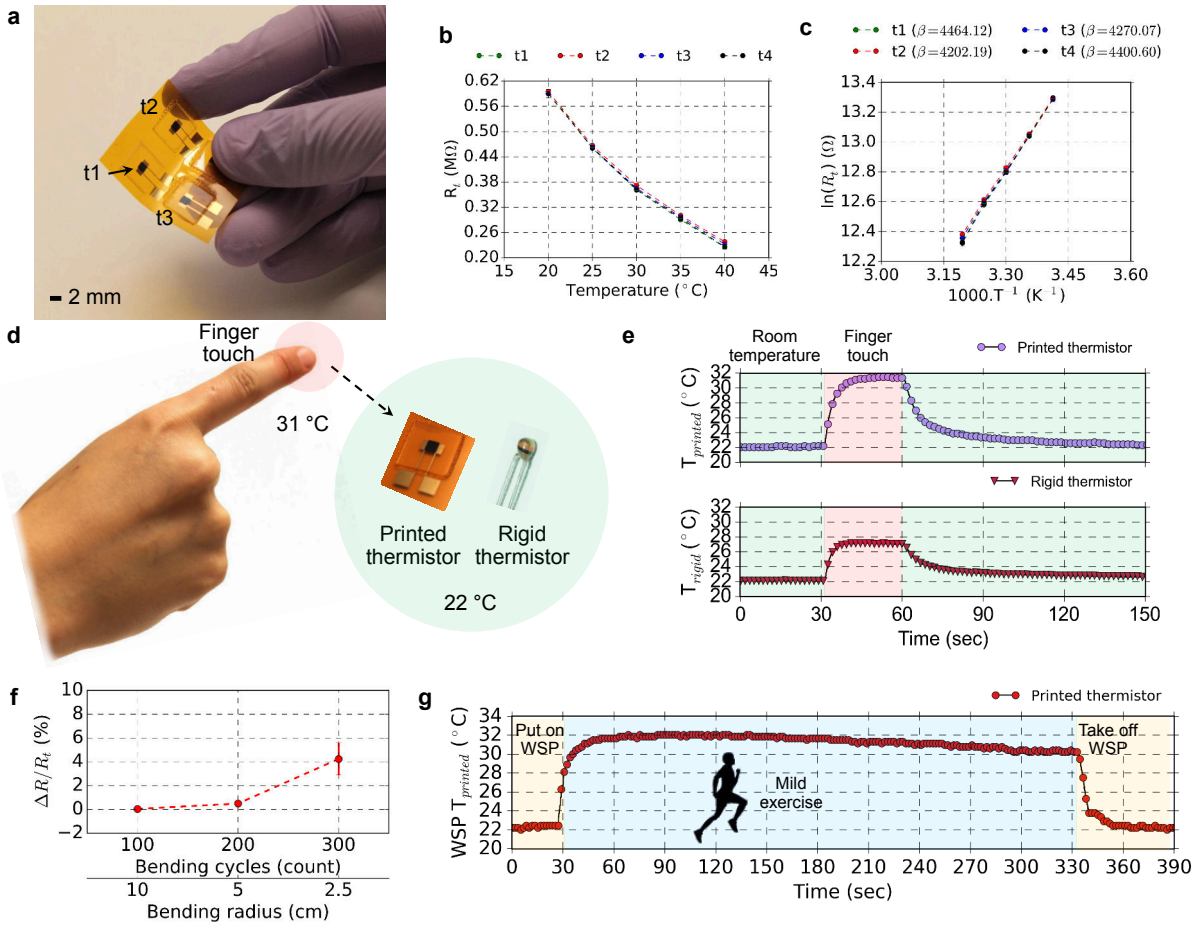

Figure 6.5. **Characterization and dynamic testing of the stencil-printed thermistors.** (**a**) Photograph of stencil-printed thermistors composed of NiO nanoparticles and PSBR binder on Kapton® PI substrate. The four thermistors are labeled t1, t2, t3, and t4. (**b**) Resistance vs. temperature plot for the thermistors. (**c**) β plot of the printed thermistors. (**d**) Characterization of the dynamic response of the printed thermistor. The printed thermistor and a commercial rigid thermistor are used to study the dynamic response. Both thermistors are touched with an index finger to record the change in temperature (22 to 31 °C). (**e**) The top panel shows the temperature read by the flexible thermistor and the bottom panel shows the temperature read by the rigid device. At normal condition (green), both thermistors show 22 °C, after touching the thermistors (red), the resistance drops due to the rise in temperature. As a result, the printed thermistor show 31 °C, and the rigid thermistor show 27 °C. (f) Durability testing of the printed thermistors. Bending radii of 10, 5, and 2.5 cm are used, and the thermistors are subjected to 100 bending cycles at every bending radius. The room temperature resistance of the thermistors roughly changed by 0, 0.5, and 4%, respectively (the error bars represent data collected from 8 devices). (g) Real-time temperature monitoring using the thermistor. The thermistor accurately measured skin temperature of 30 - 32 °C during the exercise (blue overlay).

of the thermistors by decreasing the electrode gap underneath the thermistor. The thermistors shown in Fig. 6.5a have the dimensions of width 2 mm, length 2 mm, electrode gap 80 μm, and thickness 40 μm. This configuration resulted in a $R_{t@30}$ in the range of 350 to 375 kΩ (Fig. 6.5b). For thermistors, beta (β), the slope of the graph in Fig. 6.5c, is the measure of temperature sensitivity. Higher β will result in a greater change in resistance with temperature change. We obtained $\beta \approx 4330$ K, which is comparable to $\beta \approx 4300$ K for inkjet-printed NiO thermistors reported by Huang et al. [24].

The change in resistance of the thermistor is governed by the general equation given below:

$$R_t = R_0 \exp \beta(\frac{1}{T} - \frac{1}{T_0}) \tag{6.1}$$

Here, the resistance of the thermistor decreases with temperature increase, hence, the sensor is Negative Temperature Coefficient (NTC) type. R_t is the resistance at temperature T, R_0 is the resistance at T_0 (reference temperature), and β is the material constant for the thermistor. If β is known, Equation 6.1 can be solved for the temperature T:

$$T = \frac{1}{\frac{\ln(\frac{R_t}{R_0})}{\beta} + \frac{1}{T_0}} \tag{6.2}$$

The β for the thermistor can be calculated by rearranging Equation 6.1:

$$\ln R_t = \ln R_0 + \beta(\frac{1}{T} - \frac{1}{T_0}) \tag{6.3}$$

A linear relationship between $\ln(R_t)$ and $1/T$ can be established, and β represents the slope of the $ln(R_t)$ vs. $1/T$ plot, which is related to the Boltzmann relation ($\frac{E}{kT}$), where E is the bandgap of the thermistor material and k is the Boltzmann's constant. Generally, the sensitivity of the thermistor is quantified using β and the temperature coefficient of the thermistor, α, which can be found by differentiating Equation 6.1 with respect to T and dividing by R_t:

$$\alpha = \frac{1}{R_t}\frac{dR_t}{dT} = -\frac{\beta}{T^2}(\%/K) \tag{6.4}$$

Both β and α can be used to characterize the performance of the thermistor; β has the units of Kelvin while α represents the percentage change in resistance per degree Kelvin. For calibrating the thermistors, we experimentally obtained resistance values for different temperatures and calculated β using Equation 6.3. This β is used in Equation 6.2 for calculating temperatures from the thermistor resistances. The resistance of thermistors is read from a voltage divider network composed of the thermistor in series with a 660 kΩ resistor (R). The variable voltage from the thermistor (V_t) is recorded, which is related to the resistance of the thermistor (R_t) by the equation below (V_B is the bias voltage):

$$V_t = V_B * \frac{R_t}{(R_t + R)} \tag{6.5}$$

We also performed dynamic testing of the thermistor and compared the performance to a commercially available thermistor. The thermal time constant (τ) is the time required for a thermistor to change 63.2% of the total difference between its initial and final body temperature under a step function change in temperature. When subjected to a step function temperature change from 31 to 22 °C, we measured $\tau_{printed}$ = 10 s compared to τ_{rigid} = 11 s of the rigid thermistor (Fig. 6.5e). Under dynamic conditions, both thermistors are used to sense skin temperature - the thermistors are touched with an index finger and the responses are recorded (Fig. 6.5d,e). When the thermistors are touched, the temperature rises from 22 to 31 °C. Fig. 6.5e shows the temperature read by the thermistors while testing. At normal condition, the resistances of the thermistors are high, which results in a high voltage drop across the thermistors, hence, 22 °C temperature is recorded (green zone in the panels). When touched, the voltage across the thermistors is reduced, and 31 and 27 °C temperature are recorded by the printed and rigid thermistors, respectively (red zone in the panels). The printed thermistor provides a more accurate temperature reading of the index finger (31 °C) than the rigid device (27 °C) by establishing a conformal sensor-skin interface.

The durability of the printed thermistors (in WSP form factor) is verified by subjecting the devices to bend testing. Bending radii of 10, 5, and 2.5 cm are used so that the WSP uniformly fits the curved surface (Fig. 6.5f). The room temperature resistance of the thermistors roughly changed by 0, 0.5, and 4% when the devices are subjected to bending radii of 10, 5, and 2.5 cm. For real-time temperature monitoring, a volunteer's skin temperature is recorded using the WSP mounted on the lower left rib cage while doing mild exercise. The sensor accurately measured 30 - 32 °C during the exercise as shown in Fig. 6.5g. The thermistor data is obtained using a voltage divider network, where the variable voltage across the thermistor is recorded using an ADC of a Bluetooth SoC. It is worth noting that the encapsulation of the thermistor is extremely important as it needs to provide an adequate barrier to reduce moisture intake, as well as to protect the thermistor from the later processing of the manufacturing run. Initially, we used poly(methyl methacrylate) (PMMA) as the encapsulant that failed during the copper oxide cleaning step (utilizing oxalic acid) of the fabrication flow. Therefore, the thermistor data presented here is from an individual sensor rather than the fully assembled device. Currently, we opted for an amorphous fluoropolymer (Cytop) encapsulation, which provides superior barrier properties against the oxalic acid cleaning step (the process is described in the fabrication section).

6.6 Fabrication process for the WSP

The fabrication process for the WSP is designed to be completely compatible with the FPCB assembly process. The process flow defined to manufacture the WSP is shown in Fig. 6.7. Isometric and cross-sectional views of the process steps are shown side by side, as well as photographs of the device. A double-sided copper circuitized substrate is used (Fig. 6.7a,b), where the "component side" hosts silicon ICs and rigid passive components. The sensors are

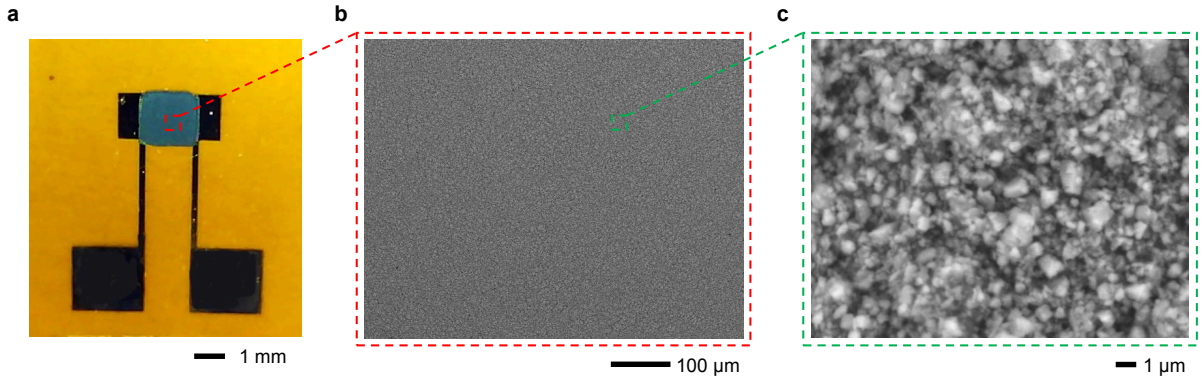

Figure 6.6. **Optical and scanning electron microscope (SEM) images of the printed thermistor.** (**a**) Optical image of the printed thermistor fabricated on top of the inkjet-printed gold electrodes. (**b**) Topological SEM image of the thermistor taken from the red dotted region of **a**. The printed film shows uniform distribution of the NiO/PSBR composite. (**c**) At higher magnification (taken from the green dotted region of **b**), the film shows well-mixed NiO/PSBR composite with particle sizes ranging from 0.5 - 1.5 μm.

printed on the opposite side of the frame - i.e., the "sensor side." The two sides of the copper circuit layers are interconnected by plated-through holes (PTH) to provide interconnection from the side to which electronic components are mounted to the side on which the ECG electrodes and the thermistor are printed. This "sensor side" will be in contact with the skin of the wearer.

As described before, untreated Kapton® PI substrates are not suitable for inkjet printing. Therefore, the substrate is CF_4 and O_2 plasma treated to adjust the surface energy for inkjet printing. Gold nanoparticle ink is inkjet printed at 30 μm drop spacing to form the gold ECG electrodes (Fig. 6.7c,d,i). Commonly, FPCBs are processed on frames, where the Kapton® PI substrate is mounted on a frame and subsequent processing is done on the frame. The side of the frame where the substrate is mounted is flat, whereas the opposite side forms a cavity between the frame and the substrate. inkjet printing is done on the flat side of the fabrication frame, and the components are assembled on the cavity side of the frame (frame photo and design layouts are shown in Fig. 6.8). Printed gold traces demonstrated minimum linewidth of 70 μm. Since copper pads show higher surface energy, ink spreading is observed on the copper pads. However, this turned out to be beneficial in the alignment process. To make electrical connection, gold traces are printed onto the surface of the copper pads. Since multiple connections are made side-by-side, the gold ink could not be allowed to flow between the tabs. The Kapton® PI surface between the copper pads demonstrates relatively less surface energy, as a result, the ink is contained on the surface of the copper pads.

The thermistor is printed on top of gold electrodes using stencil printing (Fig. 6.7e,f,j). 50 μm PET in conjunction with a glass slide as the blade are used to fabricate the thermistors. Thermistors of 2 mm length and width, and 40 μm height are reproducibly printed that demonstrated 350 - 375 kΩ resistance at 30 °C. A Cytop encapsulation layer is applied on top of the thermistor to protect the device from the later processing steps as well as to reduce the

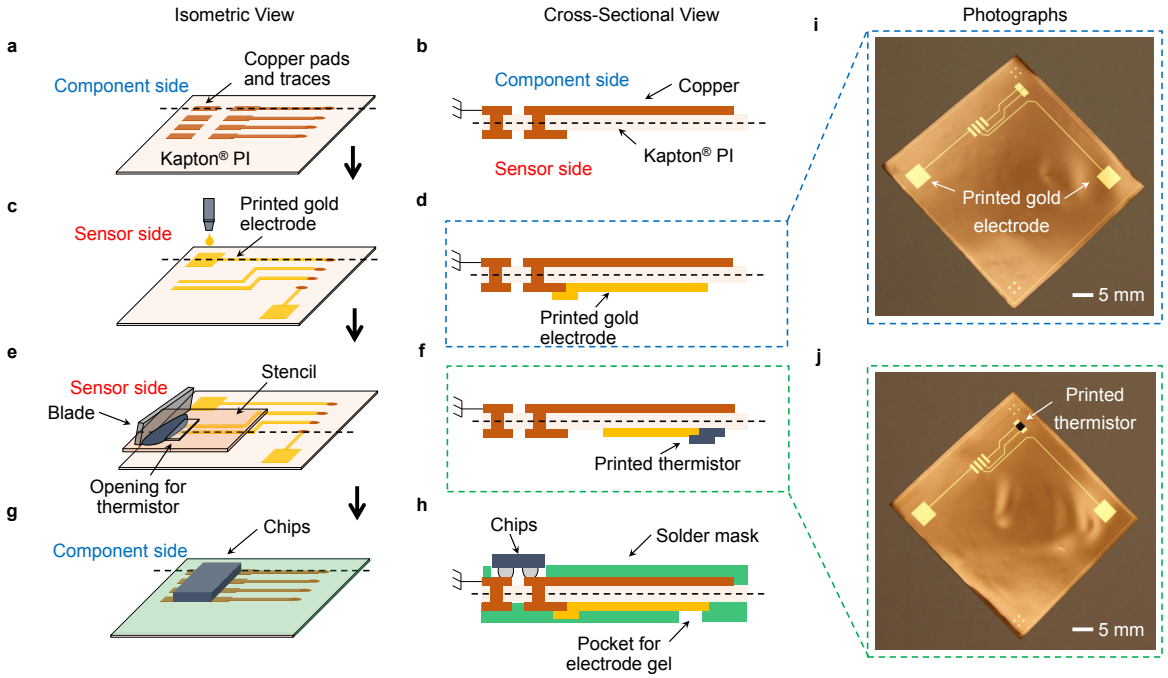

Figure 6.7. **Fabrication process for the WSP**. (**a-h**) Simplified manufacturing steps illustrating the printing of gold electrodes and nickel oxide thermistors on Kapton® PI substrate. (**a, c, e, g**) Isometric views and (**b, d, f, h**) corresponding cross-sectional views of the process steps are shown side by side. (**a, b**) Standard double-sided copper circuitization is performed to deposit copper pads and traces. (**c, d**) Gold nanoparticle ink is printed to fabricate the ECG electrodes and the electrodes for the thermistors. Surface energy optimization steps are performed before printing the gold ink. (**e, f**) After sintering the gold ink, the thermistor is printed using stencil printing. The thermistor is printed on top of gold electrodes as seen in the cross-sectional view. (**g, h**) After printing the sensors, photoimageble solder mask process is executed keeping the electronic component pads and the ECG electrode pads open. The active and passive circuit components are soldered on the component pads through solder reflow. A pocket for the electrode gel is used, where electrode gel is applied before human measurement. (**i, j**) Photographs of the printed gold electrodes (blue dotted box of **d**) and nickel oxide thermistor (green dotted box of **f**).

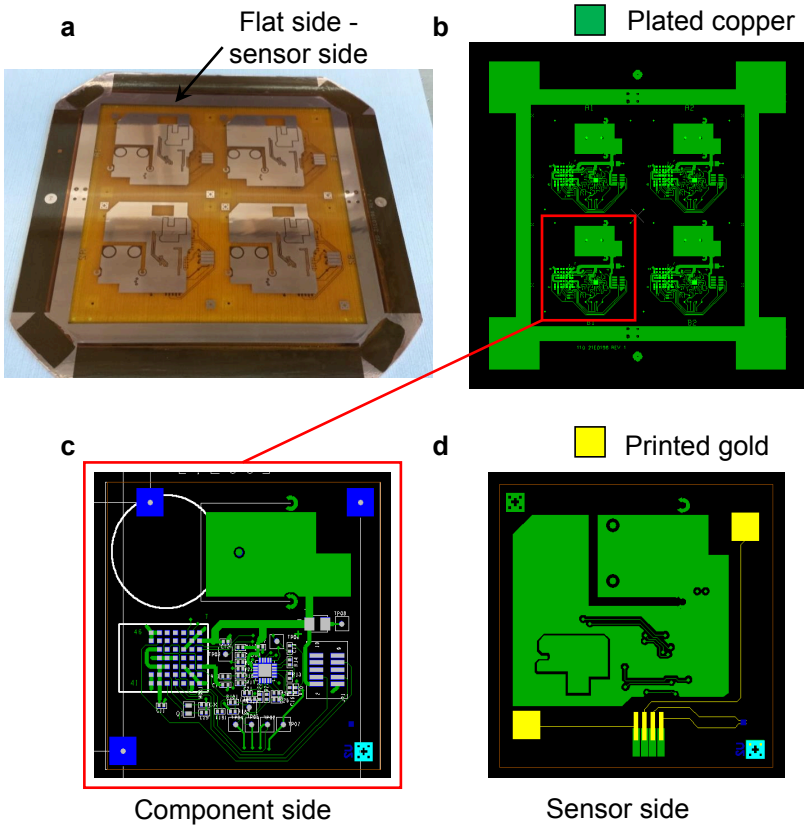

Figure 6.8. **Fabrication frame and layout of the WSP.** (**a**) A Kapton® PI substrate is mounted on a 1.27 mm thick frame. Each frame contains four WSPs. The flat side of the frame where sensors are printed, is displayed. (**b**) The layout of the full panel consisting of four WSPs. Green patterns represent the plated copper. (**c**) The layout of the component side. (**d**) The layout of the sensor side: green represents plated copper while yellow represents the printed gold. Alignment marks are visible, which are used to align the gold layer to the copper layer.

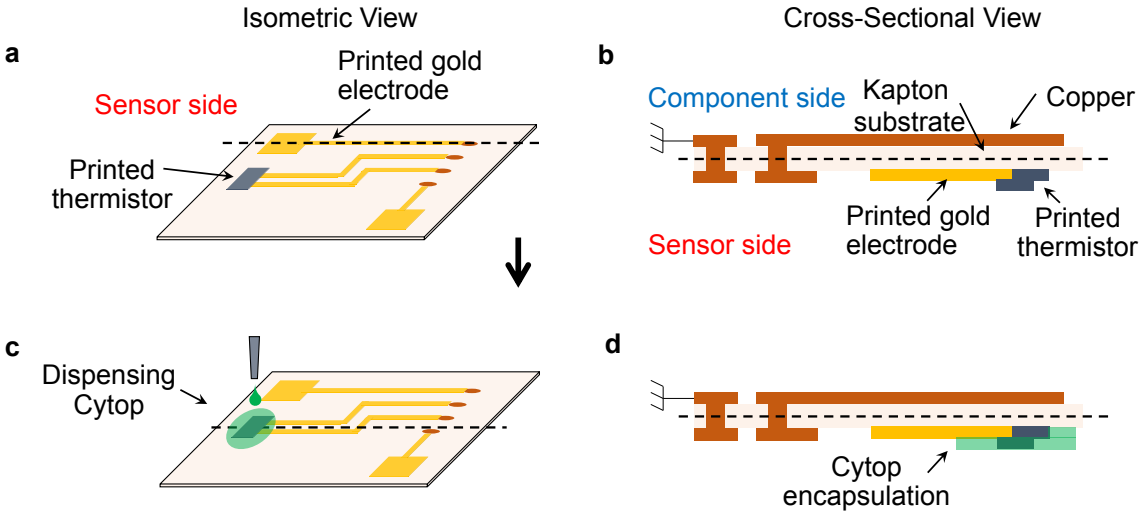

Figure 6.9. **Encapsulation process for the thermistor**. (**a, c**) Isometric views and (**b, d**) corresponding cross-sectional views of the encapsulation process are shown side by side. (**a, b**) Sensor substrate with printed gold electrodes and the thermistor is shown. At this point, the electrodes and thermistor are unencapsulated. (**c, d**) An amorphous fluoropolymer (Cytop) is drop casted on top of the thermistor. The 5 μm thick Cytop encapsulation protects the thermistor from the later processing steps, and reduces moisture intake.

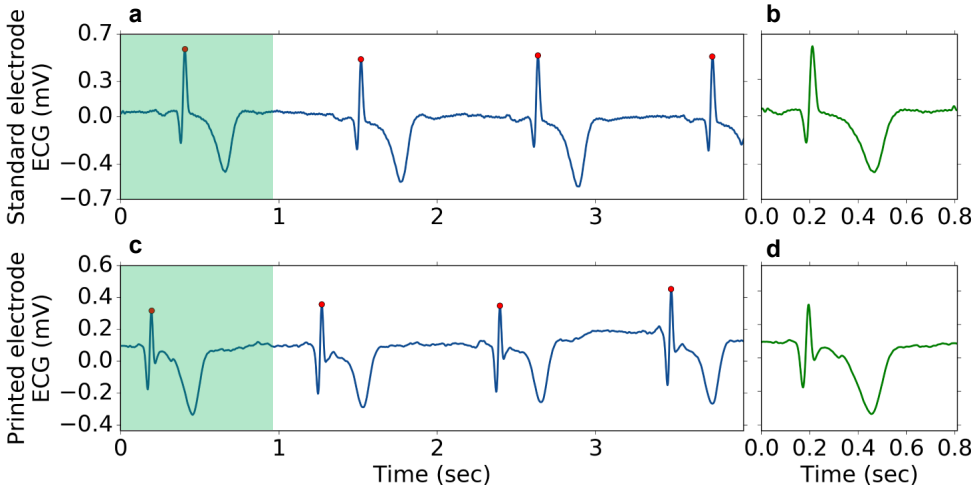

Figure 6.10. **ECG recording with standard Ag/AgCl electrodes and printed gold electrodes**. (**a**) ECG recording from the chest (V_1 - V_2 chest lead placement locations) using standard Ag/AgCl electrodes. (b) A detailed view of the recording taken from the green overlay region of **a**. (c) ECG recording from the same V_1 - V_2 chest lead placement locations using gold electrodes. (d) A detailed view of the recording taken from the green overlay region of **c**. The standard Ag/AgCl electrodes provide 0.8 mV_{p-p} ECG signal, while the printed electrodes provide 0.6 mV_{p-p} ECG signal.

moisture intake. The encapsulation process is shown in Fig. 6.9.

Upon completion of the sensor build, the substrate is prepared for component assembly by solder mask deposition and laser cutting the coin cell battery holder. On the component side, the substrate is overcoated with a solder mask except for select pads that are required for solder-attach of components. On the sensor side, the substrate is also covered with solder mask leaving openings for the electrode pads for skin contact via a conductive gel. Finally, components are assembled via solder reflow and electrode gel is applied to the opening of the ECG electrode before human testing (Fig. 6.7g,h). Photographs of the finished product are shown in Fig. 6.1c-e.

6.7 Real-time ECG signal monitoring with the WSP

Under clinical settings, ECG signal is measured using 10 electrodes placed around the body, 6 of which (V_1 - V_6) are placed on the rib cage. This configuration is called 12 - lead measurement, where the "lead" refers to a view of the electrical activity of the heart from an angle across the body using a particular pair of electrodes [111]. In recording ECG signal, the printed gold electrodes provide 0.6 mV_{p-p} signal compared to standard Ag/AgCl electrodes which provide 0.8 mV_{p-p} signal when placed on the chest, V_1 - V_2 chest lead placement locations (Fig. 6.10). Using the patch form factor, the WSP uses two electrodes to record the electrical signal. Here, the placement of the patch is of significant importance.

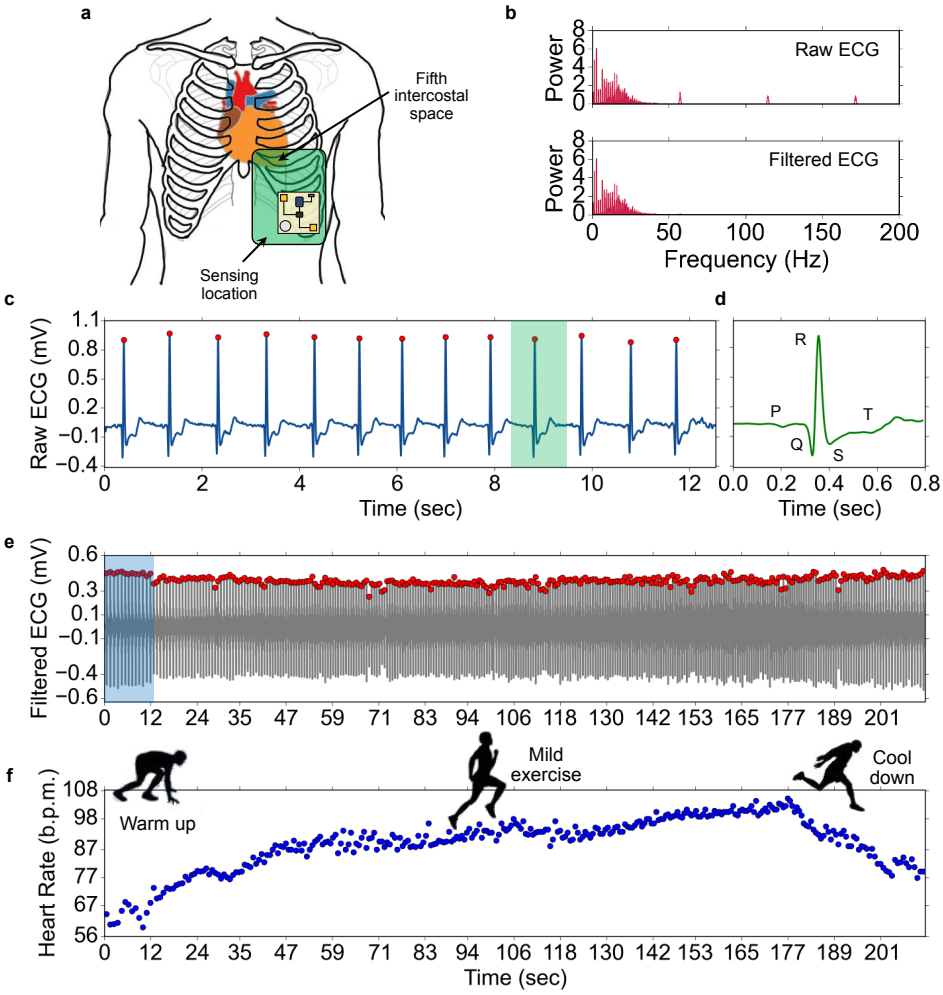

Figure 6.11. **Electrocardiography (ECG) signal and heart rate (HR) monitoring using the WSP.** (**a**) Schematic illustration of the WSP placement on a subject's lower left rib cage. The region marked in green provides a low-noise and high-quality signal. Electrodes shown in the yellow patch are used to record the ECG signal during the mild exercise. (**b**) Fourier transform of the raw and filtered ECG signal. In the raw signal, noise at over 50 Hz hinders the peak detection algorithm. Therefore, a bandpass filter with 0.2 Hz (lower cutoff) and 45 Hz (upper cutoff) is used to filter the signal. (**c-f**) ECG and HR from a subject while doing mild exercise. (**c**) Raw ECG recording of the first 13 s. Data is taken from the blue overlay of the complete recording in **e**. The red dots signify heartbeats detected by the peak detection algorithm. (**d**) A detailed view of the ECG signal collected from the green overlay in **c** with marked P, Q, R, S, and T waveforms. (**e**) The complete ECG recording (filtered) obtained during the time of exercise. Here also the red dots signify detected heartbeats. (**f**) HR in beats per min (b.p.m) for the complete duration of the exercise. Each blue dot is a representation of the time interval between two consecutive heartbeats.

We used ECG signal magnitude and ease of securing the WSP as metrics for finding the suitable sensing location. Xu et al. used 2 electrodes mounted on the sternum and recorded ECG signal [33]. We obtained 0.6 mV signal magnitude using the same configuration. While we tested multiple locations on the rib cage, the lower left rib cage area produced strong signals (green region in Fig. 6.11a, starting from the fifth intercostal space). We used medical adhesive tape for securing the WSP to the skin. The complete assembly was 6.1 gm, which was mostly dominated by the battery and the battery holder (3 gm and 2 gm). Due to the flexible form factor and lightweight, the WSP remained secured to the skin during the wearer's physical movement. The electrodes diagonal to the WSP (yellow patch location in Fig. 6.11a), aligned to the heart axis running from the upper right atrium through the lower left ventricle, provided the strongest and cleanest ECG signal. High-quality and low-noise signals are recorded using these electrodes. We used this configuration for the ECG and HR variation measurements.

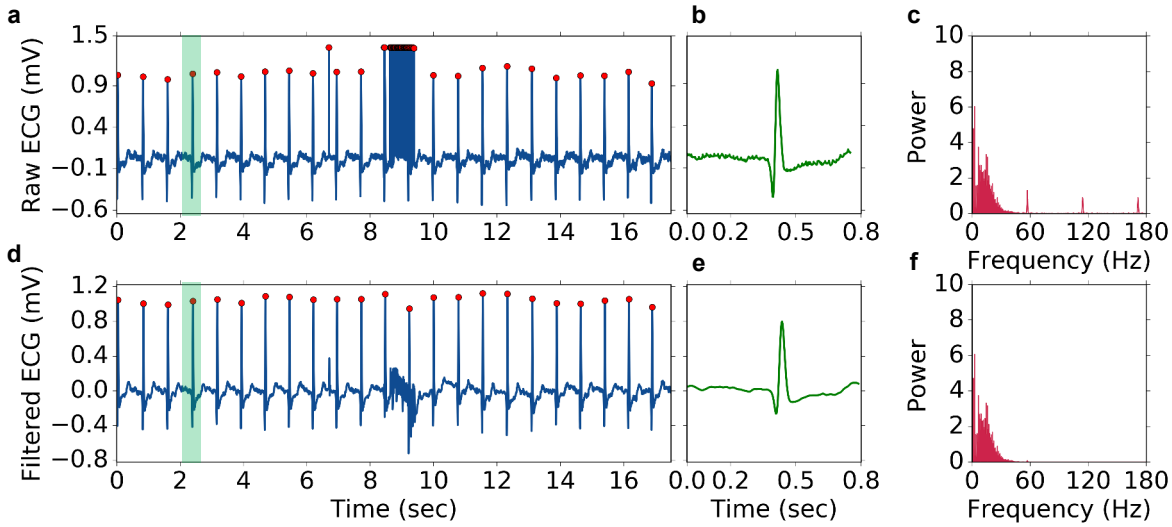

Figure 6.12. **Post processing of ECG signal for noise reduction.** (**a-c**) Raw ECG signal and corresponding signal features. (**a-b**) Raw ECG signal and a detailed view of the signal for illustrating the ECG waveform (collected from the green overlay of the raw signal. The red dots signify detected heartbeats. (**c**) Fourier transform of the signal, where motion artifacts and noise at over 50 Hz hinders the peak detection algorithm, resulting in errors in heart rate monitoring in **a**. (**d-f**) Filtered ECG signal and corresponding signal features after filtering the raw signal with a bandpass filter with 0.2 Hz (lower cutoff) and 45 Hz (upper cutoff). Filtering reduces most of the noise and eliminates all the incorrect heartbeat peaks. However, some noise still remained as seen in **d**.

To test the efficacy of the WSP, we recorded ECG signal from human volunteers while at rest, and before, during and after mild exercise (Fig. 6.11c-f). Fig. 6.11c,d show a snapshot of the raw ECG signal obtained from the hardware (from the blue overlay of Fig. 6.11e). The different peaks of an ECG signal are labeled in Fig. 6.11d. Fig. 6.11e shows the filtered ECG signal for the complete test duration of 210 s; the red dots signify heartbeats detected by the peak detection algorithm. The raw signal is filtered to reduce noise in the higher frequencies

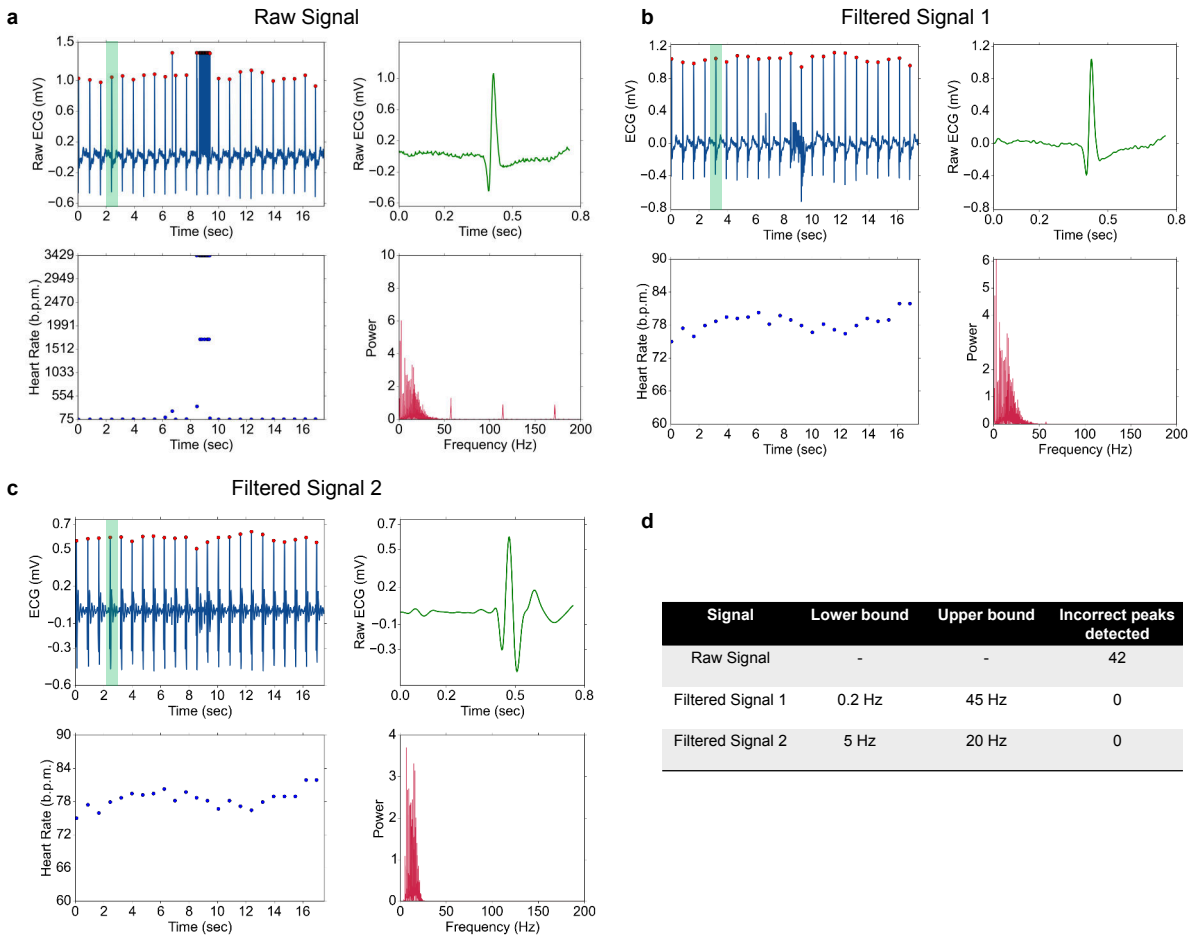

Signal	Lower bound	Upper bound	Incorrect peaks detected
Raw Signal	-	-	42
Filtered Signal 1	0.2 Hz	45 Hz	0
Filtered Signal 2	5 Hz	20 Hz	0

Figure 6.13. **Post processing of ECG signal for heart rate (HR) detection**. (**a-c**) Raw and filtered ECG signals and corresponding signal features. (**a**) The top two panels show the raw ECG signal and a detailed view of the signal for illustrating the ECG waveform (collected from the green overlay of the raw signal). In the case of the raw signal, the red dots signify detected heartbeats. The bottom two panels show extracted heart rate and the Fourier transform of the signal. Noise at over 50 Hz hinders the peak detection algorithm, resulting in errors in heart rate monitoring (lower left panel). (**b**) A similar format as the raw signal in **a** is followed to show a filtered signal. A bandpass filter with 0.2 Hz (lower cutoff) and 45 Hz (upper cutoff) is used for filtering the signal. Filtering eliminates all the incorrect heartbeat peaks, however, some noise still observed (top left panel). (**c**) Similar to the filtered signal in **b**, a bandpass filter with 5 Hz (lower cutoff) and 20 Hz (upper cutoff) is used for filtering the raw signal. Here, the ECG waveform is distorted because the filtering window cuts off frequencies associated with the ECG waveform. On the other hand, all the R-wave peaks are detected with high accuracy, and the noise is minimized. (**d**) Filtering parameters and the accuracy of heart rate detection for all three cases are presented in a tabular format.

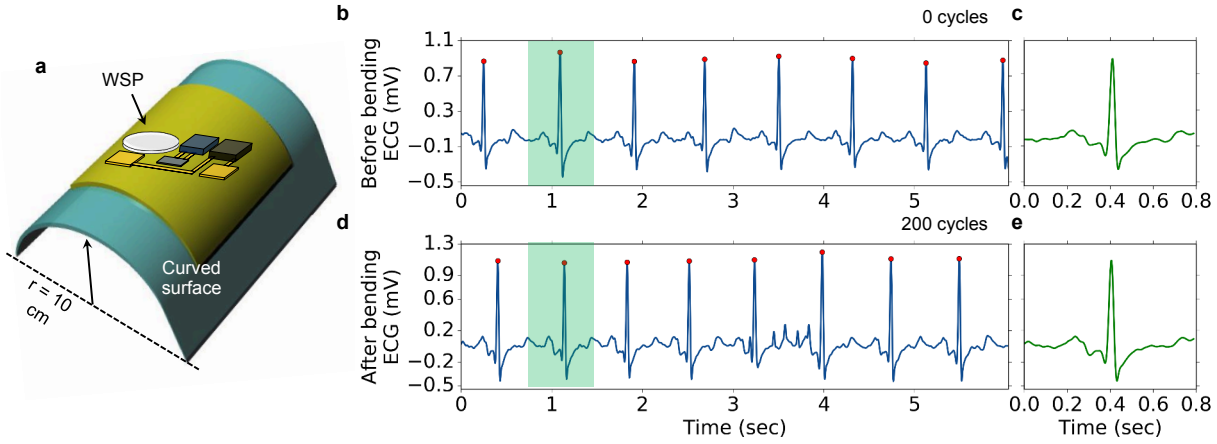

Figure 6.14. **Mechanical robustness testing of the WSP.** (**a**) Schematic illustration of the bend testing setup where the WSP is subjected to mechanical bending using a 10 cm radius of curvature mandrel. (**b**) ECG recording from a simulator before the bend testing. (**c**) A detailed view of the recording taken from the green overlay region of **b**. (**d**) ECG recording from the simulator after the WSP is subjected to 200 cycles of bending. (**e**) A detailed view of the recording taken from the green overlay region of **d**.

that resulted in incorrect heartbeat peaks. The Fourier transform of the raw and filtered ECG signal are shown in Fig. 6.11b. Noise at over 50 Hz hinders the peak detection algorithm, resulting in errors in heart rate (HR) monitoring. After filtering the signal, the WSP clearly detected the heart rate variation during the mild exercise as shown in Fig. 6.11f. HR of the volunteer picks up from the resting HR of 62 beats per min (b.p.m.) to 108 b.p.m. after 3 min, and gradually cools down to 77 b.p.m. at the end of the recording. We obtained high-quality ECG signal from the WSP that was wirelessly transmitted to a computer host with essentially perfect peak detection. The HR showed anticipated variations corresponding to whether the subject was at rest or was exercising.

Motion artifacts are observed in the recordings, which are more prominent for dry electrodes. Using electrode gel significantly reduces motion artifacts and the associated noise. Additionally, the raw data is post-processed to further reduce noise. An example recording with motion artifacts and noise at over 50 Hz is shown in Fig. 6.12a. A detailed view of the ECG and the Fourier transform of the raw signal are shown in Fig. 6.12b,c. Filtering the raw signal with a bandpass filter with 0.2 Hz (lower cutoff) and 45 Hz (upper cutoff) reduces most of the noise and eliminates all the incorrect heartbeat peaks (Fig. 6.12d-f). However, some noise is still observed. Using a tighter filtering window further reduces noise, however, the ECG waveform is distorted because the filtering window cuts off frequencies associated with the ECG waveform as shown and discussed in Fig. 6.13. Therefore, this filtering scheme is adequate for heart rate monitoring, and not suitable for recording medical-grade ECG signal.

Finally, to check the durability of the WSP, a 10 cm radius of curvature mandrel is used to bend test the complete WSP assembly as shown schematically in Fig. 6.14a. Fig. 6.14b,c show

the ECG recording from a simulator before the bend testing, and Fig. 6.14d,e show the ECG recording from the simulator after the bend testing. Here, the WSP is subjected to 200 cycles of bending. The WSP remained operational after the bending cycles. Although we observed some noise in the data, the signal was of an adequate quality for detecting the heart rate. This result indicates that the WSP platform remains functional after being subjected to mechanical bending, hence, is suitable for wearable applications. Further Design optimization in terms of thickness and shape of the printed and plated materials can be utilized to reduce corner stress concentration to further improve the mechanical robustness of the WSP.

Data related to mechanical testing presented in Fig. 6.14 is obtained from a very small sampling of the first prototype WSP modules. A number of other modules, although functional prior to stressing, proved to be less robust upon mechanical stressing. The technology is sound, i.e., there are no issues stemming from electrical design, software, materials of construction, manufacturing methods, and workmanship. It is observed that failure to survive mechanical testing is due primarily to stress points in the device induced by the first pass physical design of the module, for example, circuit line widths and routing, the size, shape, and location of openings in the solder mask layer to expose metal pads on the flexible substrate for component assembly. In addition, it is believed that changes in plated metal thickness, the thickness of the base Kapton® PI substrate, and use of a gold surface finish on plated metals that interface with inkjet-printed gold, will substantially improve module robustness.

6.8 Improving printed gold to plated copper interface

A reliability issue involving the printed gold to plated copper interface in the WSP hindered the electrical connection of the device. The WSP had two types of printed sensors - the gold ECG electrodes, and the nickel oxide (NiO) thermistor. These were electrically connected to plated copper circuits, on which rigid electronic components were surface mounted using solder reflow. The gold circuits were formed by printing continuous gold traces on the PI substrate that also overlapped onto copper circuit pads to make electrical connections between the printed sensors and the rigid electronic devices. To create a robust interface between the gold ink and the plated copper, the printed gold layer needed to have a uniform as-printed thickness, which is maintained until the ink was fully sintered to metallic gold. This requires that the gold ink exhibit favorable wetting and maintain good adhesion to the plated copper pads. However, three issues arose that compromised the printed gold to the plated copper interface. 1) Thinning of the printed gold ink occurred as it approached a copper pad and transitioned up onto it. This occurred immediately after printing and during the sintering, which vaporized the solvent and allowed the gold nanoparticles to coalesce. We observed that the ink wicked from the PI onto the adjacent copper pad due to the higher surface energy of the copper compared to that of the PI surface (Fig. 6.15). The resulting excess of ink on the copper pad resulted in the formation of mud cracks associated with solvent loss and shrinkage of the ink during drying and curing. 2) The thick uncured ink on the pads remained fluidic until an adequate solvent loss occurred that prevented flow. Until then, a movement of the ink on the copper pads was observed as the devices were transferred into the curing oven. This gave rise to areas of very thick and very thin ink on the copper pads. The thinner gold ink regions of the copper pads could also have been more susceptible to oxygen penetration during thermal cures

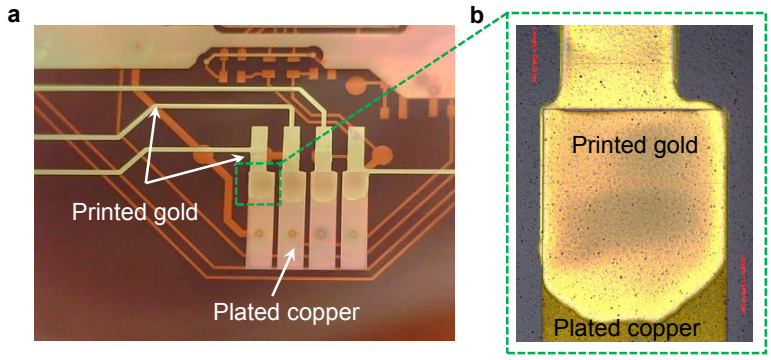

Figure 6.15. **Micrographs of the gold/copper interface.** (**a**) Gold ink spreading on copper pads. Copper pads are more hydrophilic than Kapton® PI surface, as a result, ink spreads on the pads. (**b**) Zoomed view of the gold/copper interface. Gold ink spread on the surface of copper, and gets pinned at the edges of the pad.

and the formation of copper oxide at the gold/copper interface that could degrade adhesion. The thicker regions showed cracks formed during curing that were large fissures down to the copper pads. 3) Where the ink was wicked from the circuit line adjacent to the copper pad, the line narrowed substantially, and in some cases, an open was formed. Therefore, a solution for controlling the thickness uniformity of the ink on the copper pads was needed.

To understand wetting and spreading of the gold nanoparticle ink, the surface energy of various surfaces was measured indirectly using a goniometer and contact angle measurements. When a drop of liquid is placed on a solid surface, the drop experiences adhesive forces between the liquid and the solid surface, which favor spreading of the liquid, whereas the cohesive forces within the droplet counteract the spreading. The balance of the forces yields a contact angle, θ as shown in Fig. 6.16a. Young's equation relates the forces in play to the surface free energies of the solid (S), liquid (L), and vapor (V) phases, as shown at the bottom of Fig. 6.16a. For determining the critical surface tension, a series of liquids with decreasing surface tension - hexadecane, ethylene glycol (EG), and DI water were placed on the solid surface (Fig. 6.16b). The receding surface tensions of the liquids help to create an extrapolated line, and at $\cos\theta = 1$, the plot yields the critical surface tension of the solid (Fig. 6.16 d-f). We characterized the surface tensions of: (i) Planarized PEN (PQA1) (ii) O_2 and CF_4 plasma treated Kapton PI and (iii) plated copper on Kapton PI after CF_4 and O_2 plasma treatments (Table in Fig. 6.16c). It is apparent that the plated copper surface demonstrated much higher critical surface tension than the PI. Therefore, significant ink spreading is expected on this surface.

To study the printed gold line thinning, a series of experiments were performed on different metallic surfaces. These surfaces went through CF_4 and O_2 plasma treatments, the plasma treatment conditions are described in Section 6.4. Fig. 6.17 shows a printed cross and a tab on (i) Copper, (ii) Nickel on copper and (iii) Oxidized nickel on copper. The cross and the tab on copper and nickel on copper surfaces show significant spreading. These results are aligned with the findings from the critical surface tension studies, where the metallic surfaces had significantly higher critical surface tension than CF_4 and O_2 plasma treated Kapton PI. As a result, the nanoparticle ink spreading is greater on the metallic surfaces than on CF_4 and

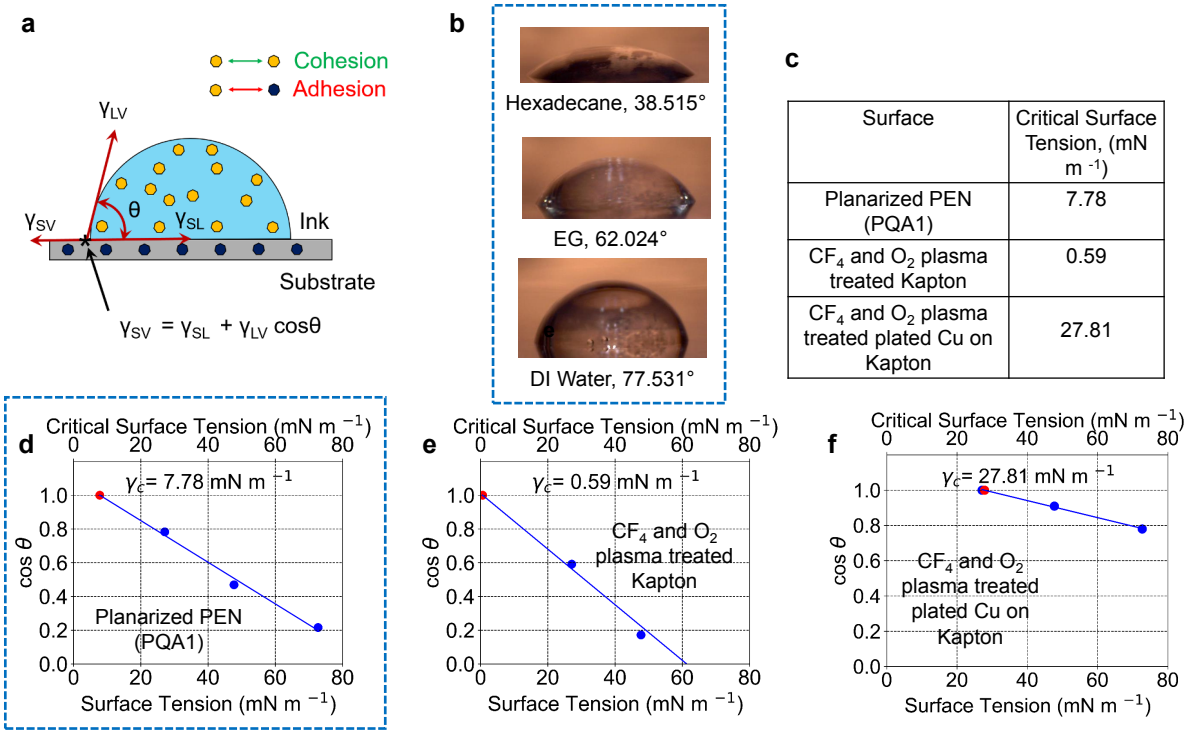

Figure 6.16. **Critical surface tension characterization for various surfaces**. (**a**) Relevant forces balanced by Young's equation when a liquid drop is placed on a solid surface. (**b**) Contact angles of various liquids on a planarized PEN (PQA1) substrate. (**c**) Summary table of critical surface tensions for relevant solid surfaces. (**d-f**) Zisman plots for determining surface energy of (**d**) planarized PEN (PQA1), (**e**) CF_4 treated Kapton, and (**f**) Copper on Kapton after CF_4 plasma treatment.

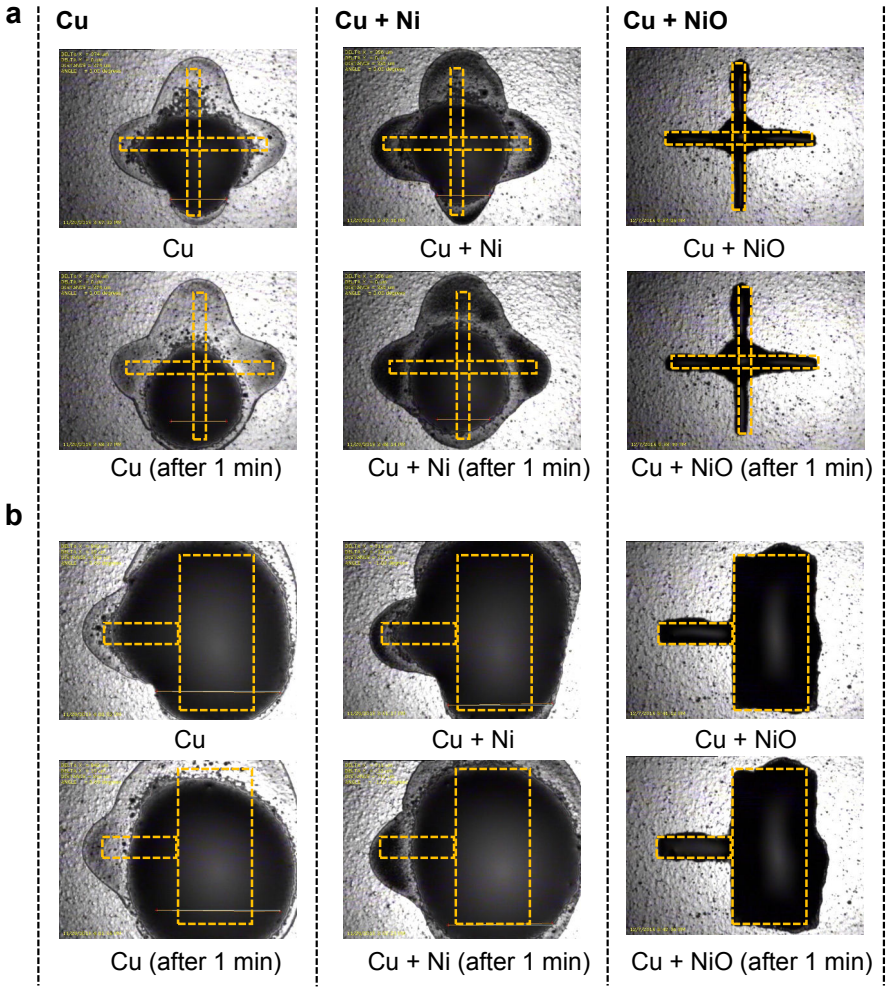

Figure 6.17. **Nanoparticle ink wetting and spreading tests on different metallic surfaces**. (**a**) 1mm × 1mm printed cross and (**b**) 1mm long and 500 μm wide printed tab on different metallic surfaces. The yellow dotted lines show the intended feature shape. In both (**a**) and (**b**), the top panel shows feature definition right after printing, while the bottom panel shows feature definition 1 min after printing. The first column in (**a**) and (**b**) shows printing on plated copper. The second column in (**a**) and (**b**) shows ink spreading on a nickel on copper surface. After a bake at 190 °C for 30 min in air, an oxide layer is formed on the top of the nickel surface which restricts ink spreading to the metal features. The third column shows printed ink on this oxide surface. The pattern fidelity of printed features on the oxidized surface demonstrates significant improvement over the bare nickel on copper surface.

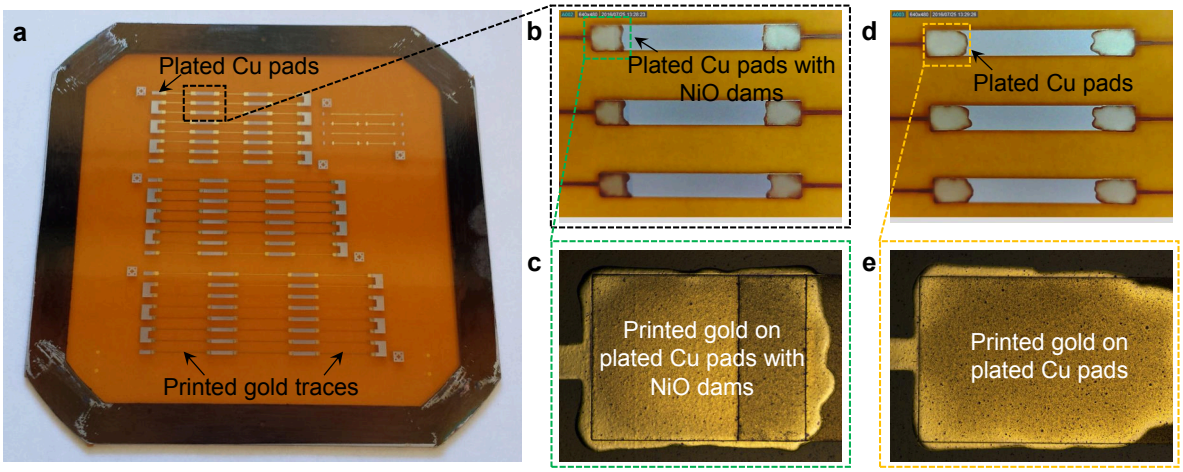

Figure 6.18. **Printing reliability improvement TV and the use of NiO dams**. (**a**) The printing TV after all metallization and printing have been completed. The copper pads were interconnected by printing gold traces between two copper pads. (**b**) Pinning of the gold ink at the edge of the NiO dam. Due to the high volume, there was some ink spill over. (**c**) Ink runout in the case of copper pads without the NiO dams. The runout resulted in thinning of the ink at the printed gold to plated copper interface.

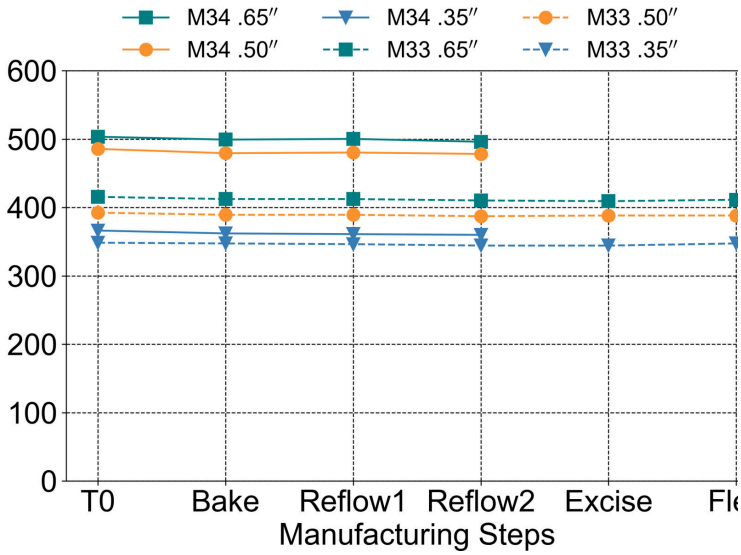

Figure 6.19. The TV array resistance after various manufacturing steps, thermal cycling, and flexing. To was immediately after the manufacturing build; bake followed solder mask cure at 150 °C for 1 hr; reflows 1 and 2 were performed at a simulated solder reflow at 205 °C, and excise was done to check for a response after the parts were cut from the substrate tensioned on a frame. Flex step was done at 1000 bend cycles on a 2 mandrel. Results for 6 arrays are shown, where the length of the arrays was varied from 0.35″ to 0.65″.

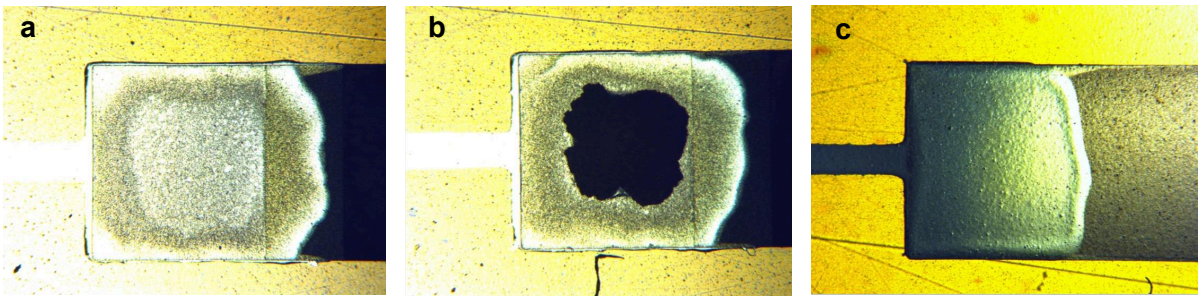

Figure 6.20. **Comparison of gold ink printed on copper pads without and with gold-plating**. (**a**) Gold ink printed on copper pads without a protective gold plating. (**b**) The bright center is indicative of the interfacial failure that worsens with abrasion during flex testing and ultimately results in peeling of the gold layer. (**c**) Gold ink printed on copper pads with gold plating demonstrates good adhesion between the plated gold and the printed gold. All images were taken following thermal cycling (a simulated solder mask cure cycle followed by 2x reflow cycles at 204 °C peak temperature).

O_2 plasma treated Kapton PI. A conclusion can be drawn from these tests that a subsequent surface treatment is required for the metallic surfaces to restrict ink spreading. While the base nickel surface was conducive to ink spreading, oxidizing the surface in air at 190 °C for 30 min drastically improved printability (Fig. 6.17, third column). The oxide layer demonstrates lower critical surface tension compared to a bare nickel surface, which restricted the ink spreading. These results are shown in Fig. 6.17. The first column shows printing on copper on Kapton PI after CF_4 and O_2 plasma treatments. The cross and the tab did not hold their shape, yellow dotted lines show the intended feature. Ink spreading on a nickel on copper surface is shown in the second column. Here too, considerable spreading of the ink hinders the pattern formation. Oxidizing the surface in air at 190 °C for 30 min improved the printability of the surface, which is clear from the printed cross and the tab in the third column of Fig. 6.17. Therefore, a barrier to ink spreading, utilizing nickel oxide - "NiO dams" can restrict ink spreading.

One of the electrical failure mechanisms for the WSP was an interfacial separation of printed gold from the plated copper pads. This overlap was required for electrical interconnection of the printed sensors to the rigid components. A robust interface between these materials is necessary to preclude interfacial separation during subsequent thermal treatments required for nanoparticle ink and solder mask cures and to survive flexing-induced mechanical stress during use. Interfacial failure at the gold/copper interface was observed to result in either partial loss (increased resistance) or total loss of electrical connections (opens) in the circuit. After studying the wetting and spreading of the nanoparticle ink on various surfaces, a test vehicle (TV) was built comprised of daisy chains of plated copper and interconnecting printed gold features. This design is shown in Fig. 6.18a. The copper features were first pattern-plated on the Kapton PI. Four types of surfaces were then prepared using the base plated copper surface. i) Bare plated copper, ii) plated copper with NiO dams, iii) plated copper with a plated gold layer, and iv) plated copper with a plated gold layer with NiO dams. Then, lines of gold

ink were printed to interconnect copper plated pads forming multiple arrays of copper, interconnected by printed gold circuit lines. Referring to Fig. 6.18a, this created three continuous electrically testable metallic serpentines of different lengths. This TV was used to test the four different metal pad surfaces, with the first goal to control printed gold ink flow, and with the second goal to learn how to form a more robust adhesive interface between the printed gold ink and plated copper pads. Additionally, the TV was tested electrically after bend testing and thermal cycling, looking for any change in conductivity that would be indicative of interfacial breakdown. Fig. 6.18b and c show a magnified view of the resultant serpentine pattern after gold printing between the copper pads. Printed gold lines were used to interconnect the copper pads with (Fig. 6.18b) and without (Fig. 6.18c) NiO dams. The NiO dams were tested for their ability to restrict the area of the pad and ink flow off the pad. The reduced area of the pad also meant a reduction in the area of the copper pads, thereby giving the means to limit ink wicking from the connected gold circuit lines. In Fig. 6.18b, the NiO dams act as a partial barrier that reduces the area and thus the volume of the wicked gold ink. While in Fig. 6.18c, without the NiO dams, the printed ink spreads onto the pads, resulting in non-uniformity of the printed ink on the copper pad.

After printing, the TV was subjected to simulated thermal and mechanical stressing followed by electrical testing. The electrical resistance measured is the sum of not only the plated copper and printed gold conductors, but also any contribution from the gold/copper interfaces. Fig. 6.19 shows results for the measured DC electrical resistance of the arrays and interfaces before and after exposure to simulated solder reflows and for bend testing. Results of TVs with plated copper pads with plated gold layer but no NiO layer on top, M33 and M34, are shown. M33 was excised and bend tested, whereas M34 was not. There was approximately 25% variation in the array resistances, but each array for all 4 surface variations was shown to be stable as a function of all thermal cycles and bend testing. The slight decrease in resistance with increasing thermal exposures can be attributed to additional sintering on gold nanoparticles by thermal annealing. Again, this indicates that the individual traces and interconnects are robust. Thus, these electrodes, traces and interconnects are suitable for application in the WSP.

Following the thermal stressing and resistance measurements, three individual conductive serpentines were excised from each frame. Each serpentine is in a format that can be readily mounted on the bend cycle fatigue tester to see if resistance changes are detected which are indicative of interfacial failure. It is notable that we did observe some blistering and peeling of gold ink on copper pads following the thermal stresses (Fig. 6.20a and b). This was not observed for gold ink on gold electroplated pads (Fig. 6.20c). We believe this delamination of the gold to be the consequence of oxidative corrosion of the copper pads at the gold ink to plated copper interface, and that protection of the copper pads with a thin capping layer of electroplated nickel/gold prior to printing the gold ink on the pads is able to passivate the copper effectively.

6.9 Battery lifetime of the WSP

Battery lifetime of the WSP depends on the operation of the ECG AFE and the Bluetooth SoC communication protocols. The WSP operates cyclically in major and minor cycles. A

major cycle has an active period followed by a quiescent period that can be of zero duration, i.e., absent. The main reason for operating in this mode is to conserve battery energy during the quiescent state, and collect and send periodic data to the host during the active period. Within a minor cycle, the WSP collects and buffers ECG signals and transmits the collected data. Running the WSP at full transmit power and 100 % duty cycle provides a battery lifetime of 8 hr. At a lower transmission power (-23 dBm) for the Bluetooth transmitter and a reduced duty cycle of 25 %, we observed a drastic improvement of the lifetime to 38 hr.

6.10 Chapter conclusions

FHE brings together flexible sensors and silicon ICs under the same platform and utilizes these two different technologies at their strengths, i.e., flexible sensors for efficient bio-interfaces and silicon ICs for computational purposes. However, interfacing flexible sensors to FPCBs is challenging due to bonding and alignment issues. Our integration scheme where both soft and hard electronics are hosted on one substrate significantly reduces fabrication complexities. Obviating the use of connectors significantly improves the flexibility of the device while keeping the connection integrity intact. Further optimization and improvement can be done on the WSP platform. For example, replacing the coin cell battery from the current design with a thin-film flexible battery would significantly enhance the flexibility of the device [242]. Moreover, integration of additional bioelectronic, biophotonic, and electrochemical sensors can take the application of this WSP platform beyond the fitness domain well into medical diagnostics. Our demonstration of direct integration of printed sensors to hard silicon ICs can serve as a stepping stone for a more sophisticated sensing platform where facile integration of novel solution-processable sensors to silicon ICs will unlock the true sensing capabilities of next-generation flexible sensors without hindering the flexibility and wearability of the device.

Chapter 7

Conclusions & outlook

In this thesis, we first presented a review of existing literature on flexible and wearable health monitoring devices and highlighted the benefits of mechanically flexible sensors and the use of printing techniques for fabricating the sensors. In Chapter 2, we presented the fabrication and low-temperature sintering of printed gold electrodes for bioelectronic interfaces. We demonstrated the efficacy of the electrodes on conformal surfaces and on the skin to record ECG, EMG, and bioimpedance data. For biophotonic sensing, in Chapters 3, we presented an all-organic optoelectronic sensor for pulse oximetry. Which performed on par with existing commercial finger probe pulse oximeters. We also showed the utility of using organic optoelectronics for oximetry. Since transmission-mode oximetry can only be performed at the extremities of the body and requires a pulsatile arterial blood signal, we opted to use reflection-mode oximetry. In Chapters 4 and 5, we demonstrated the design, sensing methodology, and fabrication of printed reflectance oximeters. Using an array of reflection-mode oximeters we performed 2D mapping of oxygen saturation. Finally, in Chapter 6, we discussed a key enabling technology for flexible and printed sensors - flexible hybrid electronics, where soft sensors are interfaced with hard silicon-based integrated circuits for wearable health monitoring.

Overall, we demonstrated two sensing modalities - bioelectronic and biophotonic. The biosignals, sensors, sensing locations and mechanisms are also discussed in detail. The system-level implementation of the flexible and printed sensors are demonstrated via flexible hybrid electronics, where the sensors are interfaced to silicon ICs, bridging soft and hard electronics. Furthermore, this thesis presented wearable medical devices for both vital signs monitoring and medical-grade diagnostics.

While continuing to add devices, tools, and techniques to the library of sensors, it is possible to bring all the sensors to an easy-to-use single platform. The materials and methods utilized here can be expanded to application areas beyond health monitoring. Structural, environmental, and industrial monitoring can be performed using printed sensors, where the large-area printability and flexibility of the sensors can be employed. Some of the prospective projects and the applications scenarios are listed below:

1. Integrated bioelectronic and biophotonic bandage for wound monitoring
2. Wearable multi-sensor platform for continuous health monitoring

3. Printed large-area sensor array for structural health monitoring
4. Flexible hybrid electronics for industrial and environmental monitoring

7.1 Integrated bioelectronic and biophotonic bandage for wound monitoring

Chronic skin wounds, a silent epidemic, results in an estimated US$25 billion cost every year. Lack of a standardized method for wound sensing and monitoring is affecting over 2.5 million patients just in the United States each year [146]. Almost a third of the dermatological health budget in the US is spent on treating chronic skin wounds [147]. An elegant solution to this problem can be realized using flexible printed bioelectronics. The scope of flexible electronics stretches beyond electronic gadgets and has the potential to revolutionize both in-hospital and in-home health monitoring. Flexible electronics for medical sensing is advantageous over conventional electronics because flexible electronics can efficiently extract biomedical signals from conformal surfaces without compromising signal quality. Two of the biggest impediments of implementing a user-friendly and efficient wound sensor are:

- Most sensors are designed using bulky and rigid electronics, which are not comfortable for the patients and do not conform to the skin.
- Wound sensing require high-end optical tools, making the instrument expensive and the measurement cumbersome.

In Chapter 2, we used electrical impedance tomography for mapping wound progression *in vivo* on a rat model [3]. We observed that impedance measurements of tissues *in vivo* correlate better tissue health with more reactive impedance values. And damaged tissue due to pressure demonstrated less reactive impedance values. Impedance was robustly correlated with tissue health across multiple animals. A flexible electrode array was used for mapping the wound, which provided a significant edge over conventional rigid printed circuit boards by conforming to the skin and reaching deep into the wound.

In addition to impedance spectroscopy of wounds (Chapter 2), wound oxygenation data (Chapters 4 and 5) would be beneficial to physicians for treatment planning [243]. A smart bandage that utilizes both impedance spectroscopy and tissue oxygenation to determine wound healing is shown in Fig. 7.1a. In this sensor, printed electrodes are used to collect impedance data from the wound, while the optoelectronics are used to perform tissue oxygenation measurements (Fig. 7.1b). The fabrication and application of the printed electrodes are discussed in Chapter 2. As for the biophotonic sensing, we developed processing techniques for manufacturing the optoelectronic sensing layer - the red (612 nm) and NIR (725 nm) OLEDs and OPDs in Chapters 4 and 5. At these wavelengths, oxyhemoglobin (HbO_2) and deoxyhemoglobin (Hb) have different absorptivities, and the absorption ratio of HbO_2 and Hb at red and NIR wavelengths provide oxygenation. Once the sensor is developed, the bandage can be utilized to monitor wounds in animal models. Different stages of wound healing: (1) the inflammatory phase, (2) the proliferative phase, and (3) the tissue remodeling phase demonstrate various concentration and behavior of wound oxygenation. Furthermore, the effect of oxygen and its

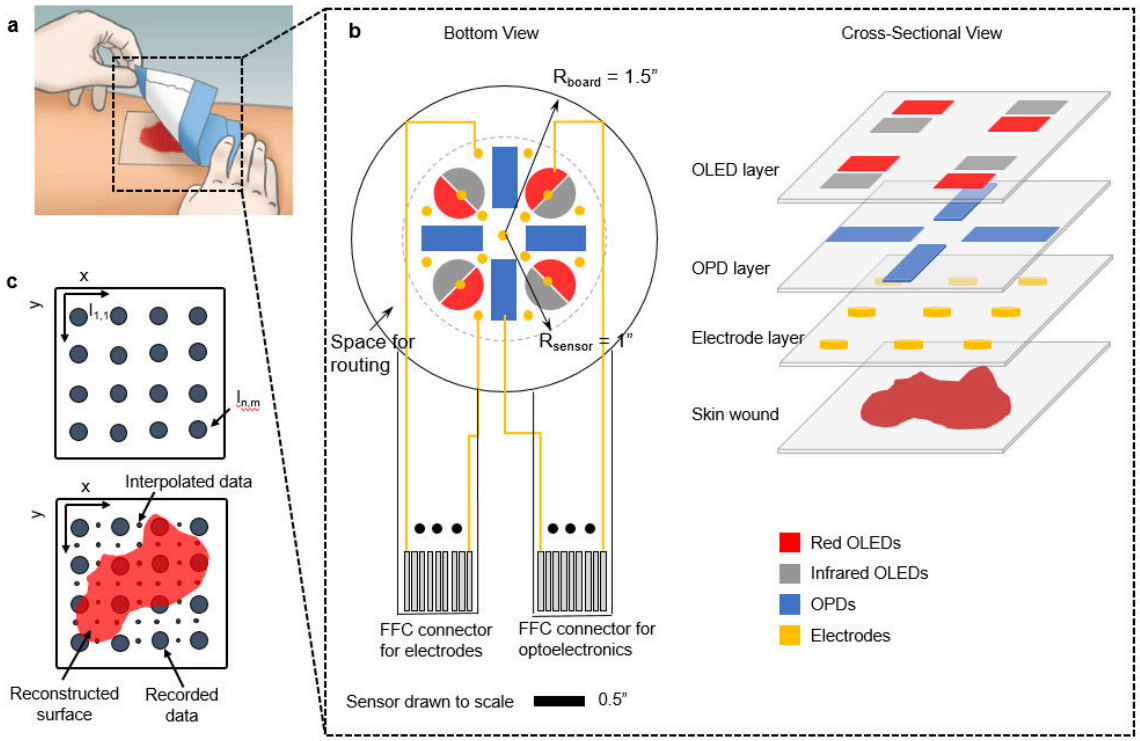

Figure 7.1. **An integrated bioelectronic and biophotonic wound sensing platform**. (**a**) Sensor placement on a skin wound. (**b**) The bottom and cross-sectional views of the sensor. The sensing area with a radius of 1″ (grey dotted circle in the bottom view). (**c**) Collected data is reconstructed by interpolating the data in a 2D space to create spatial maps of impedance and oxygenation.

reactive species on wound healing can be studied, an analytical model, which will correlate oxygen concentration to the stage of the wound can be developed.

Although a vast amount of literature can be found on flexible sensors, studies on the application of flexible sensors for wound monitoring and healing are scarce. The flexible sensor described here applies organic electronics in the medical device field. If implemented in a disposable bandage form factor, an organic medical sensor does not face the stability issues that have hindered organic electronics in long-term applications such as displays and energy harvesting due to the substantially shorter device lifetime required. Rather, the large-area scalability, inexpensive processing and flexibility of flexible organic electronics will allow medical sensors to be made in new shapes and sizes, diversifying possible sensing locations on the human body, enabling medical professionals to better monitor their patients' care. Additionally, impedance and oxygenation mapping for wounds will provide medical professionals with a quantitative measurement of the wound healing, also aid in treatment planning.

7.2 Wearable multi-sensor platform for continuous health monitoring

Wearable non-invasive medical sensing is extremely promising for monitoring stress and human performance during physically demanding tasks. These vital signs, namely, temperature, heart rate, respiration rate, and blood pressure are the measurements of the body's most basic functions and are useful in assessing the physical state of a person. In addition to vital signs, bodily fluids such as sweat and tears also contain a large amount of information on the physiological state of a person. For obtaining an overall snapshot of a person's physiological state, assessing both vital signs and analytes in bodily fluids are essential. To date, a sensor platform capable of simultaneously measuring vital signs and analytes in bodily fluids has not been demonstrated. An integrated sensor platform that can utilize electrochemical sensors and record vital signs simultaneously. This sensor platform is promising for both fitness and medical-grade sensing. Since biosignals can be measured from different parts of the body, this sensor platform can be integrated into clothes, gloves, helmets, shoes, or used standalone as a sensor patch (Fig. 7.2).

Continuous health monitoring via the sensor platform can be used by athletes, pilots, soldiers, and patients. An integrated sensor platform with electrochemical and vital signs is promising for both fitness and medical-grade sensing. An open source project where the hardware, firmware, and software are made available to researchers for enriching the multi-sensor platform will help the whole research community. Using wireless modules, physicians and medical professionals will be able to collect data seamlessly. A variant of this platform can be used for sleep apnea studies, where the electrodes are used to record EEG signal, and the reflectance oximeter records oxygenation. Additionally, developing countries, where medical resources are scarce, can benefit by using the low-cost printed sensors and diagnostic tools. Fabricating medical devices and diagnostic tools with printing techniques can greatly enhance the affordability of healthcare and medical diagnostics in developing counties. Overall, developing and enriching the printed medical sensors can create new avenues for low-cost medical devices, hence helping the developing countries where the need for healthcare is dire.

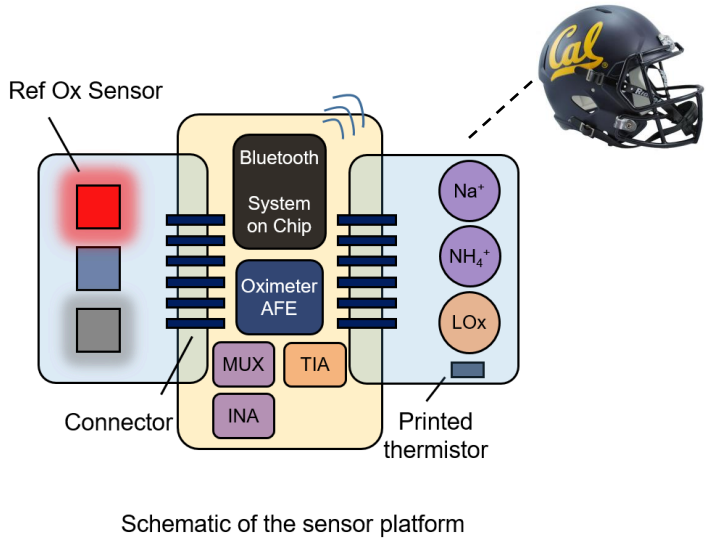

Figure 7.2. An integrated flexible and wearable multi-sensor platform. Both vital signs and analytes in bodily fluids are used to provide an overall snapshot of a person's physiological state.

7.3 Printed large-area sensor array for structural health monitoring

Structural health monitoring (SHM) is an application domain that can be considerably benefited by printed large-area electronics. Civil structures require sensors to be placed over an area to collect information from the structure – silicon electronics over large-area is not as cost-effective as the price of vacuum processing drastically increases with area scaling. On the other hand, printed electronics can be fabricated in roll-to-roll processes on flexible substrates, making them ideal for large-area SHM. The structural integrity of civil infrastructures declines gradually over time – by incorporating printed sensors on the structures, the health of the infrastructure can be estimated through statistical analysis of the sensor data. In the case of natural disasters such as earthquakes, this real-time monitoring of structural health can prove invaluable for preventing loss of life and property. Cumulative absolute velocity (CAV) can be used as an instrumental index to quantify the potential earthquake damage to structures, which can be derived from sensor data [244]. A proposed sensor array for SHM is shown in Fig. 7.3, where an array of strain gauges and accelerometers are used to collect information from the structure, this data can be utilized to monitor the local damage to the structure [245]. Similar approaches can be utilized for monitoring the structural integrity of automotive, airplanes, and machinery. Developing printing techniques for the relevant sensors, and utilizing them for monitoring of civil structures, automotive, airplanes, and machinery can vastly improve SHM.

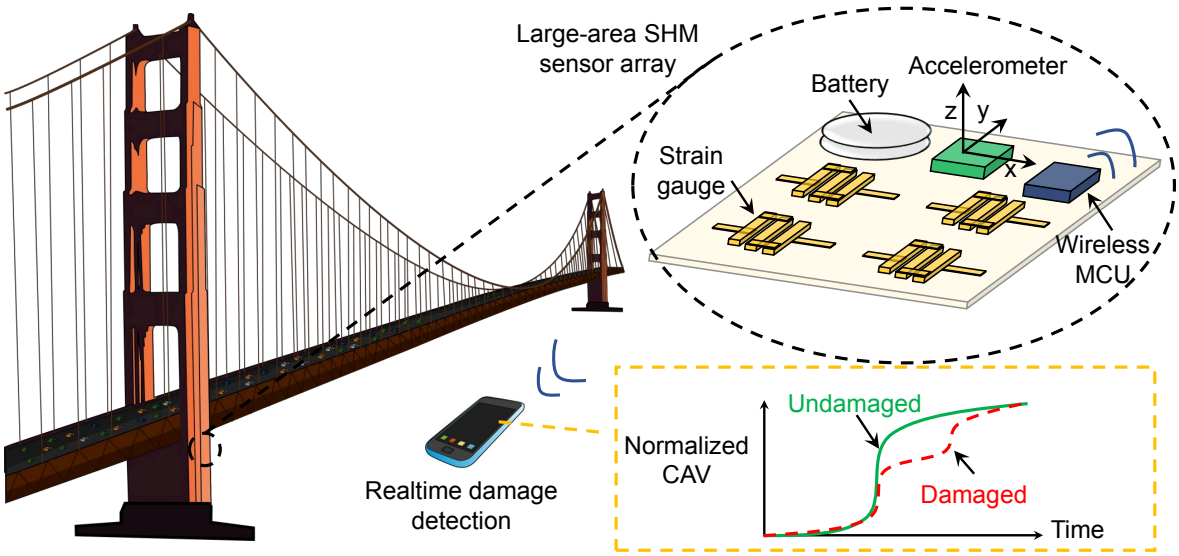

Figure 7.3. Large-area sensor array for structural health monitoring - the health of the infrastructure can be estimated through statistical analysis of the sensor data.

7.4 Flexible hybrid electronics for industrial and environmental monitoring

Flexible hybrid electronics brings together flexible sensors and silicon ICs under the same platform and utilizes these two different technologies to their strengths, i.e., flexible devices for sensing and silicon ICs for computational purposes. While in this thesis we discussed sensors that were designed for medical applications, the same sensors can be purposed for industrial and environmental monitoring. For example, using an array of NiO thermistors, the temperature of batteries can be monitored (Fig. 7.4), which can be used as a safety feature to avoid thermal runaways of batteries [246].

Moreover, printed temperature, humidity, pressure, gas, etc. sensors can be utilized for industrial, environmental, and agricultural applications. When combined with wireless connectivity these sensor nodes will be able to create a smart mesh network, which will provide insights into the products as well as the environment under industrial settings. Additionally, by implementing machine learning algorithms on these sensor systems, anomaly and erratic behavior can be predicted, which can be useful for executing preventative measures, for example, shutting down certain tools in an industry, or notifying workers of a toxic gas leak.

7.5 Outlook

Internet of things (IoT) is growing exponentially, it is expected to hit 30 billion objects by 2020. Flexible and printed sensors are most-suited for large-scale sensing. In the past few years, researchers have been aggressively investigating flexible and printed electronics for sensing applications. Conventionally semiconductor processing is a bit constrained be-

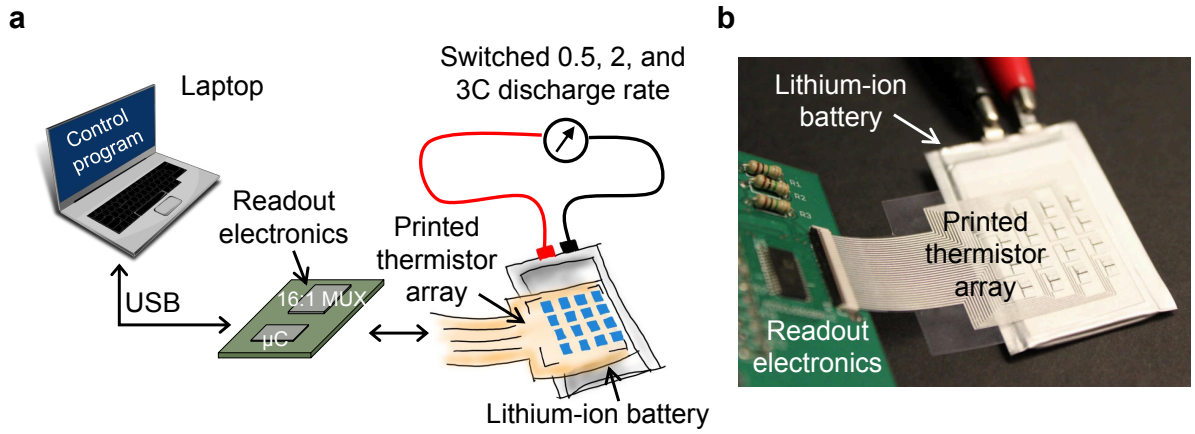

Figure 7.4. Printed nickel oxide thermistor array for mapping the temperature of batteries.

cause vacuum processing is expensive and scaling to large areas is even more challenging. If we can print sensors as we print newspapers that would be the most elegant solution. The cost, form factor and fabrication of printed electronics are a perfect match for medical/environment/agricultural/structural sensing. Coupled with the internet of things and machine learning algorithms, these devices will provide the ideal sensing platform. We will still rely on silicon ICs for data processing and communication, because of the unparallel performance advantage of the silicon ICs. Therefore, flexible hybrid electronics will become the balance of the two fields. We envision in the next 10 years, the emerging field of flexible hybrid electronics will grow not in just academic but also in industrial research. We believe if these devices are implemented using low-cost large-area manufacturing, they can positively impact our community.

Bibliography

[1] Yasser Khan, Aminy E. Ostfeld, Claire M. Lochner, Adrien Pierre, and Ana C. Arias. Monitoring of vital signs with flexible and wearable medical devices. **Advanced Materials**, 28(22):4373–4395, 2016. ISSN 1521-4095. doi: 10.1002/adma.201504366. URL http://onlinelibrary.wiley.com/doi/10.1002/adma.201504366/abstract.

[2] Yasser Khan, Felippe J. Pavinatto, Monica C. Lin, Amy Liao, Sarah L. Swisher, Kaylee Mann, Vivek Subramanian, Michel M. Maharbiz, and Ana C. Arias. Inkjet-printed flexible gold electrode arrays for bioelectronic interfaces. **Advanced Functional Materials**, 26(7):1004–1013, 2016. ISSN 1616-3028. doi: 10.1002/adfm.201503316. URL http://onlinelibrary.wiley.com/doi/10.1002/adfm.201503316/abstract.

[3] Sarah L. Swisher, Monica C. Lin, Amy Liao, Elisabeth J. Leeflang, Yasser Khan, Felippe J. Pavinatto, Kaylee Mann, Agne Naujokas, David Young, Shuvo Roy, Michael R. Harrison, Ana C. Arias, Vivek Subramanian, and Michel M. Maharbiz. Impedance sensing device enables early detection of pressure ulcers in vivo. **Nature Communications**, 6:6575, 2015. doi: 10.1038/ncomms7575. URL http://www.nature.com/ncomms/2015/150317/ncomms7575/full/ncomms7575.html.

[4] Claire M Lochner*, Yasser Khan*, Adrien Pierre*, and Ana C Arias. All-organic optoelectronic sensor for pulse oximetry. **Nature Communications**, 5:5745, 2014.

[5] Yasser Khan*, Donggeon Han*, Jonathan Ting*, Maruf Ahmed*, Ramune Nagisetty, and Ana C. Arias. Organic multi-channel optoelectronic sensors for smart wristbands. 2019. Submitted.

[6] Yasser Khan, Donggeon Han, Adrien Pierre, Jonathan Ting, Xingchun Wang, Claire M Lochner, Gianluca Bovo, Nir Yaacobi-Gross, Chris Newsome, Richard Wilson, et al. A flexible organic reflectance oximeter array. **Proceedings of the National Academy of Sciences**, 115(47):E11015–E11024, 2018.

[7] Yasser Khan, Mohit Garg, Qiong Gui, Mark Schadt, Abhinav Gaikwad, Donggeon Han, Natasha A. D. Yamamoto, Paul Hart, Robert Welte, William Wilson, Steve Czarnecki, Mark Poliks, Zhanpeng Jin, Kanad Ghose, Frank Egitto, James Turner, and Ana C. Arias. Flexible hybrid electronics: Direct interfacing of soft and hard electronics for wearable health monitoring. **Advanced Functional Materials**, 26(47):8764–8775, 2016. ISSN 1616-3028. doi: 10.1002/adfm.201603763.

[8] Varun Soman, Yasser Khan, Madina Zabran, Mark Schadt, Paul Hart, Michael Shay, Frank Egitto, Konstantinos Papathomas, Natasha A. D. Yamamoto, Donggeon Han, Ana C. Arias, Kanad Ghose, Mark D. Poliks, and James N. Turner. Reliability challenges in fabrication of flexible hybrid electronics for human performance monitors: A system level study. 2019. Submitted.

[9] Kevin Tillmann. Understanding the Connected Health and Wellness Market. Technical report, Consumer Electronics Association, 2014.

[10] Jaemin Kim, Mincheol Lee, Hyung Joon Shim, Roozbeh Ghaffari, Hye Rim Cho, Donghee Son, Yei Hwan Jung, Min Soh, Changsoon Choi, Sungmook Jung, et al. Stretchable silicon nanoribbon electronics for skin prosthesis. **Nat. Commun.**, 5, 2014.

[11] James C Barrese, Naveen Rao, Kaivon Paroo, Corey Triebwasser, Carlos Vargas-Irwin, Lachlan Franquemont, and John P Donoghue. Failure mode analysis of silicon-based intracortical microelectrode arrays in non-human primates. **J. Neural Eng.**, 10(6):066014, 2013. URL http://stacks.iop.org/1741-2552/10/i=6/a=066014.

[12] Naoji Matsuhisa, Martin Kaltenbrunner, Tomoyuki Yokota, Hiroaki Jinno, Kazunori Kuribara, Tsuyoshi Sekitani, and Takao Someya. Printable elastic conductors with a high conductivity for electronic textile applications. **Nat. Commun.**, 6, 2015.

[13] Tsuyoshi Sekitani, Hiroyoshi Nakajima, Hiroki Maeda, Takanori Fukushima, Takuzo Aida, Kenji Hata, and Takao Someya. Stretchable active-matrix organic light-emitting diode display using printable elastic conductors. **Nat. Mater.**, 8(6):494–499, 2009.

[14] Jeonghyun Kim, Anthony Banks, Huanyu Cheng, Zhaoqian Xie, Sheng Xu, Kyung-In Jang, Jung Woo Lee, Zhuangjian Liu, Philipp Gutruf, Xian Huang, et al. Epidermal Electronics with Advanced Capabilities in Near-Field Communication. **Small**, 11(8):906–912, 2015.

[15] Dae-Hyeong Kim, Nanshu Lu, Roozbeh Ghaffari, Yun-Soung Kim, Stephen P Lee, Lizhi Xu, Jian Wu, Rak-Hwan Kim, Jizhou Song, Zhuangjian Liu, et al. Materials for multifunctional balloon catheters with capabilities in cardiac electrophysiological mapping and ablation therapy. **Nat. Mater.**, 10(4):316–323, 2011.

[16] Medical Device. Technical report, US Food and Drug Administration, 2015. URL http://www.fda.gov/aboutfda/transparency/basics/ucm211822.htm.

[17] David Evans, Brent Hodgkinson, and Judith Berry. Vital signs in hospital patients: a systematic review. **Int. J. Nurs. Stud.**, 38(6):643–650, 2001.

[18] Yasutoshi Makino, Shuhei Ogawa, and Hiroyuki Shinoda. Flexible emg sensor array for haptic interface. In *SICE Annual Conference, 2008*, pages 1468–1473. IEEE, 2008.

[19] Xu Zhang, Xiang Chen, Wen-hui Wang, Ji-hai Yang, Vuokko Lantz, and Kong-qiao Wang. Hand gesture recognition and virtual game control based on 3d accelerometer and emg sensors. In *Proceedings of the 14th international conference on Intelligent user interfaces*, pages 401–406. ACM, 2009.

[20] Bjarne W Olesen. Thermal Comfort. **Technical Review**, 2:3–37, 1982.

[21] Chaoyi Yan, Jiangxin Wang, and Pooi See Lee. Stretchable Graphene Thermistor with Tunable Thermal Index. **ACS Nano**, 9(2):2130–2137, 2015. doi: 10.1021/nn507441c. URL http://dx.doi.org/10.1021/nn507441c. PMID: 25671368.

[22] Alessio Giuliani, Massimo Placidi, Fabio Di Francesco, and Andrea Pucci. A new polystyrene-based ionomer/MWCNT nanocomposite for wearable skin temperature sensors. **React. Funct. Polym.**, 76:57–62, 2014.

[23] Wataru Honda, Shingo Harada, Takayuki Arie, Seiji Akita, and Kuniharu Takei. Wearable, Human-Interactive, Health-Monitoring, Wireless Devices Fabricated by Macroscale Printing Techniques. **Adv. Funct. Mater.**, 24(22):3299–3304, 2014. ISSN 1616-3028. doi: 10.1002/adfm.201303874. URL http://dx.doi.org/10.1002/adfm.201303874.

[24] Chun-Chih Huang, Zhen-Kai Kao, and Ying-Chih Liao. Flexible miniaturized nickel oxide thermistor arrays via inkjet printing technology. **ACS Applied Materials & Interfaces**, 5(24):12954–12959, 2013.

[25] Ya Yang, Zong-Hong Lin, Techien Hou, Fang Zhang, and Zhong Lin Wang. Nanowire-composite based flexible thermoelectric nanogenerators and self-powered temperature sensors. **Nano Res.**, 5(12):888–895, 2012.

[26] Weitai Wu, Jing Shen, Probal Banerjee, and Shuiqin Zhou. Core–shell hybrid nanogels for integration of optical temperature-sensing, targeted tumor cell imaging, and combined chemo-photothermal treatment. **Biomaterials**, 31(29):7555–7566, 2010.

[27] Jin Jeon, Han-Bo-Ram Lee, and Zhenan Bao. Flexible Wireless Temperature Sensors Based on Ni Microparticle-Filled Binary Polymer Composites. **Adv. Mater.**, 25(6):850–855, 2013.

[28] Carlo Alberto Boano, Matteo Lasagni, Kay Romer, and Tanja Lange. Accurate temperature measurements for medical research using body sensor networks. In *Object/Component/Service-Oriented Real-Time Distributed Computing Workshops (ISORCW), 2011 14th IEEE International Symposium on*, pages 189–198. IEEE, 2011.

[29] Rainer Lenhardt and Daniel I Sessler. Estimation of mean-body temperature from mean-skin and core temperature. **Anesthesiology**, 105(6):1117, 2006.

[30] Margaret V Savage and George L Brengelmann. Control of skin blood flow in the neutral zone of human body temperature regulation. **J. Appl. Physiol.**, 80(4):1249–1257, 1996.

[31] Victoria L Richmond, Sarah Davey, Katy Griggs, and George Havenith. Prediction of core body temperature from multiple variables. **Ann. Occup. Hyg.**, page mev054, 2015.

[32] Xiaojiang Xu, Anthony J Karis, Mark J Buller, and William R Santee. Relationship between core temperature, skin temperature, and heat flux during exercise in heat. **Eur. J. Appl. Physiol.**, 113(9):2381–2389, 2013.

[33] Sheng Xu, Yihui Zhang, Lin Jia, Kyle E. Mathewson, Kyung-In Jang, Jeonghyun Kim, Haoran Fu, Xian Huang, Pranav Chava, Renhan Wang, Sanat Bhole, Lizhe Wang, Yoon Joo Na, Yue Guan, Matthew Flavin, Zheshen Han, Yonggang Huang, and John A. Rogers. Soft microfluidic assemblies of sensors, circuits, and radios for the skin. **Science**, 344(6179):70–74, 2014.

[34] Pierre Leleux, Camryn Johnson, Xenofon Strakosas, Jonathan Rivnay, Thierry Hervé, Róisín M Owens, and George G Malliaras. Ionic Liquid Gel-Assisted Electrodes for Long-Term Cutaneous Recordings. **Adv. Healthcare Mater.**, 3(9):1377–1380, 2014.

[35] Ebrahim Nemati, M Jamal Deen, and Tapas Mondal. A wireless wearable ECG sensor for long-term applications. **IEEE Commun. Mag.**, 50(1):36–43, 2012.

[36] Stephen E Derenzo. **Practical Interfacing in the Laboratory: Using a PC for Instrumentation, Data Analysis and Control**. Cambridge University Press, 2003.

[37] Ju-Yeoul Baek, Jin-Hee An, Jong-Min Choi, Kwang-Suk Park, and Sang-Hoon Lee. Flexible polymeric dry electrodes for the long-term monitoring of ECG. **Sens. Actuators, A**, 143(2):423–429, 2008.

[38] Ha-Chul Jung, Jin-Hee Moon, Dong-Hyun Baek, Jae-Hee Lee, Yoon-Young Choi, Joung-Sook Hong, and Sang-Hoon Lee. CNT/PDMS composite flexible dry electrodesfor long-term ECG monitoring. **IEEE Trans. Biomed. Eng.**, 59(5):1472–1479, 2012.

[39] Gi Seok Jeong, Dong-Hyun Baek, Ha Chul Jung, Ji Hoon Song, Jin Hee Moon, Suck Won Hong, In Young Kim, and Sang-Hoon Lee. Solderable and electroplatable flexible electronic circuit on a porous stretchable elastomer. **Nature communications**, 3:977, 2012.

[40] Prashanth Shyamkumar, Pratyush Rai, Sechang Oh, Mouli Ramasamy, Robert E Harbaugh, and Vijay Varadan. Wearable wireless cardiovascular monitoring using textile-based nanosensor and nanomaterial systems. **Electronics**, 3(3):504–520, 2014.

[41] Jerald Yoo, Long Yan, Seulki Lee, Hyejung Kim, and Hoi-Jun Yoo. A wearable ECG acquisition system with compact planar-fashionable circuit board-based shirt. **IEEE Trans. Inf. Technol. Biomed.**, 13(6):897–902, 2009.

[42] Gregor Schwartz, Benjamin C-K Tee, Jianguo Mei, Anthony L Appleton, Do Hwan Kim, Huiliang Wang, and Zhenan Bao. Flexible polymer transistors with high pressure sensitivity for application in electronic skin and health monitoring. **Nat. Commun.**, 4:1859, 2013.

[43] Baoqing Nie, Siyuan Xing, James D Brandt, and Tingrui Pan. Droplet-based interfacial capacitive sensing. **Lab Chip**, 12(6):1110–1118, 2012.

[44] Yu Mike Chi, Tzyy-Ping Jung, and Gert Cauwenberghs. Dry-contact and noncontact biopotential electrodes: methodological review. **IEEE Rev. Biomed. Eng.**, 3:106–119, 2010.

[45] Alexsandr Igorevitch Ianov, Hiroaki Kawamoto, and Yoshiyuki Sankai. Development of a capacitive coupling electrode for bioelectrical signal measurements and assistive device use. In *Complex Medical Engineering (CME), 2012 ICME International Conference on*, pages 593–598, 2012.

[46] Yu M Chi, Stephen R Deiss, and Gert Cauwenberghs. Non-contact low power EEG/ECG electrode for high density wearable biopotential sensor networks. In *Wearable and Implantable Body Sensor Networks, 2009. BSN 2009. Sixth International Workshop on*, pages 246–250, 2009.

[47] L. Guo, L. Berglin, U. Wiklund, and H. Mattila. Design of a garment-based sensing system for breathing monitoring. **Text. Res. J.**, 83(5):499–509, nov 2012. doi: 10.1177/0040517512444336. URL http://dx.doi.org/10.1177/0040517512444336.

[48] Se Dong Min, Yonghyeon Yun, and Hangsik Shin. Simplified Structural Textile Respiration Sensor Based on Capacitive Pressure Sensing Method. **IEEE Sensors J.**, 14(9): 3245–3251, sep 2014. doi: 10.1109/jsen.2014.2327991. URL http://dx.doi.org/10.1109/jsen.2014.2327991.

[49] Ozgur Atalay, William Richard Kennon, and Erhan Demirok. Weft-Knitted Strain Sensor for Monitoring Respiratory Rate and Its Electro-Mechanical Modeling. **IEEE Sensors J.**, 15(1):110–122, jan 2015. doi: 10.1109/jsen.2014.2339739. URL http://dx.doi.org/10.1109/jsen.2014.2339739.

[50] R. D. Allison, E. L. Holmes, and J. Nyboer. Volumetric dynamics of respiration as measured by electrical impedance plethysmography. **J. Appl. Physiol.**, 19(1):166–173, Jan 1964. URL http://jap.physiology.org/content/19/1/166.full-text.pdf+html.

[51] M. Folke, L. Cernerud, M. Ekstrm, and B. Hk. Critical review of non-invasive respiratory monitoring in medical care. **Med. Biol. Eng. Comput.**, 41(4):377383, Jul 2003. ISSN 0140-0118. doi: 10.1007/BF02348078. URL http://link.springer.com/10.1007/BF02348078.

[52] F Q Al-Khalidi, R Saatchi, D Burke, H Elphick, and S Tan. Respiration rate monitoring methods: a review. **Pediatr. Pulmonol.**, 46(6):5239, Jun 2011. ISSN 1099-0496. doi: 10.1002/ppul.21416. URL http://www.ncbi.nlm.nih.gov/pubmed/21560260.

[53] Phil Corbishley and Esther Rodriguez-Villegas. Breathing detection: Towards a miniaturized, wearable, battery-operated monitoring system. **IEEE Trans. Biomed. Eng.**, 55 (1):196204, Jan 2008. ISSN 0018-9294. doi: 10.1109/TBME.2007.910679. URL http://ieeexplore.ieee.org/lpdocs/epic03/wrapper.htm?arnumber=4404082.

[54] O. Mimoz, T. Benard, A. Gaucher, D. Frasca, and B. Debaene. Accuracy of respiratory rate monitoring using a non-invasive acoustic method after general anaesthesia. **Brit. J. Anaesth.**, 108(5):872875, Feb 2012. ISSN 0007-0912. doi: 10.1093/bja/aer510. URL http://bja.oxfordjournals.org/content/108/5/872.abstract.

[55] K P Cohen, W M Ladd, D M Beams, W S Sheers, R G Radwin, W J Tompkins, and J G Webster. Comparison of impedance and inductance ventilation sensors on adults during

breathing, motion, and simulated airway obstruction. **IEEE Trans. Biomed. Eng.**, 44(7): 55566, Jul 1997. ISSN 0018-9294. doi: 10.1109/10.594896. URL http://www.ncbi.nlm.nih.gov/pubmed/9210815.

[56] C.R. Merritt, H.T. Nagle, and E. Grant. Textile-Based Capacitive Sensors for Respiration Monitoring. **IEEE Sensors J.**, 9(1):71–78, jan 2009. doi: 10.1109/jsen.2008.2010356. URL http://dx.doi.org/10.1109/JSEN.2008.2010356.

[57] G Kim Prisk, J Hammer, and Christopher J L Newth. Techniques for measurement of thoracoabdominal asynchrony. **Pediatr. Pulmonol.**, 34(6):46272, Dec 2002. ISSN 8755-6863. doi: 10.1002/ppul.10204. URL http://www.ncbi.nlm.nih.gov/pubmed/12422344.

[58] Subrata Kumar Kundu, Shinya Kumagai, and Minoru Sasaki. A Wearable Capacitive Sensor for Monitoring Human Respiratory Rate. **Jpn. J. Appl. Phys.**, 52(4S):04CL05, apr 2013. doi: 10.7567/jjap.52.04cl05. URL http://dx.doi.org/10.7567/JJAP.52.04CL05.

[59] Takeo Yamada, Yuhei Hayamizu, Yuki Yamamoto, Yoshiki Yomogida, Ali Izadi-Najafabadi, Don N. Futaba, and Kenji Hata. A stretchable carbon nanotube strain sensor for human-motion detection. **Nat. Nanotechnol.**, 6(5):296–301, mar 2011. doi: 10.1038/nnano.2011.36. URL http://dx.doi.org/10.1038/nnano.2011.36.

[60] Yan Wang, Li Wang, Tingting Yang, Xiao Li, Xiaobei Zang, Miao Zhu, Kunlin Wang, Dehai Wu, and Hongwei Zhu. Wearable and Highly Sensitive Graphene Strain Sensors for Human Motion Monitoring. **Adv. Funct. Mater.**, 24(29):4666–4670, apr 2014. doi: 10.1002/adfm.201400379. URL http://dx.doi.org/10.1002/adfm.201400379.

[61] Ching-Tang Huang, Chien-Lung Shen, Chien-Fa Tang, and Shuo-Hung Chang. A wearable yarn-based piezo-resistive sensor. **Sens. Actuators, A**, 141(2):396–403, feb 2008. doi: 10.1016/j.sna.2007.10.069. URL http://dx.doi.org/10.1016/j.sna.2007.10.069.

[62] R. Wijesiriwardana. Inductive fiber-meshed strain and displacement transducers for respiratory measuring systems and motion capturing systems. **IEEE Sensors J.**, 6(3):571–579, jun 2006. doi: 10.1109/jsen.2006.874488. URL http://dx.doi.org/10.1109/JSEN.2006.874488.

[63] T. Hoffmann, B. Eilebrecht, and S. Leonhardt. Respiratory Monitoring System on the Basis of Capacitive Textile Force Sensors. **IEEE Sensors J.**, 11(5):1112–1119, may 2011. doi: 10.1109/jsen.2010.2082524. URL http://dx.doi.org/10.1109/JSEN.2010.2082524.

[64] Yuanqing Li, Yarjan Abdul Samad, and Kin Liao. From cotton to wearable pressure sensor. **J. Mater. Chem. A**, 3(5):2181–2187, 2015. doi: 10.1039/c4ta05810k. URL http://dx.doi.org/10.1039/c4ta05810k.

[65] Elena Laukhina, Raphael Pfattner, Lourdes R. Ferreras, Simona Galli, Marta Mas-Torrent, Norberto Masciocchi, Vladimir Laukhin, Concepció Rovira, and Jaume Veciana. Ultrasensitive Piezoresistive All-Organic Flexible Thin Films. **Adv. Mater.**, 22(9):977–981, dec 2009. doi: 10.1002/adma.200902639. URL http://dx.doi.org/10.1002/adma.200902639.

[66] Thomas Allsop, Karen Carroll, Glynn Lloyd, David J. Webb, Martin Miller, and Ian Bennion. Application of long-period-grating sensors to respiratory plethysmography. **J. Biomed. Opt.**, 12(6):064003, 2007. doi: 10.1117/1.2821198. URL http://dx.doi.org/10.1117/1.2821198.

[67] A. Grillet, D. Kinet, J. Witt, M. Schukar, K. Krebber, F. Pirotte, and A. Depre. Optical Fiber Sensors Embedded Into Medical Textiles for Healthcare Monitoring. **IEEE Sensors J.**, 8 (7):1215–1222, jul 2008. doi: 10.1109/jsen.2008.926518. URL http://dx.doi.org/10.1109/JSEN.2008.926518.

[68] W. Zheng, X. Tao, B. Zhu, G. Wang, and C. Hui. Fabrication and evaluation of a notched polymer optical fiber fabric strain sensor and its application in human respiration monitoring. **Text. Res. J.**, 84(17):1791–1802, apr 2014. doi: 10.1177/0040517514528560. URL http://dx.doi.org/10.1177/0040517514528560.

[69] Conor S. Boland, Umar Khan, Claudia Backes, Arlene O'Neill, Joe McCauley, Shane Duane, Ravi Shanker, Yang Liu, Izabela Jurewicz, Alan B. Dalton, and Jonathan N. Coleman. Sensitive High-Strain, High-Rate Bodily Motion Sensors Based on Graphene–Rubber Composites. **ACS Nano**, 8(9):8819–8830, sep 2014. doi: 10.1021/nn503454h. URL http://dx.doi.org/10.1021/nn503454h.

[70] Le Cai, Li Song, Pingshan Luan, Qiang Zhang, Nan Zhang, Qingqing Gao, Duan Zhao, Xiao Zhang, Min Tu, Feng Yang, Wenbin Zhou, Qingxia Fan, Jun Luo, Weiya Zhou, Pulickel M. Ajayan, and Sishen Xie. Super-stretchable Transparent Carbon Nanotube-Based Capacitive Strain Sensors for Human Motion Detection. **Sci. Rep.**, 3, oct 2013. doi: 10.1038/srep03048. URL http://dx.doi.org/10.1038/srep03048.

[71] Canan Dagdeviren, Yewang Su, Pauline Joe, Raissa Yona, Yuhao Liu, Yun-Soung Kim, YongAn Huang, Anoop R Damadoran, Jing Xia, Lane W Martin, et al. Conformable amplified lead zirconate titanate sensors with enhanced piezoelectric response for cutaneous pressure monitoring. **Nat. Commun.**, 5, 2014.

[72] Satu Rajala and Jukka Lekkala. Film-Type Sensor Materials PVDF and EMFi in Measurement of Cardiorespiratory Signals - A Review. **IEEE Sensors J.**, 12(3):439–446, mar 2012. doi: 10.1109/jsen.2010.2089510. URL http://dx.doi.org/10.1109/JSEN.2010.2089510.

[73] Yi-Yuan Chiu, Wan-Ying Lin, Hsin-Yao Wang, Song-Bin Huang, and Min-Hsien Wu. Development of a piezoelectric polyvinylidene fluoride (PVDF) polymer-based sensor patch for simultaneous heartbeat and respiration monitoring. **Sens. Actuators, A**, 189: 328–334, jan 2013. doi: 10.1016/j.sna.2012.10.021. URL http://dx.doi.org/10.1016/j.sna.2012.10.021.

[74] Fang Yi, Long Lin, Simiao Niu, Po Kang Yang, Zhaona Wang, Jun Chen, Yusheng Zhou, Yunlong Zi, Jie Wang, Qingliang Liao, Yue Zhang, and Zhong Lin Wang. Stretchable-Rubber-Based Triboelectric Nanogenerator and Its Application as Self-Powered Body Motion Sensors. **Adv. Funct. Mater.**, 25(24):3688–3696, may 2015. doi: 10.1002/adfm.201500428. URL http://dx.doi.org/10.1002/adfm.201500428.

[75] Brit M Quandt, Lukas J Scherer, Luciano F Boesel, Martin Wolf, Gian-Luca Bona, and René M Rossi. Body-Monitoring and Health Supervision by Means of Optical Fiber-Based Sensing Systems in Medical Textiles. **Adv. Healthcare Mater.**, 4(3):330–355, 2015.

[76] Alberto P Avolio, Mark Butlin, and Andrew Walsh. Arterial blood pressure measurement and pulse wave analysis—their role in enhancing cardiovascular assessment. **Physiol. Meas.**, 31(1):R1, 2010.

[77] Ruya Li, Baoqing Nie, Philip Digiglio, and Tingrui Pan. Microflotronics: A Flexible, Transparent, Pressure-Sensitive Microfluidic Film. **Adv. Funct. Mater.**, 24(39):6195–6203, 2014.

[78] Zetang Li and Zhong Lin Wang. Air/Liquid-Pressure and Heartbeat-Driven Flexible Fiber Nanogenerators as a Micro/Nano-Power Source or Diagnostic Sensor. **Adv. Mater.**, 23(1):84–89, 2011.

[79] Xuewen Wang, Yang Gu, Zuoping Xiong, Zheng Cui, and Ting Zhang. Silk-Molded Flexible, Ultrasensitive, and Highly Stable Electronic Skin for Monitoring Human Physiological Signals. **Adv. Mater.**, 26(9):1336–1342, 2014.

[80] Chwee-Lin Choong, Mun-Bo Shim, Byoung-Sun Lee, Sanghun Jeon, Dong-Su Ko, Tae-Hyung Kang, Jihyun Bae, Sung Hoon Lee, Kyung-Eun Byun, Jungkyun Im, et al. Highly stretchable resistive pressure sensors using a conductive elastomeric composite on a micropyramid array. **Adv. Mater.**, 26(21):3451–3458, 2014.

[81] Nan Wu, Xiaofeng Cheng, Qize Zhong, Junwen Zhong, Wenbo Li, Bo Wang, Bin Hu, and Jun Zhou. Cellular Polypropylene Piezoelectret for Human Body Energy Harvesting and Health Monitoring. **Adv. Funct. Mater.**, 25(30):4788–4794, 2015.

[82] S Terry, JS Eckerle, RD Kornbluh, T Low, and CM Ablow. Silicon pressure transducer arrays for blood-pressure measurement. **Sens. Actuators, A**, 23(1):1070–1079, 1990.

[83] Takao Someya, Tsuyoshi Sekitani, Shingo Iba, Yusaku Kato, Hiroshi Kawaguchi, and Takayasu Sakurai. A large-area, flexible pressure sensor matrix with organic field-effect transistors for artificial skin applications. **PNAS**, 101(27):9966–9970, 2004.

[84] Kyu-Ho Shin, Chang-Ryoul Moon, Tae-Hee Lee, Chang-Hyun Lim, and Yong-Jun Kim. Flexible wireless pressure sensor module. **Sens. Actuators, A**, 123:30–35, 2005.

[85] Stefan CB Mannsfeld, Benjamin CK Tee, Randall M Stoltenberg, Christopher V HH Chen, Soumendra Barman, Beinn VO Muir, Anatoliy N Sokolov, Colin Reese, and Zhenan Bao. Highly sensitive flexible pressure sensors with microstructured rubber dielectric layers. **Nat. Mater.**, 9(10):859–864, 2010.

[86] Benjamin C-K Tee, Alex Chortos, Roger R Dunn, Gregory Schwartz, Eric Eason, and Zhenan Bao. Tunable Flexible Pressure Sensors using Microstructured Elastomer Geometries for Intuitive Electronics. **Adv. Funct. Mater.**, 24(34):5427–5434, 2014.

[87] Steve Park, Hyunjin Kim, Michael Vosgueritchian, Sangmo Cheon, Hyeok Kim, Ja Hoon Koo, Taeho Roy Kim, Sanghyo Lee, Gregory Schwartz, Hyuk Chang, et al. Stretchable Energy-Harvesting Tactile Electronic Skin Capable of Differentiating Multiple Mechanical Stimuli Modes. **Adv. Mater.**, 26(43):7324–7332, 2014.

[88] Moon Kee Choi, Ok Kyu Park, Changsoon Choi, Shutao Qiao, Roozbeh Ghaffari, Jaemin Kim, Dong Jun Lee, Myungbin Kim, Wonji Hyun, Seok Joo Kim, et al. Cephalopod-Inspired Miniaturized Suction Cups for Smart Medical Skin. **Adv. Healthcare Mater.**, 2015.

[89] John G. Webster. **Design of Pulse Oximeters**. Taylor and Francis, 1997.

[90] Yasser Khan, Claire M Lochner, Adrien Pierre, and Ana Claudia Arias. System design for organic pulse oximeter. In *Advances in Sensors and Interfaces (IWASI), 2015 6th IEEE International Workshop on*, pages 83–86. IEEE, 2015.

[91] Ashu K Bansal, Shuoben Hou, Olena Kulyk, Eric M Bowman, and Ifor DW Samuel. Wearable organic optoelectronic sensors for medicine. **Advanced Materials**, 27(46):7638–7644, 2015.

[92] Markus Rothmaier, Bärbel Selm, Sonja Spichtig, Daniel Haensse, and Martin Wolf. Photonic textiles for pulse oximetry. **Opt. Express**, 16(17):12973–12986, Aug 2008. doi: 10.1364/OE.16.012973. URL http://www.opticsexpress.org/abstract.cfm?URI=oe-16-17-12973.

[93] Ana Claudia Arias, J Devin MacKenzie, Iain McCulloch, Jonathan Rivnay, and Alberto Salleo. Materials and applications for large area electronics: solution-based approaches. **Chem. Rev.**, 110(1):3–24, 2010.

[94] Heung Cho Ko, Mark P Stoykovich, Jizhou Song, Viktor Malyarchuk, Won Mook Choi, Chang-Jae Yu, Joseph B Geddes Iii, Jianliang Xiao, Shuodao Wang, Yonggang Huang, et al. A hemispherical electronic eye camera based on compressible silicon optoelectronics. **Nature**, 454(7205):748–753, 2008.

[95] Jonathan Viventi, Dae-Hyeong Kim, Joshua D Moss, Yun-Soung Kim, Justin A Blanco, Nicholas Annetta, Andrew Hicks, Jianliang Xiao, Younggang Huang, David J Callans, et al. A conformal, bio-interfaced class of silicon electronics for mapping cardiac electrophysiology. **Sci. Transl. Med.**, 2(24):24ra22–24ra22, 2010.

[96] Meriem B Akin and Ana C Arias. A Comprehensive Surface Mount Technology Solution for Integrated Circuits onto Flexible Screen Printed Electrical Interconnects. Technical report, DTIC Document, 2014.

[97] Adrien Pierre, Mahsa Sadeghi, Marcia M Payne, Antonio Facchetti, John E Anthony, and Ana Claudia Arias. All-Printed Flexible Organic Transistors Enabled by Surface Tension-Guided Blade Coating. **Adv. Mater.**, 26(32):5722–5727, 2014.

[98] Frederik C Krebs. Fabrication and processing of polymer solar cells: a review of printing and coating techniques. **Sol. Energy Mater. Sol. Cells**, 93(4):394–412, 2009.

[99] Hongki Kang, Rungrot Kitsomboonloha, Kurt Ulmer, Lisa Stecker, Gerd Grau, Jaewon Jang, and Vivek Subramanian. Megahertz-class printed high mobility organic thin-film transistors and inverters on plastic using attoliter-scale high-speed gravure-printed sub-5μm gate electrodes. **Org. Electron.**, 15(12):3639–3647, 2014.

[100] Adrien Pierre, Igal Deckman, Pierre Balthazar Lechêne, and Ana Claudia Arias. High detectivity all-printed organic photodiodes. **Advanced Materials**, 27(41):6411–6417, 2015.

[101] Matthew D Fagan, Byung H Kim, and Donggang Yao. A novel process for continuous thermal embossing of large-area nanopatterns onto polymer films. **Adv. Polym. Tech.**, 28(4):246–256, 2009.

[102] Nobutoshi Komuro, Shunsuke Takaki, Koji Suzuki, and Daniel Citterio. Inkjet printed (bio) chemical sensing devices. **Anal. Bioanal.Chem.**, 405(17):5785–5805, 2013.

[103] Wenzhao Jia, Amay J. Bandodkar, Gabriela Valds-Ramrez, Joshua R. Windmiller, Zhanjun Yang, Julian Ramrez, Garrett Chan, and Joseph Wang. Electrochemical tattoo biosensors for real-time noninvasive lactate monitoring in human perspiration. **Anal. Chem.**, 85 (14):6553–6560, 2013. doi: 10.1021/ac401573r. URL http://dx.doi.org/10.1021/ac401573r. PMID: 23815621.

[104] Amay J Bandodkar, Denise Molinnus, Omar Mirza, Tomás Guinovart, Joshua R Windmiller, Gabriela Valdés-Ramírez, Francisco J Andrade, Michael J Schöning, and Joseph Wang. Epidermal tattoo potentiometric sodium sensors with wireless signal transduction for continuous non-invasive sweat monitoring. **Biosens. Bioelectron.**, 54:603–609, 2014.

[105] Abhinav M. Gaikwad, Brian V. Khau, Greg Davies, Benjamin Hertzberg, Daniel A. Steingart, and Ana Claudia Arias. A High Areal Capacity Flexible Lithium-Ion Battery with a Strain-Compliant Design. **Adv. Energy Mater.**, 5(3), sep 2014. doi: 10.1002/aenm.201401389. URL http://dx.doi.org/10.1002/aenm.201401389.

[106] Felippe J Pavinatto, Carlos WA Paschoal, and Ana C Arias. Printed and flexible biosensor for antioxidants using interdigitated ink-jetted electrodes and gravure-deposited active layer. **Biosens. Bioelectron.**, 67(17):553–559, 2015.

[107] Dan Soltman, Ben Smith, Hongki Kang, SJS Morris, and Vivek Subramanian. Methodology for inkjet printing of partially wetting films. **Langmuir**, 26(19):15686–15693, 2010.

[108] Kyle Braam and Vivek Subramanian. A Stencil Printed High Energy Density Silver Oxide Battery Using a Novel Photopolymerizable Poly(acrylic acid) Separator. **Adv. Mater.**, 27 (4):689–694, dec 2014. doi: 10.1002/adma.201404149. URL http://dx.doi.org/10.1002/adma.201404149.

[109] Abhinav M Gaikwad, Gregory L Whiting, Daniel A Steingart, and Ana Claudia Arias. Highly flexible, printed alkaline batteries based on mesh-embedded electrodes. **Adv. Mater.**, 23(29):3251–3255, 2011.

[110] Abhinav M Gaikwad, Alla M Zamarayeva, Jamesley Rousseau, Howie Chu, Irving Derin, and Daniel A Steingart. Highly stretchable alkaline batteries based on an embedded conductive fabric. **Adv. Mater.**, 24(37):5071–5076, Sep 2012. ISSN 1521-4095. doi: 10.1002/adma.201201329. URL http://www.ncbi.nlm.nih.gov/pubmed/22760812.

[111] John Webster. **Medical Instrumentation: Application and Design**. John Wiley & Sons, 2009.

[112] Yu-Te Liao, Huanfen Yao, B. Parviz, and B. Otis. A 3μW wirelessly powered CMOS glucose sensor for an active contact lens. In *Solid-State Circuits Conference Digest of Technical Papers (ISSCC), 2011 IEEE International*, pages 38–40, Feb 2011. doi: 10.1109/ISSCC.2011.5746209.

[113] Po-Kang Yang, Long Lin, Fang Yi, Xiuhan Li, Ken C. Pradel, Yunlong Zi, Chih-I Wu, Jr-Hau He, Yue Zhang, and Zhong Lin Wang. A Flexible Stretchable and Shape-Adaptive Approach for Versatile Energy Conversion and Self-Powered Biomedical Monitoring. **Adv. Mater.**, 27(25):3817–3824, may 2015. doi: 10.1002/adma.201500652. URL http://dx.doi.org/10.1002/adma.201500652.

[114] J. Devin MacKenzie and Christine Ho. Perspectives on Energy Storage for Flexible Electronic Systems. **Proc. IEEE**, 103(4):535–553, apr 2015. doi: 10.1109/jproc.2015.2406340. URL http://dx.doi.org/10.1109/JPROC.2015.2406340.

[115] James P. Dieffenderfer, Eric Beppler, Tristan Novak, Eric Whitmire, Rochana Jayakumar, Clive Randall, Weiguo Qu, Ramakrishnan Rajagopalan, and Alper Bozkurt. Solar powered wrist worn acquisition system for continuous photoplethysmogram monitoring. In *2014 36th Annual International Conference of the IEEE Engineering in Medicine and Biology Society*. Institute of Electrical & Electronics Engineers (IEEE), aug 2014. doi: 10.1109/embc.2014.6944289. URL http://dx.doi.org/10.1109/embc.2014.6944289.

[116] Mieke Van Bavel, Vladimir Leonov, Refet Firat Yazicioglu, Tom Torfs, C. Van Hoof, Niels. E. Posthuma, and Ruud J.M. Vullers. Wearable Battery-free Wireless 2-Channel EEG Systems Powered by Energy Scavengers. **Sens. Transducers J.**, 94(7):103 – 115, 2008.

[117] Eugene Lepeschkin and Borys Surawicz. The measurement of the qt interval of the electrocardiogram. **Circulation**, 6(3):378–388, 1952.

[118] RH Bayford. Bioimpedance tomography (electrical impedance tomography). **Annu. Rev. Biomed. Eng.**, 8:63–91, 2006.

[119] G. G. Wallace, S. E. Moulton, and G. M. Clark. Electrode-cellular interface. **Science**, 324(5924):185–186, 2009. doi: 10.1126/science.1168346. URL http://www.sciencemag.org/content/324/5924/185.short.

[120] John A Rogers and Yonggang Huang. A curvy, stretchy future for electronics. **Proc. Natl. Acad. Sci. U.S.A.**, 106(27):10875–10876, 2009.

[121] Siegfried Bauer, Simona Bauer-Gogonea, Ingrid Graz, Martin Kaltenbrunner, Christoph Keplinger, and Reinhard Schwödiauer. 25th anniversary article: A soft future: From robots and sensor skin to energy harvesters. **Adv. Mater.**, 26(1):149–162, 2014.

[122] John A Rogers, Takao Someya, and Yonggang Huang. Materials and mechanics for stretchable electronics. **Science**, 327(5973):1603–1607, 2010.

[123] Andrew Carlson, Audrey M Bowen, Yonggang Huang, Ralph G Nuzzo, and John A Rogers. Transfer printing techniques for materials assembly and micro/nanodevice fabrication. **Adv. Mater.**, 24(39):5284–5318, 2012.

[124] Changhyun Pang, Chanseok Lee, and Kahp-Yang Suh. Recent advances in flexible sensors for wearable and implantable devices. **J. Appl. Polym. Sci.**, 130(3):1429–1441, 2013.

[125] Roar R Søndergaard, Markus Hösel, and Frederik C Krebs. Roll-to-roll fabrication of large area functional organic materials. **J. Polym. Sci., Part B: Polym. Phys.**, 51(1):16–34, 2013.

[126] Felippe J. Pavinatto. Biosensors with printed active layer. **Display and Imaging**, 2:69–91, 2015.

[127] Gary C Jensen, Colleen E Krause, Gregory A Sotzing, and James F Rusling. Inkjet-printed gold nanoparticle electrochemical arrays on plastic. application to immunodetection of a cancer biomarker protein. **Phys. Chem. Chem. Phys.**, 13(11):4888–4894, 2011.

[128] Janne Jalo, Hannu P Sillanpaa, and Riku M Makinen. Radio interface design for inkjet-printed biosensor applications. **Prog. Electromagn. Res.**, 142:409–422, 2013.

[129] William F Jackson and Brian R Duling. Toxic effects of silver-silver chloride electrodes on vascular smooth muscle. **Circ. Res.**, 53(1):105–108, 1983.

[130] Yang Yu, Jie Zhang, and Jing Liu. Biomedical implementation of liquid metal ink as drawable ecg electrode and skin circuit. **PLoS One**, 8(3):e58771, 2013.

[131] Dae-Hyeong Kim, Nanshu Lu, Rui Ma, Yun-Soung Kim, Rak-Hwan Kim, Shuodao Wang, Jian Wu, Sang Min Won, Hu Tao, Ahmad Islam, et al. Epidermal electronics. **Science**, 333(6044):838–843, 2011.

[132] Dae-Hyeong Kim, Jianliang Xiao, Jizhou Song, Yonggang Huang, and John A Rogers. Stretchable, curvilinear electronics based on inorganic materials. **Adv. Mater.**, 22(19): 2108–2124, 2010.

[133] Vivek Subramanian, Jialiang Cen, Alejandro de la Fuente Vornbrock, Gerd Grau, Hongki Kang, Rungrot Kitsomboonloha, Daniel Soltman, and Huai-Yuan Tseng. High-speed printing of transistors: From inks to devices. **Proc. IEEE**, 103(4):567–582, 2015.

[134] Alexander Kamyshny, Matti Ben-Moshe, Shai Aviezer, and Shlomo Magdassi. Ink-jet printing of metallic nanoparticles and microemulsions. **Macromol. Rapid Commun.**, 26 (4):281–288, 2005.

[135] Jacob A Sadie and Vivek Subramanian. Three-dimensional inkjet-printed interconnects using functional metallic nanoparticle inks. **Adv. Funct. Mater.**, 24(43):6834–6842, 2014.

[136] Valerio Zardetto, Thomas M Brown, Andrea Reale, and Aldo Di Carlo. Substrates for flexible electronics: A practical investigation on the electrical, film flexibility, optical, temperature, and solvent resistance properties. **J. Polym. Sci., Part B: Polym. Phys.**, 49 (9):638–648, 2011.

[137] Daniel Huang, Frank Liao, Steven Molesa, David Redinger, and Vivek Subramanian. Plastic-compatible low resistance printable gold nanoparticle conductors for flexible electronics. **J. Electrochem. Soc.**, 150(7):G412–G417, 2003.

[138] Teymur Bakhishev and Vivek Subramanian. Investigation of gold nanoparticle inks for low-temperature lead-free packaging technology. **J. Electron. Mater.**, 38(12):2720–2725, 2009.

[139] Ashish Gupta, Saumen Mandal, Monica Katiyar, and Yashowanta N Mohapatra. Film processing characteristics of nano gold suitable for conductive application on flexible substrates. **Thin Solid Films**, 520(17):5664–5670, 2012.

[140] Jaewon Chung, Seunghwan Ko, Nicole R Bieri, Costas P Grigoropoulos, and Dimos Poulikakos. Conductor microstructures by laser curing of printed gold nanoparticle ink. **Appl. Phys. Lett.**, 84(5):801–803, 2004.

[141] Jolke Perelaer, Patrick J Smith, Dario Mager, Daniel Soltman, Steven K Volkman, Vivek Subramanian, Jan G Korvink, and Ulrich S Schubert. Printed electronics: the challenges involved in printing devices, interconnects, and contacts based on inorganic materials. **J. Mater. Chem.**, 20(39):8446–8453, 2010.

[142] Steven K Volkman, Shong Yin, Teymur Bakhishev, Kanan Puntambekar, Vivek Subramanian, and Michael F Toney. Mechanistic studies on sintering of silver nanoparticles. **Chem. Mater.**, 23(20):4634–4640, 2011.

[143] XM Lin, CM Sorensen, and KJ Klabunde. Digestive ripening, nanophase segregation and superlattice formation in gold nanocrystal colloids. **J. Nanopart. Res.**, 2(2):157–164, 2000.

[144] Amy Liao, Monica C Lin, Lauren C Ritz, Sarah L Swisher, David Ni, Kaylee Mann, Yasser Khan, Shuvo Roy, Michael R Harrison, Ana C Arias, et al. Impedance sensing device for monitoring ulcer healing in human patients. In *Engineering in Medicine and Biology Society (EMBC), 2015 37th Annual International Conference of the IEEE*, pages 5130–5133. IEEE, 2015.

[145] Leeya Engel, Chengming Liu, Nofar Mintz Hemed, Yasser Khan, Ana Claudia Arias, Yosi Shacham-Diamand, Slava Krylov, and Liwei Lin. Local electrochemical control of hydrogel microactuators in microfluidics. **Journal of Micromechanics and Microengineering**, 2018. doi: 10.1088/1361-6439/aacc31. URL http://dx.doi.org/10.1088/1361-6439/aacc31.

[146] Chandan K Sen, Gayle M Gordillo, Sashwati Roy, Robert Kirsner, Lynn Lambert, Thomas K Hunt, Finn Gottrup, Geoffrey C Gurtner, and Michael T Longaker. Human skin wounds: a major and snowballing threat to public health and the economy. **Wound Repair and Regeneration**, 17(6):763–771, 2009.

[147] David R Bickers, Henry W Lim, David Margolis, Martin A Weinstock, Clifford Goodman, Eric Faulkner, Ciara Gould, Eric Gemmen, and Tim Dall. The burden of skin diseases: 2004: A joint project of the american academy of dermatology association and the society for investigative dermatology. **Journal of the American Academy of Dermatology**, 55 (3):490–500, 2006.

[148] Ali Moin, Andy Zhou, Abbas Rahimi, Simone Benattiz, Alisha Menon, Senam Tamakloe, Jonathan Ting, Natasha Yamamoto, Yasser Khan, Fred Burghardt, Luca Beniniyz, Ana C. Arias, and Jan M. Rabaey. A brain-inspired emg gesture recognition system with flexible, high-density sensors and high-dimensional classifier. 2018. In preparation.

[149] Mark Yelderman and William New Jr. Evaluation of pulse oximetry. **Anesthesiology**, 59 (4):349–352, 1983.

[150] J.G. Webster. **Design of Pulse Oximeters**. Series in Medical Physics and Biomedical Engineering. Taylor & Francis, 2002. ISBN 9781420050790.

[151] JH Burroughes, DDC Bradley, AR Brown, RN Marks, K Mackay, RH Friend, PL Burns, and AB Holmes. Light-emitting diodes based on conjugated polymers. **nature**, 347(6293): 539–541, 1990.

[152] A.C. Morteani, A.S. Dhoot, J.-S. Kim, C. Silva, N.C. Greenham, C. Murphy, E. Moons, S. Cin, J.H. Burroughes, and R.H. Friend. Barrier-free electronhole capture in polymer blend heterojunction light-emitting diodes. **Advanced Materials**, 15(20):1708–1712, 2003. ISSN 1521-4095.

[153] Zhicai He, Chengmei Zhong, Shijian Su, Miao Xu, Hongbin Wu, and Yong Cao. Enhanced power-conversion efficiency in polymer solar cells using an inverted device structure. **Nature Photonics**, 6(9):591–595, 2012.

[154] Julien Penders, Bert Gyselinckx, Ruud Vullers, Olivier Rousseaux, Mladen Berekovic, Michael De Nil, Chris Van Hoof, Julien Ryckaert, Refet Firat Yazicioglu, Paolo Fiorini, et al. Human++: Emerging technology for body area networks. In *VLSI-SoC: Research Trends in VLSI and Systems on Chip*, pages 377–397. Springer, 2008.

[155] Lijia Pan, Alex Chortos, Guihua Yu, Yaqun Wang, Scott Isaacson, Ranulfo Allen, Yi Shi, Reinhold Dauskardt, and Zhenan Bao. An ultra-sensitive resistive pressure sensor based on hollow-sphere microstructure induced elasticity in conducting polymer film. **Nature communications**, 5, 2014.

[156] Y Mendelson, RJ Duckworth, and G Comtois. A wearable reflectance pulse oximeter for remote physiological monitoring. In *Engineering in Medicine and Biology Society, 2006. EMBS'06. 28th Annual International Conference of the IEEE*, pages 912–915. IEEE, 2006.

[157] Jin Jeon, Han-Bo-Ram Lee, and Zhenan Bao. Flexible wireless temperature sensors based on ni microparticle-filled binary polymer composites. **Advanced Materials**, 25(6):850–855, 2013. ISSN 1521-4095.

[158] Takao Someya, Yusaku Kato, Tsuyoshi Sekitani, Shingo Iba, Yoshiaki Noguchi, Yousuke Murase, Hiroshi Kawaguchi, and Takayasu Sakurai. Conformable, flexible, large-area networks of pressure and thermal sensors with organic transistor active matrixes. **Proceedings of the National Academy of Sciences of the United States of America**, 102 (35):12321–12325, 2005.

[159] Tsuyoshi Sekitani, Ute Zschieschang, Hagen Klauk, and Takao Someya. Flexible organic transistors and circuits with extreme bending stability. **Nature materials**, 9(12):1015–1022, 2010.

[160] Donghee Son, Jongha Lee, Shutao Qiao, Roozbeh Ghaffari, Jaemin Kim, Ji Eun Lee, Changyeong Song, Seok Joo Kim, Dong Jun Lee, Samuel Woojoo Jun, et al. Multifunctional wearable devices for diagnosis and therapy of movement disorders. **Nature nanotechnology**, 9(5):397–404, 2014.

[161] Y. Sun and J.A. Rogers. Inorganic semiconductors for flexible electronics. **Advanced Materials**, 19(15):1897–1916, 2007. ISSN 1521-4095.

[162] Rui-Qing Ma, Richard Hewitt, Kamala Rajan, Jeff Silvernail, Ken Urbanik, Michael Hack, and Julie J Brown. Flexible active-matrix oled displays: Challenges and progress. **Journal of the Society for Information Display**, 16(1):169–175, 2008.

[163] Ching W Tang. Two-layer organic photovoltaic cell. **Applied Physics Letters**, 48(2): 183–185, 1986.

[164] Graeme Williams, Christopher Backhouse, and Hany Aziz. Integration of organic light emitting diodes and organic photodetectors for lab-on-a-chip bio-detection systems. **Electronics**, 3(1):43–75, 2014. ISSN 2079-9292.

[165] M Kreyenschmidt, G Klaerner, T Fuhrer, J Ashenhurst, S Karg, WD Chen, VY Lee, JC Scott, and RD Miller. Thermally stable blue-light-emitting copolymers of poly(alkylfluorene). **Macromolecules**, 31(4):1099–1103, FEB 24 1998. ISSN 0024-9297. doi: {10.1021/ma970914e}.

[166] Craig H Peters, IT Sachs-Quintana, William R Mateker, Thomas Heumueller, Jonathan Rivnay, Rodigo Noriega, Zach M Beiley, Eric T Hoke, Alberto Salleo, and Michael D McGehee. The mechanism of burn-in loss in a high efficiency polymer solar cell. **Advanced Materials**, 24(5):663–668, 2012.

[167] Marc Koetse, Peter Rensing, Gert van Heck, Ruben Sharpe, Bart Allard, Fokko Wieringa, Peter Kruijt, Nicole Meulendijks, Henk Jansen, and Herman Schoo. In plane optical sensor based on organic electronic devices. In *Photonic Devices+ Applications*, pages 70541I–70541I. International Society for Optics and Photonics, 2008.

[168] Marc M Koetse, Peter A Rensing, Gert T van Heck, Nicole NMM Meulendijks, Peter GM Kruijt, Erik H Enting, FP Wieringa, and Herman FM Schoo. Optical sensor platforms by modular assembly of organic electronic devices. In *Sensors Applications Symposium, 2008. SAS 2008. IEEE*, pages 1–3. IET, 2008.

[169] Yindar Chuo, Badr Omrane, Clint Landrock, Jasbir N Patel, and Bozena Kaminska. Platform for all-polymer-based pulse-oximetry sensor. In *Sensors, 2010 IEEE*, pages 155–159. IEEE, 2010.

[170] Jonathan V Caspar, Edward M Kober, B Patrick Sullivan, and Thomas J Meyer. Application of the energy gap law to the decay of charge-transfer excited states. **Journal of the American Chemical Society**, 104(2):630–632, 1982.

[171] Jonathan R Sommer, Richard T Farley, Kenneth R Graham, Yixing Yang, John R Reynolds, Jiangeng Xue, and Kirk S Schanze. Efficient near-infrared polymer and organic light-emitting diodes based on electrophosphorescence from (tetraphenyltetranaphtho [2, 3] porphyrin) platinum (ii). **ACS applied materials & interfaces**, 1(2):274–278, 2009.

[172] Stephen R Forrest, Donal DC Bradley, and Mark E Thompson. Measuring the efficiency of organic light-emitting devices. **Advanced Materials**, 15(13):1043–1048, 2003.

[173] Ji-Seon Kim, Linus Lu, Paiboon Sreearunothai, Alex Seeley, Keng-Hoong Yim, Annamaria Petrozza, Craig E Murphy, David Beljonne, Jérôme Cornil, and Richard H Friend. Optoelectronic and charge transport properties at organic- organic semiconductor interfaces: Comparison between polyfluorene-based polymer blend and copolymer. **Journal of the American Chemical Society**, 130(39):13120–13131, 2008.

[174] Ji-Seon Kim, Richard H. Friend, Ilaria Grizzi, and Jeremy H. Burroughes. Spin-cast thin semiconducting polymer interlayer for improving device efficiency of polymer light-emitting diodes. **Applied Physics Letters**, 87(2):023506, 2005.

[175] Th Förster. 10th spiers memorial lecture. transfer mechanisms of electronic excitation. **Discuss. Faraday Soc.**, 27:7–17, 1959.

[176] Y. Yao, Y. Liang, V. Shrotriya, S. Xiao, L. Yu, and Y. Yang. Plastic near-infrared photodetectors utilizing low band gap polymer. **Advanced Materials**, 19(22):3979–3983, 2007. ISSN 1521-4095.

[177] Julian M Goldman, Michael T Petterson, Robert J Kopotic, and Steven J Barker. Masimo signal extraction pulse oximetry. **Journal of Clinical Monitoring and Computing**, 16(7): 475–483, 2000.

[178] Rasoul Yousefi, Mehrdad Nourani, Sarah Ostadabbas, and Issa Panahi. A motion-tolerant adaptive algorithm for wearable photoplethysmographic biosensors. **Biomedical and Health Informatics, IEEE Journal of**, 18(2):670–681, 2014.

[179] WG Zijlstra, A Buursma, and WP Meeuwsen-Van der Roest. Absorption spectra of human fetal and adult oxyhemoglobin, de-oxyhemoglobin, carboxyhemoglobin, and methemoglobin. **Clinical chemistry**, 37(9):1633–1638, 1991.

[180] Narendra S. Trivedi, Ahmed F. Ghouri, Nitin K. Shah, Eugene Lai, and Steven J. Barker. Effects of motion, ambient light, and hypoperfusion on pulse oximeter function. **Journal of Clinical Anesthesia**, 9(3):179 – 183, 1997. ISSN 0952-8180.

[181] Jakaria Ahmad, Kateryna Bazaka, Liam J Anderson, Ronald D White, and Mohan V Jacob. Materials and methods for encapsulation of opv: A review. **Renewable and Sustainable Energy Reviews**, 27:104–117, 2013.

[182] Jin-Seong Park, Heeyeop Chae, Ho Kyoon Chung, and Sang In Lee. Thin film encapsulation for flexible am-oled: a review. **Semiconductor Science and Technology**, 26(3): 034001, 2011.

[183] John G Webster. **Design of pulse oximeters**. CRC Press, 1997.

[184] Tran Quang Trung and Nae-Eung Lee. Flexible and stretchable physical sensor integrated platforms for wearable human-activity monitoring and personal healthcare. **Advanced Materials**, 28(22):4338–4372. doi: 10.1002/adma.201504244.

[185] Suji Choi, Hyunjae Lee, Roozbeh Ghaffari, Taeghwan Hyeon, and Dae-Hyeong Kim. Recent advances in flexible and stretchable bio-electronic devices integrated with nanomaterials. **Advanced Materials**, 28(22):4203–4218, 2016.

[186] Takao Someya, Zhenan Bao, and George G Malliaras. The rise of plastic bioelectronics. **Nature**, 540(7633):379, 2016.

[187] Mark Poliks, James Turner, Kanad Ghose, Zhanpeng Jin, Mohit Garg, Qiong Gui, Ana Arias, Yasser Kahn, Mark Schadt, and Frank Egitto. A wearable flexible hybrid electronics ecg monitor. In *Electronic Components and Technology Conference (ECTC), 2016 IEEE 66th*, pages 1623–1631. IEEE, 2016.

[188] Sungmook Jung, Seungki Hong, Jaemin Kim, Sangkyu Lee, Taeghwan Hyeon, Minbaek Lee, and Dae-Hyeong Kim. Wearable fall detector using integrated sensors and energy devices. **Scientific reports**, 5:17081, 2015.

[189] Suji Choi, Sang Ihn Han, Dongjun Jung, Hye Jin Hwang, Chaehong Lim, Soochan Bae, Ok Kyu Park, Cory M Tschabrunn, Mincheol Lee, Sun Youn Bae, et al. Highly conductive, stretchable and biocompatible ag–au core–sheath nanowire composite for wearable and implantable bioelectronics. **Nature nanotechnology**, page 1, 2018.

[190] Muhammad Fahad Farooqui and Atif Shamim. Low cost inkjet printed smart bandage for wireless monitoring of chronic wounds. **Scientific reports**, 6:28949, 2016.

[191] Joanna M Nassar, Kush Mishra, Kirklann Lau, Andres A Aguirre-Pablo, and Muhammad M Hussain. Recyclable nonfunctionalized paper-based ultralow-cost wearable health monitoring system. **Advanced Materials Technologies**, 2(4):1600228, 2017.

[192] Aminy E. Ostfeld, Abhinav M. Gaikwad, Yasser Khan, and Ana C. Arias. High-performance flexible energy storage and harvesting system for wearable electronics. **Scientific Reports**, 6:26122, 2016. ISSN 2045-2322. doi: 10.1038/srep26122. URL http://www.nature.com/srep/2016/160517/srep26122/full/srep26122.html.

[193] Tomoyuki Yokota, Peter Zalar, Martin Kaltenbrunner, Hiroaki Jinno, Naoji Matsuhisa, Hiroki Kitanosako, Yutaro Tachibana, Wakako Yukita, Mari Koizumi, and Takao Someya. Ultraflexible organic photonic skin. **Science Advances**, 2(4):e1501856, 2016.

[194] Jeonghyun Kim, Giovanni A Salvatore, Hitoshi Araki, Antonio M Chiarelli, Zhaoqian Xie, Anthony Banks, Xing Sheng, Yuhao Liu, Jung Woo Lee, Kyung-In Jang, et al. Battery-free, stretchable optoelectronic systems for wireless optical characterization of the skin. **Science Advances**, 2(8):e1600418, 2016.

[195] Donggeon Han, Yasser Khan, Jonathan Ting, Simon M. King, Nir Yaacobi-Gross, Martin J. Humphries, Christopher J. Newsome, and Ana C. Arias. Flexible blade-coated multicolor polymer light-emitting diodes for optoelectronic sensors. **Advanced Materials**, 29(22): 1606206. doi: 10.1002/adma.201606206.

[196] M Raghu Ram, K Venu Madhav, E Hari Krishna, Nagarjuna Reddy Komalla, and K Ashoka Reddy. A novel approach for motion artifact reduction in ppg signals based on as-lms adaptive filter. **IEEE Transactions on Instrumentation and Measurement**, 61 (5):1445–1457, 2012.

[197] Fulai Peng, Zhengbo Zhang, Xiaoming Gou, Hongyun Liu, and Weidong Wang. Motion artifact removal from photoplethysmographic signals by combining temporally constrained independent component analysis and adaptive filter. **Biomedical engineering online**, 13(1):50, 2014.

[198] Hyonyoung Han, Min-Joon Kim, and Jung Kim. Development of real-time motion artifact reduction algorithm for a wearable photoplethysmography. In *Engineering in Medicine and Biology Society, 2007. EMBS 2007. 29th Annual International Conference of the IEEE*, pages 1538–1541. IEEE, 2007.

[199] Zhilin Zhang, Zhouyue Pi, and Benyuan Liu. Troika: A general framework for heart rate monitoring using wrist-type photoplethysmographic signals during intensive physical exercise. **IEEE Transactions on biomedical engineering**, 62(2):522–531, 2015.

[200] Zhilin Zhang. Heart rate monitoring from wrist-type photoplethysmographic (ppg) signals during intensive physical exercise. In *Signal and Information Processing (GlobalSIP), 2014 IEEE Global Conference on*, pages 698–702. IEEE, 2014.

[201] Shu-Tyng Lin, Wei-Hao Chen, and Yuan-Hsiang Lin. A pulse rate detection method for mouse application based on multi-ppg sensors. **Sensors**, 17(7):1628, 2017.

[202] Kristen M Warren, Joshua R Harvey, Ki H Chon, and Yitzhak Mendelson. Improving pulse rate measurements during random motion using a wearable multichannel reflectance photoplethysmograph. **Sensors**, 16(3):342, 2016.

[203] Donggeon Han, Yasser Khan, Karthik Gopalan, Adrien Pierre, and Ana C Arias. Emission area patterning of organic light-emitting diodes (oleds) via printed dielectrics. **Advanced Functional Materials**, 28(37):1802986, 2018.

[204] Hao Qu and Jean Gotman. A patient-specific algorithm for the detection of seizure onset in long-term eeg monitoring: possible use as a warning device. **IEEE transactions on biomedical engineering**, 44(2):115–122, 1997.

[205] Mathias Baumert, Vito Starc, and Alberto Porta. Conventional qt variability measurement vs. template matching techniques: comparison of performance using simulated and real ecg. **PloS one**, 7(7):e41920, 2012.

[206] Christina Orphanidou, Timothy Bonnici, Peter Charlton, David Clifton, David Vallance, and Lionel Tarassenko. Signal-quality indices for the electrocardiogram and photoplethysmogram: Derivation and applications to wireless monitoring. **IEEE journal of biomedical and health informatics**, 19(3):832–838, 2015.

[207] Yongbo Liang, Mohamed Elgendi, Zhencheng Chen, and Rabab Ward. An optimal filter for short photoplethysmogram signals. **Scientific data**, 5:180076, 2018.

[208] Francesco Rundo, Sabrina Conoci, Alessandro Ortis, and Sebastiano Battiato. An advanced bio-inspired photoplethysmography (ppg) and ecg pattern recognition system for medical assessment. **Sensors**, 18(2):405, 2018.

[209] S Nakajimi, H Hirai, H Takase, A Kuze, and S Aoyagi. New pulsed-type earpiece oximeter (author's transl). **Kokyu to junkan. Respiration & Circulation**, 23(8):709–713, 1975.

[210] Hui Fang, Ki Jun Yu, Christopher Gloschat, Zijian Yang, Enming Song, Chia-Han Chiang, Jianing Zhao, Sang Min Won, Siyi Xu, Michael Trumpis, et al. Capacitively coupled arrays of multiplexed flexible silicon transistors for long-term cardiac electrophysiology. **Nature Biomedical Engineering**, 1(3):0038, 2017.

[211] Chi Lu, Seongjun Park, Thomas J Richner, Alexander Derry, Imogen Brown, Chong Hou, Siyuan Rao, Jeewoo Kang, Chet T Moritz, Yoel Fink, et al. Flexible and stretchable nanowire-coated fibers for optoelectronic probing of spinal cord circuits. **Science Advances**, 3(3):e1600955, 2017.

[212] Wei Gao, Sam Emaminejad, Hnin Yin Yin Nyein, Samyuktha Challa, Kevin Chen, Austin Peck, Hossain M Fahad, Hiroki Ota, Hiroshi Shiraki, Daisuke Kiriya, et al. Fully integrated wearable sensor arrays for multiplexed in situ perspiration analysis. **Nature**, 529 (7587):509, 2016.

[213] Jung Woo Lee, Renxiao Xu, Seungmin Lee, Kyung-In Jang, Yichen Yang, Anthony Banks, Ki Jun Yu, Jeonghyun Kim, Sheng Xu, Siyi Ma, et al. Soft, thin skin-mounted power management systems and their use in wireless thermography. **Proceedings of the National Academy of Sciences**, 113(22):6131–6136, 2016.

[214] Shideh Kabiri Ameri, Rebecca Ho, Hongwoo Jang, Li Tao, Youhua Wang, Liu Wang, David M Schnyer, Deji Akinwande, and Nanshu Lu. Graphene electronic tattoo sensors. **ACS Nano**, 11(8):7634–7641, 2017.

[215] Benjamin C-K Tee, Alex Chortos, Andre Berndt, Amanda Kim Nguyen, Ariane Tom, Allister McGuire, Ziliang Carter Lin, Kevin Tien, Won-Gyu Bae, Huiliang Wang, et al. A skin-inspired organic digital mechanoreceptor. **Science**, 350(6258):313–316, 2015.

[216] Jeonghyun Kim, Philipp Gutruf, Antonio M Chiarelli, Seung Yun Heo, Kyoungyeon Cho, Zhaoqian Xie, Anthony Banks, Seungyoung Han, Kyung-In Jang, Jung Woo Lee, et al.

Miniaturized battery-free wireless systems for wearable pulse oximetry. **Advanced Functional Materials**, 27(1):1604373, 2017.

[217] Rasmus G Haahr, Sune B Duun, Mette H Toft, Bo Belhage, Jan Larsen, Karen Birkelund, and Erik V Thomsen. An electronic patch for wearable health monitoring by reflectance pulse oximetry. **IEEE Transactions on Biomedical Circuits and Systems**, 6(1):45–53, 2012.

[218] Chandan K Sen. Wound healing essentials: let there be oxygen. **Wound Repair and Regeneration**, 17(1):1–18, 2009.

[219] David A Boas and Maria Angela Franceschini. Haemoglobin oxygen saturation as a biomarker: the problem and a solution. **Philosophical Transactions of the Royal Society A**, 369(1955):4407–4424, 2011.

[220] MN Ericson, MA Wilson, GL Coté, JS Baba, W Xu, M Bobrek, CL Britton, MS Hileman, MR Moore, MS Emery, et al. Implantable sensor for blood flow monitoring after transplant surgery. **Minimally Invasive Therapy & Allied Technologies**, 13(2):87–94, 2004.

[221] Dmitry Yudovsky, Laurent Pilon, Aksone Nouvong, and Kevin Schomacker. Assessing diabetic foot ulcer development risk with hyperspectral tissue oximetry. **Journal of Biomedical Optics**, 16(2):026009, 2011.

[222] Dana W Atchley. Medical shock. **Journal of the American Medical Association**, 95(6): 385–389, 1930.

[223] Arlene Duncan, Judith H Meek, Matthew Clemence, Clare E Elwell, Lidia Tyszczuk, Mark Cope, and D Delpy. Optical pathlength measurements on adult head, calf and forearm and the head of the newborn infant using phase resolved optical spectroscopy. **Physics in Medicine and Biology**, 40(2):295, 1995.

[224] Seongbeom Shin, Minyang Yang, L Jay Guo, and Hongseok Youn. Roll-to-roll cohesive, coated, flexible, high-efficiency polymer light-emitting diodes utilizing ito-free polymer anodes. **Small**, 9(23):4036–4044, 2013.

[225] J. Lzaro, R. Bailn, P. Laguna, V. Marozas, A. Rapalis, and E. Gil. Difference in pulse arrival time at forehead and at finger as a surrogate of pulse transit time. In *2016 Computing in Cardiology Conference (CinC)*, pages 269–272, Sept 2016. doi: 10.23919/CIC.2016.7868731.

[226] Neil B Hampson and Claude A Piantadosi. Near infrared monitoring of human skeletal muscle oxygenation during forearm ischemia. **Journal of Applied Physiology**, 64(6): 2449–2457, 1988.

[227] Ramesh Wariar, John N Gaffke, Ronald G Haller, and Loren A Bertocci. A modular nirs system for clinical measurement of impaired skeletal muscle oxygenation. **Journal of Applied Physiology**, 88(1):315–325, 2000.

[228] Gang Hu, Quan Zhang, Vladimir Ivkovic, and Gary E Strangman. Ambulatory diffuse optical tomography and multimodality physiological monitoring system for muscle and exercise applications. **Journal of Biomedical Optics**, 21(9):091314, 2016.

[229] Ali Moin, Andy Zhou, Abbas Rahimi, Simone Benatti, Alisha Menon, Senam Tamakloe, Jonathan Ting, Natasha Yamamoto, Yasser Khan, Fred Burghardt, et al. An emg gesture recognition system with flexible high-density sensors and brain-inspired high-dimensional classifier. In *Circuits and Systems (ISCAS), 2018 IEEE International Symposium on*, pages 1–5. IEEE, 2018.

[230] Tran Quang Trung, Subramaniyan Ramasundaram, Byeong-Ung Hwang, and Nae-Eung Lee. An all-elastomeric transparent and stretchable temperature sensor for body-attachable wearable electronics. **Advanced Materials**, 28(3):502–509, 2016.

[231] Shu Gong, Willem Schwalb, Yongwei Wang, Yi Chen, Yue Tang, Jye Si, Bijan Shirinzadeh, and Wenlong Cheng. A wearable and highly sensitive pressure sensor with ultrathin gold nanowires. **Nature Communications**, 5:3132, 2014.

[232] Yan Wang, Li Wang, Tingting Yang, Xiao Li, Xiaobei Zang, Miao Zhu, Kunlin Wang, Dehai Wu, and Hongwei Zhu. Wearable and highly sensitive graphene strain sensors for human motion monitoring. **Advanced Functional Materials**, 24(29):4666–4670, 2014.

[233] Somayeh Imani, Amay J Bandodkar, AM Vinu Mohan, Rajan Kumar, Shengfei Yu, Joseph Wang, and Patrick P Mercier. A wearable chemical-electrophysiological hybrid biosensing system for real-time health and fitness monitoring. **Nature Communications**, 7: 11650, 2016.

[234] Joseph R Corea, Anita M Flynn, Balthazar Lechêne, Greig Scott, Galen D Reed, Peter J Shin, Michael Lustig, and Ana C Arias. Screen-printed flexible mri receive coils. **Nature Communications**, 7:10839, 2016. doi: 110.1038/ncomms10839. URL http://www.nature.com/ncomms/2016/160310/ncomms10839/full/ncomms10839.html.

[235] Seiichi Takamatsu, Thomas Lonjaret, Esma Ismailova, Atsuji Masuda, Toshihiro Itoh, and George G Malliaras. Wearable keyboard using conducting polymer electrodes on textiles. **Advanced Materials**, 28(22):4485–4488, 2016.

[236] Michael Drack, Ingrid Graz, Tsuyoshi Sekitani, Takao Someya, Martin Kaltenbrunner, and Siegfried Bauer. An imperceptible plastic electronic wrap. **Advanced Materials**, 27 (1):34–40, 2015.

[237] Qing Cao, Hoon-sik Kim, Ninad Pimparkar, Jaydeep P Kulkarni, Congjun Wang, Moonsub Shim, Kaushik Roy, Muhammad A Alam, and John A Rogers. Medium-scale carbon nanotube thin-film integrated circuits on flexible plastic substrates. **Nature**, 454(7203): 495–500, 2008.

[238] B Crone, A Dodabalapur, Y-Y Lin, RW Filas, Z Bao, A LaDuca, R Sarpeshkar, HE Katz, and W Li. Large-scale complementary integrated circuits based on organic transistors. **Nature**, 403(6769):521–523, 2000.

[239] SooHyun Park, You Jung Kang, and Sheereen Majd. A review of patterned organic bioelectronic materials and their biomedical applications. **Advanced Materials**, 27(46): 7583–7619, 2015.

[240] You Seung Rim, Sang-Hoon Bae, Huajun Chen, Nicholas De Marco, and Yang Yang. Recent progress in materials and devices toward printable and flexible sensors. **Advanced Materials**, 28(22):4415–4440, 2016.

[241] Aminy E. Ostfeld, Igal Deckman, Abhinav M. Gaikwad, Claire M. Lochner, and Ana C. Arias. Screen printed passive components for flexible power electronics. **Scientific Reports**, 5:15959, 2015. doi: 10.1038/srep15959. URL http://www.nature.com/articles/srep15959.

[242] Abhinav M Gaikwad, Ana Claudia Arias, and Daniel A Steingart. Recent progress on printed flexible batteries: Mechanical challenges, printing technologies, and future prospects. **Energy Technology**, 3(4):305–328, 2015.

[243] S Schreml, RM Szeimies, L Prantl, S Karrer, M Landthaler, and P Babilas. Oxygen in acute and chronic wound healing. **British Journal of Dermatology**, 163(2):257–268, 2010.

[244] Kenneth W Campbell and Yousef Bozorgnia. Cumulative absolute velocity (cav) and seismic intensity based on the peer-nga database. **Earthquake Spectra**, 28(2):457–485, 2012.

[245] Sifat Muin and Khalid M. Mosalam. Cumulative absolute velocity as a local damage indicator of instrumented structures. **Earthquake Spectra**, 33(2):641–664, 2017. doi: 10.1193/090416EQS142M. URL https://doi.org/10.1193/090416EQS142M.

[246] Jonathan Ting*, Natasha Yamamoto*, Yasser Khan*, and Ana C. Arias. Screen-printed nickel oxide thermsitor arrays. 2019. In preparation.